
Collision Studies with Electro-Sprayed Biomolecules

PhD-Thesis

submitted in partial fulfillment of the requirements for the:

Doctor of Philosophy degree in Physics,
Faculty of Mathematics, Computer Science and Physics
University of Innsbruck

Doctor of Philosophy degree in Radiation Biology and Biophysics
Applied Atomic and Molecular Physics
NOVA School of Science and Technology
Universidade NOVA de Lisboa

by

João Francisco Favinha Ameixa, MSc.

Supervisors:

Assoz. Prof. Dr. Stephan Denifl
Institut für Ionenphysik und Angewandte Physik, Universität Innsbruck

Professor Auxiliar Dr. Filipe Ferreira da Silva
Departamento de Física, Universidade NOVA de Lisboa

June, 2020

Contents

Acronyms & symbols	XIV
Abstract	XVI
Resumo	XIX
Acknowledgments	XXII
1 Introduction	1
1.1 Cancer	1
1.1.1 Cancer treatments	2
1.2 Biological effects of ionizing radiation	3
1.3 Low-energy electron induced DNA damage	7
1.4 Radiosensitizers	10
1.4.1 Modified pyrimidines	11
1.4.2 Nitroimidazolic compounds	12
1.5 Studies with electron-affinic radiosensitizers	14
1.5.1 Electrospray ionization of radiosensitizers	15
1.5.2 Electron attachment to radiosensitizers	16
1.6 Thesis objectives and outline	17
I Collision-induced dissociation of biomolecules	21
2 Theoretical overview	23
2.1 Electrospray ionization	23
2.1.1 Ion evaporation model	25
2.1.2 Charged residue model	26
2.2 Collision-induced dissociation	27
2.2.1 Energy transfer in a collision	28

3	Experimental Setup - ESI-VG	32
3.1	Electrospray ionization source	32
3.1.1	Solution	34
3.1.2	Spray needle assembly	34
3.1.3	Inlet capillary	34
3.1.4	Ion Funnel	35
3.1.5	Octopole ion guide	39
3.1.6	Three-element lens	43
3.2	Double-sector field mass spectrometer: VG-ZAB-2SE	44
3.2.1	Magnetic sector	44
3.2.2	Electric sector	47
3.2.3	Collision cell	48
3.3	Detection system	50
3.4	Data acquisition	51
3.5	Vacuum system	52
4	Results and Discussion	55
4.1	Decomposition of protonated ronidazole	55
II	Electron interactions with biomolecules	64
5	Theoretical overview	66
5.1	Born-Oppenheimer Approximation	66
5.2	Franck-Condon principle	67
5.3	Dissociative ionization	69
5.3.1	Dissociative ionization cross section	70
5.4	Electron attachment	71
5.4.1	Electron affinity	72
5.4.2	The decay of temporary negative ions	73
5.4.3	Resonances	76
5.4.4	Dissociative electron attachment cross section	81
5.4.5	Thermodynamics in DEA	84
5.5	Ion pair formation	86
6	Experimental Setup	88
6.1	Wippi	89
6.1.1	Sample inlet	91
6.1.2	The Hemispherical Electron Monochromator	92
6.1.3	Magnetic field compensation	95
6.1.4	Quadrupole mass spectrometer	96
6.1.5	Detector	99
6.1.6	Data acquisition	100

6.1.7	Vacuum system	101
6.1.8	Measuring absolute dissociative electron attachment cross sections	101
6.2	Experimental Setup - Notre Dame University	104
6.3	Energy scale calibration	106
6.3.1	Sulfur hexafluoride, SF ₆	107
6.3.2	Carbon tetrachloride, CCl ₄	107
6.4	Determination of position and onset of resonances	108
7	Results and Discussion	112
7.1	Low-energy electron-induced decomposition of OTfU	112
7.2	Formation of resonances and anionic fragments upon electron attachment to benzaldehyde	122
8	Summary & Outlook	135
8.1	Collision-induced dissociation of biomolecules	135
8.2	Electron interactions with biomolecules	136
8.3	Outlook	138
	References	141
	Appendix	160
A	List of publications and conference abstracts	160
A.A	List of publications	160
A.B	Conference abstracts	162
A.B.1	Posters	162
A.B.2	Talks	164
B	Curriculum Vitae	165

List of Figures

1.1	Incidence of the most common types of cancer, along with the most common causes of death from different cancer types globally in 2018. Data taken from [1].	2
1.2	Dose–response relationships for deterministic (tissue reactions), as well as for stochastic effects. For deterministic effect, the dose-response is represented by a threshold-sigmoid function. For stochastic effects, the dose–response relationship is a linear (or linear-quadratic) function.	4
1.3	Timeline of radiation damage.	5
1.4	Diagram representing the time scale of reactions in water radiolysis. Taken from [13].	6
1.5	Energy distribution of secondary electrons released in water upon ionization by fast charged particles, namely 1H and 4He ions. Taken from [20].	8
1.6	Schematic energy diagram showing the type of electrons produced as a result of the irradiation of water. The zero of the energy scale corresponds to the total energy of a gas-phase electron at rest, and equilibrated (relaxed) water. The adiabatic electron affinity (AEA) of the solvated electron, e_{aq}^- (blue circle), corresponds to the negative value of the free energy of solvation (-1.6 eV). The energy required to eject the solvated electron, e_{aq}^- , into the gas-phase matches with the vertical detachment energy (VDE). The VDE value of 3.4 eV corresponds to the energy difference between the lowest energy of the solvated electron (-1.6 eV), and the zero eV electron in gas-phase. The difference between the AEA and VDE gives the solvation reorganization energy (SRE) value of about 1.8 eV. The energy of the presolvated electron, e_{pre}^- , lies between the energy of e_{aq}^- , and V_0 corresponding to the adiabatic energy of the conduction band of water (blue shaded area). Quasi-free electrons, e_{qf}^- , are in the conduction band of water. The four arrows surrounding schematically represent the binding of e_{aq}^- in a cavity formed by four water molecules.[24] Adapted from [21].	9

1.7	Single- and double-strand breaks yield obtained by irradiation of plasmid DNA with low-energy electrons with 0-4 eV (left panel [25]), and 3-20 eV (right panel [26]).	11
1.8	With radiation alone, a given level (A) of tumor control is possible for a maximum tolerable level of normal, or healthy, tissue damage (C). In the presence of the radiosensitizer drug, a higher local tumor control (B) is achieved at a lower radiation dose, while keeping the same level of normal tissue damage (c). Taken from [9].	12
1.9	Molecular structure of three halogen-containing radiosensitizers.	13
1.10	Molecular structure of three nitroimidazolic compounds.	14
2.1	Schematic representation of an ESI source operated for positive ions. Adapted from [90].	24
2.2	The ion evaporation model suggests that an ion is formed by direct ejection from a charged nanodroplet. ΔG denotes the height of the activation barrier for the ejection process. Adapted from [90] and [95].	26
2.3	The release of an ion, as suggested by the charged residue model. Adapted from [90].	27
2.4	Schematic of a collision cell for CID experiments in a tandem mass spectrometer. The precursor ion was selected by the MS1, the ions formed due to CID were analysed by the MS2. Adapted from [55].	29
3.1	Home-built electrospray ionization source (ESI source). Different interfaces are used to guide and focus ions to different pressure stages. The ion inlet is realized by a spraying needle (A) and a heated capillary (B), delivering the ions into the ion funnel (C), followed by an octopole (D), which acts as an ion guide. The subsequent lens stack (E) guides the ion beam into the mass analyzer. Adapted from [61].	33
3.2	The effective potential $V^*(r, z)$ given as function of the z -axis in the ion funnel. The solid line represents the effective potential along the ion funnel axis, and at 1 mm off-axis is represented by the dashed line. The parameters used in the calculations are the following: m/z 1000, $V_{RF}=100$ V, $f=700$ KHz. Taken from [111].	37
3.3	The ion funnel.	38
3.4	Schematics of the electrical circuit of the ion funnel. The electrodes 6 to 34 are represented by the dashed line. Where, U_{RF} is the RF potential, while U_0 , U_1 and U_2 are DC voltages.	39
3.5	A: Cross section of a octopole. B: Schematic drawing of the home-made octopole. The eight stainless steel rods are mounted on Teflon components, while the mounting screws also serve as electrical connectors. Entrance and exit DC-only lenses are attached to the holders. Taken from [116].	40
3.6	The effective potential for multipole ion guides, namely quadrupole, octopole, hexapole, decapole and dodecapole.	42

3.7	Three-element lens.	44
3.8	Schematic representation of the VG-ZAB-SE double-sector field mass spectrometer. Adapted from [124].	45
3.9	Relationship between the direction of the magnetic field (B), velocity of the ion beam (I) and the resulting Lorentz force (F_L). Adapted from [55].	46
3.10	A double focusing mass spectrometer with reversed Nier-Johnson geometry. Adapted from [126].	48
3.11	A: Cross section of the collision cell. The helium pressure is regulated by a valve. CID of the precursor ion, m_p^+ , gives rise to a product ion m_f^+ and a neutral m_n . Adapted from [129]. Biasing the collision cell with $U_{Gascell}$ provides an post-acceleration (or deceleration) of the product ions.	49
3.12	A: Photograph of the second channeltron installed in VG-ZAB-2SE. B: The dynode (1) converts the ion beam into electrons, which are further detected by a channeltron. C: Representation of a <i>KBL 510</i> channeltron.	51
5.1	Schematic representation of various vertical transitions from the ground state of a diatomic molecule, AB , to different vibrational states v of a stable ionic state, denoted by AB^{+*} . The lower inset shows the Franck-Condon factors, f_{FC} , for several transitions. Adapted from [55].	68
5.2	Experimental total ionization cross section (TICS) for a collection of aromatic species. Adapted from [132].	70
5.3	The solid line represents an energy potential curve for neutral molecule, AB , and the dashed line is the respective molecular anion, AB^- . (A): The positive value of both AEA(AB) and VDE(AB^-) are illustrated. (B): The negative value of AEA(AB) is illustrated, as well as the positive value of the VAE(AB). Adapted from [125].	73
5.4	Schematic representation showing dissociative electron attachment to a diatomic molecule AB . The potential energy curves for the neutral ground state, AB , the anionic ground state, AB^- , and a dissociative anionic excited state AB^{*-} are represented. The electron capture process, labelled as EC, occurs within the Franck-Condon region (shaded area) and leads to the formation of a TNI. The TNI may relax through nuclear relaxation along the anionic potential curve, and autodetachment, labelled as AD, may occur until the crossing point, r_C , with the neutral potential curve. In the right-hand side axis, the energy dependence of the electron capture, σ_{EC} , as well as the ion yield for the formation of A^- , σ_{A^-} , at 0 eV is shown. At electron energies above 0 eV, the formation of B^- obtained by the reflection principle, σ_{B^-} , is also presented. Taken from [42, 140].	75
5.5	Electronic configuration for a single-particle resonance and for a two-particle one-hole resonance. Taken from [141].	76
5.6	Schematic energy diagram of transient negative ions formed by electron attachment by a diatomic molecule, AB . Adapted from [126].	77

5.7	Representation of a vibrational Feshbach resonance, where the molecular anion, AB^- , lies energetically below the ground state of the target molecule, AB . Taken from [125].	79
5.8	The effective potential describing the electron-molecule interaction, for $l \neq 0$ the electron may trapped within the centrifugal barrier. Taken from [134].	80
5.9	Schematic representation of potential energy curves for the formation of a TNI, AB^* , through a core excited shape (open channel) and a core excited Feshbach (closed channel) resonances from a molecule AB . Adapted from [134].	82
6.1	General scheme of the mass spectrometry experiments used to study low-energy electron interactions with biomolecules. Adapted from [55].	89
6.2	Schematic overview of Wippi: (1) - resistively heated oven; (2) hemispherical electron monochromator; (3) quadrupole mass spectrometer; (4) channel electron multiplier. Adapted from [158].	90
6.3	Schematic representation of the HEM. The orifice diameter, \varnothing , and the thickness, d , in mm, of a given lens is given on the left. The segmented lenses are hatched	94
6.4	Wippi lenses - A : Drawing of an electrostatic lens. B : Drawing of deflector 1. The dimensions are in mm. Adapted from [157].	95
6.5	Representation of the inner and outer hemispheres, with radius r_1 and r_2 , respectively. The pair of deflectors D1 and D2 are stainless steel wires mounted on the side-plates of the hemispheres. Adapted from [157].	96
6.6	Cross section of a quadrupole (a) for the cylindrical approximation and (b) for the hyperbolic profile of the rods. $2r_0$ is the spacing between the electrodes. Adapted from [55].	97
6.7	Stability diagram for a quadrupole mass spectrometer. Adapted from [55].	98
6.8	Mass scan of a quadrupole mass spectrometer; the stable region of a mass is shifted along a "scan line" towards the right. Adapted from [55].	98
6.9	Schematic representation of the interaction chamber of the HEM and the ion optics, namely <i>optik außen</i> , <i>optik innen</i> and the third element (grounded), of the quadrupole mass spectrometer. Taken from [157].	100
6.10	Crossed beam setup at the Notre Dame University. Please note that the electron gun was not used in the present studies. Adapted from [167].	105
6.11	A 3D representation of the electron impact ion source. Taken from [167].	106
6.12	Electron attachment cross section for the formation of the intact molecular anion SF_6^- , and fragment anions formed due to DEA to SF_6 . Taken from [163, 168].	108
6.13	Ion yield of Cl^-/CCl_4 measured with Wippi.	109
6.14	Representation of the Gaussian function used to determine the centre, area and onset of resonances. For a normal distribution, two standard-deviations from the center account for 95.45% of the values.	110

List of Tables

3.1	Model and type of the pumps used in the ESI-VG setup. All pumps were manufactured by <i>Pfeiffer Vacuum</i> . The working pressure, in mbar, achieved in each stage is also depicted.	53
6.1	The type and the designation of the lenses constituting the HEM.	93
6.2	Model, type and manufacturer of the pumps used in the Wippi setup. The base pressure, in mbar, is also depicted.	101

List of Tables

List of acronyms

- AC** alternating current
AE appearance energy
AEA adiabatic electron affinity
- BDE** bond dissociation energy
- CID** collision-induced dissociation
CRM charged residue model
CRT chemoradiation therapy
- DBS** dipole bound state
DC direct current
DEA dissociative electron attachment
DFT density functional theory
DI dissociative ionization
DSBs double-strand breaks
- EA** electron affinity
ESI electrospray ionization
- FFR1** first field-free region
FFR2 second field-free region
FWHM full width at half maximum
- HEM** hemispherical electron monochromator
HOMO highest occupied molecular orbital
HPLC high performance liquid chromatography
- IE** ionization energy
IEM ion evaporation model
IVR intramolecular vibrational redistribution
- KER** kinetic energy release

List of acronyms

LEEs low-energy electrons

LUMO lowest unoccupied molecular orbital

m/z mass-to-charge ratio

MALDI matrix-assisted laser desorption/ionization

MIKE mass analyzed ion kinetic energy

MOs molecular orbitals

OTfU 5-trifluoromethanesulfonyl-uracil

PEEK polyether ether ketone

QMS quadrupole mass spectrometer

RF radiofrequency

SEs secondary electrons

SSBs single-strand breaks

TEM trochoidal electron monochromator

TICS total ionization cross section

TNI temporary negative ion

VAE vertical attachment energy

VDE vertical detachment energy

VEA vertical electron affinity

VFR vibrational Feshbach resonance

Abstract

In this PhD thesis, the fragmentation of prototype radiosensitizer molecules for cancer radio- and chemo-therapy is investigated through gas-phase collision experiments. The main goal is to extend the current knowledge on the radiosensitization mechanism by assessing the formation of reactive species, ions and neutral radicals, which may lead to DNA damage during the early stages of radiation damage.

In the first part, a collision-induced dissociation study with protonated ronidazole carried out with a home-built electrospray ionization source coupled to a double-focusing mass spectrometer is presented. The main fragmentation pathway results from an intramolecular proton transfer reaction followed by release of neutral $-\text{NH}_2\text{CO}_2\text{H}$ fragment. This reaction was demonstrated in low- and high-energy CID experiments with partially deuterated ronidazole supported by DFT quantum chemical calculations. The second part of the thesis focuses on low-energy electron interactions with 5-trifluoromethanesulfonyl-uracil (OTfU), a modified pyrimidine, and benzaldehyde, a compound used in anti-cancer clinical trials. Crossed electron-molecular beam setups coupled with a quadrupole mass spectrometer were employed to identify the formed fragment anions, and to measure anion efficiency curves as function of the incident electron energy. In dissociative electron attachment (DEA) to OTfU, the triflate anion (OTf^-), along with the reactive uracil-5-yl radical was identified as the dominant anionic fragment. The efficient decomposition of OTfU into reactive species upon electron attachment endorses its potential as a radiosensitizer. For

benzaldehyde, in addition to the molecular anion detection, further nine fragment anions were observed with modest DEA cross sections of about $10^{-24} - 10^{-23} \text{ m}^2$. The study with partially deuterated benzaldehyde showed that the dehydrogenation of benzaldehyde is selective with respect to the incident electron energy. The formation of resonances was also theoretically investigated by electron scattering calculations, and a quantum chemical study predicted the thermochemical thresholds for the observed fragments.

The insights gained in this PhD thesis may contribute for a better understanding on radiation damage, which is of paramount importance for the design of new radiosensitizer drugs, as well as for the development of more efficient cancer treatments.

Resumo

Nesta tese de PhD, a fragmentação de fármacos radiosensibilizadores usados em radio- e quimioterapia é investigada experimentalmente através de colisões na fase gasosa. O objetivo principal é expandir o conhecimento actual sobre o mecanismo de radiosensibilização, através da avaliação da formação de espécies reactivas, iões e radicais neutros, que podem causar dano no DNA durante as fases iniciais dos efeitos da radiação.

Na primeira parte, um estudo de dissociação induzida por colisão com ronidazol realizado numa fonte de ionização por electrospray acoplada a um espectrómetro de massa dupla focagem. O canal de fragmentação principal resulta de uma reacção intramolecular de transferência de protão, seguida pela libertação do fragmento neutro $-\text{NH}_2\text{CO}_2\text{H}$. Esta reacção foi demonstrada em experiências de dissociação induzida por colisão a alta e baixa-energia com ronidazol parcialmente deuterado, e apoiadas por cálculos DFT. A segunda parte desta tese foca-se em interacções de electrões de baixa energia com 5-trifluorometilsulfonil-uracil (OTfU), uma pirimidina modificada, e com benzaldeído, um composto usado em ensaios clínicos. Equipamentos de feixes crossados electrão-molécula acoplados com um espectrómetro de massa do tipo quadrupolo foram usados para identificar os fragmentos aniónicos formados, e para medir curvas de eficiência iónica em função da energia dos electrões incidentes. Em captura electrónica dissociativa com OTfU, o anião triflato (OTf^-), junto com o radical reactivo uracilo-5-il foi identificado com o fragmento aniónico dominante. A decomposição eficiente de OTfU em espécies reactivas devido a

captura electrónica apoia o seu potencial com radiosensibilizador. Para o benzaldeído, para além da detecção do anião molecular, foram observados nove fragmentos aniónicos com secções eficazes para captura electrónica dissociativa modestas, de cerca de 10^{-24} - 10^{-23} m^2 . O estudo com benzaldeído parcialmente deuterado demonstrou que a dehidrogenização de benzaldeído é selectiva relativamente à energia dos electrões incidentes. A formação de ressonâncias foi também investigada por métodos teóricos, nomeadamente de cálculos de dispersão electrónica, e um estudo de química quântica previu os limiares termodinâmicos para a formação dos fragmentos observados.

Os conhecimentos adquiridos nesta tese de PhD poderão contribuir para uma melhor compreensão do dano por radiação, o que é fulcral para o design de novos fármacos radiosensibilizadores, assim como para o desenvolvimento de tratamentos do cancro mais eficientes.

Acknowledgments

Throughout the PhD studies, I was very lucky in having the opportunity to meet and work with very good people who helped me to grow as a scientist, as well as a better individual. Hence now it is the time and place to thank you all.

First, I acknowledge the financial support from the Portuguese National Funding Agency FCT-MCTES through grant PD/BD/114447/2016, and the by Radiation Biology and Biophysics Doctoral Training Programme (RaBBiT, PD/00193/2012); UIDB/04378/2020 (UCIBIO); and UIDB/00068/2020 (CEFITEC).

Thanks Professor Filipe Ferreira da Silva for believing in me, as well as for your friendship and for all the support, and motivation required to reach the end of this journey. Professor Stephan Deniff, thanks for your constant support and exceptional supervision. You always had a minute to advice me, to teach me, and also to encourage me. Both my supervisors, Prof. Filipe and Prof. Stephan, provided me with many opportunities to collaborate with other research groups, and to attend several international conferences. I hope the collaboration between you both remains strong for many years. Additionally, thanks Prof. Paul Scheier (Universität Innsbruck) for always having a kind word for me, as well as for the collaboration with his research group. I'm also thankful to Professor Paulo Limão-Vieira, the head of the RaBBiT PhD Programme, for the many scientific discussions from which I learned a lot. I am also thankful to both Dr. Andreas Mauracher and Dr. Michael Gatchell. They always had time to discuss science, but more important,

to chat while drinking a cup of coffee or tea. Thank you very much Michael for giving the chance to visit a state-of-art experiment like the double electrostatic ion ring experiment (DESIREE, University of Stockholm), and to work with the local research group.

Thanks to the staff members Ms Ana Cruz (CEFITEC, NOVA University Lisbon) and Chitra Perotti for all the support.

Throughout this thesis, I had the opportunity to work, and learn from further researchers and professors whom I thank for their collaboration. Namely, Professor Sylwia Ptasinska (Notre Dame University, USA) for receiving me in her group, and to Dr. Michal Ryszka who introduced me to the experiments available in the laboratory, as well as for the support and friendship during my stay in the USA. Dr. Linda Feketeová (Université Claude Bernard, France) for preparing the publication on ronidazole, as investigated in this thesis. And the research group led by Prof. Janusz Rak (University of Gdansk, Poland) that provided OTfU, a radiosensitizer investigated herein. Prof. Márcio Varella and Dr. Lucas Cornetta (Universidade de São Paulo, Brazil) for performing valuable theoretical calculations required to complement our experimental findings, especially electron attachment to benzaldehyde, as investigated in this thesis. Thanks Prof. Fábio Zappa for all the time spent together searching for *crazy* problems in VG's electronics, and for the constant support and good conversations (in portuguese) over a cup of coffee or a beer.

The colleagues from AG Denifl, firstly, my friend and former colleague Dr. Rebecca Meißner who made my stay in Innsbruck more happier, even in harder times. Dr. Jusuf "Joschi" Khreis thanks for introducing me to the ESI source and VG. Eugene Arthur-Baidoo, for sure, a good friend with whom I shared the lab in a daily basis. A big thanks mate for being so supportive! Thank you Christine for all the good moments spent together either in the lab or in the office.

Thank you to all the guys from AG Scheier, Lil'Paul, Felix Laimer, Lukas Tiefenthaler, Simon Albertini, Sigi, Faro, Lorenz Ballauf, Lorenz Kranabetter, Stefan Raggl, Dr. Josi Postler, Felix Duensing, Arne Schiller and Dr. Marcelo Goulart. The good energy and positive atmosphere of the group was very inspiring. Linnea (and Ben) thanks for being my choir friend! I guess life is better when people listen to the same music. I also acknowl-

edge Werner and Martin from the electronics workshop for fixing electronic problems in the experiments.

Thanks for all the colleagues of Laboratório de Colisões Atómicas e Moleculares, NOVA University Lisbon, Dr. Mónica Mendes, Dr. Emanuele Lange, Dr. Tiago Cunha, Dr. Alessandra Barbosa (Universidade Federal do Paraná, Brazil), André Rebelo, Sara Pereira, and the most recent colleagues, João Pereira da Silva, Sarvesh Kumar and Rodrigo Rodrigues. A special thanks for the colleagues from the RaBBiT Programme, Dr. Alexandra Loupas, Dr. Filipa Pires, and Telma Silva Marques for all the conversations and good moments.

My close friends, with whom I share a longstanding friendship since our times in Castro Verde: André Borralho, Alexandre Coelho, Filipe Carvalho, João Paulos, João Borralho, João Urbano, Miguel Henriques, and Bernardo Paiva and Sérgio André from Margem Sul. You know how important you are to me! Thanks for being who you are, each one of you. To my second family, the friends in anTUNiA, that were always present in my heart. So, many thanks my friends for keeping my head way from the work and for establishing a healthy life-work balance.

Finally, my sweet family, Tia Adelina and Primo Hugo, for the unconditional love and constant support during my stay in Innsbruck. It is very comforting to have a supportive family believing in me, day after day.

Introduction

1.1 Cancer

Cancer is a leading cause of death worldwide. Accordingly to the most recent statistics provided by the World Health Organization, in 2018, cancer caused the death of about 9.6 million people globally. Lung cancer alone accounted for 2.09 million of the total number of cancer cases diagnosed (figure 1.1), and for 1.76 million deaths worldwide.[1]

Cancer is a term used for a large group of diseases characterized by the rapid creation of abnormal cells, or also referred to as malignant or tumor cells, which have suffered genetic mutations. The uncontrolled proliferation of tumor cells throughout the body is considered the major cause of cancer death. In the process known as metastasis formation, the tumor cells leave their original location to attack several organs simultaneously, which often comprises their function. Furthermore, the fast proliferating malignant cells are competing with healthy cells for nutrients and oxygen, enhancing thus the complications arising from metastasis formation.

Although cancer can be inherited, it was observed that inherited cancer only affects $< 0.3\%$ of the world population, which results in less than 3-10% of all cancer cases annually diagnosed.[2] The non-hereditary cancers are caused by agents capable to induce changes in the DNA sequence, which in turn result in uncontrolled cell proliferation and tumor growth.[3] These changes arise from the combination of genetics with external agents, also

1.1. Cancer

known as carcinogens, including physical carcinogens, such as ionizing radiation, e.g. UV, X- and γ -rays; chemical carcinogens, such as asbestos, tobacco smoke, or food and water contaminants; and biological carcinogens, such as infections from viruses or bacterias.[1] At last, the incidence of cancer cases increases significantly with age, in principle due to a build-up of non-repaired damages in the DNA sequence which can give rise to cancer. Therefore, ageing is also considered a fundamental factor for cancer.[1] The biological effects of ionizing radiation which can lead to cancer will be discussed in section 1.2.

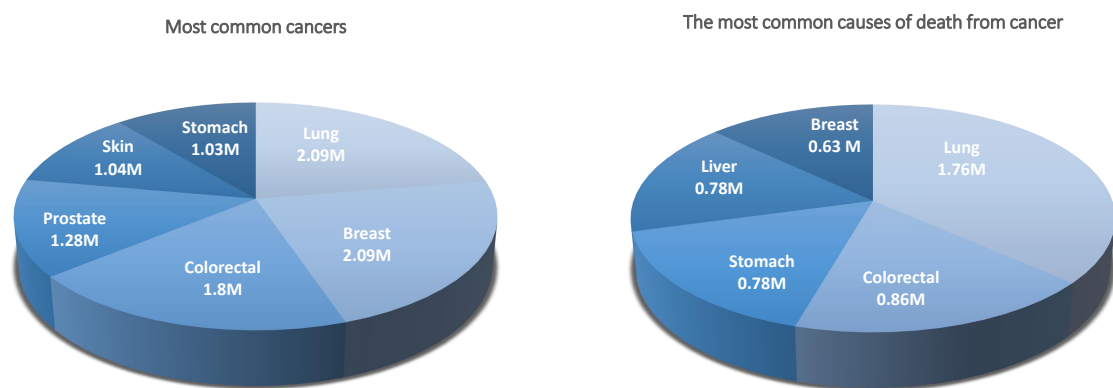


Figure 1.1. Incidence of the most common types of cancer, along with the most common causes of death from different cancer types globally in 2018. Data taken from [1].

1.1.1 Cancer treatments

The primary goals of cancer therapies are to destroy, and to prevent proliferation of tumor cells.[3] There are several treatments available depending on the type and severity of the cancer. Surgery, radio- and chemotherapy represent the three most widely used cancer therapies.[4] Surgery is the most common cancer therapy, in which the tumor is removed, as possible, from the patient body. The second most used treatment is radiation therapy. This form of therapy employs electromagnetic radiation (X-rays or γ -rays), accelerated charged particles (e.g. electrons, protons, heavy ions), or fast-neutrons to selectively damage and kill tumor cells. It is estimated that half of all patients will receive radiotherapy at some point of the treatment.[5] At last, chemotherapy represents the third most common

cancer therapy, in which chemical compounds, termed anti-cancer drugs, targeting DNA, RNA, and proteins are administered in order to trigger apoptosis (cell death) of tumor cells, however, with significant side effects to the patient.[3] A further strategy to fight cancer relies on the combination of those therapies. For instance, concomitant chemo- and radiotherapy, also referred to as chemoradiation therapy (CRT) arises as a more efficient anti-cancer strategy. In fact, several cancer studies have shown that the simultaneous administration of anti-cancer drug along with radiation, increases the survival probability of patients who received these combined therapies, with respect to those who received only radiotherapy. In CRT, the administration of anti-cancer drugs, also known as radiosensitizers, enhances the sensitivity of tumor cells towards radiation [6–8]. In the section 1.4 it will be discussed how this synergy between radiation and radiosensitizer occurs, and how it leads to an improvement in the treatment of cancer.

1.2 Biological effects of ionizing radiation

In the early 1900's, the study of biological effects of ionizing radiation had started. After carrying inadvertently a piece of radium in his vest pocket, Becquerel developed skin erythema and ulcers. In 1901, Pierre Curie reproduced the same experiment by placing radium close to his forearm. At that time, these early observations set the framework for radiobiology, which is the study of the impact of ionizing radiation on living organisms.[9] Humans are exposed to natural radiation sources, such as cosmic rays, in a daily basis, and also to artificial sources employed in medical imaging. For instance, a patient is exposed to X-rays during a CT scan, or to γ -rays produced in positron emission tomography (PET). Depending on the dose, kind of radiation, and observed endpoint, ionizing radiation, as well as fast charged particles can cause harmful effects in living organisms, which can be categorized into stochastic effects and deterministic (or non-stochastic) effects.[9, 10] Stochastic effects are due to cells that are modified by irradiation, although not killed. Carcinogenesis is the most important stochastic effect of radiation. In this case, although the probability of cancer occurrence increases linearly with the radiation dose, the severity of the cancer is independent of the radiation dose. Moreover, it is considered that there

1.2. Biological effects of ionizing radiation

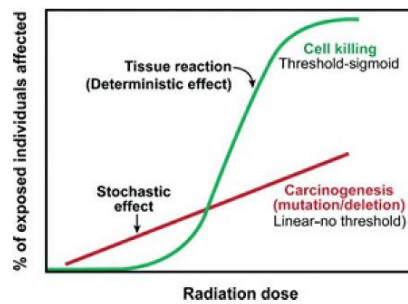


Figure 1.2. Dose–response relationships for deterministic (tissue reactions), as well as for stochastic effects. For deterministic effect, the dose–response is represented by a threshold-sigmoid function. For stochastic effects, the dose–response relationship is a linear (or linear-quadratic) function.

is no dose threshold in stochastic effects. Deterministic effects create damage due to cell death and removal from a tissue or organ. The severity due to loss of tissue function is zero at low radiation doses, and increases quickly above a given tissue-specific dose level, or also called threshold dose. Cataracts and pulmonar fibrosis are examples of adverse deterministic effects in humans. The dose–response relationship for both deterministic and stochastic effects is represented in figure 1.2.

Most biological effects of radiation arise from DNA damage. Ionizing radiation may promptly cause modifications in the DNA sequence resulting in apoptosis. However, other consequences such as carcinogenesis, cataracts or fibrosis are not immediate and may only be observed after days, months or, even some mutations may be expressed by descendants after many years.[9, 11] Therefore, it is useful to sort out the physical, chemical and biological processes triggered by ionizing radiation accordingly to their time scale, as schematically represented in figure 1.3.

In the physical stage, electronic excitation and ionization events take place within femtoseconds ($< 10^{-15}$ s) due to direct interaction of radiation with molecules constituting the biological medium. The direct action of radiation induces DNA damage through ionization or excitation of subunits of the DNA molecule. Water composes about 80% of biological systems, the set of radiation-induced reactions with water, known as water

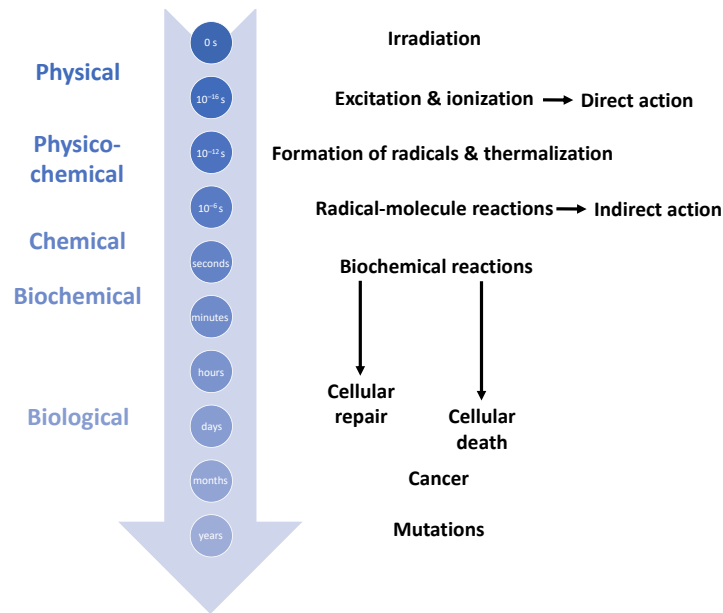
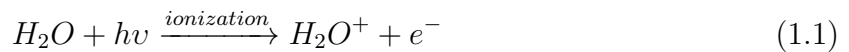


Figure 1.3. Timeline of radiation damage.

radiolysis results in a wide assortment of highly reactive species, specially hydroxyl (OH^\bullet) and hydrogen (H^\bullet) radicals, as well as secondary electrons (SEs) which are precursors for DNA damage. Figure 1.4 shows the sequence of events occurring during water radiolysis, in line with the timescale of radiation damage (figure 1.3). Water radiolysis begins with the physical stage ($< 10^{-15} - 10^{-16}s$), followed by the physico-chemical ($< 10^{-15} - 10^{-12}s$), and chemical stages ($< 10^{-6}$ up to seconds).[12] Within $< 10^{-15} - 10^{-16}s$ in the physical stage, water ionization upon irradiation yields SEs and water cations:



Water cations, H_2O^+ , may undergo ion-molecule reactions within $< 10^{-14}s$ to form a hydronium ion, H_3O^+ , and a hydroxyl radical, OH^\bullet , as follows[12]:



Electronically excited water molecules, H_2O^* can also dissociate into H^\bullet and OH^\bullet

1.2. Biological effects of ionizing radiation

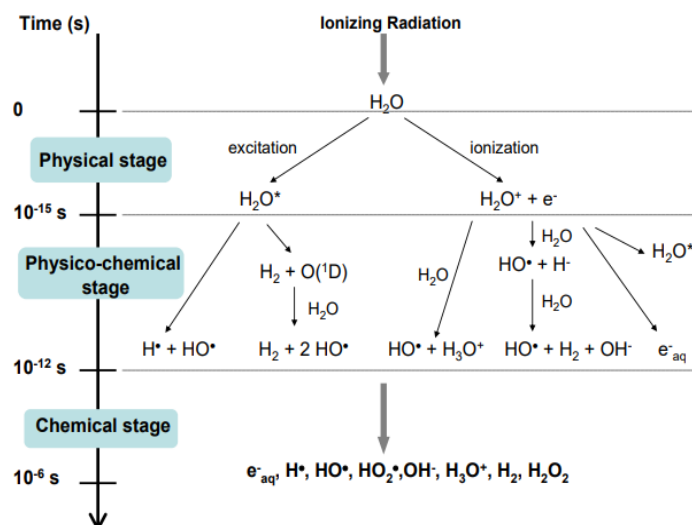


Figure 1.4. Diagram representing the time scale of reactions in water radiolysis. Taken from [13].

radicals within $< 10^{-13}$ s:



Within the physico-chemical stage of radiation damage ($\sim 10^{-12}$ s), all products are then close to be thermalized, i.e. in thermal equilibrium with the bulk. In addition to the highly reactive products of water radiolysis, OH^\bullet , H^\bullet and SEs, radicals formed by interaction of radiation with the molecules in the vicinity of the DNA molecule, namely salts, proteins and oxygen molecules, are also able to cause DNA damage. This DNA damage caused by radicals is known as free radical damage.[14] The damage observed in DNA include single-strand breaks (SSBs), double-strand breaks (DSBs), base release and tandem or clustered lesions which result from combinations of the first three lesions.[14, 15] Hence, besides the direct effect of radiation, the DNA free radical damage is called indirect effect of ionizing radiation.[9, 12] The relative importance of direct and indirect effects for DNA damage is still under investigation. It was assumed that the DNA damage by ionizing radiation was about one-third due to the direct effects, and two-thirds due to the

indirect effects.[16, 17] However, ultrafast electron transfer experiments with DNA have proposed that two-thirds of the damage is direct and one-third is indirect.[15, 18]

During the chemical stage of radiation damage, the highly reactive radicals engage in a succession of diffusion controlled radical-molecule reactions that occur within milliseconds up to seconds.[9] Afterwards, the cellular machinery proceeds to repair the radiation-induced damage in the living cell, especially in DNA during the biochemical and biological stages. SSBs and base release can be repaired, whereas severe DSBs lead in most cases to apoptosis. Nevertheless, if some lesions fail to be repaired causing cell death, the biological effect may be exhibited hours or days later. As discussed in section 1.1, among other carcinogens, ionizing radiation can cause cancer. If radiation induces a mutation in a germ cell, it can be passed to the descendants, which may not be exhibit in the future generations.

1.3 Low-energy electron induced DNA damage

About 80% of the incoming projectile's energy is deposited in the biological medium through ionization. As a result, secondary electrons (SEs) are produced at a rate of 5×10^4 per MeV of deposited energy [19] and are the most abundant secondary species formed. Through Monte Carlo simulations of liquid water irradiated with fast heavy particles with MeV, such as 1H and 4He ions, it was shown that SEs have a energy distribution peaking at about 9-10 eV, and are barely produced with energies above 100 eV [20], as shown in figure 1.5. Electrons with energy between 0 and 20 eV will be referred to as low-energy electrons (LEEs).

After the formation of SEs, they lose kinetic energy by successive excitation and ionization events, before they polarize the phonon modes of water forming electrons in different solvation (or hydration) states, namely quasi-free electrons (e_{qf}^-), pre-hydrated electrons (e_{pre}^-), and fully solvated electrons (e_{aq}^-).[12, 21] Each type of electron produced during the irradiation exhibits different reactivity with biomolecules depending on the electron energy, state of solvation and the distance to further reactive species.[21, 22] Quasi-free electrons, e_{qf}^- , are electrons in the water conduction band. The energy of quasi-

1.3. Low-energy electron induced DNA damage

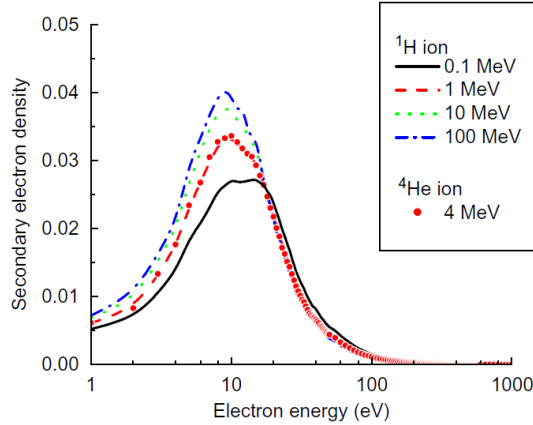


Figure 1.5. Energy distribution of secondary electrons released in water upon ionization by fast charged particles, namely 1H and 4He ions. Taken from [20].

free electrons ranges from near 0 to -0.2 eV, and e_{qf}^- has a lifetime of about 100-550 femtoseconds.[12, 22] The capture of quasi-free electrons by DNA subunits forms temporary negative ions that may result in bond cleavages via dissociative electron attachment, and thereby DNA damage.[22, 23] Pre-hydrated electrons, e_{pre}^- may be defined as electrons in a presolvated state having little or no kinetic energy.[23] Within 10^{-12} s, e_{pre}^- are solvated by the neighbouring water molecules leading to the formation of solvated electrons (e_{aq}^-) with a energy of -1.6 eV corresponding to the free energy of solvation. The energy of e_{pre}^- lies in the range of -0.2 eV to -1.6 eV, which is in between the energy of the water conduction band and the solvated electron, e_{aq}^- . [21] Although it is recognized that e_{aq}^- does not induce strand breaks in DNA, it may bind to nucleobases in aqueous phase. The nucleobase radical anions protonate, that eventually leads to production of dihydrothymine and dihydrocytosine.[21, 22] These products can create clustered damage and are relevant for radiation induced damage in DNA.

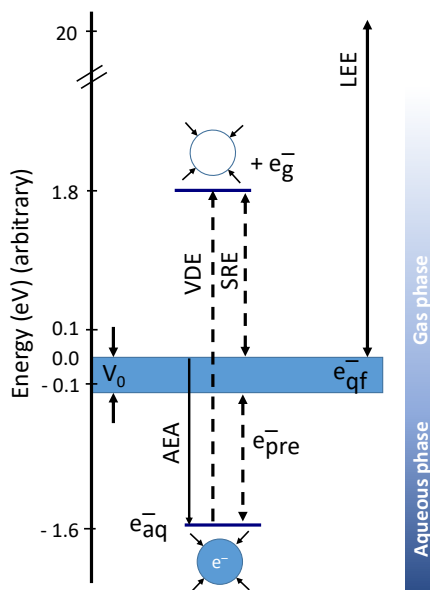


Figure 1.6. Schematic energy diagram showing the type of electrons produced as a result of the irradiation of water. The zero of the energy scale corresponds to the total energy of a gas-phase electron at rest, and equilibrated (relaxed) water. The adiabatic electron affinity (AEA) of the solvated electron, e_{aq}^- (blue circle), corresponds to the negative value of the free energy of solvation (-1.6 eV). The energy required to eject the solvated electron, e_{aq}^- , into the gas-phase matches with the vertical detachment energy (VDE). The VDE value of 3.4 eV corresponds to the energy difference between the lowest energy of the solvated electron (-1.6 eV), and the zero eV electron in gas-phase. The difference between the AEA and VDE gives the solvation reorganization energy (SRE) value of about 1.8 eV. The energy of the presolvated electron, e_{pre}^- , lies between the energy of e_{aq}^- , and V_0 corresponding to the adiabatic energy of the conduction band of water (blue shaded area). Quasi-free electrons, e_{qf}^- , are in the conduction band of water. The four arrows surrounding schematically represent the binding of e_{aq}^- in a cavity formed by four water molecules.[24] Adapted from [21].

In 2000, Boudaïffa *et al.* demonstrated that LEEs cause strand breaks in DNA [25]. In this study, both single- and double- strand breaks yields were determined by irradiation of plasmid DNA with LEEs of energy between 3-20 eV, followed by agarose gel electrophoresis analysis. As shown in figure 1.7 right panel, the DSB yield peaks at about

10 eV, and the SSB yield exhibits an intense contribution at about the same energy. These remarkable results suggest that the highest yield for DNA damage, in terms of single- and double-strand breaks, occurs at the most probable energy of SEs formed in water upon irradiation, accordingly to reference [20]. Afterwards, in 2004, Martin *et al.* covered the electron energy range from 0-4 eV. [26] The SSB yield exhibits a sharp contribution at (0.8 ± 0.3) eV with an absolute intensity of about 11×10^{-3} strand break per incident electron, as shown in figure 1.7 left panel. Furthermore, given the observed behavior of the strand break formation, it was demonstrated that LEEs efficiently damage DNA by attaching temporarily to DNA subunits (nucleobase, sugar, or phosphate group) to form temporary negative ions (TNI).[27] In a second step, TNIs decay via fragmentation yielding a negative ion and neutral fragments. This decomposition process known as dissociative electron attachment (DEA) is very efficient at low-energies, even at about 0 eV. Thus, electron-driven DNA damage occurs at energies below the DNA ionization threshold of 7.5 to 10.0 eV.[25, 28] The studies based on the interaction of LEEs with DNA provided a motivation for a significant number of gas-phase investigations with DNA sub-units, namely nucleobases adenine [29, 30], uracil [31, 32], thymine[33–35] and cytosine [36, 37], the nucleoside thymidine [38], as well as deoxyribose sugar unit [39–41].

1.4 Radiosensitizers

In concomitant chemo- and radiotherapy, or chemoradiation therapy (CRT), radiosensitizers are administered to the patient in order to enhance the sensitivity of tumor cells towards ionizing radiation.[9] Comparatively to radiotherapy alone, the addition of the radiosensitizer promotes tumor control without further damage to healthy tissue, as illustrated in figure 1.8.[9] Within the physico-chemical stage of radiation damage, radiosensitizers can be activated by LEEs released due to irradiation of the biological medium. Although the exact mode of action of radiosensitization at the molecular level is not yet clarified, the observed synergy between the radiation and the radiosensitizer, can be ascribed to LEE-driven reactions, especially dissociative electron attachment.[6, 15, 42] In the case of the radiosensitizer cisplatin ($\text{PtCl}_2(\text{NH}_3)_2$, figure 1.9) an electron with about 0 eV firstly

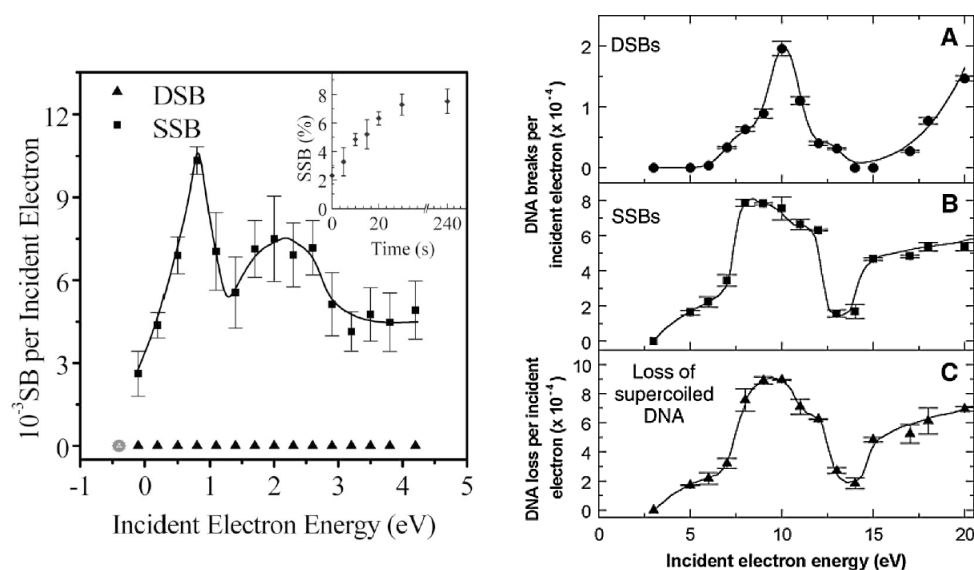


Figure 1.7. Single- and double-strand breaks yield obtained by irradiation of plasmid DNA with low-energy electrons with 0-4 eV (left panel [25]), and 3-20 eV (right panel [26]).

induces the simultaneous release of both Cl atoms through DEA, which activates cisplatin for DNA binding. Then, cisplatin covalently binds to DNA and distorts the double helix structure of DNA inhibiting replication.[6, 43] LEEs-cisplatin interactions represent a prime example of the role played by LEEs in chemoradiation therapy.

Most radiosensitizer compounds can be categorized accordingly to the mechanism of action into (i) modified pyrimidines, or (ii) nitroimidazolic radiosensitizers that selectively target hypoxic cells.[9, 44] There are more radiosensitizer classes which will not be addressed in the present work, see reference [44] for further details.

1.4.1 Modified pyrimidines

Pyrimidine derivatives, in particular halogenated pyrimidines, or other 5-substituted uracils have been suggested as radiosensitizers.[45] 5-fluorouracil is a radiosensitizer currently used in clinic. Further, thymidine analogues such as bromodeoxyuridine (BrdU) as illustrated in figure 1.9, were also proposed for CRT.[46] These compounds can be efficiently incorporated into DNA, since the dimensions of the halogen atom and the methyl group at C₅-position are similar.[44] Within the physico-chemical stage of radiation damage, the incorporation

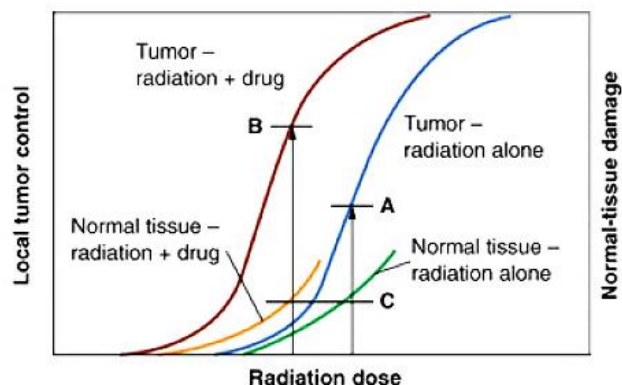


Figure 1.8. With radiation alone, a given level (A) of tumor control is possible for a maximum tolerable level of normal, or healthy, tissue damage (C). In the presence of the radiosensitizer drug, a higher local tumor control (B) is achieved at a lower radiation dose, while keeping the same level of normal tissue damage (c). Taken from [9].

of halogens, or electrophilic groups either in the nucleobase, or in the sugar moiety (e.g. gemtacicbine), results in a higher reactivity towards LEEs. The cleavage of the halogen-carbon bond by dissociative electron attachment produces a negatively charged halogen atom and a highly reactive carbon-centered radical. Subsequently, the radical can cause both single- and double-strand breaks in DNA as caused by hydroxyl radicals.[44] For instance, the interaction of LEEs with a structurally similar compound 5-bromouracil (5-BrU) has been extensively studied.[47, 48] All studies show that an electron with about 0 eV can efficiently break the C₅-Br bond resulting in Br⁻ formation, as well as uracil-5-yl radical which is a precursor for DNA strand breakage.[49]

1.4.2 Nitroimidazolic compounds

Within most solid tumors, there are regions composed of cells with low oxygen concentration, called hypoxic cells. Unfortunately, the lack of oxygen increases the resistance of tumor cells towards ionizing radiation, which reduces the efficiency of radiotherapy in treating solid tumors. This effect is the so-called "oxygen-effect", in which cells are more sensitive to ionizing radiation in the presence of oxygen, than in its absence (hypoxia).[9]

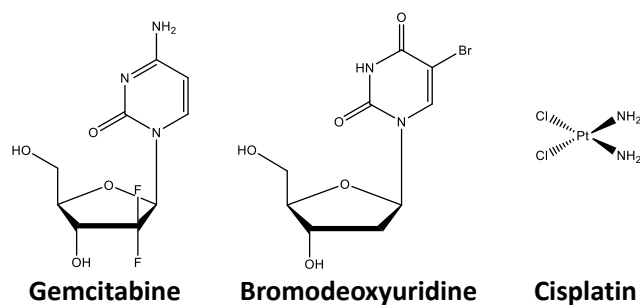


Figure 1.9. Molecular structure of three halogen-containing radiosensitizers.

The incorporation of electron-affinic radiosensitizers, which are compounds that mimic the oxygen effect in hypoxic cells and thereby increase the sensitivity towards radiation. Nitroimidazolic compounds have been proposed as radiosensitizer as they consist of a nitro moiety ($-\text{NO}_2$), an imidazole ring and a side chain. The chemical structure of different nitroimidazolic compounds are included in figure 1.10. The side chain often defines the toxicity of the compound, whereas the nitroimidazole moiety is responsible for the observed high electron-affinity.

The first studied nitroimidazolic radiosensitizer was misonidazole, a drug based on 2-nitroimidazole (see figure 1.10). Although the successful *in vitro* studies, it was verified that the composition of the side chain caused significant side effects in humans, and the concomitant use of misonidazole with radiation was therefore abandoned.[50] Further nitroimidazole-based compounds were developed in order to reduce the side effects to the patient. Nimorazole, a less toxic radiosensitizer based on 5-nitroimidazole was then proposed even in spite of its reduced sensitization efficiency compared to misonidazole. Nowadays in Danish radiotherapy centers, nimorazole is a standard drug employed for the CRT of hypoxic tumors.[51] Although a complete description of the mode of radiosensitization by nitroimidazolic compounds is still unclear, a hypothesis suggested that nitroimidazoles are prodrugs which can be activated by intracellular one-electron reductases, such as cytochrome P450 reductase, to form a radical anion. This species may be responsible for the fixation of DNA damage induced by OH radicals. [44, 52]



Figure 1.10. Molecular structure of three nitroimidazolic compounds.

1.5 Studies with electron-affinic radiosensitizers

Despite the current use of radiation along with radiosensitizers, the full potential of this form of therapy is yet not known, since the exact description of the mechanism of radiosensitization in the physico-chemical stage of radiation damage remains incomplete. Hence, in order to improve radiation therapy protocols, as well as to design novel and better radiosensitizer drugs, a comprehensive understanding of how reactive radicals and charged fragments are formed from radiosensitizer molecules upon irradiation is of paramount importance. In order to tackle this fundamental question, researchers have performed experiments with thin films, in solution, or in the gas phase.[42] Naturally, all existing approaches have advantages and drawbacks whose discussion will not, however, be addressed in the present thesis, see reference [42] for more details. A large number of research groups preferred the study of biomolecules in the gas-phase, because it allows investigations on how an isolated molecule reacts towards an energetic particle, including photons, electrons and ions.

Over the last years, mass spectrometry studies have lead to the identification of charged products formed in decomposition reactions with radiosensitizers, and therefore contributing to a better understanding of the mechanism of radiosensitization at the molecular level. Usually, two different strategies of measurement are adopted, either the top-down approach[53], or the bottom-up approach[54]. In the top-down approach, macromolecules, e.g. DNA/RNA, proteins or large radiosensitizer compounds, are transferred

to the gas-phase by matrix-assisted laser desorption/ionization (MALDI) or electrospray ionization (ESI) and identified by mass spectrometry (MS). A precursor molecular ion is then decomposed in the gas phase into product ions, which are analyzed by tandem mass spectrometry (MS/MS) techniques. Collision-induced dissociation (CID) is a widely used technique by which a molecular ion is decomposed into fragments, due to a collision with a gas, typically helium, argon or nitrogen.[55] However, high-energy CID can lead to a complex fragmentation pattern, which might be difficult to interpret. Therefore, ESI mass spectrometry is often supported by theoretical studies to clarify the formation of fragment ions. In the bottom-up approach, firstly, the studies are carried out with small molecules, or building blocks of the macromolecules, e.g. DNA or radiosensitizers. After data acquisition and further analysis, molecules of gradually increased complexity are selected to study. In electron attachment studies with biomolecules, the bottom-up approach is a tool to investigate which reactions remain and which modifications of the electron attachment process may occur in terms of resonance energies and fragmentation pathways.[42]

1.5.1 Electrospray ionization of radiosensitizers

Electrospray ionization (ESI) coupled to a tandem mass spectrometer represents a suitable method for studying the formation of biomolecular ions and clusters, and, in a second stage, the respective fragmentation.[56, 57] Feketeová *et al.*[58] have observed the formation of radical anions, $M^{\bullet-}$, for the radiosensitizers misonidazole and nimorazole, as well as for other nitroimidazole-based compounds. Hence, the formation of molecular anions of nitroimidazole-based compounds in ESI matches with the first and key step of the radiosensitization mechanism, and it allows studying fragmentation reactions of nitroimidazoles, which are important for radiation therapy as previously mentioned. In ESI of misonidazole and nimorazole, as well as for other nitroimidazole-based compounds, the protonated molecular ion, $[M + H]^+$, is the most common ion observed in positive mode.[58] The products ions formed by either collision-induced dissociation (CID, see section 2.2) and electron-induced dissociation of $[M + H]^+$ were identified by mass spectrometry. Afterwards, Pandeti *et al.*[59] have investigated the fragmentation through low-energy CID

of protonated nitroimidazolic radiosensitizers (1-methyl-5-nitroimidazole, metronidazole, ronidazole, ornidazole and nimorazole). At last, Khreis *et al.*[60] have extended the previous study by investigating high-energy CID of nimorazole and misonidazole anions using a home-built ESI source coupled to a double focusing mass spectrometer. The kinetic energy release (KER) of the most important dissociation channels was determined. In positive mode, low-energy CID of protonated metronidazole and ornidazole leads to neutral NO₂ loss, and NO loss for ronidazole and ornidazole. These two fragmentation channels were not observed for protonated nimorazole. On the other hand, NO₂⁻ formation was observed in CID of radical anion of nimorazole and metronidazole, and it was thereby suggested as ion marker for the detection of these two compounds. Moreover, the comparison between the KER values associated with the loss of the side-chain from the N1 position in nimorazole (99 meV) and metronidazole (~300 meV) suggests that the molecular structure of the side-chain is relevant for the design of novel nitroimidazolic radiosensitizers.[61] Recently, Pandeti *et al.*[62] has investigated the formation of proton bound biomolecular clusters of five different nitroimidazolic compounds and all nucleobases, and respective nucleosides.

1.5.2 Electron attachment to radiosensitizers

The electron induced-reactions with various nitroimidazoles, including nitroimidazolic radiosensitizers have been thoroughly investigated. In studies involving simpler nitroimidazole molecules, Ribar *et al.*[63] have found that the position of the nitro group affects the formation of anions upon electron attachment. The most abundant anion observed in DEA to 4- and 5-nitroimidazole is formed by single hydrogen loss, while in DEA to 2-nitroimidazole the release of neutral water represents the dominant fragmentation channel. In addition, the formation of the reactive hydroxyl radical was observed for all molecules; however the hydroxyl radical formation was much stronger for 2-nitroimidazole than for the other isomers. Thus, when considering that the mechanism of radiosensitizer is solely based on its efficient dissociation into charged fragments, and radicals, 2-nitroimidazole appears to be a better radiosensitizer.[63] Tanzer *et al.*[64, 65] showed that methylation of 4- and 5-nitroimidazole quenches completely the fragmentation in the electron energy range

below 2 eV. The theoretical study by Kossoski *et al.* [66] on electron scattering from 4- and 5-nitroimidazole demonstrated that DEA at around 1.5 eV is quenched, since the autodetachment lifetime of the π_2^* resonance is considerably shorter in the N₁-methylated forms of 4- and 5-nitroimidazole. More recently, in a study on the interaction of LEEs with bare and hydrated nimorazole, Meißner *et al.* [67] observed that nimorazole efficiently forms a radical through attachment of electrons with about 0 eV. Therefore, in addition to the enzyme-mediated reduction of nimorazole to form a cytotoxic radical anion, the electron attachment mechanism may be also responsible for the activation of the radiosensitizer nimorazole.

Electron attachment to modified pyrimidines has been extensively studied by both experimental and theoretical methods.[68] Such studies have been carried out with various molecules, including ones that have been administered in CRT treatments, as well as compounds which were not considered in anticancer therapies yet, but suggested as potential radiosensitizers. For example, 5-fluorouracil [49, 69–71], 5-chlorouracil [49, 69, 71–73], 6-chlorouracil [70, 73], 5-bromouracil [47, 48, 74–76], and 5-iodouracil [49, 77]. Further, the potential action of halogenated adenine derivatives as radiosensitizers, such as 2-fluoroadenine[78], 8-bromoadenine[79] and 2-chloroadenine[80] has been also investigated.

1.6 Thesis objectives and outline

The main objective of the present PhD thesis consists in furthering the current knowledge on the radiosensitization mechanism of potential radiosensitizer compounds. In part I, a home-built ESI source coupled to a double-focusing mass spectrometer was employed to study the fragmentation of protonated ronidazole, a nitroimidazolic compound whose radiosensitizer properties are yet under investigation. In high-energy CID of ronidazole, the most abundant fragment ion is formed by proton transfer to the side-chain followed by neutral $-\text{NH}_2\text{CO}_2\text{H}$ release. Studies with deuterated solvents were performed to shed light on the proton transfer reaction. In addition to high-energy CID, the decomposition of ronidazole was investigated in low-energy CID and supported by density functional theory

(DFT). In part II, electron attachment to radiosensitizers was investigated in two crossed electron-molecular beams setups coupled to a quadrupole mass spectrometer. In a first study, 5-trifluoromethanesulfonyl (OTfU), a potential radiosensitizer of the class of the modified pyrimidines was studied. Benzaldehyde, a compound used as anticancer agent in clinical trials, was also investigated and, the potential radiosensitization by benzaldehyde in terms of negative ion formation upon electron attachment was assessed. Both studies were supported by theoretical calculations.

The outline of this thesis is as follows:

Part I - Collision-induced dissociation of biomolecules

The goal of part I is to investigate the fundamental properties *via* high-energy collision-induced dissociation of ronidazole, a compound of the class of the nitroimidazoles, at the molecular level.

- **Chapter 2** provides an introduction on the electrospray ionization technique used for the formation of protonated ronidazole, as well as on general aspects of the collision-induced dissociation (CID) process required to support the analysis of the results.
- **Chapter 3** presents a comprehensive description of the experimental setup used to carry out the high-energy CID studies.
- **Chapter 4** contains the obtained results, namely high-energy CID of protonated ronidazole, which are summarized in a peer-reviewed scientific publication.

Part II - Electron interactions with biomolecules.

The goal of part II is to investigate the formation of anions upon the interaction of low-energy electrons with biomolecules, especially radiosensitizers.

- **Chapter 5** provides an overview of the fundamental concepts of dissociative ionization, and in more detail, electron attachment.
- **Chapter 6** presents a comprehensive description of the experimental setups employed for investigating electron attachment to OTfU and benzaldehyde. For both experimental setups, the methods used for calibration of the energy scale are presented. A description of data analysis methodology used in order to determine the

position and onset of resonances comprising DEA signals is also provided.

- **Chapter 7** contains the obtained results, electron attachment to OTfU and benzaldehyde, which are summarized in two peer-reviewed scientific publications respectively.

Finally, the thesis is summarized in chapter 8 wherein an outlook of the work is also given.

Part I

Collision-induced dissociation of biomolecules

Theoretical overview

”A few years ago the idea of making proteins or polymers “fly” by electrospray ionization seemed as improbable as a flying elephant, but today it is a standard part of modern mass spectrometers.”

Prof. Dr. John B. Fenn, Chemistry Nobel laureate (2002)

In the present chapter electrospray ionization (ESI) is described, followed by a brief description of the collision-induced dissociation process as investigated in this thesis.

2.1 Electrospray ionization

The pioneering work of Dole *et al.* [81] has shown that electrospray is a process capable to generate gas-phase ions from macro-molecules, e.g. polymers, diluted in a solution. However, the first electrospray ionization ion source coupled to a mass spectrometer was designed by Fenn and co-workers.[56, 82] In 2002, for this development, Fenn and Tanaka were awarded with the Nobel Prize in Chemistry.

The underlying principle of ESI has been deeply investigated and then summarized in the following reviews [83–86], thereafter just a short description will be provided. The sample dissolved in a suitable solution is forced through a needle located near an inlet capillary. As represented in figure 2.1, by applying a kV potential between these two

2.1. Electrospray ionization

components, a strong electric field is created. Ions of either charge state can be generated through electrospray, where cations are produced due to a positive potential of the needle with respect to the capillary, and anions due to a negative potential. As the solution emerges from the tip of the spraying needle, a mist of charged droplets, also referred to as Taylor cone, is formed [87]. Once the charged droplets leave the tip of Taylor cone, solvent molecules evaporate very quickly. Consequently, a microscopic charged droplet will shrink until a maximum charge density, which overcomes the droplet surface tension is attained, leading to droplet fission. This value of charge density is known as the Rayleigh limit, z_R . For a charged droplet of radius R and surface tension γ , it is expressed as [88]:

$$z_R = \frac{8\pi}{e} \sqrt{\varepsilon_0 \gamma R^3} \quad (2.1)$$

ε_0 denotes the vacuum permittivity. The successive fission events yield nanodroplets which are in turn closer to the Rayleigh limit. Ultimately, gas-phase ions are produced from these charged nanodroplets as a result of successive subdivision of larger microscopic droplets [83–85, 89].

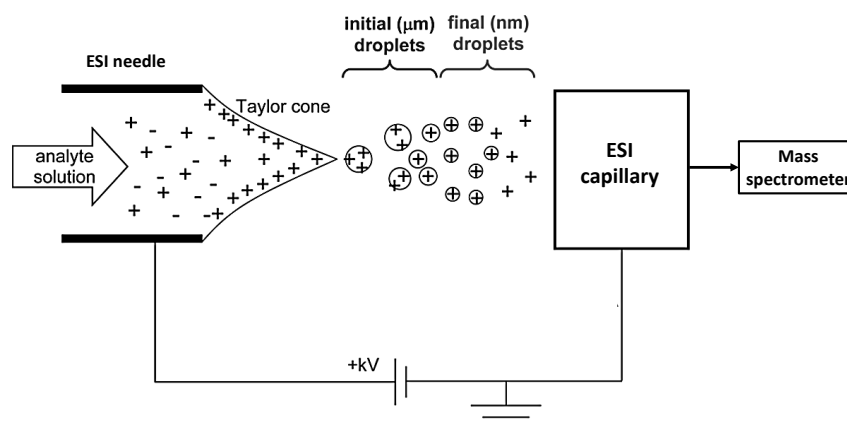


Figure 2.1. Schematic representation of an ESI source operated for positive ions. Adapted from [90].

Despite the recognition of electrospray as a standard analytical technique, the mech-

anism producing gas-phase ions is yet unclear. However, two models have been proposed, namely (i) the ion evaporation model (IEM), and (ii) the charged residue model (CRM). The most relevant aspects of those models are outlined in the following subsections.

2.1.1 Ion evaporation model

The ion evaporation model (IEM) was originally proposed by Iribarne *et al.* [91]. By considering that small (low mass weight) ions may exist in a charged state in solution, the IEM explains the generation of small gas-phase ions through electrospray. Accordingly to the IEM, the Coulombic repulsion within a charged nanodroplet at the Rayleigh limit creates an electric field sufficiently high to trigger the ejection of small solvated ions from the droplet's surface, as represented in figure 2.2. Moreover, the ejection rate constant, k for ion evaporation can be calculated by the transition state theory, as [84, 90, 91]:

$$k = \frac{k_B T}{h} \exp\left(-\frac{\Delta G}{k_B T}\right) \quad (2.2)$$

where ΔG denotes the height of the activation free energy barrier (see figure 2.2), k_B and h are the Boltzmann's and Planck's constants, respectively, and, T is the temperature. The IEM states that the activation barrier arises from the difference between the opposing forces that act on an ion just after its ejection from a droplet: (i) the solvent polarization acts as a restoring force that pulls the ion back into the droplet, and (ii) the droplet's charge tends to repel the ion from the droplet. In other words, the activation barrier is associated with the energy required to take an ion from a droplet to a certain distance from the surface [92].

The molecular dynamic simulations carried out by Ahadi *et al.* [93] have provided a detailed picture of the ejection of solvated ions from electrosprayed nanodroplets. In brief, a solvated ion located close to the surface of the droplet can move beyond the surface by the formation of a bridge consisting of H-bonded solvent molecules. As the solvated ion is ejected, the bridge collapses. As a result, the main product of the IEM is a small charged cluster consisting of the ion accompanied by a few solvent molecules.[90, 93] The solvation shell is, in principle, lost at the first vacuum stage of the ESI source, where it collides with

2.1. Electrospray ionization

particles of the background gas.[94]

In summary, the IEM is well suited to explain the direct ejection of a small ion preformed in solution to the gas-phase, as supported by theory and experiments.

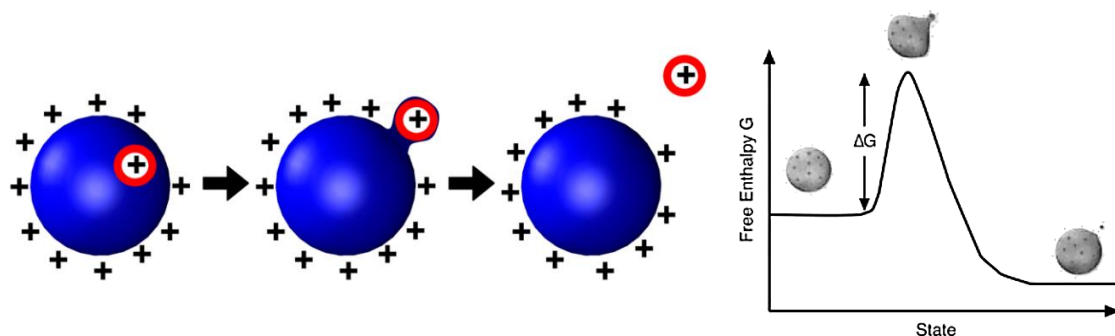


Figure 2.2. The ion evaporation model suggests that a ion is formed by direct ejection from a charged nanodroplet. ΔG denotes the height of the activation barrier for the ejection process. Adapted from [90] and [95].

2.1.2 Charged residue model

The charged residue model (CRM) was originally proposed by Dole *et al.* [81] to explain the production of gas-phase polymer ions. Today, it is widely accepted that CRM explains properly the release of large molecules, like proteins, into the gas-phase. In fact, de la Mora [96] has demonstrated that CRM is the only operative mechanism for producing gas-phase ions from species heavier than 6500 Da.

In summary, CRM considers that solvent evaporation occurs from nanodroplets at the Rayleigh-limit, until they contain a single analyte molecule. As the last solvent molecule evaporates, a fraction of the vanishing droplet's charge is transferred to the analyte molecule becoming thus a gas-phase ion. The figure 2.3 provides a representation of CRM.[84, 90, 97] However, the nanodroplets remain intact even at Rayleigh limit, which implies that the droplet loses charges while its radius decreases. This charge reduction can occur by evaporation of small ions, as explained by the IEM.[90]

Molecular dynamic simulations of the CRM are complicated due to the long (μs)

timescale of the evaporation event. However, some theoretical investigations have confirmed that a solvation shell around a protein is able to trap the analyte within the droplet [98–100], which supports the CRM. Additionally, mass spectrometry studies with globular proteins have reported that ESI produces ions $[M + z_r H]^{z_r^+}$ with a number of charges z_r^+ close to Rayleigh limit (equation 2.1) determined for a water droplet with the same diameter than the protein.[96]

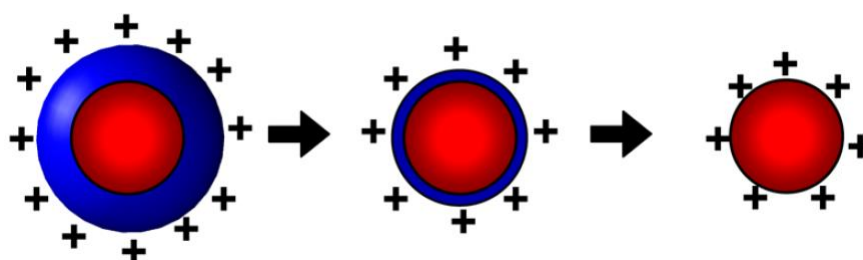


Figure 2.3. The release of an ion, as suggested by the charged residue model. Adapted from [90].

In spite of the proposed methods for ion production by electrospray, more studies are required to fully assess the predictions obtained by these models. For example, studies on where the borders that divide the IEM and CRM models are located in terms of analyte size, structure and polarity are required.[89] Hence *”it is possible that additional ESI mechanisms will be discovered in the future”*, as stated by Konermann *et al.* [90]. For instance, Metwally *et al.*[101] have proposed a new ESI model, referred to as the chain ejection model, to explain the ejection of nonpolar polymer chains from charged nanodroplets.

2.2 Collision-induced dissociation

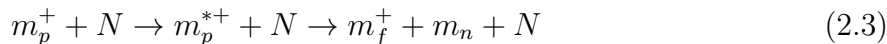
In mass spectrometry, the most widely used collision technique is collision-induced dissociation (CID) of a selected precursor ion.[55] CID is a process by which a stable projectile ion is decomposed into product ions, as a result of a collision with a collisional gas’ particle. Usually, noble and inert gases, such as He, Ar or N₂, serve as collisional gases. Therefore,

the CID process provides insights about the structure of the precursor ion.

A tandem mass spectrometer (MS1/MS2) is required to probe the product ions formed due to a CID reaction with a mass-selected precursor ion.[55] As shown in figure 2.4, CID can be achieved by passing the ion beam through a collision cell filled with a collision gas at a pressure substantially above the high vacuum of the chamber. Different mass spectrometers have been used to investigate either low- or high-energy CID. Low-energy CID (2-200 eV of energy in the laboratory frame) can be studied with a quadrupole mass spectrometer (QMS) in tandem with a reflectron time-of-flight. For instance, the Ultima ESI Q-ToF MS (*Waters-Micromass, UK*) mass spectrometer, described in [59, 102], was used to study low-energy CID of ronidazole, see section 4.1. In this case, the precursor ion was mass-selected by the QMS, and then subjected to CID in a hexapole collision cell. The product ions arising from the decomposition reactions were probed by the reflectron time-of-flight. Other instruments, for instance triple quadrupole mass spectrometers also allow the study of low-energy CID.[55] On the other hand, high-energy CID studies (1-20 keV of energy in the laboratory frame) are usually carried out in sector or time-of-flight mass spectrometers.[55]. The present studies were performed with a Nier-Johnson double-focusing mass spectrometer in reversed geometry equipped with a collision cell, as is described in chapter 3.

2.2.1 Energy transfer in a collision

CID of an ion m_p^+ is described as a two-step process: (i) activation and (ii) dissociation of the ion. The first step is the collisional activation wherein a fraction of the ion's kinetic energy is converted into internal energy forming an activated ion, m_p^{*+} . Due to energy conservation, some of the ion's kinetic energy is also converted into both internal and kinetic energy of the neutral target, N . As described by the next reaction [55, 103], the second step corresponds to the dissociation of the activated ion into a charged product ion, m_f^+ and neutral(s), m_n :



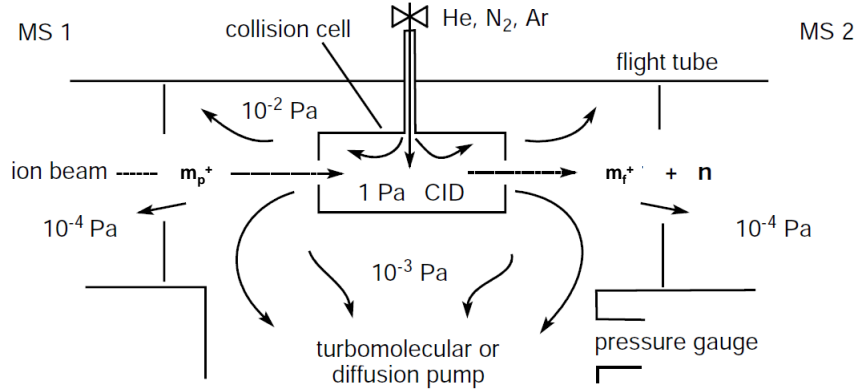


Figure 2.4. Schematic of a collision cell for CID experiments in a tandem mass spectrometer. The precursor ion was selected by the MS1, the ions formed due to CID were analysed by the MS2. Adapted from [55].

The internal energy of the activated ion, $E_{m_p^{*+}}$, comprises the energy carried by the ion before the collision, $E_{m_p^+}$, and the energy transferred during the collision, Q [55]:

$$E_{m_p^{*+}} = E_{m_p^+} + Q \quad (2.4)$$

For high-energy CID, the activation process is mainly a result of electronic excitation as the ion-neutral interaction time is in the range of $10^{-15} - 10^{-14}$ s. [55, 103] In the second step the additional internal energy is distributed among the internal degrees of freedom of the system leading to bond cleavage followed by dissociation of the activated ion m_p^{*+} . The upper limit of the energy transferred, Q , is defined as the center-of-mass energy, E_{CM} :

$$E_{CM} = \frac{m_N}{m_N + m_{m_p^+}} E_{Lab} \quad (2.5)$$

m_N denotes the mass of the neutral target, N , while $m_{m_p^+}$ denotes the mass of the projectile, i.e. the mass of the precursor ion m_p^+ . Further, E_{Lab} corresponds to the precursor ion's kinetic energy in the laboratory frame, associated with the acceleration voltage, U_{acc} , of

2.2. Collision-induced dissociation

the mass spectrometer:

$$E_{Lab} = \frac{m_{m_p^+} \cdot v^2}{2} = qU_{acc} \quad (2.6)$$

Please note that the center-of-mass energy is an upper limit for the energy to be transferred to the precursor ion, because most of the collisions occur at a scattering angle θ . The effect of the scattering angle on CID of an ion has been summarized by Bordas-Nagy *et al.* [104]. In general, for a given collision gas, the center-of-mass energy at various acceleration voltages is then a function of the mass of the projectile. The results for this study were achieved, however at a constant acceleration voltage of 6 kV. The fragmentation pathways of protonated ronidazole in low- and high-energy experiments have been studied and the results are presented in section 4.1.

Experimental Setup - ESI-VG

The present chapter provides a detailed description of the experimental setup ESI-VG, as it was used to investigate high-energy collision-induced dissociation of ronidazole. The ESI-VG experiment consists of a home built electrospray ionization source (ESI) source coupled to a double focusing mass spectrometer in reversed geometry, VG-ZAB-2-SEQ, manufactured by *Vacuum Generators Analytical (Manchester, UK, 1988)*.

The following sections will address the individual components of the ESI source as well as the mass spectrometer.

3.1 Electrospray ionization source

The home-made ESI source consists of a spraying needle (A), a heated capillary (B), an ion funnel (C), an octopole ion guide (D) and a three-element lens (E), as schematically represented in figure 3.1.

A solution of the molecule of interest is pushed by a motor driven syringe through a hypodermic needle at constant flow rate. The ionization occurs by applying 4-5 kV on the spray needle with respect to the inlet capillary. Then, through the inlet capillary, the electrosprayed ions pass from the atmospheric pressure region to the ion funnel placed in the first vacuum stage at a pressure of 3 mbar. The ion funnel was designed after Julian *et al.*[105], and it is an ion guide consisting of an electrode stack. The simultaneous

application of a DC voltage gradient and radio frequency (RF) potentials phase-shifted by 180° on adjacent electrodes results in an electric field guiding the ions to next vacuum stage. The octopole is mounted on the second and third vacuum stage. The second vacuum stage has a pressure of 10^{-1} mbar, and the third one has a pressure of 10^{-4} mbar. The octopole consists of eight cylindrical stainless steel rods. By applying RF voltage with a phase-shift of 180° on alternating rods, the ions are guided into the next stage. A three-element lens focuses the ion beam in the entrance slit of the mass spectrometer. This vacuum stage of the ESI sources is connected to the first field-free region (FFR1) of the mass spectrometer. All components of the ESI source were electrically isolated from the mass spectrometer, since a voltage drop of 6 kV was used to accelerate the ions between the ESI source and the first lens stack of the mass spectrometer.

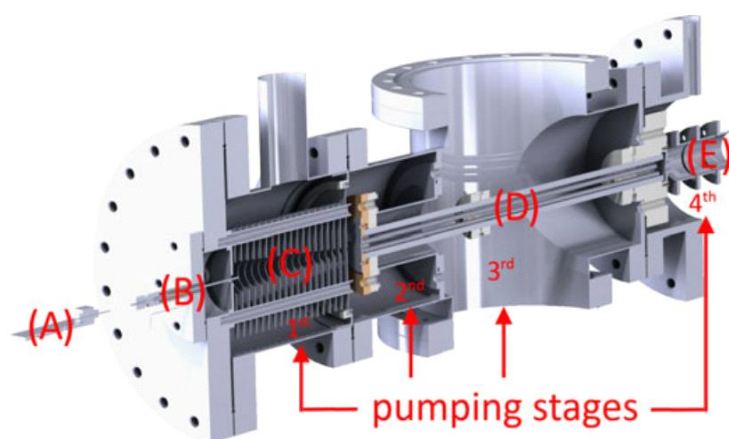


Figure 3.1. Home-built electro spray ionization source (ESI source). Different interfaces are used to guide and focus ions to different pressure stages. The ion inlet is realized by a spraying needle (A) and a heated capillary (B), delivering the ions into the ion funnel (C), followed by an octopole (D), which acts as an ion guide. The subsequent lens stack (E) guides the ion beam into the mass analyzer. Adapted from [61].

3.1.1 Solution

The solution of the molecule of interest was filled in a 10 mL gas tight syringe (*Hamilton Company*) mounted on a motor driven syringe pump (Elite pump 11, *Harvard Apparatus, GmbH*) controlling the flow rate, i.e. the amount of solution sprayed per unit of time. A silica tube with an inner diameter of $150\mu\text{m}$ (*Optronic GmbH*) connected the syringe and the spray needle, and it also serves as an insulator.

In order to prepare a solution, the sample was dissolved in a mixture of water and a solvent, e.g. methanol (CH_3OH) or acetonitrile (CH_3CN). A further substance which enhances the ionization efficiency may be added to the solution.[106] For instance, acetic acid (CH_3COOH) was added for the cation production, while ammonium hydroxide (NH_4OH) was added for anion production. A typical solution has a concentration of 10 mmol of the sample dissolved in a mixture of 1:1 water with methanol.

3.1.2 Spray needle assembly

The spray needle of inner diameter $100\mu\text{m}$ was placed in a PTFE (teflon) holder, as represented by (A) in figure 3.1. Usually, the position of spray needle was adjusted to angles higher than 30° with the respect to the z -axis, to prevent accumulation of residuals on the inlet capillary. Furthermore, a home built motor drive positioning system allowed for a fine tuning of the position of the spray needle.[107] The spray needle was biased by a bipolar high voltage power supply (*HCN140-2000, FuG Elektronik GmbH*), to produce either cations and anions by electrospray ionization.

3.1.3 Inlet capillary

The inlet capillary delivers the electrosprayed ions into the ion funnel. It also serves as an interface between the atmospheric pressure and the first vacuum stage. The capillary was installed in a Teflon holder mounted, on turn, on the chamber. As represent by (B) in figure 3.1, the inlet consists of a stainless steel tube with a length of 5 cm and an inner diameter of 0.75 mm. The ions arriving at the first two DC-only electrodes of the ion funnel (see subsection 3.1.4) are thus positioned inside the ion funnel. Additionally, in

order to avoid a potential barrier between these components within the ESI source, the inlet capillary is kept at the same potential as the entrance electrode of the ion funnel.

A heating wire (*WNC-32-100, LakeShore Cryotonics, Inc.*) was wrapped around the inlet capillary. By passing a current through the heating wire, the capillary was thus warmed. In principle, the evaporation of the solvents is more efficient due to higher temperatures leading to continuous spray conditions. As result, the ion yield may increase. However, the yield of electrosprayed ions as a function of the temperature depends on the studied sample, therefore the temperature was adjusted for each case.

3.1.4 Ion Funnel

In commercial ESI mass spectrometers, the ions are usually transferred from the capillary through a conductance limit (e.g. a cone, or a skimmer) to the mass analyzer.[55, 108] A major limitation of this process lies on the inefficient transfer of ions from the high pressure region to the high-vacuum conditions required for mass analysis. Because only a minor fraction of the ions passes through the orifice of the skimmer into the following high-vacuum stage. Due to the supersonic expansion of the gas exiting the capillary, as well as the collisions with the residual gas, the ion beam entering the first vacuum stage becomes highly divergent.[55] All these factors make it difficult to control and focus the ion beam by regular ion optics based on electrostatic devices [108–111]. Shaffer *et al.* [109–111] have developed the ion funnel, a device consisting of a series of ring electrodes with decreasing internal diameters. Under elevated pressures ranging from a few up to 40 mbar, by co-applying a RF alternating-phase (180°) potential on adjacent electrodes with a DC potential gradient, the ion funnel is capable of focusing and transmitting the ions. This approach offers a better transmittance and control over the ion beam when compared to a skimmer-based interface. A comprehensive review by Kelly *et al.* [108] summarizes the current knowledge on ion funnels, and hence just a brief description on the ion funnel will be presented here.

A RF voltage phase-shifted by 180° applied on adjacent electrodes creates an effective potential, V^* , capable to radially confine the ions. Gerlich [112] expressed the effective

3.1. Electrospray ionization source

potential, $V^*(r, z)$, for a given radial (r) and axial (z) in cylindrical coordinates, as:

$$V^*(r, z) = \frac{q |E_{rf}(r, z)|^2}{4m(2\pi f)^2} \quad (3.1)$$

where $E_{rf}(r, z)$ represents the RF electric field, f is the RF frequency, q and m are the charge and the mass of the ion, respectively. The geometry of the ring electrodes, in terms of the distance, d , between adjacent electrodes as well as their radii, R , affects the spatial distribution of the effective potential $V^*(r, z)$ accordingly to [112, 113]:

$$V^*(r, z) = V_{trap} \left[I_0^2\left(\frac{r}{\delta}\right) \sin^2\left(\frac{z}{\delta}\right) + I_1^2\left(\frac{r}{\delta}\right) \cos^2\left(\frac{z}{\delta}\right) \right] \quad (3.2)$$

$$V_{trap} = \frac{V_{max}}{I_0^2(R/\delta)} \quad (3.3)$$

$$V_{max} = \frac{z_i q V_{rf}^2}{4m(2\pi f)^2 \delta^2} \quad (3.4)$$

V_{trap} is the axial effective potential well depth. I_0 and I_1 are zero and first order modified Bessel functions. V_{max} is the maximum value of the effective potential at the position $r = R_i$, where R_i is inner radius of the i^{th} electrode, $z_i = d(i + 1/2)$, $i = 0, 1, \dots$; d is the distance between the ring electrodes, and $\delta = d/\pi$. V_{RF} represents half of the peak-to-peak RF amplitude [108]. Shaffer *et al.* [109] have numerically derived the profile of $V^*(r, z)$ along the z -axis of the ion funnel accordingly to the equation 3.1. Please note that it does not account for the DC potential gradient. As shown in figure 3.2, the effective potential appears to be smaller around the z -axis ($r=0$ mm) [111, 113]. However, towards the end of the ion funnel where the internal diameter of the electrodes is comparable with the spacing between them, the RF effective potential shows local maxima occurring in between pair of electrodes. As a result, axial potential wells capable of trapping the ions and impair the transmission are created; however in the real experiment this effect is not significant.[111, 113] At elevated pressures, the ions will undergo collisions with atoms and molecules of the residual gas losing gradually kinetic energy, as they travel through the ion funnel. Then, slower ions come closer to the z -axis, where the effective potential is smaller. Therefore,

an initially divergent ion beam will be confined close the axis of the ion funnel by the phase-alternating (180°) RF potential, due to a process referred to as collisional focusing or collisional cooling.

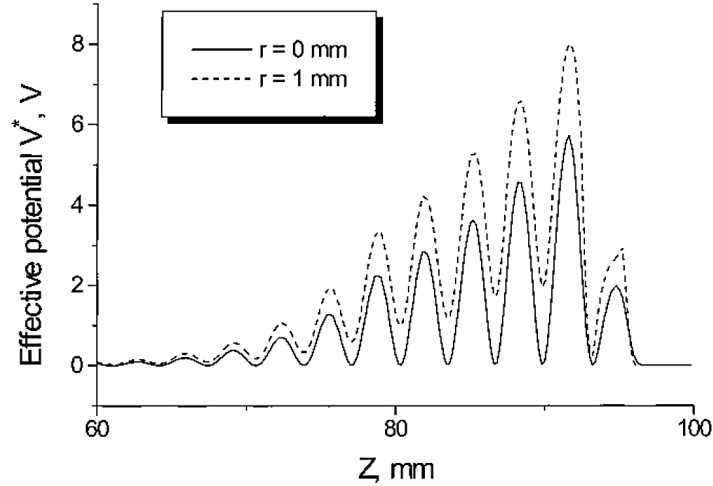


Figure 3.2. The effective potential $V^*(r, z)$ given as function of the z -axis in the ion funnel. The solid line represents the effective potential along the ion funnel axis, and at 1 mm off-axis is represented by the dashed line. The parameters used in the calculations are the following: m/z 1000, $V_{RF}=100$ V, $f=700$ KHz. Taken from [111].

In addition to the phase-alternating RF potential, a DC potential gradient is applied on the electrodes comprising the ion funnel. This gradient pushes the ions along the z -axis of the ion funnel and provides more control over the ion beam.[110] Therefore, when a capillary transfers an ion beam to an ion funnel, the divergent ions are radially confined around the z -axis due to the RF potential. The DC potential gradient leads the ions towards electrodes with gradually reduced inner diameter, enhancing the focusing. In addition, the flow of gas exiting the first vacuum stage also supports the movement of the ions. The synergy between the RF potentials and DC gradient results in a focused and directed ion beam. To sum up, an ion funnel is capable to efficiently transmit an ion beam from a high-pressure region to a lower pressure region.

In the present experiment, a home-built ion funnel, as shown in figure 3.3, and as (C) in figure 3.1, was used. It consists of 36 stainless steel ring electrodes with a thickness of 0.5

3.1. Electrospray ionization source

mm. The first three electrodes have an inner diameter of 20 mm. While the inner diameter of the following electrodes is gradually reduced by 0.5 mm ending in the last electrode with an inner diameter of 3.5 mm. The adjacent ring electrodes are equally spaced by 2.5 mm-thick insulating plain bearings (*igus GmbH*). The ion funnel is mounted on four M8 threaded rods placed on the entrance flange, covered by 1mm-thick insulating polyether ether ketone (PEEK) hollow rods. Additionally, two further DC-only electrodes, referred to as funnel entrance electrode and funnel exit electrode, were placed immediately before and after the stack of ring electrodes, respectively. The entrance electrode is electrically connected to the inlet capillary, resulting in a sharing of the same DC potential, and avoiding a potential barrier between these components. The exit electrode also serves as a closure element of the first vacuum stage.

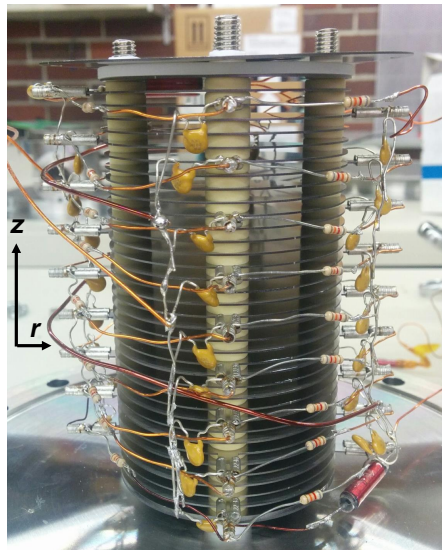


Figure 3.3. The ion funnel.

A voltage divider consisting of 10 k Ω resistors connecting adjacent electrodes creates a linear DC potential gradient, that moves the ions along the funnel. For positive ions, the first lens of the ion funnel has the most positive voltage while the later electrodes have gradually decreasing voltages. Coils with an inductance of 470 μ H are connected in series to decouple the DC from the RF power supply. Additionally, the DC voltage

is decoupled from the RF power supply by 10 nF capacitors connected in parallel to the electrodes, assuring that the RF voltage is not applied to the DC power supply and vice-versa. The DC voltages (U_0 , U_1 and U_2) are provided by a power supply *EBS Bipolar Distributor H Modules with Common Floating-GND* (*iseq Spezialelektronik GmbH*). The RF potential was delivered by the first frequency head of a *PSRF-125: Dual RF Power Supply* (*Ardara Technologies L.P.*). It had a frequency of 2 MHz and phase-shifted of 180° on the outputs, while the amplitude may be adjusted from 0 up to 900 V. Finally, the ion current transmitted by the ion funnel may be measured at the exit lens L38 (represented in figure 3.4).

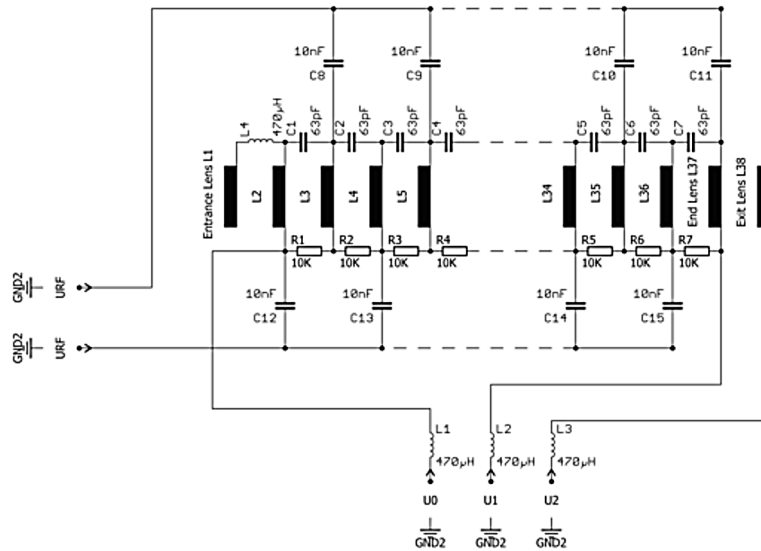


Figure 3.4. Schematics of the electrical circuit of the ion funnel. The electrodes 6 to 34 are represented by the dashed line. Where, U_{RF} is the RF potential, while U_0 , U_1 and U_2 are DC voltages.

3.1.5 Octopole ion guide

Following the ion funnel, an octopole ion guide transports the ions from the first vacuum stage towards the fourth vacuum stage. The application of RF-only multipoles as ion guides, and traps, have been summarized in a review by Gerlich [112] and in a tutorial by Wester [114]. Furthermore, the relevance of ion traps and multipoles for mass spectrometry

3.1. Electrospray ionization source

has been extensively discussed by Douglas *et al.*[115] Hence, just a brief description on the octopole performing as an ion guide will presented here.

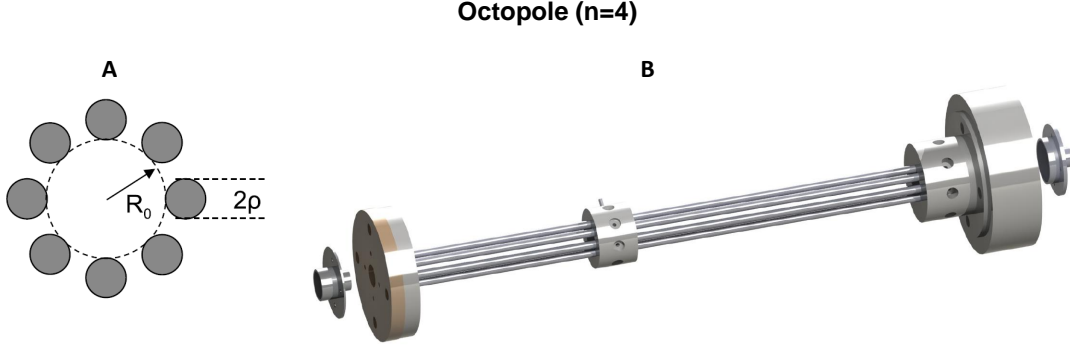


Figure 3.5. **A:** Cross section of a octopole. **B:** Schematic drawing of the home-made octopole. The eight stainless steel rods are mounted on Teflon components, while the mounting screws also serve as electrical connectors. Entrance and exit DC-only lenses are attached to the holders. Taken from [116].

Multipoles consist of n pairs of hyperbolic or cylindrical rod electrodes positioned equidistantly along a circle. An octopole is thus a multipole of order $n=4$. Figure 3.5 shows the cross section of an octopole with cylindrical electrode rods of radius ρ positioned along a circle of inner radius R_0 . By applying phase-alternating (180°) RF on pairs of electrodes, the octopole will operate as a wide band pass for ions. This property makes the octopole an ion guide.[55] The time dependent potential created along the z -axis of n^{th} order multipole with cylindrical rod electrodes, may be given in cylindrical coordinates, as follows [112, 114]:

$$V(r, \phi, t) = V_{RF} \cos(n\phi) \left(\frac{r}{R_0} \right)^n \sin(2\pi t) \xrightarrow[\text{octopole}]{n=4} V(r, \phi, t) = V_{RF} \cos(4\phi) \left(\frac{r}{R_0} \right)^4 \sin(2\pi t) \quad (3.5)$$

V_{RF} and f are the amplitude and frequency of the RF potential, respectively. The equations of motion of ions in a n^{th} order multipole cannot be solved analytically, because the equation of motion in the position coordinates is nonlinear. In contrast to the motion in a quadrupole ($n=2$), where the trajectory of the ions is analytically expressed as solutions

of the Mathieu equations (please see section 6.1.4 for further details). Therefore, one must employ the effective potential approximation suggested by Dehmelt [117] to calculate the ion trajectories in a multipole field. First, the motion of an ion can be separated into a micro and a secular motion. The micromotion is rapid and follows the RF frequency, while the latter may be realized as a slowly varying drift motion.[114] And, second, by time averaging the equation of motion of an ion (not shown here) over the period of one RF oscillation, the effective potential approximation, $V^*(r, z)$, for a n^{th} order multipole is achieved, and expressed as [114]:

$$V^*(r, z) = \frac{q^2 n^2 V_{RF}^2}{4m(2\pi f)^2 R_0^2} \left(\frac{r}{R_0}\right)^{(2n-2)} \xrightarrow[n=4]{\text{octopole}} V^*(r, z) = \frac{4q^2 V_{RF}^2}{m(2\pi f)^2 R_0^2} \left(\frac{r}{R_0}\right)^6 \quad (3.6)$$

The equation 3.6 demonstrates that the ion motion in a multipole field has an effective potential proportional to $r^{(2n-2)}$, that is proportional to r^6 for an octopole. However, it is no longer valid if the ion motion becomes unstable. If so, the amplitude of the ion motion will increase until the ion collides with an electrode rod. For an ideal multipole, a stability parameter, η , was thus introduced and is given by [114]:

$$\eta = 2n(n-1) \frac{|q| V_{RF}}{m(2\pi f)^2 R_0^2} \left(\frac{r}{R_0}\right)^{(n-2)} \xrightarrow[n=4]{\text{octopole}} \eta = 24 \frac{|q| V_{RF}}{m(2\pi f)^2 R_0^2} \left(\frac{r}{R_0}\right)^2 \quad (3.7)$$

In contrast to quadrupoles ($n = 2$), it is not possible to plot a stability diagram for multipoles. In fact, the stability parameter for quadrupoles is a constant value, which is equal to the q value used in the Mathieu equation (please see subsection 6.1.4). Instead, Gerlich [112] has introduced two conditions that define a stable trajectory in a multipole. First, the radius of the ion trajectory, r must be lower than $0.8 \cdot R_0$, second, the stability parameter η must be lower than 0.3.[112, 114, 118] Therefore, by assuming that the amplitude of the RF potential V_{RF} leads to a stability parameter η less than 0.3, an ion of mass m and charge q will be transmitted by a the multipole of inner radius R_0 with a stable trajectory of radius smaller than 0.8 of the inner radius.

The effective potential created by phase-alternating (180°) RF potentials can be described as a "restoring force" to the center of the ion guide. For positive ions, the ion

3.1. Electrospray ionization source

beam is pulled by the negative rods and repelled by the positive rods at any instant of time.[115] Then, by setting properly the amplitude and frequency of the RF potential, the ions will be thus radially confined along the z -axis preventing collisions with the rods. The effective potentials shown in figure 3.6 demonstrate that higher order multipoles ($n > 2$) show a *quasi* flat and low effective potentials near the center ($r = 0$) and increasing towards the rods ($r = R_0$). In the present setup, the octopole occupies the second and third vacuum stage that corresponds to a pressure regime of $10^{-2} - 10^{-3}$ mbar. Thus, as the ions travel along the octopole, a fraction of their kinetic energy will be lost due to collisions with the atoms and molecules of the residual gas. As a result, the ions will come closer to the z -axis of the octopole where the effective potential is smaller.[55, 119] Therefore, collisional cooling contributes to the radial confinement of the ions.[55]

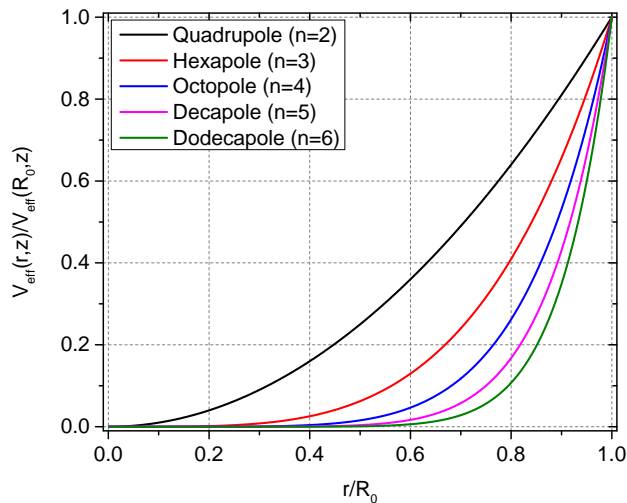


Figure 3.6. The effective potential for multipole ion guides, namely quadrupole, octopole, hexapole, decapole and dodecapole.

In the present experiment, the home-built octopole, as shown as B in figure 3.5, and as (D) in figure 3.1 consists of eight stainless-steel electrode rods with a diameter of 4 mm each, and a length of 326 mm. The electrode rods are placed along a circle of inner radius $R_0 = 5.6$ mm. Further, two DC-only electrodes positioned at both ends of the

octopole support a better control over the ion beam. Both have an outer diameter of 36 mm and an orifice with a 2 mm opening. All these components are directly mounted on two teflon holders, as shown in figure 3.5. The teflon holder on the left-hand side seals the second vacuum stage, and the one on the right-hand side, the third vacuum stage. The RF potential is applied on the rods through the screws fixing a Teflon ring. The RF potential was supplied by the second frequency head of the *PSRF-125: Dual RF Power supply (Ardara Technologies L.P.)*. The RF potential floats on a DC voltage supplied by the *EBS Bipolar Distributor HV Modules with Common Floating-GND (iseg Spezialelektronik GmbH)*. This power supply also supplies the voltage of both, entrance and exit octopole lenses. At this point, the ions will be transported by the octopole to the mass analyzer via a three-element lens, as described in the next subsection.

3.1.6 Three-element lens

The three-element lens is an electrostatic device used to focus the ion beam into the first stack of lens of the mass analyzer. A comprehensive knowledge on this topic can be found in literature, namely in textbooks [120–122], as well as in the review by Sise *et al.* [123] In brief, focusing of a charged-particle, e.g. electron or ion beams, is achieved by passing it from one electrode to another, i.e. from L1 to L2 and then to L3. Each single electrode is biased with DC electric potentials, U_{L1} , U_{L2} and U_{L3} . Thus, the focusing of the ion beam may be controlled by adjusting the mentioned voltages.

In the present experiment, the three-element lens, as shown as (E) in figure 3.1 and, in figure 3.7, is comprised of three identical stainless steel cylindrical electrodes. The 1 mm-thick lenses have a length of 22 mm, while their inner diameter is of 24.88 mm. The lenses are spaced and insulated by ceramics of a length of 2.5 mm. The lens stack was mounted on a ring shaped holder by using four threaded rods covered by hollow ceramic rods. The DC voltages were supplied by the *EBS Bipolar Distributor HV Modules with Common Floating-GND (iseg Spezialelektronik GmbH)*.

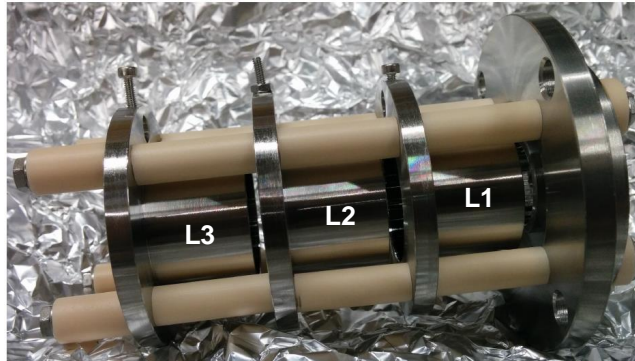


Figure 3.7. Three-element lens.

3.2 Double-sector field mass spectrometer: VG-ZAB-2SE

The study of collision-induced dissociation of biomolecules was carried out with a VG-ZAB-2SE double-focusing mass spectrometer, as shown in figure 3.8. The main focus of this section is to provide an overview of the mass spectrometer, although it was already described elsewhere [61, 124]. The mass spectrometer has been constructed in reversed Nier-Johnson geometry. The ions first pass a magnetic sector followed by an electric sector, thereby constituting a double focusing mass spectrometer. The mass spectrometer consists of a first field-free region (FFR1), a magnetic sector, a second field-free region (FFR2), an electric sector and a detection system connected to a computer for data acquisition.

3.2.1 Magnetic sector

After the FFR1, the ion beam with kinetic energy E_{kin} enters the magnetic sector. The working principle of the magnetic sector relies in the magnetic component of the Lorentz force, \vec{F}_L :

$$\vec{F}_L = z(\vec{v} \times \vec{B}) \quad (3.8)$$

where z and \vec{v} are the charge and velocity of the ions. As represented in figure 3.9, within the magnetic sector the the magnetic field, \vec{B} , is orthogonal to the velocity \vec{v} of the ions.

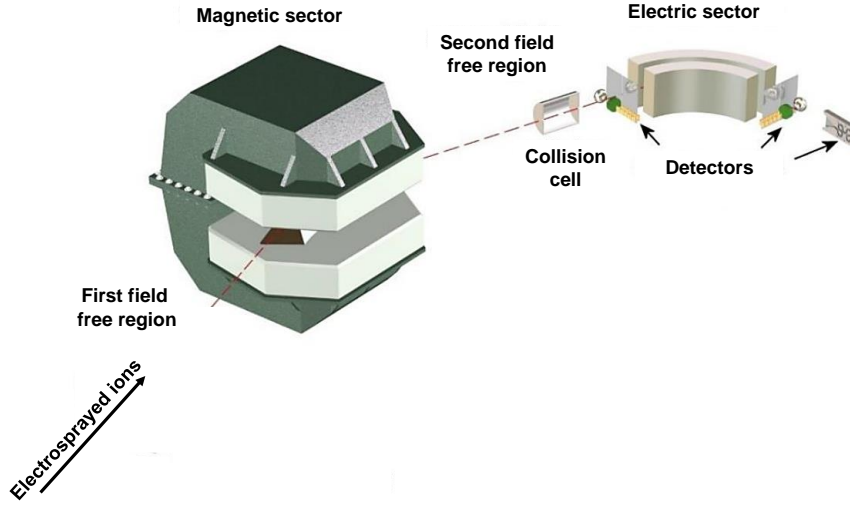


Figure 3.8. Schematic representation of the VG-ZAB-SE double-sector field mass spectrometer. Adapted from [124].

Hence, the Lorentz force can be rewritten in a scalar form:

$$F_L = qzB \quad (3.9)$$

The F_L is perpendicular to the velocity of the ions, therefore it acts as the centripetal force, F_C :

$$F_L = F_C \Rightarrow zvB = \frac{mv^2}{r} \Leftrightarrow \frac{m}{z} = \frac{rB}{v} \Leftrightarrow r = \frac{mv}{zB} \quad (3.10)$$

The equation 3.10 describes the working principle of the magnetic sector and shows that the magnetic sector is a momentum analyzer, rather than a mass analyzer.

As described previously, the electrosprayed ions were accelerated towards the mass spectrometer by a voltage drop U . The kinetic energy E_{kin} of the ions, and consequently their velocity, is determined by the voltage drop, which can be given by:

$$\begin{cases} E_{kin} = \frac{mv^2}{2} \\ E_{kin} = zU \end{cases} \Leftrightarrow v^2 = \frac{2zU}{m} \quad (3.11)$$

Taken into account the equation 3.11, the equation 3.10 can be rewritten as:

$$\frac{m^2}{z^2} = \frac{r^2 B^2}{v^2} \Leftrightarrow \frac{m^2}{z^2} = r^2 B^2 \frac{\pi}{2zU} \Leftrightarrow \frac{m}{z} = \frac{r^2 B^2}{2U} \quad (3.12)$$

The relation 3.12 demonstrates that for constant voltage drop U and constant magnetic field B , the ions with a particular m/z will describe a circular trajectory with a radius r . Therefore, if the radius is limited by a flight-tube with a fixed curvature, e.g. 66 cm such as in VG, only the ions with a m/z that verifies the relation 3.12 will be transmitted by the magnetic sector. Furthermore, by changing the intensity of the magnetic field, ions with different m/z can be transmitted.

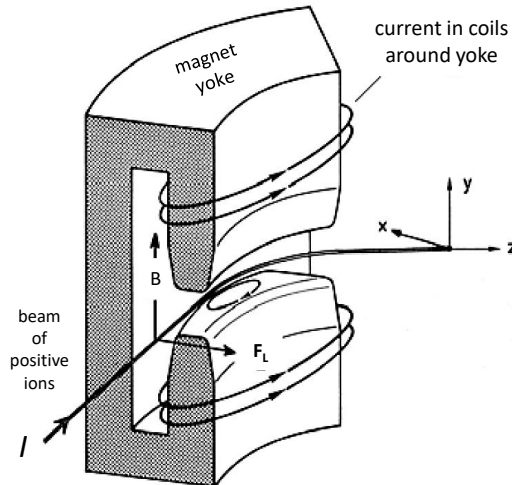


Figure 3.9. Relationship between the direction of the magnetic field (B), velocity of the ion beam (I) and the resulting Lorentz force (F_L). Adapted from [55].

Although the voltage drop U is kept constant during the experiments, the ions are produced with some kinetic energy distribution. As a result, the ions have trajectories with different radii, accordingly to the equation 3.13, leading to a broadening of the ion beam and lower mass resolution.

$$r = \frac{\sqrt{2mE_{kin}}}{zB} \quad (3.13)$$

In order to reduce the kinetic energy distribution of the ion beam and thus enhance the mass resolution, an electric sector is used.

3.2.2 Electric sector

As mentioned previously in subsection 3.2.1, the ions that leave the ESI source have a kinetic energy spread. To improve mass resolution, an electric sector is placed after the magnetic sector. The instrument represents thereby a double-focusing mass spectrometer, because it combines direction and energy focusing.

The momentum-analyzed ions will pass the FFR2 entering into the electric sector. It consists of two plates, with a curvature of 81° and a mean radius of 38 cm. A radial electric field is produced when the outer plate is kept at positive potential, whereas the inner plate is kept at a symmetric and negative potential.[55, 125] The working principle of the electric sector relies on the electric component of the Lorentz force, \vec{F}_L :

$$\vec{F}_L = z\vec{E} \quad (3.14)$$

where z and \vec{v} are the charge and the velocity of the ion, respectively. Within an electric sector, the Lorentz force may be given in a scalar form:

$$F_L = zE \quad (3.15)$$

Since the electric field, \vec{E} is always orthogonal to the velocity of the incoming ions, the Lorentz force \vec{F}_L will act as a centripetal force, \vec{F}_C . Therefore, the ions will have a circular trajectory with a radius r , given by:

$$F_L = F_C \Rightarrow zE = \frac{mv^2}{r} \Leftrightarrow r = \frac{mv^2}{zE} \quad (3.16)$$

Taking into account that $E_{kin} = \frac{mv^2}{2}$, the equation 3.16 may be rewritten as:

$$r = \frac{2E_{kin}}{zE} \quad (3.17)$$

The equation 3.17 demonstrates that the electric sector acts a kinetic energy analyzer. Thus, the electric sector reduces the kinetic energy distribution of the momentum-analyzed ions and, consequently enhances the mass resolution of the spectrometer. At last, after exiting the electric sector the ions are focused on the detector. The figure 3.10 shows the double focusing of both magnetic and electric sector in a double focusing mass spectrometer with reversed Nier-Johnson geometry.

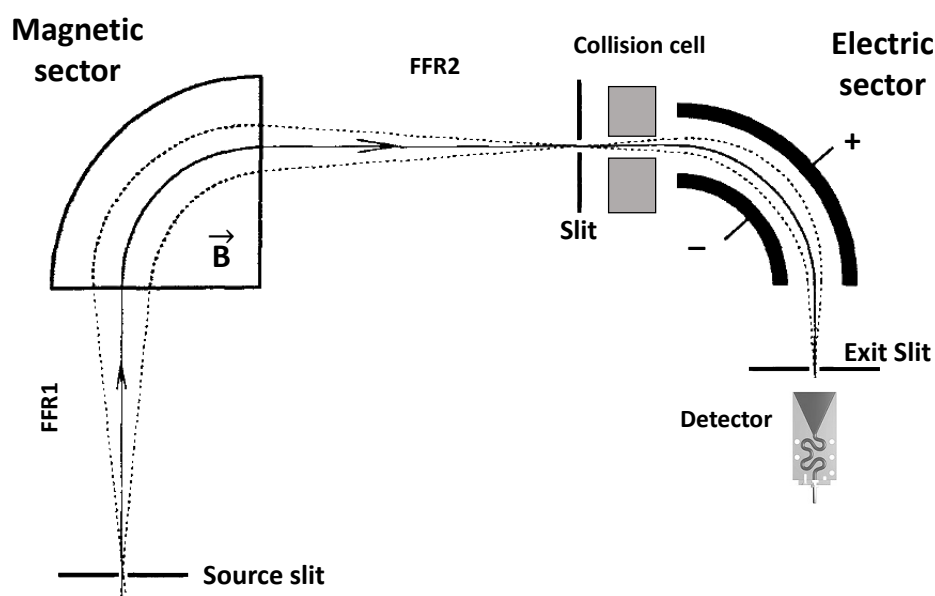


Figure 3.10. A double focusing mass spectrometer with reversed Nier-Johnson geometry. Adapted from [126].

3.2.3 Collision cell

The collision cell placed before the electric sector allows studying collision-induced dissociation (CID) of a precursor ion. Usually, the collision cell is filled with a noble gas, referred to as collision gas. As described in section 2.2, the dissociation of the precursor ion passing through the gas-filled collision cell results from the conversion of a fraction of the kinetic energy of the ion to internal energy.[55, 127]

For the high-energy CID experiments with ronidazole described in the section 4.1 helium served as collision gas. The real pressure within the collision cell is unknown.

However, it was estimated to be up to three orders of magnitude higher than the reading given by a cold-cathode gauge connected to the vacuum chamber.[128] Thus, a measured pressure value of 4.0×10^{-6} mbar corresponds to a pressure of about 4.0×10^{-3} mbar within the collision cell. Furthermore, the product ions forming due to CID are accelerated, or decelerated by applying a voltage $U_{Gascell}$ on the collision cell. This feature is useful to sort out the ions formed by dissociation within the collision cell from those arising by metastable decay in the FFR2. Although this feature was not employed in this studies, it was used for instance to differentiate the fragments formed due to either CID or metastable decay in the studies with chromium hexacarbonyl.[61] At last, the ions leave the collision cell to enter into the electric sector.

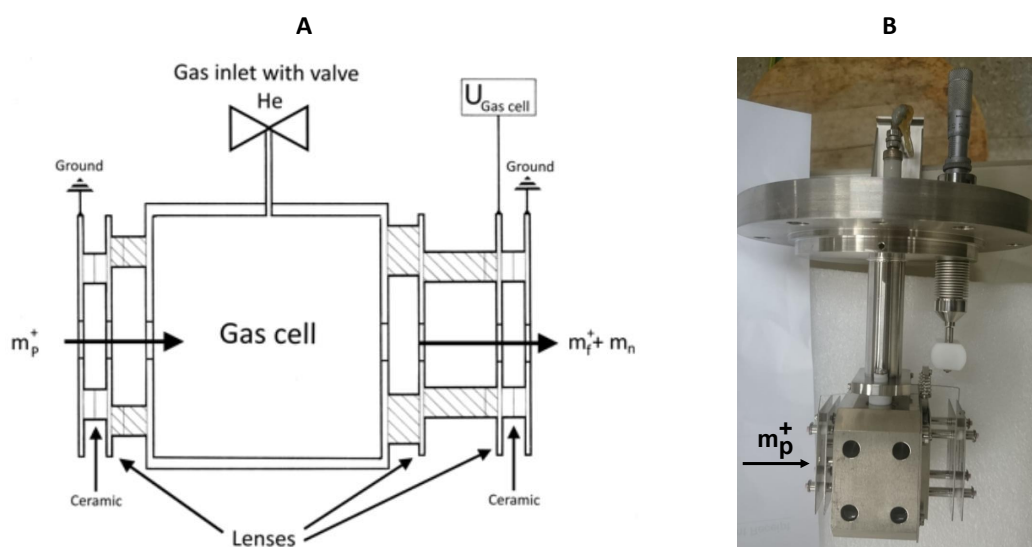


Figure 3.11. A: Cross section of the collision cell. The helium pressure is regulated by a valve. CID of the precursor ion, m_p^+ , gives rise to a product ion m_f^+ and a neutral m_n . Adapted from [129]. Biasing the collision cell with $U_{Gascell}$ provides an post-acceleration (or deceleration) of the product ions.

3.3 Detection system

The detection system installed in VG-ZAB-2SE mass spectrometer comprises three detectors. First, the ion current yielded by the ESI source is measured in a slit installed in the FFR1 prior to the magnetic sector. The current of electrosprayed ions is hence monitored by a picoammeter *Model 6485 (Keithley)*. Second, the detector installed in the FFR2, after the collision cell, is an electron multiplier of the continuous dynode type - channel electron multiplier, or also referred to as channeltron. This detector was mainly used to check whether the ions were passing through the magnetic sector. Since this detector was installed orthogonally to the ion beam, a pusher plate was employed to deflect the beam towards it. Afterwards, when an ion enters into the detector colliding with its surface, secondary electrons are released and accelerated by a high voltage drop between the terminals of the detector. These secondary electrons will further collide with the surface creating additional electrons, thus initiating a cascade or avalanche of electrons. This process results in amplification of the input ion signal in a brief time interval (~ 1 ns), leading to a detectable current as output signal.

At last, a second channeltron coupled to a dynode, as shown in figure 3.12, placed after the electric sector was usually used for the measurements. An ion hitting the dynode yields an electron, that is accelerated towards the detector due to a voltage difference between the channeltron, and the dynode kept at ground potential. Then the channeltron produces an output signal, as explained earlier. Therefore, the combination of a channeltron and a dynode assures the detection of ions of either charge state without changing the voltages applied on the detector's terminals. Both channeltrons installed in the mass spectrometer are *KBL 510 standard CEM (Dr. Sjuts Optotechnik GmbH)*. It consists of a ceramic body, with silver-coated terminals and a lead glass detection surface on the inner side of the device. As represented in figure 3.12 C, the channeltron has a curved design, in order to suppress the ion-feedback arising from secondary ionization of the molecules of the residual gas, as well as to enhance the gain of the detector.[55] The typical gain of a channeltron is about 10^8 and it may deliver up to 10^6 counts per second of acquisition.

However, the acquisition of such high yields may harm the detector contributing to a reduction in its lifetime.[130] The applied voltage ranged from 2.5 up to 3.0 kV represents a good compromise between the highest gain and the lifetime of the detector.

The output signal of the channeltron was connected to a home built electrical circuit, designed as suggested by the manufacturer, used to decouple the signal from the applied high voltage. Afterwards, the signal was preamplified by a *PDA06* unit (*WMT-Elektronik GmbH*). At last, the amplified output signal was connected to a computer via a custom made interface, and further processed by a software.

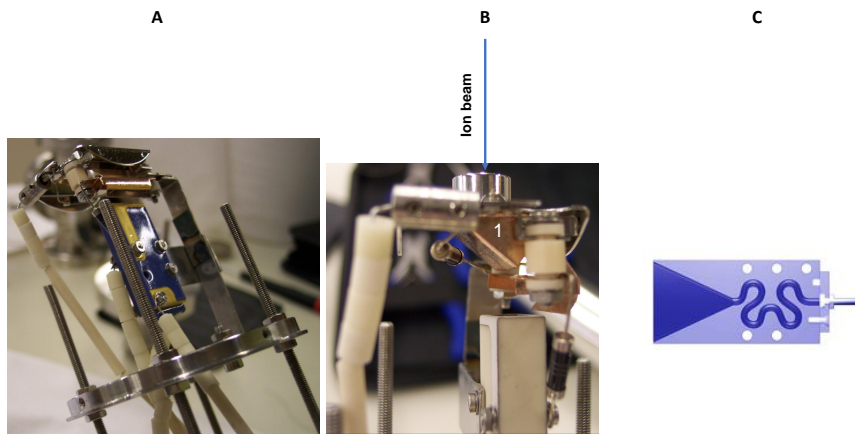


Figure 3.12. **A:** Photograph of the second channeltron installed in VG-ZAB-2SE. **B:** The dynode (1) converts the ion beam into electrons, which are further detected by a channeltron. **C:** Representation of a *KBL 510* channeltron.

3.4 Data acquisition

The mass spectrometer is set by a custom made software (designed by Dr. Arntraud Bacher). The computer communicates with the VG-ZAB-2SE via a home built interface box and receives the output signal from a selected channeltron. The software allows the setting of the acquisition parameters, such as the gate time, the step size and the number of runs. Different scan modes are possible, like mass spectra, mass analyzed ion kinetic energy (MIKE), electron energy, and high voltage scans. However, the latter two options

were not used during the course of this work.

3.5 Vacuum system

The vacuum pumps used in the ESI-VG experiment are summarized in the table 3.1. *Compact FullRangeTM* (Pfeiffer Vacuum) gauges controlled by a *MAXIGAUGE*, model *TPG 256 A* (Pfeiffer Vacuum) were employed to monitor the pressure in each vacuum stage.

The ESI source consists of three differentially pumped chambers, as shown in the figure 3.1. The ion funnel chamber corresponds to the 1st vacuum stage. A roots pump reduces the pressure to 3 mbar depending on the inner diameter of the inlet capillary. The opening of the 2nd stage has a diameter of 3 mm, where a pressure is reduced by a order of magnitude to 10^{-1} mbar by a rotary vane pump. The octopole ion guide chamber (3rd stage) is pumped by a turbomolecular pump baked by two rotary vane pumps. The entrance orifice has a diameter of 3 mm. The pressure in the 3rd vacuum stage is thus 10^{-3} mbar. Since the turbomolecular pump must be operated with respect to the Earth, an 160CF ceramic flange insulates the pump from the ESI source chamber. The three-element lens is installed in 4th stage. This vacuum stage was connected to the first field-free region (FFR1) of mass spectrometer, thus an additional pump was not required. The pressure in this stage is in the range of 10^{-6} mbar. The FFR1 and the FFR2 were evacuated by turbomolecular pumps baked by rotary vane pumps, respectively. At last, the detector chamber housing the main channeltron was pumped by a turbomolecular pump baked by a rotary pump. In contrast to FFR1 where the pressure was about 10^{-6} mbar, the pressure at FFR2 and detector chamber was about 10^{-8} mbar.

The ESI-VG setup is equipped with a vacuum security device. In case of a vacuum failure in any stage of the setup, this device protects the most sensitive components of the setup, by switching off the power supplies connected to the acceleration voltage and channeltron.[131]

Table 3.1. Model and type of the pumps used in the ESI-VG setup. All pumps were manufactured by *Pfeiffer Vacuum*. The working pressure, in mbar, achieved in each stage is also depicted.

Stage	Pump Model	Type	Pressure (mbar)
1 st	Revo-Dry	Roots	3.0
2 nd	DUO M35	Rotary	$\times 10^{-1}$
3 rd	TMU 521 Y P	Turbomolecular	$\times 10^{-4}$
	DUO 10 M	Rotary	
	DUO 35 M	Rotary	
4 th or FFR1	TPH 510	Turbomolecular	$\times 10^{-6}$
	DUO M35	Rotary	
FFR2	TPH 510	Turbomolecular	$\times 10^{-8}$
	DUO M35	Rotary	
Detector chamber	TMH 521 P	Turbomolecular	$\times 10^{-8}$
	DUO M35	Rotary	

Results and Discussion

4.1 Decomposition of protonated ronidazole

In this chapter, a combined theoretical and experimental study on the decomposition of protonated ronidazole is presented. This nitromidazole-based compound is used as an antibiotic in veterinary medicine, yet its use as potential radiosensitizer is unclear. At the Université de Lyon, the decomposition of protonated ronidazole was studied by low-energy collision-induced dissociation and density functional theory. While, at Universität Innsbruck, such decomposition was studied by high-energy collision-induced dissociation. The results are summarized in the following publication:

Decomposition of protonated ronidazole studied by low-energy and high-energy collision-induced dissociation and density functional theory

S. Pandeti, **J. Ameixa**, J. M. Khreis, L. Feketeová, F. Chirot, T. J. Reddy, H. Abdoul-Carime, F. Ferreira da Silva, S. Denifl, R. O’Hair, B. Farizon, M. Farizon, T. D Märk, *J. Chem. Phys.* **151**, 164306 (2019).

Author’s contribution: I performed the high-energy CID measurements and analyzed the obtained data. Afterwards, I prepared the final figures. At last, I wrote the experimental section regarding the high-energy CID measurements.

Decomposition of protonated ronidazole studied by low-energy and high-energy collision-induced dissociation and density functional theory

Cite as: J. Chem. Phys. 151, 164306 (2019); doi: 10.1063/1.5118844

Submitted: 5 July 2019 • Accepted: 8 October 2019 •

Published Online: 24 October 2019



View Online



Export Citation



CrossMark

Sukanya Pandeti,^{1,2,3} João Ameixa,^{4,5} Jusuf M. Khreis,^{4,6} Linda Feketeová,^{1,a)} Fabien Chirof,⁷ Thota J. Reddy,³ Hassan Abdoul-Carime,¹ Filipe Ferreira da Silva,⁵ Stephan Denifl,^{4,6} Richard A. J. O'Hair,⁸ Bernadette Farizon,¹ Michel Farizon,¹ and Tilmann D. Märk⁴

AFFILIATIONS

¹Université de Lyon; Université Claude Bernard Lyon1; Institut de Physique des 2 Infinis de Lyon, CNRS/IN2P3 UMR 5822, 69622 Villeurbanne Cedex, France

²Medicinal and Process Chemistry Division, CSIR-Central Drug Research Institute, Lucknow-226 031, India

³Analytical Chemistry and Mass Spectrometry Division, CSIR-Indian Institute of Chemical Technology, Hyderabad 500 007, India

⁴Institut für Ionenphysik und Angewandte Physik, Leopold Franzens Universität Innsbruck, Technikerstrasse 25, 6020 Innsbruck, Austria

⁵Laboratório de Colisões Atômicas e Moleculares, CEFITEC, Departamento de Física, Faculdade de Ciências e Tecnologia, Universidade NOVA de Lisboa, Campus de Caparica, 2829-516 Caparica, Portugal

⁶Center for Molecular Biosciences Innsbruck (CMBI), Leopold Franzens Universität Innsbruck, Technikerstrasse 25, 6020 Innsbruck, Austria

⁷Université de Lyon, Université Claude Bernard Lyon 1, CNRS, UMR5280 Institut Sciences Analytiques, 69100 Villeurbanne, France

⁸School of Chemistry, Bio21 Institute of Molecular Science and Biotechnology, The University of Melbourne, Parkville, Victoria 3010, Australia

^{a)} Author to whom correspondence should be addressed: l.feketeova@ipnl.in2p3.fr

ABSTRACT

Nitroimidazoles are important compounds in medicine, biology, and the food industry. The growing need for their structural assignment, as well as the need for the development of the detection and screening methods, provides the motivation to understand their fundamental properties and reactivity. Here, we investigated the decomposition of protonated ronidazole $[\text{Roni}+\text{H}]^+$ in low-energy and high-energy collision-induced dissociation (CID) experiments. Quantum chemical calculations showed that the main fragmentation channels involve intramolecular proton transfer from nitroimidazole to its side chain followed by a release of $\text{NH}_2\text{CO}_2\text{H}$, which can proceed via two pathways involving transfer of H^+ from (1) the N3 position via a barrier of TS2 of 0.97 eV, followed by the rupture of the C–O bond with a thermodynamic threshold of 2.40 eV; and (2) the $-\text{CH}_3$ group via a higher barrier of 2.77 eV, but with a slightly lower thermodynamic threshold of 2.24 eV. Electrospray ionization of ronidazole using deuterated solvents showed that in low-energy CID, only pathway (1) proceeds, and in high-energy CID, both channels proceed with contributions of 81% and 19%. While both of the pathways are associated with small kinetic energy release of 10–23 meV, further release of the NO^\bullet radical has a KER value of 339 meV.

Published under license by AIP Publishing. <https://doi.org/10.1063/1.5118844>

I. INTRODUCTION

Nitroimidazole-based compounds are of importance in biology and medicine due to their ability to selectively accumulate in cells deprived of oxygen.^{1,2} Thus, nitroimidazoles are used to combat

anaerobic bacteria,³ target hypoxic cancer cells as radiosensitizers,^{2,4} and act as potential imaging agents for hypoxia.^{5,6} Nitroimidazoles have also attracted interest in the context of high energy containing materials, such as explosives, propellants, and pyrotechnics.^{7,8} In veterinary medicine and, in particular, in the food industry,⁹

some nitroimidazoles such as ronidazole (Roni; Scheme 1) have been shown to not only be effective as antibiotics to treat poultry, cattle, pigs,¹⁰ shrimps,¹¹ and bees,¹² but also to promote growth and feed efficiency. The downside of the usage of antibiotics is that some 30%–90% of the administered compounds remain undegraded in the human or animal body and are excreted as active compounds,¹³ thus becoming a problem of pollution to the aquatic environment.^{9,13} Moreover, these antibiotics can enter the human diet through edible tissues of treated farm animals,¹⁰ fish and seafood,^{9,11} or honey.^{12,14,15} As a consequence, there is a growing need for fast and reliable methods for food screening,^{16–21} tap water pollution detection,⁹ and a need for the development of methods for the removal of these nitroimidazole antibiotics from aqueous solutions.^{13,22–24} Thus, it is essential to understand the fundamental properties and reactivity of nitroimidazole based compounds.

Electrospray ionization (ESI) has been shown to be effective not only in producing protonated nitroimidazole derivatives but also in formation of their respective radical anions,²⁵ which is rare in ESI but possible for compounds exhibiting a high electron affinity as is the case of some nitroimidazoles. It has been shown that simple molecular modification such as replacing an H atom at the N1 position by a methyl group can completely block reactivity triggered by low-energy electrons.²⁶ Moreover, decomposition of simple nitroimidazoles investigated by different methods of excitation showed that for all decomposition pathways the nitro functional group $-\text{NO}_2$ is involved, while the loss of the NO^\bullet radical was associated with a high kinetic energy release (KER) amounting to nearly 1 eV.²⁷ In addition, in the case of other nitrobases containing nitroguanidine functional group, it was shown that the nitroguanidine functional group directs the fragmentation for all ionization states, while the NO_2 loss dominates only in the case of the protonation.^{28,29} Furthermore, there are differences noted in the decomposition depending on the position of the nitro group $-\text{NO}_2$ attached to the imidazole ring.^{27,30} In a recent study, the fundamental properties of several 5-nitroimidazoles including Roni were studied, such as proton affinity, deprotonation energy, electron affinity, and dipole moment.³¹ The proton affinity of Roni was reported to be 9.33 eV at the N3 position of the imidazole ring.³¹ From a comparison of the low-energy collision-induced dissociation (CID) of protonated 5-nitroimidazoles at a collision energy of 15 eV, it was concluded

that 1-methyl-5-nitroimidazole, metronidazole, and ornidazole lose mainly the nitro functional group NO_2 , while Roni and ornidazole undergo loss of the NO^\bullet radicals.³¹ In contrast, nimorazole did not show any of these losses in the positive ion mode. It was suggested that nitroimidazolic compounds are first prone to dissociation at the N1 position, unless the group at the N1 site is a methyl group such as in the case of Roni. On the other hand, the radical anions of nimorazole mainly lose the NO^\bullet radical under low-energy CID conditions.²⁵ Dissociation at the N1 position was observed also for radical anions and deprotonated nitroimidazolic radiosensitizers in low-energy and also high-energy CID.^{25,32} It is well-known that low-energy CID, which is dominated by multiple collisions with slow velocities, and high-energy CID proceeding via single collision at high-velocity will result in different kinds of excitation of the precursor ion, thus resulting in different product ions.^{25,32–34}

Here, we investigated the main dissociation pathways of protonated Roni in low-energy and high-energy CID. Additionally, we used deuterated solvents to clarify the dissociation pathways involving proton transfer. Due to the different proton transfer reactions that can lead to the main product ion, we have also evaluated the KER for this dissociation channel. Additionally, we have also evaluated the KER for dissociation channel involving the release of NO^\bullet radical due to the high KER observed in the case of simple nitroimidazoles.²⁷

II. METHODS

A. Materials

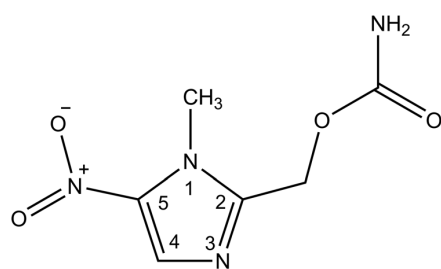
Ronidazole (Scheme 1) was purchased from Sigma Aldrich (purity $\geq 95\%$) and was used as received. Roni was dissolved in methanol, water, and acetic acid ($\text{CH}_3\text{OH}/\text{H}_2\text{O}/\text{CH}_3\text{COOH}$) in a ratio 50/50/1. For the deuterated experiments, we used a solution of methanol- d_4 , D_2O , and acetic acid- d_4 . Deuterated solvents result in the exchange of the labile hydrogens of the NH_2 group of Roni and addition of D^+ on the N3 position of the imidazole ring during ESI.

B. Low-energy CID

1. Waters ultima ESI Q-TOF MS

The CID experiments with protonated Roni, $[\text{Roni}+\text{H}]^+$, were carried out using a commercial instrument (Ultima ESI Q-TOF MS, Waters-Micromass, UK), described elsewhere.³¹ The ions are generated in a Z-spray ESI source, i.e., the ions follow a Z-shaped trajectory between their formation and a skimmer, which is placed right before a hexapole ion guide that transports the ions into the mass spectrometer. A solution of 5 mM of Roni was continuously sprayed at 4.5 bars of the nitrogen drying gas into a differentially pumped region at a working pressure of 1.6 mbar. The constant injection rate of 15 $\mu\text{l}/\text{min}$ was controlled by means of a syringe pump (NewEra Syringe pump Systems, Inc.). The ESI needle was biased at +2.55 kV, and a voltage of +19 V was applied to the cone relative to the extraction lens. The source and desolvation temperatures were set to 363 K and 423 K, respectively.

The instrument consists of a quadrupole (Q), followed by a hexapole collision cell, hexapole transfer lens, a reflectron



Ronidazole

SCHEME 1. Molecular structure of ronidazole (Roni).

time-of-flight mass spectrometer (TOF MS), and a microchannel plate (MCP) for detection of the ions. For the CID experiments, a given precursor is mass-selected by the Q and then subjected to CID within a hexapole collision cell. Argon was used as collision gas at a pressure of 5.7×10^{-5} mbar.

2. Bruker ESI Q-TOF MS

Due to the insufficient resolution of the quadrupole selection achievable with our Ultima ESI Q-TOF MS, we have carried out the CID experiments with deuterated Roni, $[\text{dRoni}+\text{D}]^+$, using a commercial instrument (Q-TOF2, Bruker Bremen, Germany), which is also an ESI Q-TOF MS. Here, a solution of 100 μM of Roni was continuously sprayed at the constant injection rate of 150 $\mu\text{l/h}$ using nitrogen buffer gas. The ESI needle was grounded, while the ESI capillary was biased at -4.2 kV. The desolvation temperature was set to 353 K. This instrument consists of ion transfer stage, analytical quadrupole, quadrupole collision/cooling cell, reflectron TOF, and MCP detector. CID experiments were performed in the collision cell using nitrogen gas at 18% of the maximum flow rate of this instrument.

C. High-energy CID

The collision-induced dissociation of protonated and deuterated ronidazole cations was investigated by means of a home-built ESI source combined with a VG-ZAB-2SE double-focusing mass spectrometer (V.G. Analytical, Ltd., Manchester, UK). The ESI source as well as the mass spectrometer were already described in detail elsewhere;³⁵ therefore, only a brief description will be provided. The ions were produced by ESI,³⁶ where ionization occurred by applying a voltage ranging from +4.75 kV to +5.01 kV on the spray needle with respect to the inlet capillary (inner diameter of 750 μm). Here, a solution of 10 mM of Roni was continuously sprayed at the flow rate set to 650–750 nl/min, and the inlet capillary was kept at room temperature in order to assure continuous spray conditions. The mentioned inlet delivered the formed ions into a homemade ion funnel, based on the design of Julian *et al.*³⁷ Thereafter, an octupole ion guide and an einzel lens setup transferred the ions to the mass spectrometer. All components of the ESI-source were electrically isolated from the mass spectrometer since a voltage drop of 6 kV was used to accelerate the ions between the ESI-source and the first lens stack of the mass spectrometer.

The mass spectrometer has been constructed in a reversed Nier-Johnson geometry, i.e., ions first pass a magnetic sector followed by an electrostatic sector, thereby constituting a double focusing mass spectrometer. The magnetic sector analyzes the ions by their momentum, and then, the electrostatic sector analyzes the ions by their energy. After the electric sector, a channeltron type secondary electron multiplier (Dr. Sjuts, Germany) is used for ion detection. A collision cell before the electrostatic sector allows studies of CID. Helium was used as a collision gas. The exact pressure within the collision-cell is unknown since a cold-cathode gauge was used to measure the pressure in the vacuum chamber of the collision-cell. Consequently, the real pressure within the cell can be roughly estimated to be up to three orders of magnitude higher than the stated pressure values.³⁸ Thus, the measured pressure value of 4×10^{-6} mbar gives an estimation of the real pressure of 4×10^{-3} mbar in the collision cell.

The product ions formed via CID can be assessed by means of the mass-analyzed ion kinetic energy (MIKE) scan method.³⁹ In general, if CID of a precursor ion with mass m_p yields a product ion with mass m_f , this product ion is transmitted at the electric sector field voltage E ,

$$E = E_0 m_f/m_p, \quad (1)$$

with E_0 as the corresponding electric sector field voltage, at which the precursor ion is transmitted. It should be noted that for a given precursor ion, complete electrostatic sector voltage scans were performed in the first step. Subsequently, only scan regions indicating a product ion were selectively measured with better statistics. The latter scans are shown below.

Furthermore, we determined the KER regarding the most abundant CID reactions, as follows:

$$\text{KER} = \frac{y^2 m_1^2 eV}{16xm_2m_3} \left(\frac{\Delta E}{E} \right)^2, \quad (2)$$

where m_1 denotes the mass of the precursor ion and m_2 and m_3 , respectively, the masses of the neutral and charged products. The charge state of the precursor ion and the product ion (in our case both +1) are denoted by x and y and V is the acceleration voltage (6 kV). E is the corresponding electrostatic sector voltage, and in the case of a Gaussian peak shape, ΔE is the width of the peak in the MIKE scan (of which the width of the precursor beam has to be subtracted). The relative uncertainty of the KER value reported for the protonated Roni is $\sim 10\%$, while for the deuterated Roni due to the largely overlapping peaks in question increased the relative uncertainty to $\sim 50\%$.

D. Theoretical calculations

The geometries of all molecules and ions were optimized at the M062x/6-311+G(d,p) level of theory⁴⁰ with the Gaussian-09D01 program package.⁴¹ All the product ions were calculated in their singlet states. Frequencies were calculated to confirm that the structures are local minima on the potential energy surface and not the transition states (TS). All energies were corrected for zero-point energies. Transition states (TS) for the fragmentation pathways of the protonated Roni $[\text{Roni}+\text{H}]^+$ and their frequencies were calculated with the same theory and basis set. Calculations of the intrinsic reaction coordinates (IRC) connected the TS to reactants and products.

III. RESULTS AND DISCUSSION

Electrospray ionization of a solution of Roni leads to $[\text{Roni}+\text{H}]^+$ at m/z 201 through protonation at the N3 position of the imidazole ring, which has the highest proton affinity.³¹ The low-energy CID of $[\text{Roni}+\text{H}]^+$ was measured at several nominal laboratory collision energies up to 20 eV, and the results are summarized in Fig. 1, which shows the product ion at m/z 140 increasing in intensity with the nominal laboratory collision energy and dominating in the spectra above 8 eV. It is interesting to note that the product ion at m/z 140 is also the most abundant product ion that appears in the high-energy CID (Fig. 2) of the protonated Roni, $[\text{Roni}+\text{H}]^+$ m/z 201.

The high-energy CID of $[\text{Roni}+\text{H}]^+$ (Fig. 2) was measured with a two-sector field instrument here for the first time. In the work of

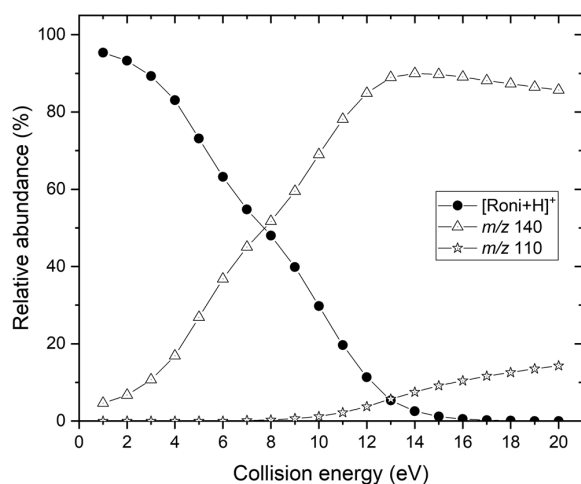


FIG. 1. Summary of the low-energy collision-induced dissociation reactions of the electro spray generated ion $[\text{Roni}+\text{H}]^+$ as a function of the nominal laboratory collision energy measured at Ultima ESI Q-TOF MS. Each of the points corresponds to the integrated peak of the corresponding m/z . For the assignment of the product ions at m/z 140 and m/z 110, refer to the text. Minor product ions (m/z 94 and 82) of relative abundance $<2\%$ appearing above 13 eV of the nominal laboratory collision energy were omitted for clarity. The collision cell was filled with argon gas.

Kumar *et al.*,²¹ protonated Roni was studied at Q Exactive mass spectrometer that employs C-trap dissociation; however, only product ion at m/z 140 was reported. The two-sector field mass spectrometer is unique as it can give information on the KER of the dissociation

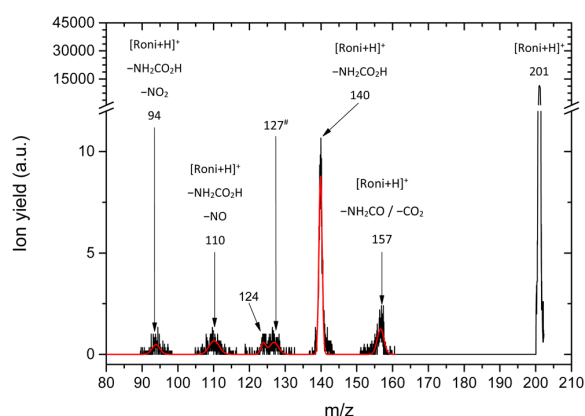


FIG. 2. High-energy collision-induced dissociation mass spectrum of $[\text{Roni}+\text{H}]^+$ formed via electrospray ionization and accelerated to 6 keV (black line). The collision cell was filled with helium gas. The red line shows the convoluted Gaussian fit line to guide the eye. For the assignment of the ion designated by #, see text for details.

processes, which is lost in other types of high-energy CID instruments. The high-energy CID of $[\text{Roni}+\text{H}]^+$ (Fig. 2) leads to fragment ions at m/z 157, 140, 127, 110, and 94. The product ion at m/z 157 is due to the loss of a nominal mass of 44 Da, which could be formed either due to the simple C–O bond cleavage and release of the neutral radical NH_2CO , or due to the rearrangement reaction releasing CO_2 . The product ion at m/z 140 arises from the loss of $[\text{C}_2\text{H}_3\text{N}_2\text{O}_2]$ and its assignment is discussed in the next paragraph. The product ion at m/z 127 is due to the loss of a nominal mass of 74 Da, which could be formed either directly from $[\text{Roni}+\text{H}]^+$ by a simple C2–C bond cleavage of the side chain releasing the neutral radical $\text{CH}_2\text{CO}_2\text{NH}_2$, or by concomitant loss of NO^\bullet radical from product ion at m/z 157. The product ion at m/z 110 also appeared under low-energy CID (Fig. 1) conditions and as previously suggested by Pandeti *et al.*,³¹ it is formed from the main product ion at m/z 140 via subsequent loss of the NO^\bullet . Usually, the loss of NO^\bullet is an exothermic reaction associated with a high KER, as in the case of simple nitroimidazoles.²⁷ The evaluated KER for this dissociation channel amounts to 339 meV, which is lower than the KER reported for simple nitroimidazoles of nearly 1 eV.²⁷ Due to the high internal energy content of the electrosprayed ions observed already previously for this experimental setup,³⁵ the main product ion of m/z 140 is also visible in the ESI mass spectrum. The high-energy CID of mass selected m/z 140 (Fig. S1 of the supplementary material) showed that the product ion at m/z 94 is also formed from further dissociation of m/z 140 likely through the loss of a complete NO_2^\bullet group.

The main product ion at m/z 140 observed in both low-energy CID (Fig. 1) and high-energy CID (Fig. 2) is formed due to the loss of a nominal mass of 61 Da and is not a simple bond cleavage. Different structures have been considered for the product ion at m/z 140 ion associated with different neutral losses. All the structures considered are shown in Fig. S2 of the supplementary material. The loss of CH_3NO_2 can be excluded as a possible dissociation route due to the high threshold for this process, which is calculated to be 4.50 eV (Fig. S2). Instead, the loss of 61 Da associated with a proton H^+ transfer to the side group attached to C2 position of the imidazole ring leading to the release of $\text{NH}_2\text{CO}_2\text{H}$ appears to be more favorable. Two relevant pathways were found for this mechanism and are shown in Fig. 3. One involves transfer of a proton H^+ from the N3 position via TS2 of 0.97 eV, followed by the rupture of the C–O bond, eventually leading to the release of $\text{NH}_2\text{CO}_2\text{H}$ with a thermodynamic threshold of 2.40 eV. The second pathway includes proton transfer from the $-\text{CH}_3$ group. It has a higher barrier through TS1 of 2.77 eV. However, it results in a slightly lower thermodynamic threshold of 2.24 eV. To distinguish which of the pathway takes place under CID, we performed experiments with deuterated solvents. As mentioned earlier, using deuterated solvents results in exchange of the labile hydrogens of the NH_2 group of Roni (Scheme 1) and in the addition of D^+ on the N3 position of the imidazole ring upon ESI. Thus, the precursor ion $[\text{Roni}+\text{H}]^+$ at m/z 201 will change to m/z 204 upon full deuteration due to the exchange of three H by D. We label this compound hereafter as $[\text{dRoni}+\text{D}]^+$. Thus, if $[\text{dRoni}+\text{D}]^+$ dissociates via TS1, a neutral loss of $\text{ND}_2\text{CO}_2\text{H}$ will lead to the formation of the product ion at m/z 141, while the dissociation via TS2 will lead to neutral loss of $\text{ND}_2\text{CO}_2\text{D}$, resulting in the formation of the product ion at m/z 140.

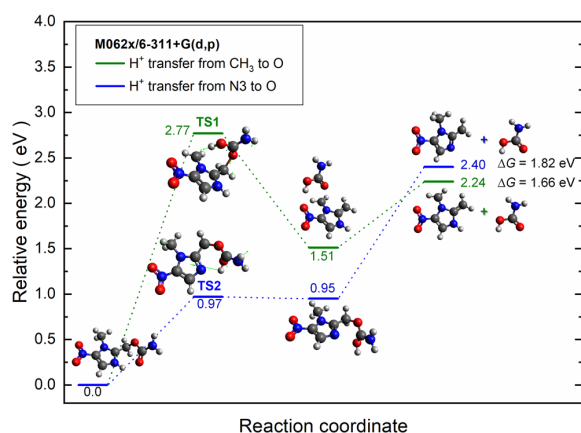


FIG. 3. M062x/6-311+G(d,p) calculated potential energy diagram for the dissociation of $[\text{Roni}+\text{H}]^+$ leading to the product ion at m/z 140. The free reaction energy $\Delta G_{298\text{K}}$ is also shown in eV. The green arrows in the respective TS show the displacement vectors.

The low-energy CID of the fully deuterated $[\text{dRoni}+\text{D}]^+$ as a function of the nominal laboratory collision energy is summarized in Fig. 4. An example mass spectrum of CID at 15 eV is shown in Fig. S3 of the supplementary material. The spectrum shows dominant product ion at m/z 140 and a very small amount of product ion at m/z 141. However, from the data, we can conclude that the ion at m/z 141 is only due to the ^{13}C isotope of the partially deuterated

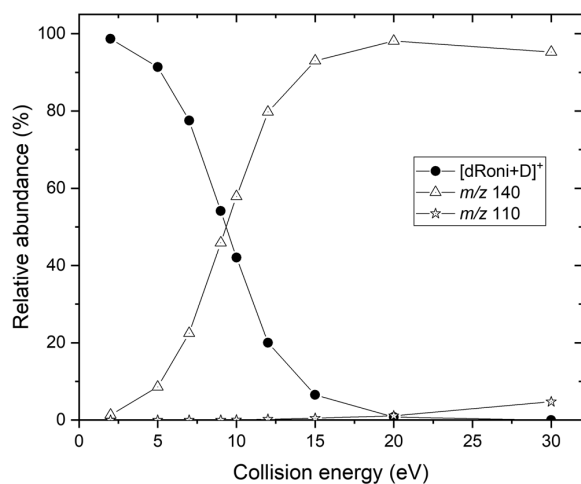


FIG. 4. Summary of the low-energy collision-induced dissociation reactions of the electrospray generated ion $[\text{dRoni}+\text{D}]^+$ as a function of the nominal laboratory collision energy measured at Bruker ESI Q-TOF MS. Each of the points corresponds to the integrated peak of the corresponding m/z . For the assignment of the product ions at m/z 140 and m/z 110, refer to the text. The collision cell was filled with nitrogen gas.

Roni at m/z 203, labeled hereafter $[\text{dRoni}+\text{H}]^+$. In the ESI mass spectrum, the fully deuterated Roni at m/z 204 $[\text{dRoni}+\text{D}]^+$ is the most abundant ion, while $[\text{dRoni}+\text{H}]^+$ at m/z 203 is at 27% abundance of m/z 204 (see Fig. S4). Taking into account the natural abundance of 8.2%, the ^{13}C isotope of the m/z 203 contributes to the m/z 204 by 2.2%. The contribution is probably slightly higher, as the ^{13}C isotope of the m/z 204 has abundance of 9.8% instead of the natural abundance of 8.2% (Fig. S4). In the case of taking 9.8% as the amount of ^{13}C isotope, the contribution of m/z 203 to m/z 204 is 2.6%. In the Table S1 of the supplementary material, one can see that the number of counts of product ion at m/z 141 formed at different nominal laboratory collision energies (2–30 eV) is always below <2.6%. Thus, we can conclude that in low-energy CID measured in the (2–30 eV) nominal laboratory collision energy range with the present experimental setup, we do observe only pathway, where D^+ (H^+) is transferred from the N3 position to release the neutral $\text{ND}_2\text{CO}_2\text{D}$ (Fig. 3).

The result concerning high-energy CID of $[\text{dRoni}+\text{D}]^+$ accelerated to 6 keV with a focus on the main dissociation channel in question is shown in Fig. 5. A clear broadening to the right of the m/z 140 is visible, i.e., a product ion at m/z 141 appeared. A zoom of this m/z region is shown in the inset. In this case, the fully deuterated Roni $[\text{dRoni}+\text{D}]^+$ at m/z 204 was not the most abundant ion in the ESI mass spectrum. The most abundant ion was partially deuterated Roni $[\text{dRoni}+\text{H}]^+$ at m/z 203. Indeed, D/H back-exchange can occur rapidly due to the humidity before the ions enter into the mass spectrometer or in the inlet capillary. Due to this strong presence of the partially deuterated ions at mass 203, the mass peak at m/z 204 is contaminated by partially deuterated ions containing instead of ^{12}C the ^{13}C isotope, according to our measurements amounting to 20.47%. Additionally, we have performed CID of the partially deuterated Roni $[\text{dRoni}+\text{H}]^+$ at m/z 203, which is shown in Fig. S5 of the supplementary material. Only the product ion at m/z 140 is observed, making the two different pathways shown in Fig. 3 undistinguishable. This means that the partially deuterated Roni $[\text{dRoni}+\text{H}]^+$ has two D atoms at the NH_2 group (see Scheme 1) while on the N3 position of the imidazole ring there sits a proton H^+ . This is also confirmed by the low-energy CID experiments of $[\text{dRoni}+\text{H}]^+$ shown in Fig. S6, which also leads only to product ion at m/z 140. Thus, the m/z 203 ^{13}C isotopic contamination of m/z 204 upon CID will contribute by (1/6) of 20.47% to the product ion at m/z 140 and by (5/6) to the product ion at m/z 141. Since the widths of the product ion peaks at m/z 140 and 141 are different (see Fig. 5), we made a correction of the peak heights and not the peak areas. These corrected peaks of the formed product ion abundances are shown by dashed lines in the inset of Fig. 5. This gives a contribution of 81% for the pathway that proceeds through proton transfer from N3 position and 19% contribution for the pathway involving proton transfer from CH_3 group (see Fig. 3).

According to Eq. (2), we have calculated KER values for both pathways. The KER values are relatively small. The pathway leading to the product ion at m/z 140 via proton transfer from N3 position is associated with a KER of about 10 meV, while the second pathway leading to the product ion at m/z 141 via proton transfer from CH_3 group is associated with a KER of about 23 meV. According to the potential energy diagram (Fig. 3), the latter reaction is indeed expected to be associated with the higher KER value due to the TS

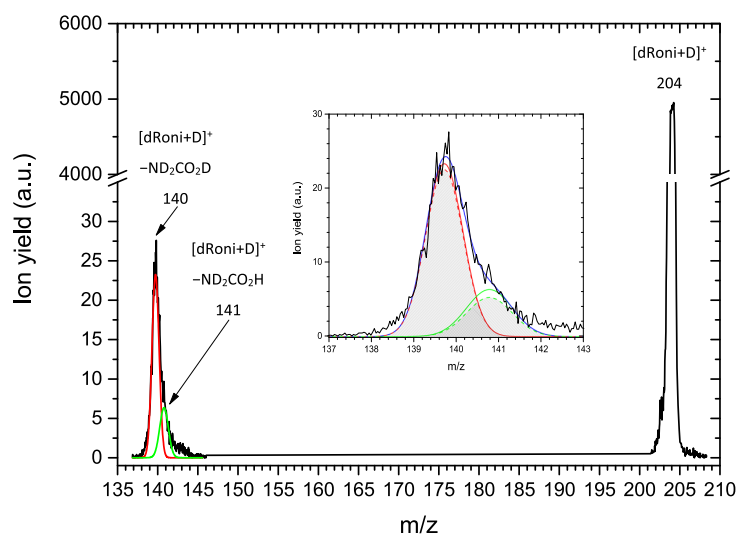


FIG. 5. High-energy collision-induced dissociation mass spectrum of $[dRoni+D]^+$ formed via electrospray ionization and accelerated to 6 keV (black line). The spectrum shows only the product ions of interest. The collision cell was filled with helium gas. The red and green lines are Gaussian fits of m/z 140 and 141, respectively. The inset shows a blow-up of the m/z 140 and 141 peak. The dashed red and green lines correspond to the correction of the abundance due to the ^{13}C isotope contaminant of the m/z 203, where only two H are exchanged in Roni by D. For details, refer to the text.

above the thermodynamic threshold. Thus, the KER value obtained for this process suggests that most of the energy is carried away as internal energy of the products.

IV. CONCLUSIONS

We have investigated decomposition of protonated Roni, $[Roni+H]^+$, in low-energy and high-energy CID experiments and by density functional theory. The main dissociation channel forming product ion at m/z 140 observed in both low-energy and high-energy CID involves proton transfer reaction followed by a release of neutral NH_2CO_2H . The experiments of CID of deuterated Roni, $[dRoni+D]^+$ have shown that while in low-energy CID only proton transfer from the N3 position of the imidazole ring is observed, in the high-energy CID also proton transfer from the $-CH_3$ group is observed with contributions of 81% and 19%, respectively. Both dissociation channels were shown to have small KER values of 10–23 meV. However, the neutral loss of NH_2CO_2H associated with further loss of NO^\bullet radical has substantially higher KER value of 339 meV. Other product ions observed in the high-energy CID were due to the simple and homolytic bond cleavages forming radical product ions and neutral radicals.

Characterization of the dissociation products and the pathways for ions derived from nitroimidazoles will contribute to the knowledge of fundamental chemistry of nitroimidazoles that is needed for the development of the nitroimidazole based compounds and their detection in food or water.

SUPPLEMENTARY MATERIAL

See [supplementary material](#) for the following: high-energy CID of m/z 140, calculated thermodynamic threshold energies for the dissociation of $[Roni+H]^+$, low-energy CID of $[dRoni+D]^+$,

high-energy CID of $[dRoni+H]^+$, low-energy CID of $[dRoni+H]^+$, and table with data for low-energy CID of $[dRoni+D]^+$.

ACKNOWLEDGMENTS

L.F. is thankful for the support from the University of Innsbruck via Grant No. P7440-035-011, the Institut de Physique Nucléaire de Lyon (Institut de Physique des 2 Infinis de Lyon), and the LABEX Lyon Institute of Origins (Grant No. ANR-10-LABX-0066) of the Université de Lyon for its financial support within the program “Investissements d’Avenir” (Grant No. ANR-11-IDEX-0007) of the French government operated by the National Research Agency (ANR). The crucial computing support from the HPC infrastructures CCIN2P3 (France) is gratefully acknowledged. S.D. acknowledges support from the Austrian Science Fund, FWF, Vienna (Grant No. P30332). This work was also supported by Fundação para a Ciência e a Tecnologia (FCT-MCTES), Radiation Biology and Biophysics Doctoral Training Programme (Grant Nos. RaBBiT and PD/00193/2012), UID/Multi/04378/2019 (UCIBIO), UID/FIS/00068/2019 (CEFITEC), and scholarship Grant No. PD/BD/114447/2016 to J.A.

Dedicated to our friend and collaborator, Professor Leo Radom on the occasion of his 75th birthday and in recognition of his outstanding contributions to theoretical chemistry.

REFERENCES

- 1 A. M. Rauth, R. S. Marshall, and B. L. Kuehl, *Cancer Metastasis Rev.* **12**, 153 (1993).
- 2 P. Wardman, *Clin. Oncol.* **19**, 397 (2007).
- 3 A. H. Lau, N. P. Lam, S. C. Piscitelli, L. Wilkes, and L. H. Danziger, *Clin. Pharmacokinet.* **23**, 328 (1992).
- 4 J. Overgaard, H. S. Hansen, M. Overgaard, L. Bastholt, A. Berthelsen, L. Specht, B. Lindeløv, and K. Jørgensen, *Radiother. Oncol.* **46**, 135 (1998).
- 5 L. Bentzen, S. Keiding, M. R. Horsman, T. Grønroos, S. B. Hansen, and J. Overgaard, *Acta Oncol.* **41**, 304 (2002).

- ⁶A. R. Padhani, K. A. Krohn, J. S. Lewis, and M. Alber, *Eur. Radiol.* **17**, 861 (2007).
- ⁷X. Su, X. Cheng, C. Meng, and X. Yuan, *J. Hazard. Mater.* **161**, 551 (2009).
- ⁸Z. Yu and E. R. Bernstein, *J. Chem. Phys.* **137**, 114303 (2012).
- ⁹C. Han, J. Chen, X. Wu, Y.-W. Huang, and Y. Zhao, *Talanta* **128**, 293 (2014).
- ¹⁰M. Arias, O. P. Chevallier, S. F. Graham, A. Gasull-Gimenez, T. Fodey, K. M. Cooper, S. R. H. Crooks, M. Danaher, and C. T. Elliott, *Food Chem.* **199**, 876 (2016).
- ¹¹A. Gadaj, K. M. Cooper, N. Karoonuthaisiri, A. Furey, and M. Danaher, *Food Addit. Contam., Part A* **32**, 180 (2015).
- ¹²K. Mitrowska, A. Posyniak, and J. Zmudzki, *Anal. Lett.* **47**, 1634 (2014).
- ¹³A. Fakhri, S. Rashidi, M. Asif, and A. A. Ibrahim, *Appl. Sci.* **7**, 205 (2017).
- ¹⁴K. Mitrowska and M. Antczak, *Food Addit. Contam., Part A* **34**, 573 (2017).
- ¹⁵X. Li, Y. Ke, Y. Wang, C. Wang, D. Ye, X. Hu, L. Zhou, and X. Xia, *Molecules* **23**, 3350 (2018).
- ¹⁶A. Rúbies, G. Sans, P. Kumar, M. Granados, R. Companyó, and F. Centrich, *Anal. Bioanal. Chem.* **407**, 4411 (2015).
- ¹⁷W. Han, Y. Pan, Y. Wang, D. Chen, Z. Liu, Q. Zhou, L. Feng, D. Peng, and Z. Yuan, *J. Pharm. Biomed. Anal.* **120**, 84 (2016).
- ¹⁸E. Daeseleire, H. De Ruyck, and R. Van Renterghem, *Analyst* **125**, 1533 (2000).
- ¹⁹H. Zhao, J. Zulkoski, and K. Mastovska, *J. Agric. Food Chem.* **65**, 7268 (2017).
- ²⁰G. Cao, J. Zhan, X. Shi, X. Deng, J. Zhu, W. Wu, and X. Chen, *Chromatographia* **81**, 707 (2018).
- ²¹P. Kumar, A. Rúbies, F. Centrich, and R. Companyó, *Meat Sci.* **97**, 214 (2014).
- ²²L. Qin, Y.-L. Lin, B. Xu, C.-Y. Hu, F.-X. Tian, T.-Y. Zhang, W.-Q. Zhu, H. Huang, and N.-Y. Gao, *Water Res.* **65**, 271 (2014).
- ²³L. Sun, D. Chen, S. Wan, Z. Yu, and M. Li, *Chem. Eng. J.* **326**, 1030 (2017).
- ²⁴W. Yang, X. Wu, T. Liu, T. Wang, and X. Hou, *Analyst* **143**, 5744 (2018).
- ²⁵L. Feketeová, A. L. Albright, B. S. Sørensen, M. R. Horsman, J. White, R. A. J. O'Hair, and N. Bassler, *Int. J. Mass Spectrom.* **365-366**, 56 (2014).
- ²⁶K. Tanzer, L. Feketeová, B. Puschnigg, P. Scheier, E. Illenberger, and S. Denifl, *Angew. Chem., Int. Ed.* **53**, 12240 (2014).
- ²⁷L. Feketeová, J. Postler, A. Zavras, P. Scheier, S. Denifl, and R. A. J. O'Hair, *Phys. Chem. Chem. Phys.* **17**, 12598 (2015).
- ²⁸W. A. Donald, M. G. Leeming, and R. A. J. O'Hair, *Int. J. Mass Spectrom.* **316-318**, 91 (2012).
- ²⁹M. G. Leeming, J. M. White, R. A. J. O'Hair, and W. A. Donald, *J. Am. Soc. Mass Spectrom.* **25**, 427 (2014).
- ³⁰P. Bolognesi, A. R. Casavola, A. Cartoni, R. Richter, P. Markus, S. Borocci, J. Chiarinelli, S. Tošić, H. Sa'adeh, M. Masić, B. P. Marinković, K. C. Prince, and L. Avaldi, *J. Chem. Phys.* **145**, 191102 (2016).
- ³¹S. Pandeti, L. Feketeová, T. J. Reddy, H. Abdoul-Carime, B. Farizon, M. Farizon, and T. D. Märk, *RSC Adv.* **7**, 45211 (2017).
- ³²J. M. Khreis, S. Pandeti, L. Feketeová, and S. Denifl, *Int. J. Mass Spectrom.* **431**, 1 (2018).
- ³³H. I. Kenttämää and R. G. Cooks, *Int. J. Mass Spectrom. Ion Processes* **64**, 79 (1985).
- ³⁴J. A. Wyer, L. Feketeová, S. B. Nielsen, and R. A. J. O'Hair, *Phys. Chem. Chem. Phys.* **11**, 8752 (2009).
- ³⁵J. M. Khreis, J. Reitsammer, V. Vizcaino, K. Klawitter, L. Feketeová, and S. Denifl, *Rapid Commun. Mass Spectrom.* **32**, 113 (2018).
- ³⁶J. Fenn, M. Mann, C. Meng, S. Wong, and C. Whitehouse, *Science* **246**, 64 (1989).
- ³⁷R. R. Julian, S. R. Mabbett, and M. F. Jarrold, *J. Am. Soc. Mass Spectrom.* **16**, 1708 (2005).
- ³⁸I. W. Griffiths, E. S. Mukhtar, R. E. March, F. M. Harris, and J. H. Beynon, *Int. J. Mass Spectrom. Ion Phys.* **39**, 125 (1981).
- ³⁹R. G. Cooks, J. H. Beynon, R. M. Caprioli, and G. R. Lester, *Metastable Ions* (Elsevier Scientific Pub. Co, Amsterdam, 1973).
- ⁴⁰Y. Zhao and D. G. Truhlar, *Theor. Chem. Acc.* **120**, 215 (2008).
- ⁴¹M. J. Frisch, G. W. Trucks, H. B. Schlegel, G. E. Scuseria, M. A. Robb, J. R. Cheeseman, G. Scalmani, V. Barone, B. Mennucci, G. A. Petersson, H. Nakatsuji, M. Caricato, X. Li, H. P. Hratchian, A. F. Izmaylov, J. Bloino, G. Zheng, J. L. Sonnenberg, M. Hada, M. Ehara, K. Toyota, R. Fukuda, J. Hasegawa, M. Ishida, T. Nakajima, Y. Honda, O. Kitao, H. Nakai, T. Vreven, J. A. Montgomery, Jr., J. E. Peralta, F. Ogliaro, M. Bearpark, J. J. Heyd, E. Brothers, K. N. Kudin, V. N. Staroverov, T. Keith, R. Kobayashi, J. Normand, K. Raghavachari, A. Rendell, J. C. Burant, S. S. Iyengar, J. Tomasi, M. Cossi, N. Rega, J. M. Millam, M. Klene, J. E. Knox, J. B. Cross, V. Bakken, C. Adamo, J. Jaramillo, R. Gomperts, R. E. Stratmann, O. Yazyev, A. J. Austin, R. Cammi, C. Pomelli, J. W. Ochterski, R. L. Martin, K. Morokuma, V. G. Zakrzewski, G. A. Voth, P. Salvador, J. J. Dannenberg, S. Dapprich, A. D. Daniels, O. Farkas, J. B. Foresman, J. V. Ortiz, J. Cioslowski, and D. J. Fox, *GAUSSIAN 09*, Revision D.01, Gaussian, Inc., Wallingford CT, 2013.

Part II

Electron interactions with biomolecules

Theoretical overview

This chapter provides a brief description of the mechanisms underlying the interaction of an electron with a neutral molecule, in the gas-phase. The most relevant concepts are related to the formation of anions through the resonant attachment of electrons by neutral molecules, and cations through electron ionization.

5.1 Born-Oppenheimer Approximation

The Born-Oppenheimer approximation relies on the large difference between the electronic motion and the nuclear motion, such as vibrational and rotational motions. For a given amount of kinetic energy, the displacement of nuclei is much slower than the displacement of electrons, due to the huge ratio between the nuclear and electronic mass. Hence, the electron configuration is considered as well-defined for each nuclei configuration. So from the mathematical point of view, the molecular wave function, ψ_{total} can be expressed as the product between the electronic wavefunction, ψ_e , and the nuclear wavefunction, ψ_N , [125]:

$$\psi_{total} = \psi_e \psi_N \quad (5.1)$$

According to the Born-Oppenheimer approximation, the electronic and nuclear wave functions are decoupled. A second approximation consists in separating the nuclei motion

into its different components, vibrational, ψ_{N_v} , and rotational, ψ_{N_R} as follows:

$$\psi = \psi_e \psi_{N_v} \psi_{N_R} \quad (5.2)$$

Therefore, a given molecular state is characterized through its electronic, vibrational and rotational state, and total energy of a molecular state corresponds to the summed contribution of each of them:

$$E_t = E_{N_R} + E_{N_v} + E_e \quad (5.3)$$

The Born-Oppenheimer approximation sets the framework for the Franck-Condon principle, which will be introduced in the following section.

5.2 Franck-Condon principle

The Franck-Condon principle states that the molecular geometry is preserved when a molecule undergoes an electronic transition. For a diatomic molecule, a so-called vertical transition takes place from a point in the potential energy curve of the ground state to a point located directly above in the potential energy curve of a given excited state [55, 125]. An adiabatic transition is defined as a transition from vibrational state $v = 0$ in the ground state, to the vibrational state $v = 0$ in a given excited state. Both vertical and adiabatic transitions are schematically represented in figure 5.1.

The probability of occurring a vertical transition depends on the molecular geometry of the respective molecular states involved. By using the Born-Oppenheimer approximation (see section 5.1), this probability is defined by the Franck-Condon overlap integral, or also referred to as Franck-Condon factor, f_{FC} . Hence, the probability $P_{l,u}$ for a transition from a vibrational state v in the first state l , to a vibrational state v' in a second state u , can be calculated by [125]:

$$f_{FC} \equiv P_{l,u} \sim \left(\int \psi_l^v \psi_u^{v'} dR \right)^2 \quad (5.4)$$

5.2. Franck-Condon principle

The distribution of Franck-Condon factors reflects the distribution of vibrational states for an excited ionic state, as depicted in the lower panel of figure 5.1 [55].

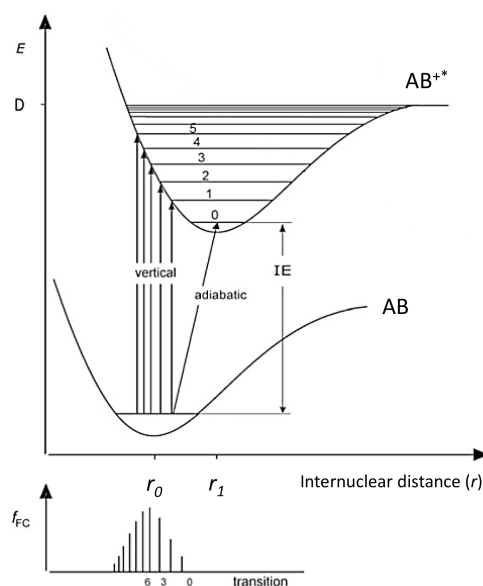
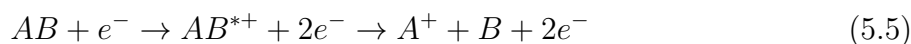


Figure 5.1. Schematic representation of various vertical transitions from the ground state of a diatomic molecule, AB , to different vibrational states v of a stable ionic state, denoted by AB^{+*} . The lower inset shows the Franck-Condon factors, f_{FC} , for several transitions. Adapted from [55].

It should be noted that the considerations on the Born-Oppenheimer approximation, as well as the Franck-Condon Principle quantitatively describes vertical transitions in diatomic molecules. In the case of a polyatomic molecule comprising n atoms, the energy potential curves are thus to be replaced by n -dimensional potential energy surfaces. For a polyatomic molecule, although a vertical transition will proceed without changes in the molecular geometry, accordingly to the Franck-Condon principle, the subsequent dynamics is different as the excited molecular ion may undergo relaxation along other n coordinates.[125]

5.3 Dissociative ionization

The interaction of a free electron with a target molecule can be categorized as direct scattering and resonant scattering, depending on the amount of time spent by the incoming electron in the vicinity of the target molecule. Dissociative ionization is an inelastic direct scattering process, in which the incoming electron initially ionizes the target molecule AB to form a parent cation, AB^{*+} , which dissociates into a positively charged fragment, A^+ and one or more neutral fragments, denoted as B . Such process is described by the following equation [42]:



The superscript $*$ indicates that the ion is in a vibrationally and/or electronically excited state.

The formation of the parent cation corresponds to a vertical transition to the ionization continuum within the Franck-Condon region. However, when the energy transferred by the incoming electron to the molecule exceeds the ionization energy (IE), the parent cation is left in a vibrationally and/or electronically excited state. The distribution of the internal energy of the parent cation among the internal degrees of freedom of the molecule often leads to fragmentation [42].

For DI to a diatomic molecule AB in which the single bond is cleaved, the energy threshold is, in general, given as the sum of the respective bond dissociation energy (BDE) and the ionization energy of the neutral precursor of the positively charged fragment formed, because of the vertical transition. Thus, the energy threshold for A^+ formation by DI to AB is given by [42]:

$$E_{th} = BDE(A - B) + IE(A) \quad (5.6)$$

5.3.1 Dissociative ionization cross section

The energy threshold of DI is usually slightly above the ionization energy of the target molecule. With increasing energy, more fragmentation pathways are possible as the parent cation is formed with internal energy.[55] The DI cross section as function of the electron energy increases till it reaches a plateau at energies of about 70-100 eV, and then gradually decreases. Generally, as shown in figure 5.2, the total ionization cross section (TICS) which corresponds to the sum of all ionization processes follows the same trend.[42, 55] This behavior correlates with the de Broglie wavelength of the electron, as at an energy of 70 eV the electron's wavelength is comparable with the average bond length of most molecules, that is in range of 100 up to 200 pm. At higher electron energies, the energy transfer to the target molecule decreases, because (i) the de Broglie wavelength gets shorter, and (ii) the interaction time is shorter.[55]

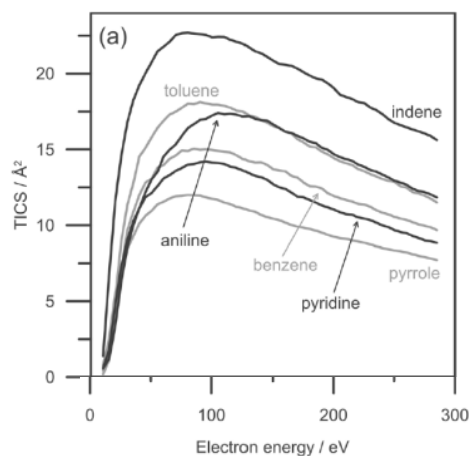


Figure 5.2. Experimental total ionization cross section (TICS) for a collection of aromatic species. Adapted from [132].

At an incident electron energy of 70 eV, the DI process often results in a characteristic fragmentation pattern, and is considered a useful technique in mass spectrometry for identification of compounds.[42, 55] Nowadays, electron ionization mass spectra are available in different databases, such as the NIST Chemistry Webbook [133]. As an example,

within this thesis, the mass spectrum of OTfU acquired at an electron energy of 70 eV was reported for the first time, see section 7.

5.4 Electron attachment

Electron attachment constitutes a resonant scattering process through which a temporary negative ion (TNI), also referred to as resonance, is formed. In this case, the electron is temporarily trapped in the vicinity of the target molecule; the dwell time is therefore large when compared to the transit time the electron needs to travel through the molecule. In comparison to electron attachment, dissociative ionization (see section 5.3) is, however a direct scattering process, in which the incoming electron transfers energy to the molecule leading to ionization. An electron with an energy of 70 eV travels at a speed of approximately $v = 5.0 \times 10^6$ m/s. Considering the typical molecular size of a few angstroms, the transit time of the electron in the vicinity of the molecule is thereby just a few picoseconds, and smaller than the lifetime of resonances observed for molecules constituted by more than three atoms.

The first step in the formation of the TNI by electron capture corresponds to a vertical transition from the ground state of the neutral molecule to a given anionic state within the Franck-Condon region, depicted by the shaded area in figure 5.4. Hence, the TNI may be formed in an excited state [42, 126, 134]:



The superscript * denotes that the TNI may be in an electronically and/or vibrationally excited state. The classification of resonances depending on the electronic structure will be discussed in the section 5.4.3.

The resonance or TNI lifetime, may vary depending on the electronic structure, molecular size, the electron energy and its internal energy. [42, 126] Accordingly to the

Heisenberg's uncertainty principle, the resonance width, Γ , may be defined as:

$$\Gamma \geq \frac{\hbar}{\tau} \quad (5.8)$$

\hbar denotes the reduced Planck constant and τ the lifetime.

For most diatomic molecules, the TNI lifetime is a few femtoseconds [135], while for CCl_4 the respective TNI may survive for a few picoseconds [136], and it may survive for longer times up to a few tens microseconds, as in the case for SF_6 [137].

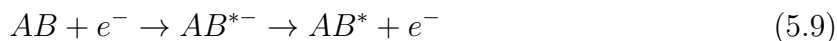
5.4.1 Electron affinity

An important quantity in electron attachment processes is the electron affinity (EA). The vertical electron affinity (VEA) which is defined as the energy difference between the neutral molecule, AB , and one electron at infinity, and the molecular anion AB^- (equation 5.7). Equivalently, the adiabatic electron affinity (AEA) is defined as the difference between the energy of the neutral molecule plus the electron at infinity and the energy of the respective molecular anion, when both are in their respective electronic, vibrational and rotational ground state [125, 138]. By definition, if the ground state of AB^- lies below the ground state of neutral AB , as illustrated in figure 5.3, it is considered that the adiabatic electron affinity of AB , $AEA(AB)$, is positive. Conversely, the AEA is negative, if the ground state of AB^- lies above the ground state of neutral AB . Hence, a positive adiabatic electron affinity suggests a long-lived molecular anion might be formed.

The vertical detachment energy (VDE) is defined as the energy required to detach the extra electron from the molecular anion in the ground state, without changing the internuclear distance. The figure 5.3 (A) represents a situation that prevails for the majority of molecules, $|VDE(AB^-)| > AEA(AB)$ [125]. This figure also depicts the formation of a vibrational Feshbach resonance, as defined in section 5.4.3.

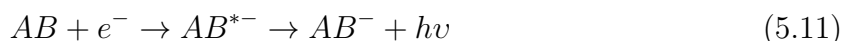
The vertical attachment energy (VAE) is also related to the EA, and it is defined as energy difference between the neutral molecule in its ground state plus the electron at infinity, and the molecular anion formed by attachment of the electron without changing the internuclear distance. The figure 5.3 (B) illustrates the case where $VAE(AB) \leq$

lifetime varies from a few tens of femtoseconds to the millisecond time scale for larger molecules [138].



Radiative stabilization

Radiative stabilization of the excited TNI, through reaction 5.11, to the anionic ground state is possible for molecules having a positive electron affinity. A photon is emitted by the excited TNI carrying away energy $h\nu$ in order to stabilize the molecular anion. Radiative stabilization is typically a slow process with a lifetime in order of $10^{-9} - 10^{-8}$ s.[126]



Dissociative electron attachment – DEA

DEA is a process where the TNI dissociates into one negatively charged fragment and one or more neutrals, as described by reaction 5.12. As schematically represented in figure 5.4, electron capture by the target molecule AB occurs through a vertical transition from the neutral ground state, AB, to a repulsive or dissociative anionic excited state, AB^{*-} , forming thus a TNI. It undergoes relaxation through nuclear displacement wherein the internuclear distance, r , gradually increases until the anionic excited state crosses with the neutral ground state (crossing point, r_C). At this point, the nuclear relaxation may lead to bond cleavage and the formation of a negatively charged fragment and one or more neutrals.[42, 126, 134] In addition to this mechanism, the formation of a given fragment anion by DEA occurs when the thermodynamic requisites are fulfilled, as discussed in section 5.4.5. Considering a complex polyatomic molecule, in addition to single bond cleavage, further fragmentation pathways may involve rearrangement reactions by which neutral and charged fragments are formed with a structure not found in the parent molecule.[42]

DEA is an event that typically occurs for a simple bond cleavage on a time scale

ranging from 10^{-14} up to 10^{-12} s, and thus in the same timescale as autodetachment. Therefore, autodetachment competes with dissociative electron attachment.[42, 126, 134]

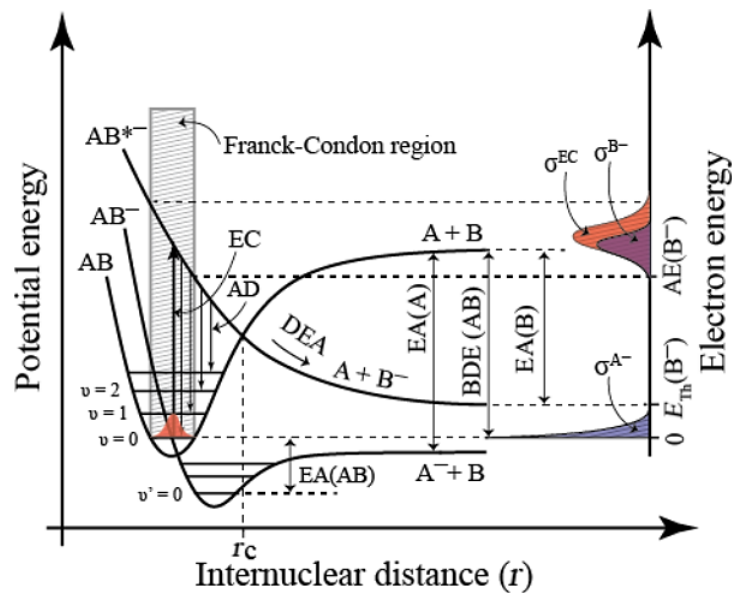


Figure 5.4. Schematic representation showing dissociative electron attachment to a diatomic molecule AB. The potential energy curves for the neutral ground state, AB, the anionic ground state, AB⁻, and a dissociative anionic excited state AB^{*-} are represented. The electron capture process, labelled as EC, occurs within the Franck-Condon region (shaded area) and leads to the formation of a TNI. The TNI may relax through nuclear relaxation along the anionic potential curve, and autodetachment, labelled as AD, may occur until the crossing point, r_C , with the neutral potential curve. In the right-hand side axis, the energy dependence of the electron capture, σ_{EC} , as well as the ion yield for the formation of A⁻, σ_{A^-} , at 0 eV is shown. At electron energies above 0 eV, the formation of B⁻ obtained by the reflection principle, σ_{B^-} , is also presented. Taken from [42, 140].

5.4.3 Resonances

The focus of the present section is to answer the following question:

”What is the mechanism responsible for trapping an incoming electron for times considerably longer than the direct transit time through the molecule’s dimension?”

Prof. Dr. Eugen Illenberger in *Gaseous Molecular Ions, Part III - Electron attachment processes in molecules and molecular aggregates, 1992*

The mechanisms underlying electron attachment by a target molecule to form a TNI, or resonance may be generally categorized based on the changes caused by the incorporation of the extra electron into the molecular structure. The figure 5.5 shows the electronic configuration of TNIs. In the case of single-particle (1p) resonances, the extra electron is added to the lowest unoccupied molecular orbital (LUMO), while the core electron configuration remains unchanged. On the other hand, in the case of two-particle one-hole (2p-1h) resonances, the electron attachment process causes a concomitant electronic transition in the neutral molecule, in which both electrons are added to two normally empty molecular orbitals (MOs).[42]

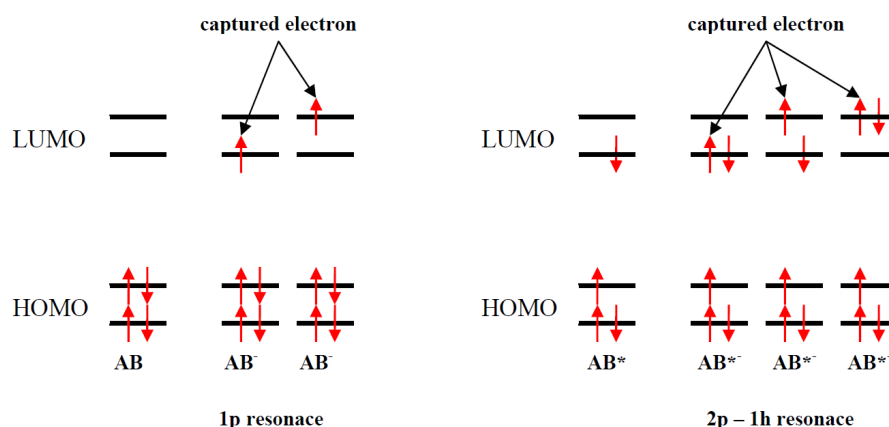


Figure 5.5. Electronic configuration for a single-particle resonance and for a two-particle one-hole resonance. Taken from [141].

Furthermore, the resonances may be also categorized accordingly to two mechanisms of electron capture. First, the incoming electron can be trapped by the centrifugal barrier from the effective potential which arises from the interaction between the incoming electron and the neutral molecule. This process is thus termed open-channel resonance or shape resonance, because, as the name suggests, the TNI is formed due to the "shape" of the energy potential surface. In terms of energy, the TNI formed through a shape resonance lies above the neutral precursor. Shape resonances often have short lifetimes.[42, 126, 134] Second, the incoming electron may be trapped by the excitation caused by itself on the neutral target molecule, if the TNI lies energetically below the neutral molecule. This process is termed Feshbach resonance, or closed-channel resonance. Since the decay of such resonances back into the neutral requires a change in the electronic configuration, Feshbach resonances often have longer lifetimes.[42, 126, 134]

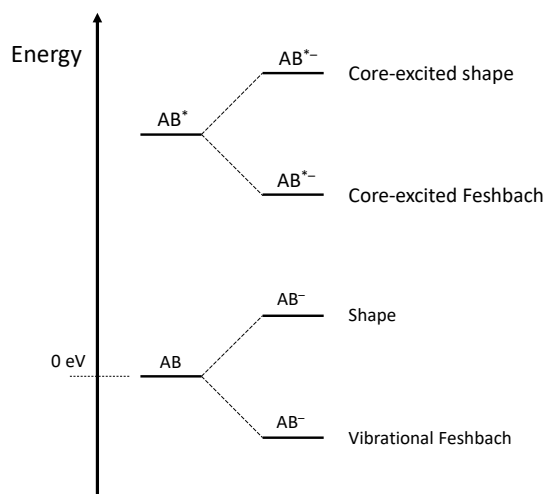


Figure 5.6. Schematic energy diagram of transient negative ions formed by electron attachment by a diatomic molecule, AB . Adapted from [126].

By combining both criteria for characterization of resonances, the formation of TNIs may be sorted out in four categories: vibrational Feshbach resonance, shape resonance,

core-excited Feshbach resonance, and core-excited shape resonance, as represented in figure 5.6. At last, the types of resonances will be discussed in greater detail below.

Vibrational Feshbach resonance

A vibrational Feshbach resonance (VFR) can be formed at low energies close to ~ 0 eV, if the TNI lies below the ground state of the neutral, as represented in figure 5.7. Hence, VFR are formed in molecules with positive electron affinity. The formed TNI can survive beyond microseconds in molecules that enable redistribution of the energy released into the vibrational degrees of freedom, preventing thus autodetachment. This process known as intramolecular vibrational redistribution (IVR) results in the formation of metastable TNIs. For instance, the formation of metastable TNIs with high cross sections at about 0 eV from, sulphur hexafluoride, SF₆, and hexafluorobenzene C₆F₆ is well known.[42, 125, 134]

On the other hand, strong long-range interactions give rise to TNIs through VFRs. In the case of a sufficiently large dipole moment above 1.65 Debyes, the incoming electron can be temporarily trapped in a dipole bound state (DBS). The binding energies of the DBS are usually in the meV range.[142, 143] The excess energy can be also deposited into vibrational levels of the DBS. In this case, the TNI formed may decay through autodetachment or, if energetically possible, it can also undergo DEA.[42, 125] For example, DBS were suggested as doorway states for the dehydrogenation of nucleobases. [32, 144–146] In this context, the studies with 5-trifluoromethanesulfonyl-uracil (OTfU) [147] have shown that the loss of a hydrogen atom proceeds through the coupling between the vibrational levels of the TNI and a DBS, see section 7 for further details. Moreover, the potential role of a DBS in the dehydrogenation of benzaldehyde was also investigated, please see section 7.

Shape resonance

Shape or open channel resonances represent single-particle (1p) resonances. In this case, the incoming electron is trapped in a potential barrier induced by the electron-molecule interaction.[42, 126] At large distance, the electron-molecule interaction is dominated by

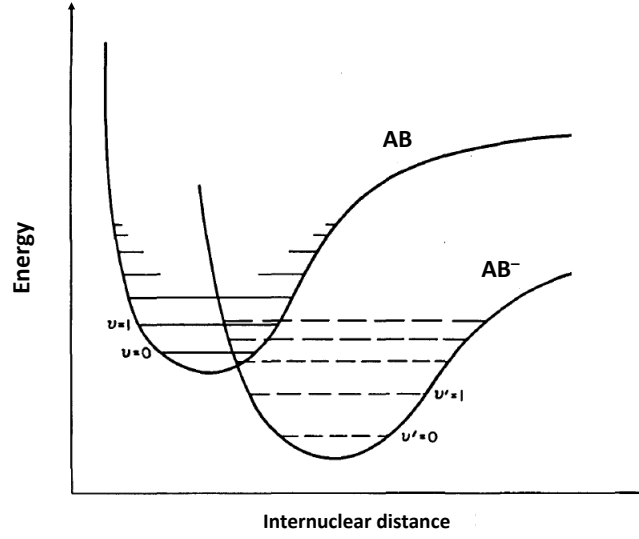


Figure 5.7. Representation of a vibrational Feshbach resonance, where the molecular anion, AB^- , lies energetically below the ground state of the target molecule, AB . Taken from [125].

the attractive polarization potential, V_α , given by [42, 134]:

$$V_\alpha = -\frac{\alpha e^2}{2r^4} \quad (5.13)$$

where α denotes the polarizability of the molecule, e is the elementary charge of the electron, and r corresponds to the electron-molecule distance. However, at shorter distances, the repulsive centrifugal potential, V_l , which describes the angular momentum dependence becomes more important, and it is given by [42, 134]:

$$V_l = \frac{\hbar^2 l(l+1)}{2\mu r^2} \quad (5.14)$$

μ denotes the reduced mass of the electron-molecule system ($\mu \approx m_e$), \hbar is the reduced Planck's constant, and l is the angular momentum quantum number.

For $l \neq 0$, the sum of these potentials, also referred to as effective potential V_{eff} , is given by [42, 134]

$$V_{eff} = V_l + V_\alpha \Leftrightarrow V_{eff} = \frac{\hbar^2 l(l+1)}{2\mu r^2} - \frac{\alpha e^2}{2r^4} \quad (5.15)$$

5.4. Electron attachment

and it is represented in figure 5.8. Since no centrifugal barrier is created for $l = 0$, s-wave attachment does not constitute a shape resonance. For $l > 0$, the incoming electron can tunnel through the barrier becoming temporarily trapped within the vicinity of the molecule. Thus, the TNI lifetime is equal to the time required for the electron to tunnel out the centrifugal barrier.[42, 126, 134]

As already mentioned and represented in figure 5.6, the formed TNI lies above the ground state of the neutral molecule, that means that the electron affinity is negative. In terms of electron energy, shape resonances occur at low energy between ~ 0 and 4 eV.[125] Usually, shape resonances decay by autodetachment within 10^{-15} to 10^{-10} s, or if the thermochemical prerequisites are fulfilled, by DEA.[125] Thus, the lifetime of a shape resonance is considered short, and may be observed as broad features in electron scattering studies, accordingly to Heisenberg's uncertainty principle (eq. 5.8).[42]

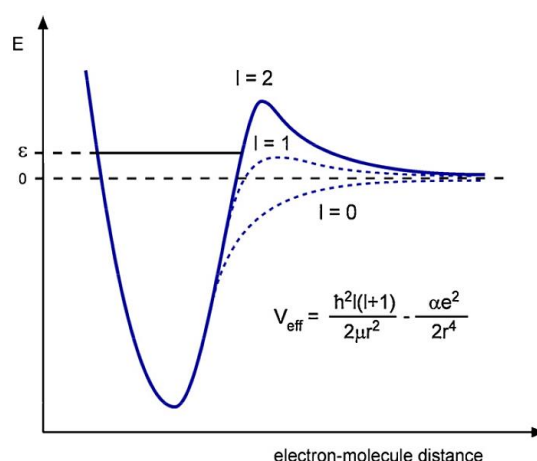


Figure 5.8. The effective potential describing the electron-molecule interaction, for $l \neq 0$ the electron may be trapped within the centrifugal barrier. Taken from [134].

Core-excited Feshbach resonance

A resonance is defined as a core-excited Feshbach resonance if the incoming electron is captured with concomitant electronic excitation of the target molecule. [42, 134] This kind of resonances are two-particle one-hole (2p-1h) of electron configuration depicted in

figure 5.5. Figure 5.9 schematically shows a core-excited resonance, AB^{*-} formed via an electronically excited state, AB^* .

In an electronically excited molecule, the positive charge of the nuclei is less screened by the electron cloud, as result the incoming electron is attracted by the small positive charge becoming temporarily captured by the molecule.[125] The autodetachment of the extra electron is usually not possible if the TNI is energetically below the corresponding electronically excited of the neutral. In this case, the TNI can only relax through a two electron transition to a lower lying excited state, which involves rearrangements of the molecular electronic structure. The autodetachment lifetime for core-excited Feshbach resonances is, in turn, relatively long.[42, 125, 134] Hence, as in the case of VFRs, these resonances appears as narrow contributions observed in electron scattering studies.[42]

Core-excited shape resonance

The formation of core-excited shape resonances proceeds as for the case of shape resonances, except that in the present case the incoming electron is trapped by the centrifugal barrier of an excited state of the neutral molecule, instead of its ground state. Thus, core-excited shape resonances are considered two-particle one-hole (2p-1h) resonances, provided the incoming electron carries sufficient energy to electronically excite the target molecule.[42, 125, 134] The TNI formed through a core-excited shape resonance lies energetically above the excited electronic state of the target molecule, AB^* , and therefore these kinds of resonances occur at higher electron energies, as depicted in figure 5.9.

5.4.4 Dissociative electron attachment cross section

As mentioned in section 5.4.2, the dissociation of a TNI depends on (i) its lifetime with respect to autodetachment, τ_{AD} , and (ii) the time required for TNI to relax beyond the point from which autodetachment is not possible, τ_{diss} . In a diatomic molecule, as represented in figure 5.4, this corresponds to the crossing point, r_C . In terms of cross section, the DEA cross section, σ_{DEA} , is the product of the attachment cross section, σ_0 , and the

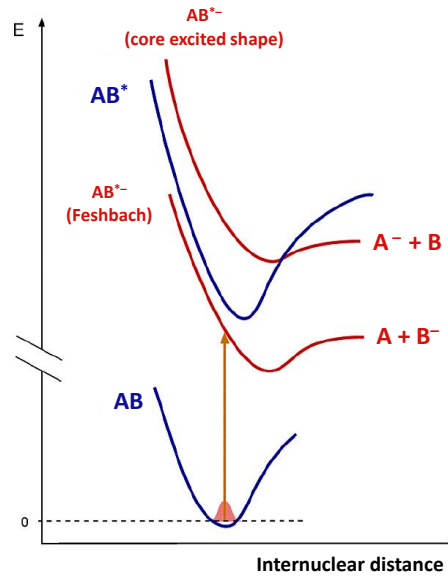


Figure 5.9. Schematic representation of potential energy curves for the formation of a TNI, AB^* , through a core excited shape (open channel) and a core excited Feshbach (closed channel) resonances from a molecule AB . Adapted from [134].

dissociation probability, P_{diss} [42, 134]:

$$\sigma_{DEA} = \sigma_0 P_{diss} \quad (5.16)$$

Attachment cross section σ_0

For electron energies above 0 eV, the energy dependence of the attachment cross section, σ_0 , is explained by the reflection principle.[126, 148] This is displayed on the right-hand side y -axis of figure 5.4 wherein the attachment cross section, denoted as σ_{EC} , is achieved as the reflection of the initial vertical transition over the TNI potential curve. The DEA cross section overlaps with the attachment cross section, however the maximum DEA cross section is typically shifted towards lower electron energies, because (i) the autodetachment lifetime is longer at lower electron energies, since the width of the TNI increases with gradually increasing energies; and (ii) for transitions at lower electron energies, the internuclear

distance to the crossing point is shorter, and consequently the time needed for the TNI to reach that point.[42]

At electron energies close to 0 eV, the Wigner threshold law [149] predicts the attachment cross section, σ_0 , where the electron involved may have a angular momentum quantum number, l , as follows:

$$\sigma_0(E, l) \propto E^{(l-\frac{1}{2})} \quad E \rightarrow 0 \quad (5.17)$$

E is the incident electron energy. For s-wave attachment ($l=0$), the attachment cross section is thus proportional to $E^{-\frac{1}{2}}$, and it dominates at 0 eV. In addition, for halogens Cl_2 [150] and F_2 [151], it has been demonstrated that p-wave attachment ($l=1$) proportional to $E^{\frac{1}{2}}$ may also contribute to electron attachment at lower energies from above 0 eV up to 200 meV . Later, the Vogt-Wannier model included the polarizability of the molecule. [152] Hotop, Fabrikant and coworkers [153–155] extend the Vogt-Wannier model for molecules with a dipole moment lower than 1.625 D.[42] Further details on models describing electron attachment are given in references [152–155].

TNI survival probability P_{diss}

The DEA cross section also depends on the TNI survival probability, P_{diss} which is in turn associated with both autodetachment and relaxation lifetimes by the following relation [42, 134]:

$$P_{diss} = \exp\left(-\frac{\tau_{diss}}{\tau_{AD}}\right) \quad (5.18)$$

The autodetachment lifetime, τ_{AD} , is associated to the energy width of the resonance, $\Gamma(r)$, through the Heisenberg's uncertainty principle [42, 134]:

$$\tau_{AD} = \frac{\hbar}{\Gamma(r)} \quad (5.19)$$

The relaxation time, τ_{diss} , may be expressed from the radial velocity between the

fragments formed according to [42, 134]:

$$\tau_{diss} = \int_r^{r_C} \frac{dr}{v(r)} \quad (5.20)$$

r denotes the initial internuclear distance from where the vertical transition takes place, and r_C is, once again, the crossing point.

By taking into account the relations 5.19 and 5.20, the TNI survival probability may be written as [42]:

$$P_{diss} = \exp\left(-\frac{\tau_{diss}}{\tau_{AD}}\right) \Leftrightarrow P_{diss} = \exp\left[-\frac{1}{\hbar} \int_r^{r_C} \Gamma(r) \frac{dr}{v(r)}\right] \quad (5.21)$$

Therefore, the DEA cross section is described as:

$$\sigma_{DEA} = \sigma_0 \exp\left(-\frac{\tau_{diss}}{\tau_{AD}}\right) \quad (5.22)$$

Hence, one would expect higher DEA cross sections when the exponent of the exponential term is small, that is when the relaxation lifetime is smaller than the autodetachment lifetime. Furthermore, the observation of fragment anions depends on the thermodynamic threshold for a given DEA reaction to a target molecule, which will be discussed in the following section 5.4.5.

5.4.5 Thermodynamics in DEA

The thermochemical threshold, E_{th} , for a DEA reaction with a diatomic molecule, AB, which leads to the formation of A^- along with neutral B can be calculated as [42, 126, 134]:

$$E_{th} = BDE(A - B) - EA(A) \quad (5.23)$$

$BDE(A - B)$ denotes the bond dissociation energy required for bond cleavage ($BDE(A - B) > 0$), and $EA(A)$ the electron affinity of A . In the case illustrated in figure 5.4, the fragment A^- is promptly formed at 0 eV electron energy, since the respective DEA reaction has a negative thermochemical threshold as the $EA(A)$ is larger than

the $BDE(A - B)$. On the other hand, the $EA(B)$ is lower than $BDE(A - B)$. The DEA reaction leading to B^- formation is thus endothermic and therefore thermochemically not possible at 0 eV electron energy.

Except for 0 eV peaks, the onset of a given ion yield, also indicated as appearance energy (AE), is associated to the low-energy onset obtained through the reflection principle, instead of the thermochemical threshold. However, the ion yield for a fragment anion formed through an exothermic DEA reaction may show a peak at 0 eV. For this reason, it is considered that the onset of an ion yield with a 0 eV peak is also zero. Since DEA is often operative at energies above the thermochemical threshold, there is an excess of energy, E^* . Considering a polyatomic molecule, such excess of energy is distributed among both internal and translational degrees of freedom of the formed fragments. [42, 126, 134] For a diatomic molecule, AB, the AE of a DEA reaction which yields A^- may be rewritten as [42]:

$$AE = BDE(A - B) - EA(A) + E^* \quad (5.24)$$

Therefore, the excess energy, E^* is the difference between the thermochemical threshold, E_{th} and the experimental appearance energy, AE [42, 126, 134].

In the case of DEA to polyatomic molecules, more complex fragmentation pathways including multiple bond cleavages as well as rearrangements may occur. In order to calculate the thermochemical threshold for the formation of X^- through a complex reaction with a polyatomic molecule, the relation 5.24 may be written as [42]:

$$E_{th}(X^-) = \sum BDE(educt) - \sum BDE(product) - EA(X) \quad (5.25)$$

The thermochemical threshold for X^- formation is the difference between the energy invested in multiple bond cleavage within the target molecule, $\sum BDE(educt)$, the energy gain from new bond formations within the product fragment anion, and the binding of the excess charge.

The thermochemical calculations discussed above only consider the initial and final

states of the DEA process, however some dissociation pathways involve reaction barriers which might arise from transition states above the thermochemical threshold. Therefore, quantum chemical calculations may be employed to clarify the formation of negative ions, and neutrals from polyatomic molecules through DEA.

5.5 Ion pair formation

Ion pair formation is non-resonant process by which both negative and positive ions may be formed through electron scattering by a target molecule, as follows [42, 125]:



This process occurs at electron energies sufficiently high to induce an electronic transition in the target molecule, AB , to an dissociative state, which dissociates thereafter into a positive-negative ion pair.[125] The ion pair formation cross section gradually increases until it reaches a maximum at an energy of two or four-fold the threshold energy, and declines thereafter.[125]

In the DEA study to OTfU, F^{-} formation proceeds through ion-pair formation, in addition to DEA. Please see section 7 for more details.

Experimental Setup

Low-energy electron interactions with biomolecules were investigated by using two mass spectrometry experiments. Hence, this chapter provides a detailed description of both experiments. The electron attachment studies with OTfU and benzaldehyde were carried out with the so called Wippi experiment available at the *Institut für Ionenphysik und Angewandte Physik*, Universität Innsbruck, Austria. Further studies with benzaldehyde, and its deuterium labelled derivative (benzaldehyde- α -d1) were performed with the experiment available at the Radiation Laboratory, University of Notre Dame, USA.

In general, both experiments are mass spectrometers composed by the same components, as schematically represented in figure 6.1:

- The **sample inlet** enables the introduction of the sample to be investigated. Since only gas-phase studies are allowed, the sample inlet must be capable of changing the physical state of the sample, i.e. solid or liquid, to gas. Both setups allow the introduction of gases and liquids, whereas solids are only investigated on the Wippi experimental setup.
- The **e^- impact ion source** creates ions from a sample, through interactions with electrons. A hemispherical electron monochromator acts as the ion source in the Wippi experiment, while an e^- impact ion source is installed in Notre Dame.
- A **quadrupole mass spectrometer** sorts out the ions formed due to electron in-

teractions within the ion source accordingly to their mass-to-charge ratio (m/z).

- A **detector** of the electron multiplier of the continuous dynode type, also referred to as channeltron, was installed in each experiment for ion detection.
- A **computer for control and data acquisition** was used to acquire and further process the data. A custom made software was used in Wippi, while a commercially available software was used in Notre Dame.

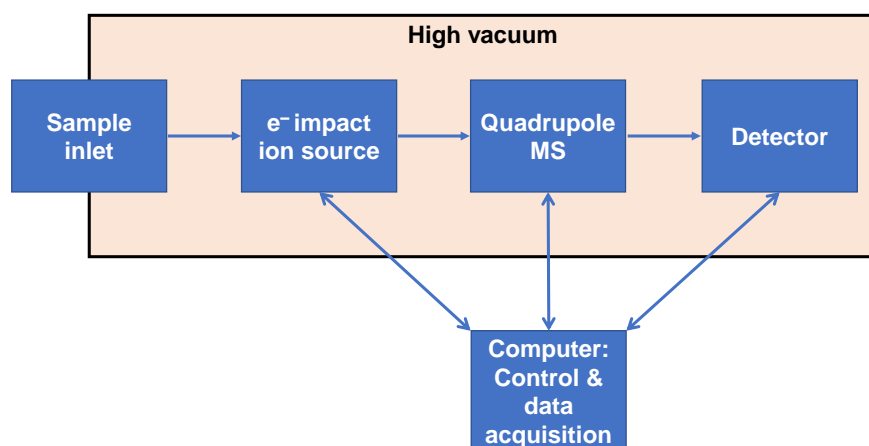


Figure 6.1. General scheme of the mass spectrometry experiments used to study low-energy electron interactions with biomolecules. Adapted from [55].

6.1 Wippi

The experiment known as Wippi is a crossed electron-molecule beam apparatus, represented in figure 6.2. The electron monochromator used in this experiment was designed by Dr. Daniela Muigg and Dr. Günter Denifl.[156, 157] The neutral beam is formed by a sample inlet suitable for either solids (oven with a capillary), liquids or gases. Additionally, a stagnant gas inlet is used to introduce calibration compounds, such as SF₆ or CCl₄, as explained in section 6.3. Then, the beam effuses into the interaction chamber of the hemispherical electron monochromator (HEM) through a 1 mm-diameter capillary where it intersects orthogonally with the electron beam. For the present investigations, an energy resolution of 100-120 meV at full width at half maximum (FWHM) was set,

which is a suitable compromise between energy resolution and electron beam intensity. The ions resulting from the electron attachment process are extracted by a weak electrostatic field into a quadrupole mass spectrometer (QMS) where they are mass-analyzed. For a given ion, the ion yield is recorded as a function of the electron energy. In order to record a mass spectrum, the electron energy is kept constant and the quadrupole m/z range is scanned. Since, the quadrupole is aligned with the neutral beam, the formed ions are deflected towards the detector by a deflector thereby suppressing noise resulting from neutrals which may eventually reach the detector. The ions were detected by channeltron electron multiplier.

In the following subsections a description of the components comprising both experiments will be provided.

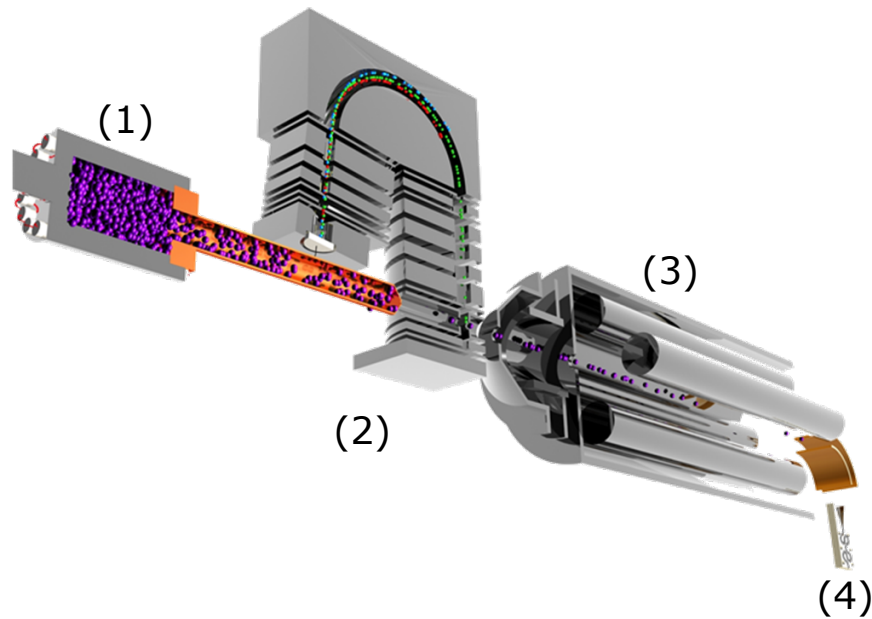


Figure 6.2. Schematic overview of Wippi: (1) - resistively heated oven; (2) hemispherical electron monochromator; (3) quadrupole mass spectrometer; (4) channel electron multiplier. Adapted from [158].

6.1.1 Sample inlet

A stagnant gas inlet used for introduction of calibration compounds, namely sulfur hexafluoride SF₆ and carbon tetrachloride CCl₄, is permanently installed. Since the admission is realized via a valve connected to the chamber, an effusive beam is not created. On the other hand, a capillary can introduce directly an amount of sample to be investigated into the interaction region of the HEM. However, considering that the samples are available as gas, liquids or even solids, a suitable sample inlet is thus needed, and it will be described in the following subsections.

Gases

The influx of gas from a pressurized gas cylinder into the chamber is controlled by a combination of two valves: (i) a bellows-sealed valve which opens and closes the access to the chamber, and (ii) a needle precision valve precisely controls the influx of gas. The pressure prior to the set of valves is adjustable by a suitable gas reducer attached to the gas cylinder.

Liquid samples

A reservoir is filled with the liquid and then attached to a set of valves, as described for gas introduction. On the vacuum side, the sample enters into the interaction zone of the HEM through a 1 mm-diameter stainless steel capillary.

Nonetheless, liquids tend to condensate on the walls of the inlet, which may hinder a continuous-flowing of sample into the chamber. A heating band can be used in order to avoid any sample condensation in the inlet system. Furthermore, the vapor pressure of the liquid may be increased by warming up the sample's reservoir with heating tape. This is particularly relevant for samples with a low vapor pressure.

Before starting the studies, the volatile contaminants in the sample were removed by performing several freeze-pump-thaw cycles.

Solid samples - The oven

Solid samples, e.g. OTfU, were vaporized in a resistively heated reservoir made of copper installed on the vacuum side, in order to achieve a suitable vapor pressure. The formed molecular effusive beam enters in the HEM interaction zone via a 1 mm-diameter capillary. The oven is heated by a heating element, as well as by the halogen bulbs inside the chamber. The temperature was monitored by a PT100 sensor placed in a orifice in the copper oven. A pair of halogen bulbs was used to keep a temperature of 100-120°C in order to avoid condensation of sample at the elements of the monochromator. Notwithstanding, when a solid sample have sufficient vapor pressure, its introduction is performed analogous to liquids.

6.1.2 The Hemispherical Electron Monochromator

The HEM, as represented in figure 6.3, consists of an electron emitter (filament), an electrode stack collimating the electron beam into two concentric hemispheres acting as the energy dispersing element, followed by a second electrode stack where the monochromatized electron beam is guided into the interaction chamber of the HEM. In the end, the electrons were collected in a Faraday cup and the current monitored by a picoammeter.

Within the HEM, the electron beam is controlled by a set of electrostatic lenses summarized in table 6.1. In figure 6.4 **A** it is represented a lens, which may correspond to an aperture (denoted by an A), thick or virtual lens (denoted by a L). Segmented lenses, as shown in 6.4 **A**, consist of four parts (a , b , c), though both c parts are electrically connected. A shared potential, V_c , is applied on the parts a , b and c , while the potentials V_a and V_b are further adjustable. The segmented lenses will thus act as deflectors improving the transmission of electron beam throughout the HEM. Each lens was biased by a home built power supply. The lenses were electrical insulated by zirconium spheres (*Swarovski GmbH*) with an inner diameter of 1.55 mm, while A3, SK1 and SK2 were insulated by spheres with a larger inner diameter of 2.5 mm.

At the beginning of the HEM, the electrons were emitted by a tungsten hairpin

Table 6.1. The type and the designation of the lenses constituting the HEM.

Type	Designation
Aperture	Anode, A1, A2, A3
Deflector	1(a,b,c), 2(a,b,c), 3(a,b,c), 4(a,b,c)
Thick	L2, L3, L6, L7, L8
Virtual	L4, L5

filament (*AGA054, Agar scientific*) mounted in a block based on the Pierce design.[125] The filament was heated up by a current of about 2.35 A, which results in electron emission through Edison effect. Thermal electron emission from pure metals, e.g. tungsten, requires temperatures above 2000K. As a result, the thermally emitted electrons are produced with a broad kinetic energy distribution (0.5 up to 1 eV), given by [125]:

$$dN(E) \propto \exp \left[-\frac{W + E}{kT} \right] dE \quad (6.1)$$

where $dN(E)$ is the number of electrons emitted per second with energies between E and $E+dE$, k is the Boltzmann constant, T is the absolute temperature and W is the metal work function. A stack of lenses focused the electron beam into an energy dispersing element employed to increase the energy resolution. This element comprising a pair of concentric hemispheres acts as a kinetic energy analyzer. Thus, by producing a potential difference, ΔV , between the pair of concentric hemispheres, the electrons with kinetic energy eV_0 will be transmitted. The relationship between ΔV and V_0 is [126]:

$$\Delta V = V_0 \left(\frac{r_2^2 - r_1^2}{r_1 r_2} \right) \quad (6.2)$$

where $r_1 = 27$ mm and $r_2 = 33$ mm are the inner and outer radii of the hemispheres, as represented in figure 6.5. Additionally, the in-going electrons are deflected by a pair of stainless steel wires (deflectors D1 and D2) mounted on the side plates of the hemispheres and centered on the entrance. The hemispheres have an angle of 174° , instead of 180° , to

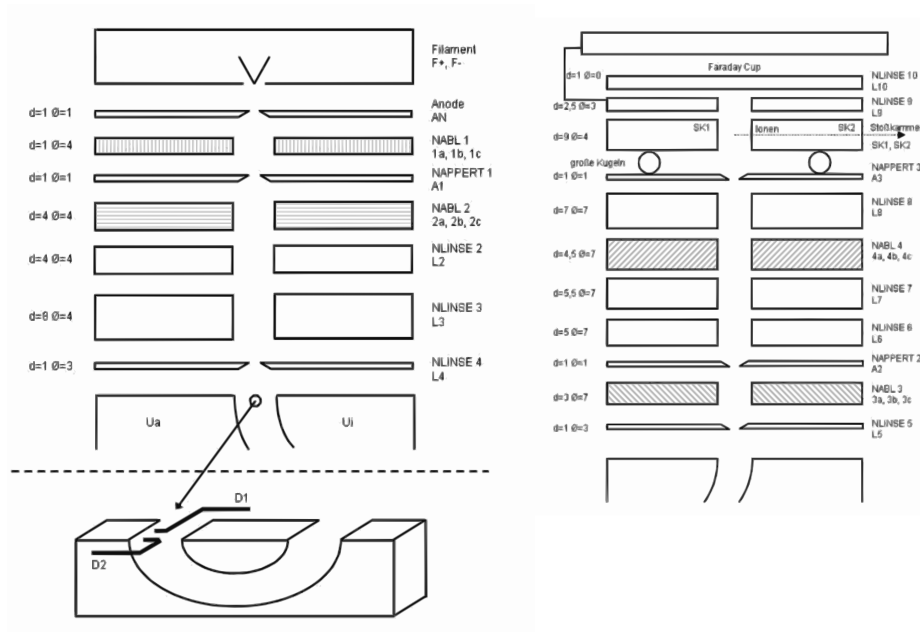


Figure 6.3. Schematic representation of the HEM. The orifice diameter, \varnothing , and the thickness, d , in mm, of a given lens is given on the left. The segmented lenses are hatched

compensate for the fringing field effect.[157]

The energy dispersing element is followed by the second electrode stack, which delivers the electron beam into the interaction chamber. Within the interaction chamber (SK1 and SK2), the electrons interact with the molecular beam to form negative or positive ions which are extracted towards the mass spectrometer. The neutral molecules introduced via the capillary and, that did not interact with the electron beam follow the same trajectory as the ions, that is, towards the QMS. In order to achieve high energy resolution, the potential applied on the neighbouring lenses (A3, SK1, SK2, L9, L10) must be equal to zero volts. Charging effects, as well as artifacts produced by scattered electrons, may reduce significantly the energy resolution. Moreover, perturbing electric and magnetic fields lower the the electron beam stability close to zero kinetic energies. In order to reduce this effect, the HEM was set to a given above zero electron energy, while $U_{exmitte}$, the potential shared by the interaction chamber elements SK1 and SK2, was set to a negative voltage

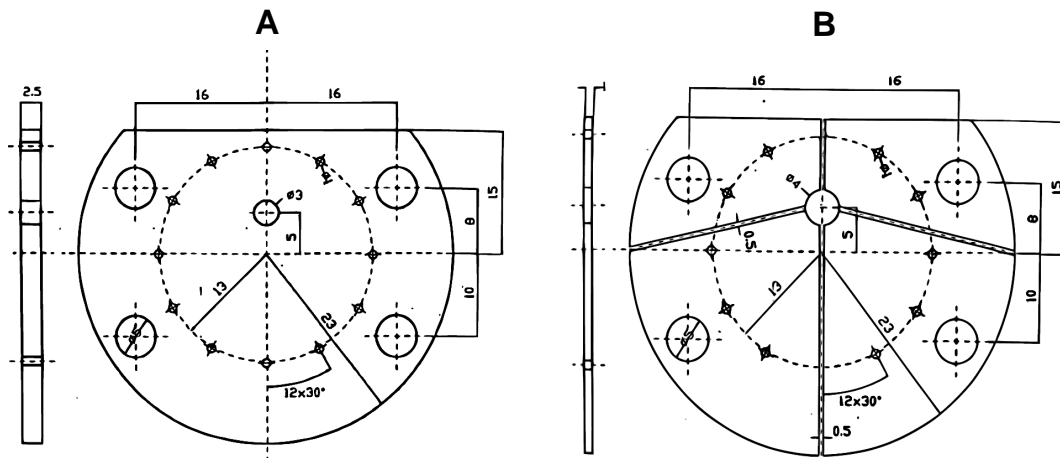


Figure 6.4. Wippi lenses - **A:** Drawing of an electrostatic lens. **B:** Drawing of deflector 1. The dimensions are in mm. Adapted from [157].

of about -1.9 V retarding the electron beam and allowing the formation of negative ions upon electron attachment. Finally, the electrons which passed the interaction region were collected by the last lenses, L9 and L10, acting as a Faraday cup. The incident electron current was thus monitored by a home built picoammeter.

6.1.3 Magnetic field compensation

Magnetic fields, such as the Earth's magnetic field and other perturbative fields are able to affect the trajectory of the electron beam. To cancel the effect of the Earth's magnetic field, the setup was placed within three pairs of square Helmholtz coils in the direction of the three directions of space. In the current version of the Wippi experiment, the Helmholtz coils are squared with a length of 1.25 m.

The intensity of each component of the magnetic field produced by each pair of Helmholtz coils must be optimized to preserve the intensity of ~ 0 eV electrons reaching the HEM interaction zone.

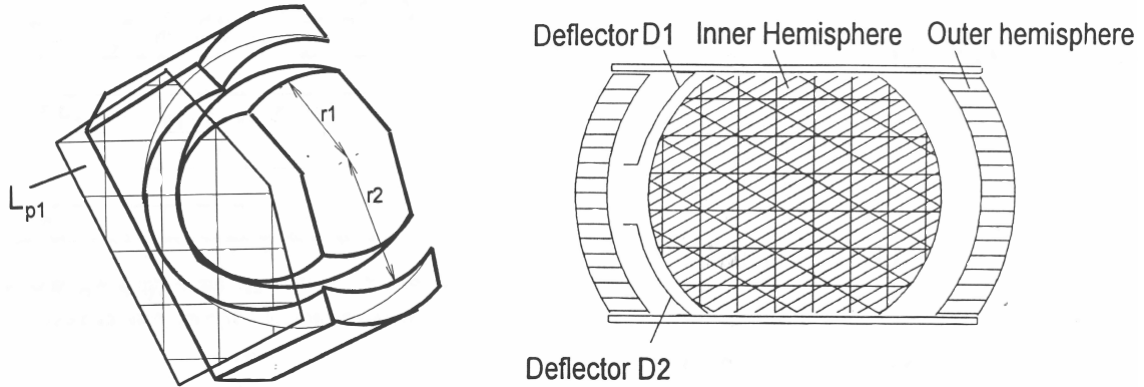


Figure 6.5. Representation of the inner and outer hemispheres, with radius r_1 and r_2 , respectively. The pair of deflectors D1 and D2 are stainless steel wires mounted on the side-plates of the hemispheres. Adapted from [157].

6.1.4 Quadrupole mass spectrometer

A QMS is comprised of four cylindrical or hyperbolic shaped rod electrodes positioned along a circle of radius r_0 , as presented in figure 6.6. A pair of opposite rods are electrically connected and held at the same potential composed of a DC voltage and a radiofrequency (RF) voltage. The voltage applied on the pair A is equal to $U + V \cos(\omega t)$, while the voltage applied on the pair B is equal to $-(U + V \cos(\omega t))$, where U is the DC amplitude, V and ω denote the amplitude and frequency of the RF voltage. As explained for the octopole guide in section 3.1.5, when an ion enters the quadrupole along the z -axis, a "restoring force" is exerted on it by the pairs of electrode rods. That is, a positive ion will be attracted towards negative rods, while it is repelled by positive rods at any instant of time.

Based on the charged particle's motion equation, its motion along the x -, y -, and z - axis through the quadrupole can be described by the following equations [55]:

$$\frac{d^2x}{dt^2} + \frac{e}{mr_0^2}(U + V \cos(\omega t))x = 0 \quad (6.3)$$

$$\frac{d^2y}{dt^2} - \frac{e}{mr_0^2}(U + V \cos(\omega t))y = 0 \quad (6.4)$$

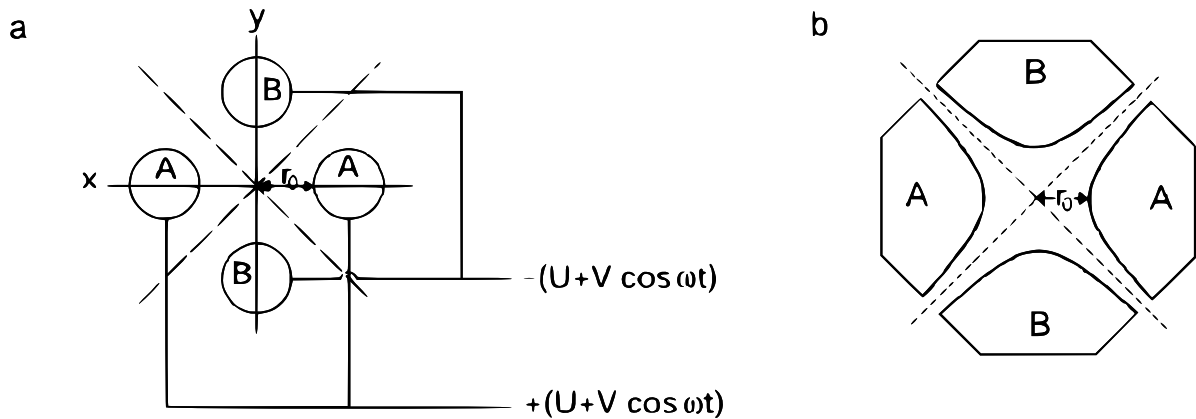


Figure 6.6. Cross section of a quadrupole (a) for the cylindrical approximation and (b) for the hyperbolic profile of the rods. $2r_0$ is the spacing between the electrodes. Adapted from [55].

$$\frac{d^2 z}{dt^2} = 0 \quad (6.5)$$

The motion equations on the x , y directions may be rewritten as Mathieu equations by defining $\xi = \frac{1}{2}\omega t$:

$$\frac{d^2 u}{d\xi^2} + (a_u - q_u \cos(2\xi))u = 0 \quad (6.6)$$

The stability parameters a_u and q_u can be either obtained for the directions $u = x, y$:

$$a_x = -a_y = \frac{8eU}{mr_0^2\omega^2} \quad (6.7)$$

$$q_x = -q_y = \frac{4eV}{mr_0^2\omega^2} \quad (6.8)$$

The Mathieu equations 6.6 are well-known and its solutions describe the trajectory of an ion oscillating in the x and y directions.[159] The figure 6.7 shows a stability diagram (a vs. q) for a two-dimensional quadrupole field. For an ion transmitted by a QMS, its trajectory is stable along the x - and y -axis.[126] This means that the stability parameters a_u and q_u are located under the area labeled as " xy stable" in figure 6.7. In order to transmit ions with a different mass through the QMS U and V are scanned, while its ratio

6.1. Wippi

is kept constant, as represented by the "scan line" in figure 6.8 comprising all points of constant ratio $a/q = 2U/V$. For instance, the ions with m/z m_1 and m_2 will possess stable trajectories and would be transmitted by the QMS, while the ions with mass m_3 will be lost due to the instability. The mass resolution of the QMS is described by the width of the stable region Δq . The mass resolution is infinite at the apex of the stability region corresponding to $2U/V = 0.237/0.706 = 0.336$.

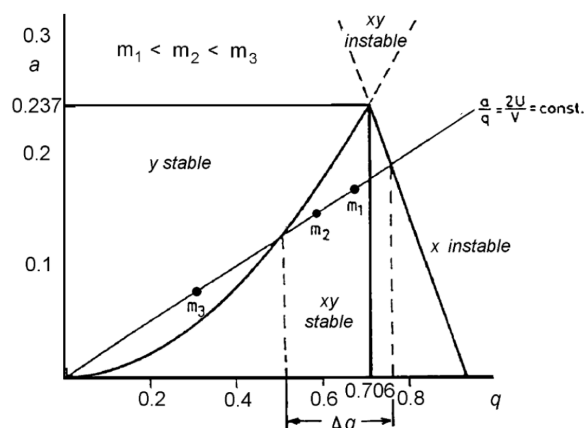


Figure 6.7. Stability diagram for a quadrupole mass spectrometer. Adapted from [55].

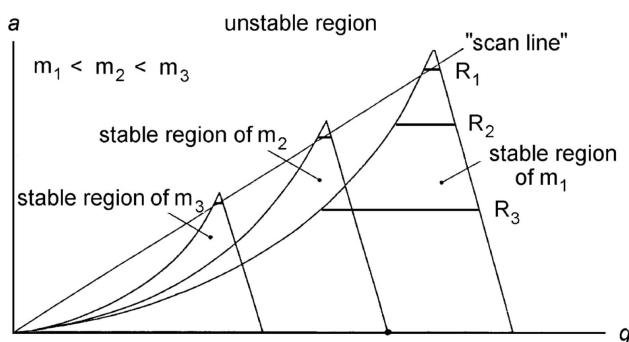


Figure 6.8. Mass scan of a quadrupole mass spectrometer; the stable region of a mass is shifted along a "scan line" towards the right. Adapted from [55].

As previously mentioned, the ions formed within the HEM are extracted by a weak electrostatic towards the QMS for mass-analysis. The QMS installed is a *QMG 700 HiQuad*

coupled to a radiofrequency head (*QMH 410-2* both manufactured by *Pfeiffer Vacuum*. This combination enables mass-analysis of ions with m/z up to 2048.

The kinetic energy of the ions passing the QMS is defined as the potential difference between the HEM, which floats on the *ionenenergie* voltage, and the potential applied on the quadrupole rods, floating on the *feldachse* voltage. As a result, the QMS mass resolution relating to the ion's kinetic energy, gets worsen with the increase of the difference between *ionenenergie* and *feldachse* voltages.

In order to achieve the best sensitivity, the ion beam must be focused into the the QMS. The figure 6.9 shows a representation of the interaction chamber of the HEM alongside the extraction ion optics denoted as *optik außen*, *optik innen* and a grounded element. The ions are thereby focused by adjusting the voltage applied on both *optik außen* and *optik innen*, while the third lens is grounded. The extracting field produced by the ion optics may also lead to the extraction of electron with kinetic energies close to zero eV, since the distance between the *optik außen* and the SK2 is a few tenths of a millimeter. Therefore, it is of great importance to keep the potential applied on the *optik außen* below 70 V.[160, 161]

At last, the mass-selected ions are 90° deflected towards the detector by a two-element deflector, as shown in figure 6.2.

6.1.5 Detector

The detector installed in Wippi is an electron multiplier of the continous dynode type - channel electron multiplier, namely a *KBL 510 standard CEM (Dr. Sjuts Optotechnik GmbH)*, like the ones installed in VG-ZAB-2SE. For details on the working principle of channeltrons, please see section 3.3.

The channeltron can detect either positive or negative ions, depending on the potential gradient created within the device. For positive ion detection, a voltage of about -2.4 kV was applied on the back of channeltron and the entrance was kept grounded. While for negative ion detection, +1000 V were applied on the entrance of the channeltron, and +3.2 kV were applied on the back of the detector.

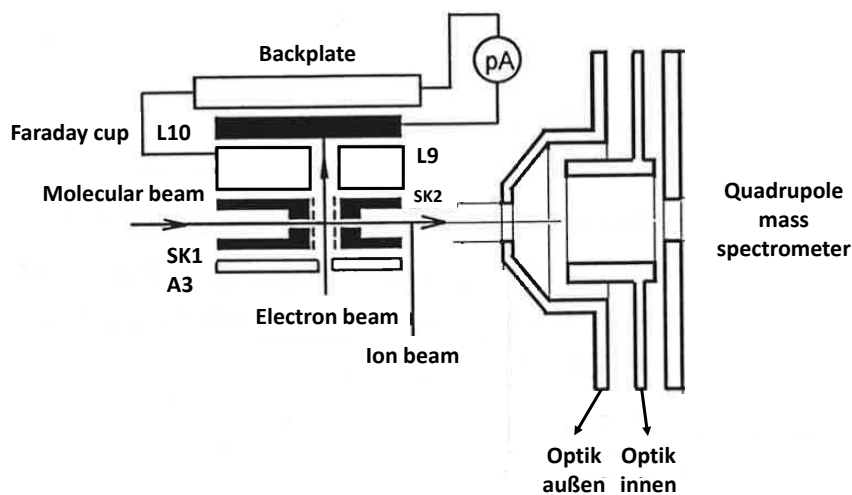


Figure 6.9. Schematic representation of the interaction chamber of the HEM and the ion optics, namely *optik außen*, *optik innen* and the third element (grounded), of the quadrupole mass spectrometer. Taken from [157].

6.1.6 Data acquisition

The unit CP 400 ion counter (*Pfeiffer Vacuum*) is connected to the channeltron. Although this unit comprises pulse counting, preamplifier and a discriminator, it is used just to decouple the high voltage from the output signal of the detector. The decoupled output signal is thereafter fed into a commercial preamplifier discriminator unit (*PAD06, WMT-Elektronik GmbH*). Afterwards, the amplified output signal was connected to a computer and processed by a custom made software.

In brief, the software (designed by Dr. Arntraud Bacher) allows recording the measurements. It controls all experimental parameters, such as the gate time, the step-width, number of runs, the electron energy for measuring a mass scan or to set the QMS for a particular ion and measure an electron energy scan. The software is also able to log the pressure value read by the pressure gauge(s) while acquiring. Furthermore, the software also poses an optimization mode which displays the ion yield of a mass-selected ion for a

given gate time. This mode is, as suggested, used to optimize the ion yield. So, the data is only displayed on the software interface, although it is not stored in a data file.

6.1.7 Vacuum system

The experiment comprises a high-vacuum chamber evacuated by a turbomolecular pump baked by a 3-stage diaphragm pump, as listed in table 6.2. The present vacuum system can thus achieve a base pressure of about 10^{-8} mbar as measured by a Bayard-Alpert ionization gauge (*UHV-24 Nude Bayard-Alpert, Varian Agilent*) connected to the chamber.

In case the pressure in the chamber increases above 6.0×10^{-6} mbar, a vacuum safety device switches off the power supplies connected to sensitive components of the experiment, namely the filament, QMS and the detector.

Table 6.2. Model, type and manufacturer of the pumps used in the Wippi setup. The base pressure, in mbar, is also depicted.

Model	Type	Manufacturer	Base pressure (mbar)
TMU 521 P	Turbomolecular	<i>Pfeiffer Vacuum</i>	$\times 10^{-8}$
MD 4C NT	Diaphragm pump	<i>Vacuubrand</i>	

6.1.8 Measuring absolute dissociative electron attachment cross sections

Crossed-beams experiments, such as Wippi, allow for the determination of absolute dissociative electron attachment cross-sections, σ_{DEA} . The measured ion yield, i_{ion} , is related to σ_{DEA} , by the following expression [42]:

$$i_{ion} = \sigma_{DEA} \cdot i_e \cdot N_t \cdot l \quad (6.9)$$

where i_e is the incident electron current, N_t is the density of neutrals in the interaction region, and l is the interaction length between electrons and neutrals within, in this case, the HEM. In crossed-beam experiments, the σ_{DEA} may be determined by comparing the

measured ion yield for a fragment anion formed from a sample with well-known cross sections occurring at ~ 0.8 eV for Cl^- from CCl_4 ($\sigma_{DEA,\text{Cl}^-/\text{CCl}_4} = 5.0 \times 10^{-20} \text{ m}^2$) [162] or at 5.2 eV for F^- from SF_6 ($\sigma_{DEA,\text{F}^-/\text{SF}_6} = 5.0 \times 10^{-22} \text{ m}^2$) [163].

The different experimental conditions were considered by normalizing the anion signal intensity with respect to the partial pressures, as well as to the intensity of the incident electron current by using the following relation:

$$\frac{i_{ion}}{i_{\text{Cl}^-/\text{CCl}_4}} = \frac{\sigma_{DEA,ion}}{\sigma_{DEA,\text{Cl}^-/\text{CCl}_4}} \times \frac{i_{e,ion}}{i_{e,\text{Cl}^-/\text{CCl}_4}} \times \frac{N_{t,ion}}{N_{t,\text{Cl}^-/\text{CCl}_4}} \times \frac{l_{ion}}{l_{\text{Cl}^-/\text{CCl}_4}} \quad (6.10)$$

The interaction length between the electrons and the neutrals either from the sample, l_{ion} , or calibrant, $l_{\text{Cl}^-/\text{CCl}_4}$ is assumed to be the same. Furthermore, the target density N_t is directly proportional to the partial pressure value, P . The partial pressure of both sample, P_{ion} , and calibrant, P_{CCl_4} , is defined as the difference between the working pressure and the base pressure measured by a ionization gauge connected to the chamber. The target density of sample delivered by a capillary directly into the interaction region of the HEM is, however substantially higher than the target density of calibrant introduced in the chamber via the stagnant gas inlet. At the same incident electron current, and partial pressure of calibrant compound, through a comparison between the intensity of the ion yield obtained when the compound was introduced (i) via the stagnant gas inlet, or (ii) via the capillary; it was determined that the target density of neutrals may be increased by 25 times when the sample is introduced as in the latter case. Thus, this correction factor must be taken into account when calculating the cross section.

Absolute dissociative electron attachment cross sections, $\sigma_{DEA,ion}$, can be thus determined through the following relation:

$$\sigma_{DEA,ion} = \sigma_{DEA,\text{Cl}^-/\text{CCl}_4} \times \frac{i_{ion}}{i_{\text{Cl}^-/\text{CCl}_4}} \times \frac{i_{e,\text{Cl}^-/\text{CCl}_4}}{i_{e,ion}} \times \frac{1}{25} \frac{P_{\text{CCl}_4}}{P_{ion}} \quad (6.11)$$

The experimental uncertainty of the cross section values of about one order of magnitude results from the several sources of experimental errors in the experiment. Namely, the estimation of the partial pressure ratio, the efficiency of ion extraction towards the QMS,

which in turn exhibits a non-constant transmission for different masses, and at last the channeltron detection efficiency.

Partial pressure ratio

The partial pressure ratio between the calibrant and the sample, P_{CCl_4}/P_{ion} , was determined from the pressure values measured with the ionization gauge connected to the chamber. In ionization gauges, the measured pressure value depends on the ion current, which in turn depends on the electron current emitted by the filament, as well as the ionization cross section of the gas, at electron energies of 70 eV, in the gauge [164]. Therefore, the error associated with the partial pressure ratio results from the difference between the ionization cross sections at 70 eV of either the calibrant compound, and of the sample of interest.[43]

Ion extraction field

In Wippi, a weak electric field extracts the ions from the HEM, in order to avoid extraction of ~ 0 eV electrons. The electric field extracts, however less efficiently fragment anions which are formed with high kinetic energy release (KER) in respect to Cl^-/CCl_4 or F^-/SF_6 anions used for calibration. By simulating the extraction field and the geometry of the interaction region of a trochoidal electron monochromator (TEM), Engmann *et al.* [165] have found that the extraction efficiency for fragment anions formed with KER values between 50 and 100 meV is reduced from about 30 up to 60% when compared to thermal ions, i.e. formed at rest (KER=0 eV). In Wippi, this effect, and how it contributes to the accuracy of the determined cross sections is yet to be investigated.

QMS transmission

The mass dependent transmission of the QMS can lead to a less efficient detection of ions with heavier masses. For positive ions, Engmann *et al.* [165] have reported a linear dependency between transmission through the QMS and mass. This was achieved by normalizing the ion counts obtained for the formation of N_2^+/N_2 , Ar^+/Ar , Kr^+/Kr and Xe^+/Xe against the well-known ionization cross sections for which case. To the best of my

knowledge, the mass dependency of QMS transmission for negative ions was not investigated so far. Therefore, in this context, it was considered a constant transmission for the different fragment anions. Consequently, the exact contribution of the QMS transmission to the inaccuracy of the determined cross section values is yet to be estimated.

Channeltron detection efficiency

For a given incident particle, the channeltron detection efficiency is defined as the probability of this particle or photon producing an output pulse. In the case of the channeltrons manufactured by *Dr. Sjuts Optotechnik GmbH*, detection efficiency for electrons, positive ions and UV light have been investigated.[130] However, to the best of my knowledge, the mass dependency for both positive and negative ions on the detection efficiency was not investigated so far. In this thesis, the channeltron detection efficiency for different anions was considered to be constant.

6.2 Experimental Setup - Notre Dame University

At the Radiation Laboratory at the University of Notre Dame, the experiments were carried out in a crossed electron-molecule beam apparatus coupled with a QMS (*HAL/3F PIC Hiden Analytical, Inc.*) operated in RGA (residual gas analyzer) mode, as shown in figure 6.10.[166] An electron impact source is installed at the front of the QMS, as represent in figure 6.11. A description of the mode of operation of QMS was already provided in the section 6.1.4.

In the electron impact ion source, the electron emission occurs from one of two filaments made of oxide coated iridium. The incident electron current, i.e., the current of electrons which pass the grid, is set by the software and it may range from $0.2 \mu\text{A}$ up to a few μA . For the studies carried out with benzaldehyde (see section 7.2), a constant incident current of $2 \mu\text{A}$ was used. The positive bias voltage, V_{cage} , is applied to the cage and to the filament power supply ($V_{filament}$) to simultaneously attract the electrons to the cage, as well as to repel them from the grounded side walls. This cage can transmit the electrons, because it is made of a fine metal mesh. The ions are thereby formed within the

cage due to interactions with the electrons emitted by a heated filament. The electrons are accelerated to a given kinetic energy by a positive voltage drop, $V_{electron}$, between the cage and the filament. The electron energy scale was calibrated by measuring the well-known resonances of SF_6^- and F^- from SF_6 , see section 6.3. The electron energy resolution was estimated to be approximately 500 meV (FWHM) for an incident electron current of $2 \mu A$. There is also a focus lens right before the QMS entrance.

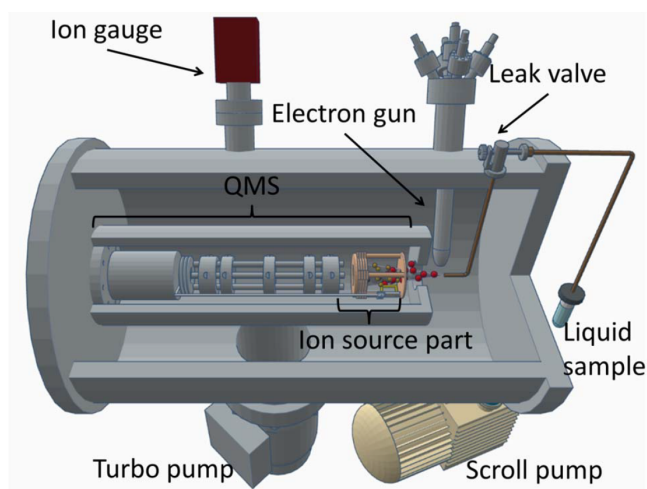


Figure 6.10. Crossed beam setup at the Notre Dame University. Please note that the electron gun was not used in the present studies. Adapted from [167].

The installed QMS enables mass-analysis of ions with unit mass resolution up to m/z 300. A channel electron multiplier was used for ion detection (see section 3.3 for details on the working principle).

The base pressure of 10^{-9} mbar was achieved by a turbomolecular pump baked by an oil-free scroll pump. An ionization gauge was used to monitor the pressure. Furthermore, the chamber was heated by a set of halogen bulbs, in order to reduce the adsorption of material on the cold surfaces of setup.

During a study, the vapor of a liquid sample or gas was introduced in the chamber by an external gas line coupled with a needle precision valve and a bellow-sealed valve. On the vacuum-side, the sample's vapor enters in the ion source of the QMS through a 1 mm-diameter stainless-steel capillary. Before performing the studies, the liquid samples

6.3. Energy scale calibration

went through several freeze-pump-thaw cycles .

The MASsoft version 7 Professional software (*Hidden Analytical, Inc.*) controlled all experimental parameters involved in the acquisition of both mass scans and electron energy scans, that is, the number of runs, gate time and step-width. Furthermore, the voltages applied on each particular component of the ion source, QMS and detector were also controlled by the software.

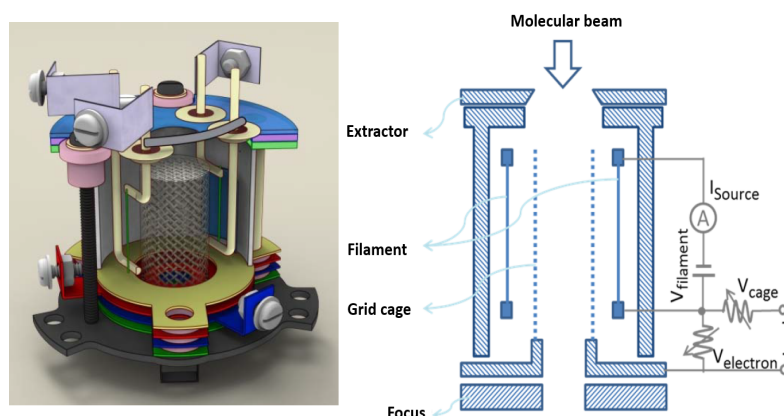


Figure 6.11. A 3D representation of the electron impact ion source. Taken from [167].

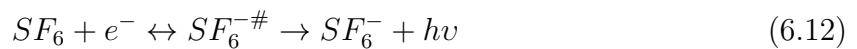
6.3 Energy scale calibration

For both experimental setups, the electrons were accelerated towards the interaction region by a voltage difference. In Wippi, the electrons were accelerated towards the interaction chamber by a voltage drop between the tip of the filament and all the electrostatic elements (from anode to L8) with respect to the interaction chamber.[156, 157] In the Notre Dame experiment, the electron energy was defined by adjusting a potential difference between the cage and the filament. In both setups the electron energy scale requires calibration in order to determine resonance positions. In Wippi, the electron energy scale and the electron energy resolution were determined by measuring the well-known resonances for the formation of SF_6^- from SF_6 and Cl^- from CCl_4 . While at Notre Dame, both parameters were determined by measuring the well-known resonances for the formation of SF_6^- and F^- from SF_6 .

6.3.1 Sulfur hexafluoride, SF₆

A comprehensive knowledge on the interactions of low-energy electrons with SF₆ may be found in the literature, e.g. Christophorou *et al.* [163, 168], Fabrikant *et al.* [169] and Fenzlaff *et al.* [170]. As shown in figure 6.12, the electron attachment cross section for the formation of SF₆⁻ close to ~0 eV dominates. At electron energies ranging between 0.3 and ~ 2.0 eV, SF₅⁻ is the most abundant fragment anion. Though, at energies above 3 eV, the formation of F⁻ starts to dominate.

The parent anion is formed at ~0 eV through s-wave attachment of an electron, as described by reaction 6.12. The lifetime of SF₆⁻ is long enough to be detected in this mass spectrometer. The electron energy resolution was determined as the FWHM of the ~0 eV SF₆⁻/SF₆ resonance. The electron energy scale was calibrated by shifting downwards the peak position associated with the maximum intensity to 0 eV.



At Notre Dame, the electron energy scale was calibrated using F⁻/SF₆. As described by reaction 6.13, the formation of F⁻ occurs through three resonances centered at 5.5, 9.0 and 11.5 eV (see figure 6.12).[163, 168].



Therefore, by fitting the measured ion yield with Gaussian functions, the resonance positions were determined and the energy scale shifted accordingly.

6.3.2 Carbon tetrachloride, CCl₄

CCl₄ is a compound previously used as solvent and precursor agent for several industrial processes [171], as well as an element in fire extinguishers [172]. DEA to CCl₄ has been extensively studied. In contrast to SF₆, the TNI CCl₄^{-#} has a reduced lifetime of ~ 5-10 ps before dissociation [136], which invalidates its detection by mass spectrometry. The reaction 6.14 describes the formation of the anion Cl⁻, that corresponds to the most

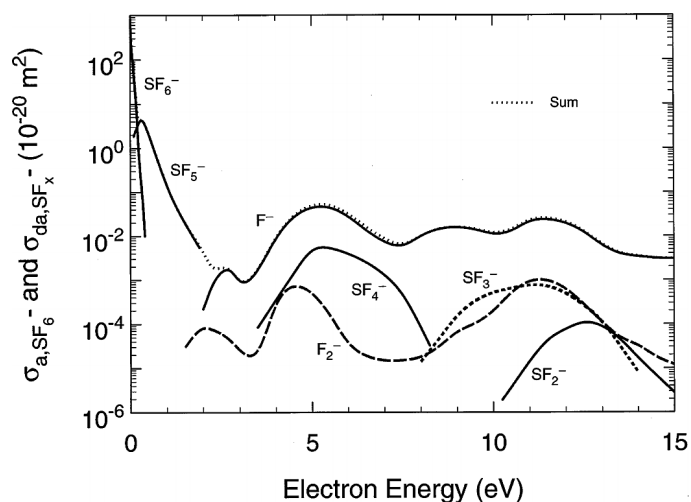
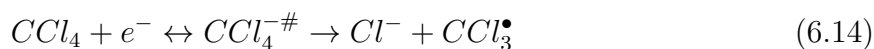


Figure 6.12. Electron attachment cross section for the formation of the intact molecular anion SF_6^- , and fragment anions formed due to DEA to SF_6 . Taken from [163, 168].

abundant ion formed upon DEA to CCl_4 :



In a s-wave attachment process of a 0 eV electron, Cl^- is formed with a large electron attachment cross section of $1.3 \times 10^{-14} \text{ cm}^2$ [173]. Additionally, a broader higher-lying resonance centered at $\sim 0.8 \text{ eV}$ also leads to Cl^- formation, though with a reduced electron attachment cross section amounting to $5.0 \times 10^{-16} \text{ cm}^2$ [162, 174]. For instance, Cl^-/CCl_4 formation measured with Wippi is shown in figure 6.13.

6.4 Determination of position and onset of resonances

As a first approximation, by fitting a Gaussian function, equation 6.15, to the experimental data; the center, onset and area of peaks can be determined.

$$y = y_0 + \frac{A}{w\sqrt{\frac{\pi}{2}}} \cdot \exp\left(-2\frac{(x - x_c)^2}{w^2}\right) \quad (6.15)$$

where y_0 denotes the offset, x_c is the center, or the position of the maximum, w the width, and A corresponds to the area under the Gaussian. Additionally, the standard deviation,

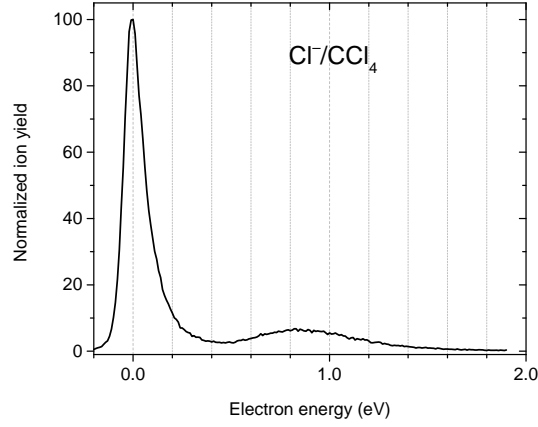


Figure 6.13. Ion yield of Cl^-/CCl_4 measured with Wippi.

σ , may be calculated as:

$$\sigma = \frac{w}{2} \quad (6.16)$$

In statistics, the *68-95-99.7 rule* is an empirical rule which states the percentage of values lying in a interval around the center of a normal, or Gaussian distribution, with a width of one, two or three standard deviations [175]. The figure 6.14 shows that, more precisely, 68.27%, 95.45% and 99.73% of the values from a normal distribution lie within one, two or three standard deviations away from the center, respectively. Based on this statistic rule, the onset of a resonance, x_{onset} maybe defined as:

$$x_{onset} = x_c - 2\sigma = x_c - w \quad (6.17)$$

At last, since an ion yield may comprise several resonances, a multiple Gaussian fitting of the data may be employed to determine the position, area and onset of individual resonances.

6.4. Determination of position and onset of resonances

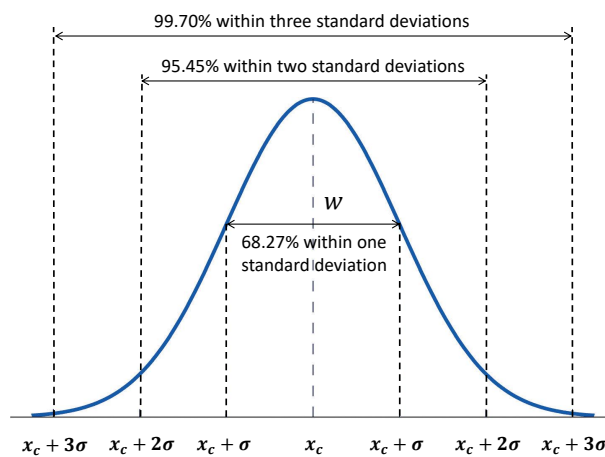


Figure 6.14. Representation of the Gaussian function used to determine the centre, area and onset of resonances. For a normal distribution, two standard-deviations from the center account for 95.45% of the values.

Results and Discussion

7.1 Low-energy electron-induced decomposition of OTfU

A combined theoretical and experimental on the electron-induced decomposition of 5-trifluoromethanesulfonyl-uracil (OTfU), in the gas-phase is presented. This compound is a potential radiosensitizer synthesized in the research group led by Professor Dr. Janusz Rak, Gdansk University, Poland. The DEA investigations were carried out with Wippi. Quantum chemical calculations on the thermochemical thresholds for the formation of the observed fragments were performed by Samanta Makurat from Professor Janusz Rak group. The results are summarized in the following publication:

Low-energy electron-induced decomposition of 5-trifluoromethanesulfonyl-uracil: A potential radiosensitizer:

J. Ameixa, E. Arthur-Baidoo, R. Meißner, S. Makurat, W. Kozak, K. Butowska, F. Ferreira da Silva, J. Rak, and S. Denifl, *J. Chem. Phys.* **149**, 164307 (2018).

Author's contribution: I performed the measurements and analyzed the obtained data. Afterwards, I prepared the final figures and wrote the first version of the manuscript.



Low-energy electron-induced decomposition of 5-trifluoromethanesulfonyl-uracil: A potential radiosensitizer

J. Ameixa,^{1,2,a)} E. Arthur-Baidoo,¹ R. Meißner,^{1,2} S. Makurat,³ W. Kozak,³ K. Butowska,⁴ F. Ferreira da Silva,² J. Rak,^{3,b)} and S. Denifl^{1,c)}

¹*Institut für Ionenphysik und Angewandte Physik and Center for Molecular Biosciences (CMBI), Leopold-Franzens Universität Innsbruck, Technikerstraße 25/3, 6020 Innsbruck, Austria*

²*Laboratório de Colisões Atômicas e Moleculares, CEFITEC, Departamento de Física, Faculdade de Ciências e Tecnologia, Universidade NOVA de Lisboa, Campus de Caparica, 2829-516 Caparica, Portugal*

³*Laboratory of Biological Sensitizers, Physical Chemistry Department, Faculty of Chemistry, University of Gdańsk, 80-308 Gdańsk, Poland*

⁴*Laboratory of Biophysics, Department of Molecular and Cellular Biology, Intercollegiate Faculty of Biotechnology of the University of Gdańsk and Medical University of Gdańsk, 80-307 Gdańsk, Poland*

(Received 1 August 2018; accepted 5 October 2018; published online 29 October 2018)

5-trifluoromethanesulfonyl-uracil (OTfU), a recently proposed radiosensitizer, is decomposed in the gas-phase by attachment of low-energy electrons. OTfU is a derivative of uracil with a triflate (OTf) group at the C₅-position, which substantially increases its ability to undergo effective electron-induced dissociation. We report a rich assortment of fragments formed upon dissociative electron attachment (DEA), mostly by simple bond cleavages (e.g., dehydrogenation or formation of OTf⁻). The most favorable DEA channel corresponds to the formation of the triflate anion alongside with the reactive uracil-5-yl radical through the cleavage of the O–C₅ bond, particularly at about 0 eV. Unlike for halouracils, the parent anion was not detected in our experiments. The experimental findings are accounted by a comprehensive theoretical study carried out at the M06-2X/aug-cc-pVTZ level. The latter comprises the thermodynamic thresholds for the formation of the observed anions calculated under the experimental conditions (383.15 K and 3×10^{-11} atm). The energy-resolved ion yield of the dehydrogenated parent anion, (OTfU–H)⁻, is discussed in terms of vibrational Feshbach resonances arising from the coupling between the dipole bound state and vibrational levels of the transient negative ion. We also report the mass spectrum of the cations obtained through ionization of OTfU by electrons with a kinetic energy of 70 eV. The current study endorses OTfU as a potential radiosensitizer agent with possible applications in radio-chemotherapy. *Published by AIP Publishing.* <https://doi.org/10.1063/1.5050594>

I. INTRODUCTION

Regardless of the noticeable effort in finding and improving anticancer therapies, radiotherapy is still one of the prevailing strategies to defeat cancer. However, hypoxia is the *Achilles heel* of radiotherapy, which significantly decreases the efficiency of such therapy in hypoxic tumors.¹ The concomitant application of radiotherapy with chemotherapeutic drugs, namely, radiosensitizers, represents thus an alternative as well as more efficient type of therapy. An ideal radiosensitizer selectively binds to tumor cells which enhances their radiosensitivity² and results in the reduction of the administered dose of radiation, ultimately leading to little or no effect to healthy cells. In fact, incorporation of an electrophilic substituent into DNA substantially enhances its radiosensitivity

toward high-energy radiation, without altering gene expression prior to irradiation.^{3–5} For instance, a uracil derivative with an electrophilic group (e.g., halogen) in the C₅-position has been extensively used as radiosensitizers^{5,6}—such compounds are known as 5-halouracils. However, in spite of the intensive research devoted to this subject, the fundamental reactions underlying the operation of such compounds are still unclear. Nevertheless, it is acknowledged that in the physicochemical stage of radiation damage the reactivity of such compounds to low-energy electrons plays a crucial role in the sensitization process notably through dissociative electron attachment (DEA) reactions.⁷ In brief, the interaction of high-energy radiation with a biological medium yields low-energy (<20 eV) electrons (LEEs), at a number of 10⁴/MeV of incident radiation.⁸ Thereafter, these LEEs are thermalized, within the picosecond time scale, to subexcitation energies, thereby generating highly reactive species, namely, OH[•] and H[•] which may also react further with DNA.⁹ However, prior to thermalization, radiosensitizer molecules, which are present in the biological medium, may capture these LEEs

^{a)}E-mail: j.ameixa@campus.fct.unl.pt

^{b)}E-mail: janusz.rak@ug.edu.pl

^{c)}E-mail: stephan.denifl@uibk.ac.at

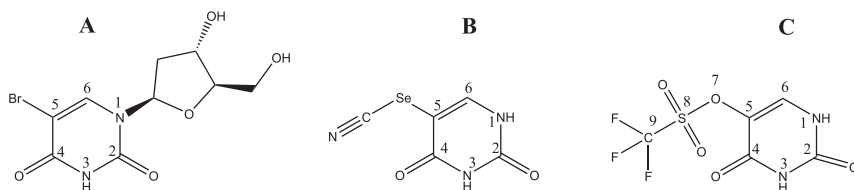


FIG. 1. Structures of (a)—5-bromo-2'-deoxyuridine (5-BrdU), (b)—5-selenocyanatouracil (SeCNU), and (c)—5-trifluoromethanesulfonyl-uracil (OTfU).

and then undergo DEA, particularly at energies below the threshold for electronic excitation. Therefore, an effective radiosensitizer must be decomposed efficiently upon electron attachment, thus generating reactive radicals (i.e., uracil-yl) which may react with DNA, leading to the loss of integrity of such a key biomolecule.⁶ Notably, the interaction of LEEs with 5-halouracils in the gas phase has been comprehensively studied experimentally as well as by theoretical methods.¹⁰ In particular, such studies have been carried out for 5-chlorouracil,^{11–16} 5-fluorouracil,^{11,14–16} 5-iodouracil,^{11,17} and 6-chlorouracil.^{13,15} Electron transfer from potassium atoms to 5-fluorouracil and 5-chlorouracil has been assessed as well.¹⁸ To our best knowledge, 5-bromo-2'-deoxyuridine (5-BrdU), shown in Fig. 1(a), is the most comprehensively studied radiosensitizer.^{19,20} Consequently, there is an urgent need for new and more efficient compounds with radiosensitizing properties. A methodology concerning the proposal of new radiosensitizers was suggested,⁶ in addition to several analogs proposed by Rak and co-workers.⁵ The most efficient compound turned out to be 5-selenocyanatouracil (SeCNU), shown in Fig. 1(b), which is 1.5-fold more effectively decomposed by solvated electrons when compared to BrU.²¹ In the light of such findings, a novel compound was proposed—5-trifluoromethanesulfonyl-2'-deoxyuridine (OTfU). It possesses a substantial adiabatic electron affinity (AEA) and appears to be prone to undergo effective electron-induced dissociation,²² thereby can be treated as a pseudohalouracil. Its fragmentation induced by solvated electrons was studied by steady-state radiolysis combined with theoretical methods.²² However, no DEA study in the gas-phase has been reported so far. Therefore, we have investigated DEA to 5-trifluoromethanesulfonyl-uracil (OTfU), shown in Fig. 1(c), in the gas-phase in order to unravel the fundamental dissociation channels induced by LEEs. Moreover, the mass spectrum of cations formed via dissociative electron ionization at the electron energy of ~ 70 eV is also presented in order to study the fragmentation pathways upon positive ion formation. Finally, the observed DEA reactions were studied by theoretical calculations; in particular, the respective thermodynamic thresholds as well as the AEA for the observed anions and the neutral OTfU molecule were calculated.

II. METHODS

A. Dissociative electron attachment

The experiments were performed in a crossed electron-molecular beam apparatus coupled with a quadrupole mass spectrometer available at the Innsbruck laboratory, described

in detail previously.²³ The molecular effusive beam is produced by the evaporation of the solid sample in a resistively heated oven inside the vacuum chamber. Then it effuses into the interaction chamber of the hemispherical electron monochromator (HEM) through a capillary of 1 mm diameter where it intersects orthogonally with a monochromatized electron beam. The HEM was shown to generate an electron beam with an energy resolution around 35 meV at full width at half-maximum (FWHM). In the present experiment, an energy resolution of 100 meV (FWHM) was set, which is a suitable compromise between energy resolution and beam intensity. The anions resulting from the electron attachment process are extracted from the interaction chamber by a weak electrostatic field into a quadrupole mass spectrometer where they are mass-analyzed and further detected by a channeltron electron multiplier in single pulse-counting mode. For a given anion, the ion yield is recorded as a function of the electron energy. In order to record a mass spectrum, the electron energy is kept constant and the ion yield is recorded as a function of the mass. The electron energy scale and energy resolution are determined by measuring the well-known ion yields for the formation of $\text{SF}_6^-/\text{SF}_6$ or Cl^-/CCl_4 at 0 eV. The remaining electrons, which crossed the interaction region, are collected in a Faraday plate and monitored using a picoammeter.

B. Synthesis of 5-trifluoromethanesulfonyl-uracil

The compound was obtained via the procedure described by Crisp and Flynn.²⁴ To the solution of 5-hydroxyuracil (75 mg, 0.59 mmol) in pyridine (2 ml), N-phenyltriflimide (251 mg, 0.70 mmol) was added (Fig. 2). The mixture was stirred overnight at room temperature. After concentration under vacuum, the resulting residue was purified by column chromatography using hexane:AcOEt 1:1 as an eluent to give the desired product in a 66.3% yield.

¹H NMR (Bruker AVANCE III, 500 MHz, DMSO), δ : 11.9 (s, 1H), 11.5 (s, 1H), 8.26 (d, 1H); ³C NMR (125 MHz, DMSO), δ : 158.7, 150.5, 133.2, 126.5, and 118.5 (q);

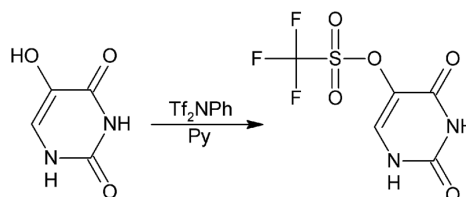


FIG. 2. Synthetic route for 5-OTfU.

HRMS (TripleTOF 5600+, SCIEX), m/z : $[M-H]^-$ calcd for $C_5H_3F_3N_2O_5S$ 258.9642, found 258.9547. For the MS, 1H and ^{13}C NMR spectra see Figs. S1–S3 in the [supplementary material](#).

C. Computational

In order to achieve a more comprehensive knowledge about the DEA process, a set of theoretical calculations was performed at the M06-2X²⁵/aug-cc-pVTZ^{26,27} level of theory, which has proven to give comparable results to the G4²⁸ extrapolation scheme.²⁹ However, the latter method is much more computationally demanding. In particular, the thermodynamic thresholds of various DEA reactions as well as the AEA of the neutral OTfU and of the observed anions were calculated. Additionally, the dipole-bound states (DBS) of OTfU were predicted. All the calculations were performed with the Gaussian09 suite³⁰ and the visualizations with the VMD package.³¹

1. Thermodynamic thresholds

The thermodynamic threshold for the DEA reactions was calculated as a difference, ΔG , between the Gibbs free energies of reactants in their ground state [Eq. (1)], as it was performed in the previous studies³²

$$\Delta G = G_{products} - G_{substrate}. \quad (1)$$

The substrate was the neutral OTfU [see Fig. 1(c)], and the products consisted of both the anion and radical formed after electron-induced dissociation. The lowest-energy geometry resulted from the conformational scan for the neutral. First, the structures were optimized at the M06-2X/aug-cc-pVTZ level of theory (0 K). Afterwards, in order to obtain thermochemical characteristics (free energies of reactions), the frequency calculations were performed at the same level, both in the standard state (298.15 K, 1 atm) and in the experimental conditions (383.15 K, 3×10^{-11} atm). The pressure correction to the G value for the experimental pressure was obtained using [Eq. (2)],

$$G_{3 \times 10^{-11} \text{ atm}, T} = G_{1 \text{ atm}, T} + TS_{\text{trans}; 1 \text{ atm}, T} - TS_{\text{trans}; 3 \times 10^{-11} \text{ atm}, T}, \quad (2)$$

where $G_{p,T}$ is the free enthalpy at the pressure p and temperature T and $TS_{\text{trans};p,T}$ denotes the product of temperature and translational entropy at the pressure p and temperature T .³³

Furthermore, the AEA was calculated for OTfU and the anionic products as the free energy difference between the optimized pairs of the neutral and its corresponding anion [Eq. (3)]. For some of the products, the neutral was unstable; therefore, the vertical detachment energy (VDE) was calculated [Eq. (4)],

$$AEA = E_{\text{neut,geom:neut}} - E_{\text{anion,geom:anion}}, \quad (3)$$

$$VDE = E_{\text{neut,geom:anion}} - E_{\text{anion,geom:anion}}. \quad (4)$$

2. Conformational scan

The conformational scan was performed with the use of the M06-2X/aug-cc-pVTZ constrained optimizations. Two

dihedral angles $\varphi_{C6-C5-O7-S8}$ and $\varphi_{C5-O7-S8-C9}$ [for atoms numbering see Fig. 1(c)] were systematically changed in steps of 30° to perform a scan of the conformational PES. The lowest-energy points were further subjected to further unconstrained geometry optimizations at the same level of theory and the difference in their Gibbs free energies allowed us to calculate the composition of the gas-phase equilibrated mixture under the experimental conditions. The details and results concerning the conformational scan are provided in the [supplementary material](#).

3. Dipole-bound states

In order to provide the excess electron binding energy for the dipole-bound state (DBS) of OTfU, the neutral conformers (see Fig. S4 of the [supplementary material](#)) of the neutral molecule were first optimized at the MP2/aug-cc-pVTZ level of theory.³⁴ Two of them converged to the same conformations, thus only two neutral conformations exist at the MP2 level. The standard aug-cc-pVTZ basis set was then supplemented with the diffuse functions necessary to describe the diffuse character of the loosely bound electron.³⁵ These basis set functions, centered on the C_6 atom as suggested by the position of the dipole moment vector [for numbering see Fig. 1(c)], were subsequently added with a geometric progression ratio equal to 5.³⁶ The exponent was build up for each symmetry starting from the lowest exponent in the original basis set;³⁷ i.e., the first additional s symmetry was built from the lowest exponent of s symmetry included in the aug-cc-pVTZ basis set for carbon, the second extra s function was equal to the 1/5 of the first function added, and so on. A 5s4p3d2f set of diffuse functions was sufficient to obtain a saturated basis set. Indeed, addition of the further set of diffuse functions extending the space of diffuse atomic orbitals to 6s5p4d3f increases the VEA calculated at the MP2 level by less than 1 cm^{-1} . Therefore, we set up at aug-cc-pVTZ augmented with 5s4p3d2f diffuse functions centered at the C_6 atom to characterize the respective dipole-bound states.

The two-electron integrals were calculated with the accuracy of 10^{-20} (default 10^{-12}), and the full accuracy was switched on during the SCF procedure.³⁸ Thereafter, the vertical electron binding energy was calculated, first, at Koopman's theorem (KT) level as $E_{\text{bind}}^{\text{KT}}$, equal to the negative energy of the LUMO orbital of the neutral, and then, supplemented with the orbital relaxation and electron correlation contributions (VEA^{MP2}). Similarly, the adiabatic electron affinity, AEA^{MP2}, was calculated at the MP2 level.

III. RESULTS AND DISCUSSION

A. Formation of cations through dissociative ionization of OTfU

Figure 3 shows the electron ionization mass spectrum of OTfU measured at the electron energy of about 70 eV. To the best of our knowledge, the formation of cations upon dissociative ionization has not been reported so far. We recorded different mass spectra at different oven temperatures (not shown here) in order to achieve a suitable ion yield as well as to rule out thermal decomposition of the compound. It is worth

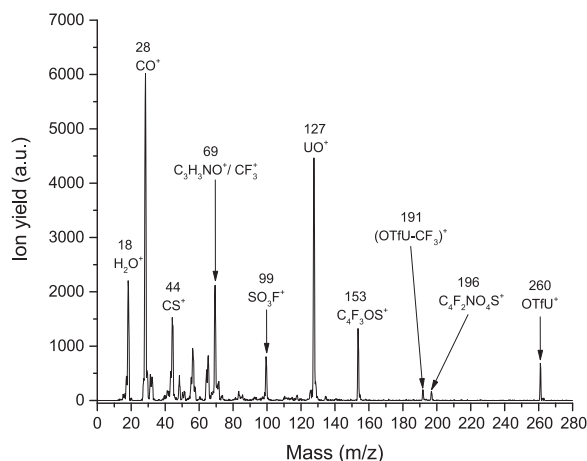
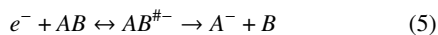


FIG. 3. Mass spectrum of cations formed by electron ionization of OTfU at the electron energy of 70 eV. The oven temperature was set to 383.15 K.

noting that the reported relative ion yields depend on the transmission of the quadrupole mass spectrometer as well as the ion collection efficiency of the cations formed with high initial kinetic energy. The ion at m/z 18 arises from residual water present in the vacuum chamber during the measurements. The cation with the highest yield is CO^+ (m/z 28). Another highly abundant cation is UO^+ (m/z 127) formed by the cleavage of the S–O bond in the triflate group. At m/z 69, two isobaric fragment ions may be present, $\text{C}_3\text{H}_3\text{NO}^+$ and CF_3^+ . They represent the mass peak with the third highest yield. $\text{C}_3\text{H}_3\text{NO}^+$ is the dominant fragment ion upon electron ionization of uracil.³⁹ The complementary cation of CF_3^+ formed by cleavage of the C–S bond within the triflate group, $(\text{OTfU}-\text{CF}_3)^+$ (m/z 191), appears with minor abundance in the mass spectrum. The cations at m/z 153 and m/z 196 are possibly $\text{C}_4\text{F}_3\text{OS}^+$ and $\text{C}_4\text{F}_2\text{NO}_2\text{S}^+$, respectively, which only form by complex rearrangements involving the molecule. The intact parent cation at m/z 260 is also observed. Compared to electron ionization of uracil studied with the same setup,³⁹ one may conclude that the formation of NCO^+ is substantially reduced by the substitution of uracil at the C_5 position with the triflate group.

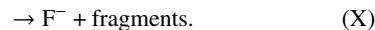
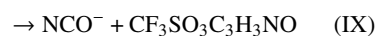
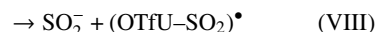
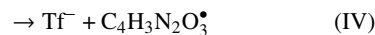
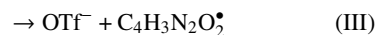
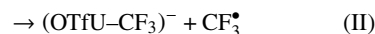
B. Formation of anions upon dissociative electron attachment to OTfU

In general, DEA is a resonant two-step process characterized by the capture of an electron by a molecule AB forming a transient negative ion (TNI), $\text{AB}^{\#-}$. The TNI is formed through a vertical transition (following the Franck-Condon principle) from the ground state of the molecule to an accessible excited state of the anionic molecule, $\text{AB}^{\#-}$. Consequently, the electronically and/or vibrationally excited TNI can relax through several fragmentation channels leading to the formation of an anionic fragment and a neutral fragment [DEA, Eq. (5)],



or via emission of the excess electron thus leaving the molecule in an excited state (autodetachment).

We studied DEA to OTfU in the energy range from about 0 to 14 eV. The following dissociation channels were detected within the experimental detection limit:



The ion yields for all anions detected are discussed in Secs. III B 1–III B 5. To our surprise, the stable parent anion OTfU^- is not observed within the experimental detection limits. Most halonucleobases XU (X = Cl, Br, I) do form a stable parent anion upon attachment of a free electron in the gas phase,^{4,12,40–43} in contrast to fluorinated derivatives,⁴⁴ unsubstituted DNA bases,^{45–47} and amino acids.^{48,49} The stabilisation of the parent anion is associated with the positive EA. In fact, the calculated AEA of OTfU at the M06-2X/aug-cc-pVTZ level is about 0.90 eV which is remarkably higher when compared to the AEA calculated by Li *et al.* for particular 5-halouracils (5-XU),⁵⁰ i.e., $\text{EA}(5\text{-FU}) = 0.48$ eV, $\text{EA}(5\text{-ClU}) = 0.60$ eV, and $\text{EA}(5\text{-BrU}) = 0.63$ eV. Therefore, assuming that the metastable parent anion of OTfU is formed, the TNI will be vibrationally excited such that the decay will occur on sub- μs time scales by autodetachment or through the DEA reactions (I)–(X) invalidating its detection. The resonance position for the observed anions, the respective thermodynamic thresholds, as well as the predicted AEA compared to other values available in the literature are summarized in Table I (and for more calculation data, see Table SI in the supplementary material).

1. Dehydrogenated parent anion $(\text{OTfU}-\text{H})^-$

The ion yield for the formation of the closed shell anion $(\text{OTfU}-\text{H})^-$ is represented by reaction (I). The peak positions for the corresponding resonances are listed in Table I. The formation of the closed shell anion $(\text{OTfU}-\text{H})^-$ mainly occurs through the attachment of electrons with energy well below the threshold for electronic excitation. The anion yield exhibits a rich structure consisting of a set of peaks observed at about ~ 0 , 0.24, 0.56, 0.95, and 1.28 eV, as shown in Fig. 4. The formation of the first three sharp peaks (the one at ~ 0 eV is not resolved) may be assigned as vibrational Feshbach resonances (VFR) arising from the vibrational levels of the TNI or from a dipole-bound state (DBS) where an incoming electron may be temporally bounded. Indeed, the dipole moment of the most stable conformer (Fig. S5–A) of the neutral OTfU is estimated to be 3.2 D, while for the second conformer (Fig. S5–B) a considerably higher

TABLE I. Mass for each anion formed upon DEA to OTfU with the respective resonance position, the respective experimental threshold as well as thermodynamic threshold calculated at the M06-2X/aug-cc-pVTZ level (383.15 K, 3×10^{-11} atm) and the predicted adiabatic electron affinity compared to other values available in the literature. The AEA of OTfU is 0.9 eV at M06-2X/aug-cc-pVTZ.

Mass (m/z)	Anion	Resonance position (eV)					Threshold (eV)		AEA (eV)	
		1	2	3	4	5	Exp.	Calc.	Calc.	Lit.
259	[OTfU-H] ⁻							N ₁ -H -1.05 ^a	4.19	...
								N ₃ -H -0.56 ^a	4.70	...
								C ₆ -H -0.01 ^a	3.67	...
191	[OTfU-CF ₃] ⁻	~0	2.53	~0	-3.09 ^a	4.02 ^b	...
149	OTf ⁻	~0	0.14	1.05	3.65	...	~0	-2.44 ^a	6.22 ^b	5.50 ^c
133	Tf ⁻	~0	0.13	1.04	3.60	...	~0	-3.22 ^a	3.61	...
127	[OTfU-CF ₃ SO ₂] ⁻ /OU ⁻	~0	0.13	1.07	~0	-2.00 ^a	2.38	...
111	[OTfU-CF ₃ SO ₃] ⁻ /[U-H] ⁻	~1.2	~0.2	1.25	2.26	2.34 ^d
69	CF ₃ ⁻	~0	2.35	4.75	8.45	...	~0	-0.74 ^a	1.69	2.01 ^e
64	SO ₂ ⁻	~0	~0	-3.92 ^a	1.42	1.11 ^e
42	NCO ⁻	~0	~1.8	~4.0	~8.1	...	~0
19	F ⁻	~4.8	~8.0	~3.1	0.61	3.27	3.40 ^e

^aThe negative value obtained from the calculations corresponds to the experimental threshold of 0 eV.

^bThe neutral product is unstable. AEA is calculated for the neutral geometry with the frozen bond that is prone to break. Additionally VDE was calculated for both anions. $VDE_{[OTfU-CF_3]^-} = 4.47$ eV and $VDE_{[CF_3SO_2O]^-} = 6.67$ eV.

^cData taken from Refs. 51 and 52.

^dData taken from Ref. 50, i.e., AEA(Ur-5-y1*).

^eData taken from Ref. 53.

dipole moment of 5.4 is predicted at the M06-2X/aug-cc-pVTZ level of theory. These values are above the critical value (2.0–2.5 D)⁵⁴ required for the existence of a dipole-bound state (DBS).

In Fig. 5, the characteristic distributions of the SOMO orbital for DBSs formed by both conformers are depicted. As indicated by the numbers gathered in Table II, the anion originated from conformer A, of smaller dipole moment, is bound by only 9 meV at the KT level, while the more polar structure forms DBS characterized by the KT vertical energy attachment of 47 meV. Electron correlation is significant for DBSs since dipole moment is seriously overestimated at the HF level.

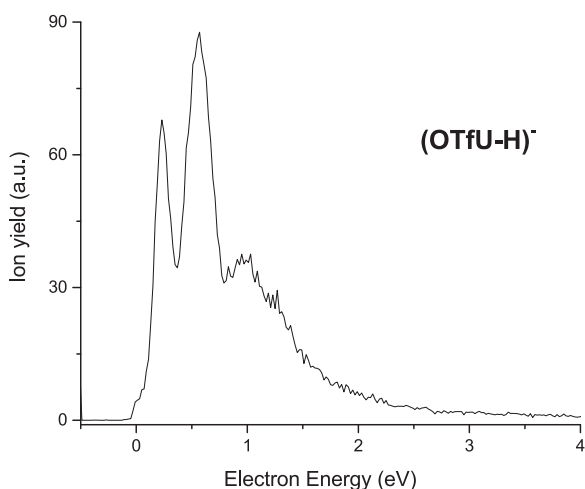


FIG. 4. Ion yield of (OTfU-H)⁻ formed upon DEA to OTfU.

On the other hand, dynamic correlation stabilizes DBSs to a large extent. Although these two effects have opposite signs, they usually do not cancel out which makes the calculations at the correlated level obligatory.⁵⁵ Actually, the VEA^{MP2} values gathered in Table II constitute a good illustration of the mentioned above (9 vs. 39 and 47 vs. 97 meV for conformation A and B, respectively; see Table II). An additional stabilization of DBS results from geometry relaxation due to anion formation. However, since the excess electron density of DBS is beyond the molecular framework (see Fig. 5), this effect, unlike for valence bound anions, is relatively small, cf. VEA^{MP2} with AEA^{MP2} (Table II).

Therefore, the coupling between the vibrational levels of the TNI with DBSs may arise as an effective DEA channel leading to the dehydrogenation of OTfU. In fact, DBS for the most abundant conformation of OTfU was predicted to lie 54 meV below the neutral (see Table II). Concerning the second conformer (Fig. 5), its DBS lies as much as 110 meV (see Table II) lower than the neutral. Notably, the same mechanism involving DBS underlying the dehydrogenation of uracil and thymine upon attachment of electrons with an energy below 3 eV has been proposed by a combination of experimental and theoretical methods.⁵⁶ In the case of OTfU, different anionic isomers may form by dehydrogenation depending on the site of H-loss—N₁, N₃, or C₆ in the uracil moiety. As so, the variation of the Gibbs free energy for each possible isomer is listed in Table I. The thermodynamic calculations show that in spite of the dehydrogenation site, the loss of a hydrogen from OTfU is always an exothermic reaction, whereas the dehydrogenation from the N₁ position appears to be thermodynamically most favorable. Note that the energetically most favorable loss of hydrogen upon DEA to uracil occurs from the N₁ position as well.^{56,57} Furthermore, the predicted AEA for (OTfU-H)⁻

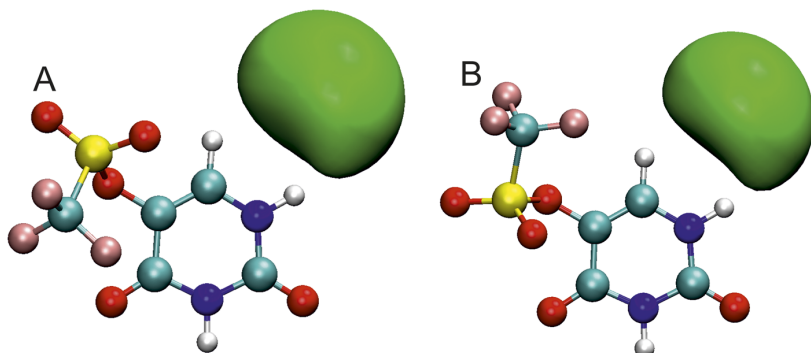


FIG. 5. The SOMO orbitals of the anions for both conformers considered. The isosurface value for the most stable conformer (a) is $0.001 \text{ a.u.}^{-3/2}$, while the second one (b) is equal to $0.018 \text{ a.u.}^{-3/2}$.

depends on the dehydrogenation site, and it varies from 3.67 to 4.19 eV, as shown in Table I.

2. Cleavage of the C–S bond in the triflate group

The cleavage of the C–S bond within the triflate group leads to the formation of two complementary anions with the ion yields shown in Fig. 6. First, $(\text{OTfU}-\text{CF}_3)^-$ is formed via reaction (II) where the trifluoromethyl radical ($-\text{CF}_3^\bullet$) is formed as a neutral byproduct. The experimental threshold of about 0 eV is in agreement with the calculated thermochemical threshold of -3.09 eV . The AEA of $(\text{OTfU}-\text{CF}_3)^-$ is predicted to be 4.02 eV. However, the trifluoromethyl radical appears to be unstable. Second, the closed shell anion CF_3^- is formed via the complementary reaction (VII) together with $(\text{OTfU}-\text{CF}_3)^\bullet$. The respective experimental threshold is also about 0 eV, which matches with the calculated thermochemical threshold of -0.74 eV . The theoretical AEA of 1.69 eV for CF_3^- is comparable to the AEA of 2.01 eV obtained by photoelectron spectroscopy reported in the literature.⁵³ In addition to a strong resonance near 0 eV for the former anion and hardly present for the latter anion, the ion yields of $(\text{OTfU}-\text{CF}_3)^-$ as well as CF_3^- exhibit a broad resonance centered at about 2.4 eV. The anion yield of CF_3^- further exhibits a resonance at 4.75 eV and a broad structure at 8.45 eV. The presence of a resonance for both anions at the same positions, i.e., about 2.4 eV, is the evidence that the formation of both species may occur from a common electronic state of the TNI. The formation of the aforementioned anions was previously reported by Ptasińska *et al.* in DEA studies with the triflate analogs in the gas-phase.⁵² In brief, they reported the formation of the counterpart of the $-\text{CF}_3^\bullet$ radical through resonances near 0 eV and 2.5–3.0 eV electron energies for the triflates containing a phenyl ring and only at 3 eV for the methyl triflate. Notably, a good agreement is observed between the resonance positions

TABLE II. Electron binding characteristics for dipole bound states supported by conformers A and B. All values shown in meV.

	Conformer A	Conformer B
$E_{\text{bind}}^{\text{KT}}$	9	47
VEA^{MP2}	39	97
AEA^{MP2}	54	110

that lead to the formation of $(\text{OTfU}-\text{CF}_3)^-$ by C–S bond cleavage either in OTfU or in triflate analogs. Therefore, one may conclude, based on this similarity, that the uracil ring attached to the triflate in OTfU has little effect on the electron energies required to cleave the C–S bond within the triflate. On the other hand, the formation of CF_3^- in the triflate analogs occurs mainly through a resonant state at 3 eV in addition to other states located at higher electron energies which depend on the considered analog, i.e., at 8 eV for methyl triflate and at 6 and 7.5 eV for tolyl triflate. In the present study, CF_3^- is formed from OTfU by the same number of resonant states such as in tolyl triflate, even though the respective positions appear to be different.

3. Cleavage of the O–S bond in the triflate group versus cleavage of the O–C₅ bond in the uracil group

The triflate (OTf^-) and triflyl (Tf^-) anions are formed upon a simple bond cleavage, i.e., the O–C₅ bond within the triflate group and the O–S bond in uracil and they are represented by reactions (III) and (IV), respectively. The calculations show that the neutral by-product, $\text{C}_4\text{H}_3\text{N}_2\text{O}_2^\bullet$, which is formed alongside OTf^- appears to be unstable. These two DEA

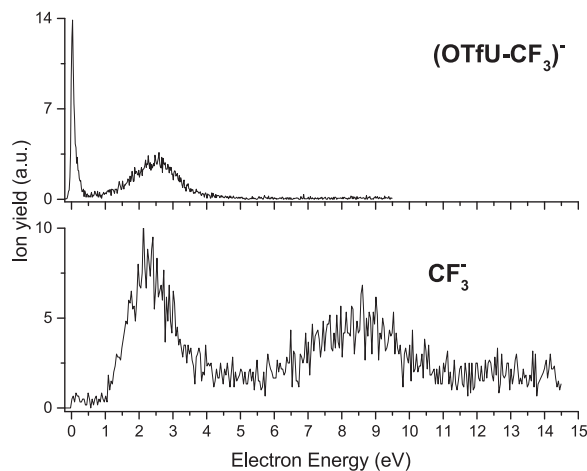


FIG. 6. Ion yield of $(\text{OTfU}-\text{CF}_3)^-$ and CF_3^- formed by the cleavage of the C–S bond within the triflate upon DEA to OTfU.

reactions represent the most favorable fragmentation channels, particularly close to 0 eV. Further resonances at about 0.13 eV, 1.05 eV, and at around 3.65 eV were observed as well for both anions (see Fig. 7). Such finding is in line with the outcomes of the DEA^{4,41} and theoretical¹⁷ studies with 5-BrU, where the abstraction of the halide anion Br⁻ represents the main dissociation pathway. The highly exothermic character is not surprising though since the anionic products possess a large AEA, i.e., AEA(Tf) = 3.61 eV and AEA(OTf) = 6.22 eV (see Table I). The calculated thermochemical thresholds of -2.44 eV for the formation of OTf⁻ and -3.22 eV for the formation of Tf⁻ are in good agreement with the peaks at about 0 eV obtained experimentally. However, Ptasińska *et al.* reported an energy barrier of about 0.5 eV for the formation of OTf⁻ through DEA to triflate analogs,⁵² which is not observed in the present study. The predicted AEAs of about 6.22 eV for the triflate group and about 3.61 eV for the triflyl group represent the driving forces of these DEA reactions. Albeit, to our best knowledge, the AEA of the triflyl group is not reported in the literature. Under the same experimental conditions, the intensity of the triflate anion is higher when compared to the intensity of the triflyl anion, which may suggest that the O-C₅ bond is more readily cleaved than the O-S bond within the triflate group. These findings can be compared with the outcomes obtained by Makurat *et al.* upon electron attachment in an aqueous 5-trifluoromethanesulfonyl-2'-deoxyuridine (OTfdU) solution.²² Briefly, this study was carried out in a deoxygenated aqueous OTfdU solution containing an OH[•] radical scavenger and phosphate buffer (pH = 7.0). Solvated electrons were generated in the solution through irradiation with X-rays. Thereafter, the products formed by electron attachment to OTfdU were probed by liquid chromatography mass spectrometry (LC-MS) operated in the negative mode. The authors reported that in the experiment the most abundant dissociation channel leads to the formation of dU by the cleavage of the C₅-O bond in the triflate group, in opposition to calculations, which indicated that in solution the O-S bond cleavage would be thermodynamically more

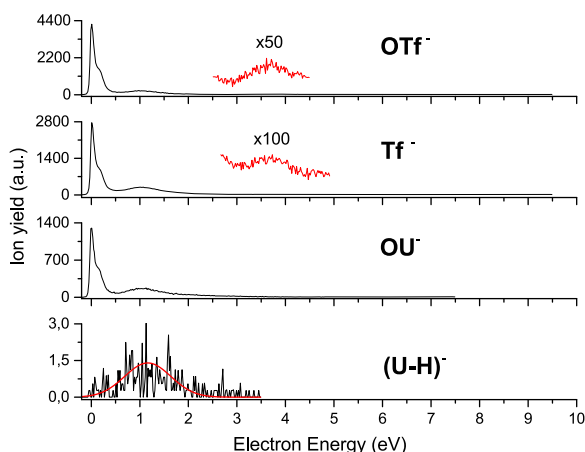


FIG. 7. Ion yield of OTf⁻, Tf⁻, OU⁻, and (U-H)⁻ formed either by the cleavage of the S-O bond or the O-C₅ bond in the uracil upon DEA to OTfU. The ion yield for (U-H)⁻ can be likely ascribed to a weak impurity since the resonance is below the calculated threshold for the DEA reaction (VI).

favorable. This discrepancy was finally explained by protonation of the compound at the C₅ position in solution which promotes the cleavage of the C₅-O bond rather than the O-S bond.²² The present calculations for the gas phase also predict that the cleavage of the O-S bond should be more favorable (see Table I); however, the total ion yields for cleavage of the C₅-O bond *vs.* the O-S bond are approximately equal. In this context, we note that under single collision conditions, the yield of a particular anion formed by DEA is associated to the DEA cross section σ_{DEA} , which is influenced by autodetachment. This situation is expressed by

$$\sigma_{DEA} = \sigma_0 P_{diss}, \quad (6)$$

where σ_0 represents the electron attachment cross section and P_{diss} represents the dissociation probability which is a function of the autodetachment lifetime, τ_{AD} , and the dissociation time, τ_{DEA} , as follows:

$$P_{diss} = \exp\left(-\frac{\tau_{DEA}}{\tau_{AD}}\right). \quad (7)$$

Thus, despite the inferior thermodynamic threshold for the cleavage of the O-S bond within the triflate group leading to the formation of Tf⁻, it does not imply that the formation of this particular anion should be favored over the formation of OTf⁻ upon cleavage of the O-C₅ bond in uracil.

In addition to reactions (III) and (IV), which lead to the formation of negatively charged triflate and triflyl ions, we report the formation of OU⁻ upon cleavage of the O-S bond within the triflate group, represented by reaction (V), mainly through a resonance at about 0 eV as well as others at 0.13 and 1.07 eV (see Fig. 7). The experimental threshold of about 0 eV is in accordance with the predicted thermodynamic threshold of -2.00 eV. The reaction (VI) represents the formation of dehydrogenated uracil, (U-H)⁻, upon cleavage of the O-C₅ bond in uracil, which is endothermic and characterized by the predicted thermodynamic threshold of about 1.25 eV. This dissociation channel appears to be unfavorable in the experiment, with a very low intensity of the ion yield as shown in Fig. 7. The experimental onset of ~0.2 eV was obtained, which is lower than the theoretical threshold and thus indicating rather an impurity.

Finally, we note that the energy-resolved ion yields regarding the above mentioned DEA reactions (III)-(V) exhibit peaks at the same electron energy, which suggests that the anions may be generated from a common electronic state of the TNI. Moreover, this set of reactions represents a prime example where a particular bond was cleaved, and the negative charge stayed on complementary parts of the molecule.

4. Complex fragmentation pathways: SO₂⁻ and NCO⁻

Apart from single bond cleavages, DEA to OTfU leads to the formation of further anionic species by multiple bond cleavages or through complex rearrangements within the molecule. Namely, the sulphur dioxide (SO₂⁻) anion results from the cleavage of two bonds, i.e., the C-S and the S-O bond in the triflate group, upon attachment of a single electron with 0 eV energy, as represented by reaction (VIII) and shown in Fig. 8. The experimental outcome is in line with the predicted

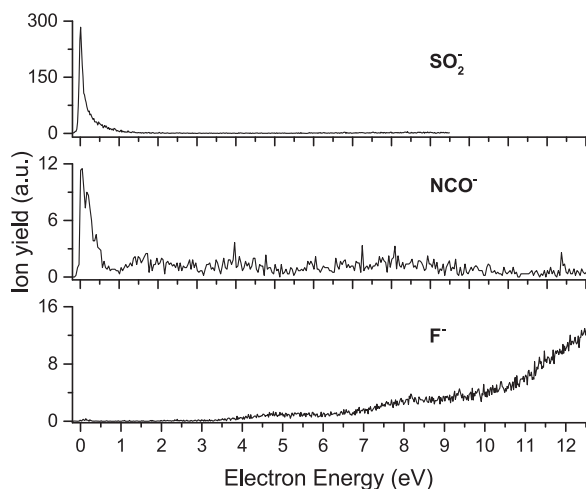


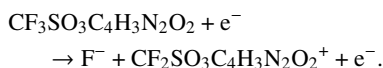
FIG. 8. Ion yields of SO_2^- , NCO^- , and F^- formed upon DEA to OTfU.

thermodynamic threshold for this reaction of about -3.92 eV (Table I). The theoretical AEA of 1.42 eV (Table I) for SO_2^- is comparable to the AEA of 1.11 eV reported in the literature.⁵³ We note that the formation of SO_2^- through DEA to triflate analogs in the gas-phase seems to be a more complex process⁵² since SO_2^- ion yields exhibit resonances at different positions for each analog.

We report the formation of NCO^- by DEA to OTfU as represented by reaction (IX) and shown in Fig. 8. The anion is rather weakly formed in a resonance centered at about 0 eV and even less intense in resonances at energies above 0 eV. Under the present experimental conditions, the ion yield seems to be reduced which hinders the identification of resonances at higher electron energies. It is worth noting that the underlying mechanism regarding the formation of NCO^- upon DEA to pyrimidine bases⁵⁸ and halouracils XU ($X = \text{Cl}, \text{Br}$)^{4,12} has been already intensively investigated in recent years (see Ref. 58). Therefore, we omit a detailed description regarding the formation of this only weakly abundant anion based on quantum chemical calculations for OTfU.

5. Cleavage of the C–F bond in the triflate group: Formation of F^-

The formation of F^- occurs by a single bond cleavage in the triflate group, as represented by reaction (X). The anion yield shows very interesting features resulting from the superimposition of two resonances at about 4.8 and 8.0 eV, which are formed by electron attachment, and a continuous ion signal, which results from the non-resonant ion pair formation process, as shown in Fig. 8. The weak contribution at 0 eV is not due to the DEA reaction, and it may be assigned as an artifact.⁵⁹ The ion pair formation usually occurs at higher electron energies than the DEA process and, in this case, may be described as follows:



The calculated thermodynamic threshold concerning the DEA reaction is 0.61 eV, which is considerably lower than the experimental onset of about 3.2 eV. Therefore, fragmentations, which are more complex, have been further investigated. The thermodynamic thresholds, which lead to the formation of F^- , are presented in Table SII in the supplementary material. The DEA reaction appears to be endothermic in most cases. Notably, the experimental onset lies above the thermodynamic threshold in all cases, which does not allow an unambiguous assignment. Furthermore, the predicted AEA of 3.27 eV for the fluorine anion matches with the value (3.40 eV) reported in the literature.⁵³

IV. CONCLUSION

We studied electron attachment in the gas-phase to the recently synthesized radiosensitizer OTfU in the electron energy range 0 – 14 eV. OTfU may be considered as a pseudo-halouracil. The triflate group present at the C_5 position in the uracil ring possesses a large electron affinity (6.22 eV) which overcomes the electron affinity of all halogens. We observed ten different anionic species formed through DEA to OTfU either upon simple bond cleavage (e.g., formation of OTf^- and loss of H^\bullet) or upon complex reactions (e.g., formation of SO_2^- and NCO^-). In most cases, we observed that an anion and its counterpart are formed by the decay of the same electronic state of the TNI since the ion yields concerning both anions exhibit resonance(s) at similar positions. The best example is represented by the cleavage of the S–O bond in the triflate group leading to the formation of TF^- and the OU^- as well as by the cleavage of the O– C_5 bond in the uracil leading to the formation of OTf^- through resonant states at similar positions. Moreover, the features presented in the energy-resolved ion yield concerning the loss of H^\bullet were assigned as VFR involving the dipole-bound state of the neutral OTfU. The AEA of the formed anions is comparable to the values previously reported in the literature in most cases.

In contrast to negative ion formation, the stable parent ion can be detected upon electron ionization. Also for this ionization process, reactions accompanied by the cleavage of the S–O bond in the triflate group are dominant. For example, the formation of OU^+ , which is the second most abundant cation observed, is only possible by the cleavage of this bond. However, otherwise the electron ionization mass spectrum shows several abundant cations formed by complex fragmentation reactions.

Ultimately, this study endorses OTfU as a potential radiosensitizer, in particular due to its high reactivity toward low-energy electrons. These LEEs very efficiently decompose OTfU and thereby generate radicals (e.g., uracil-yl) which may further react with DNA. This property is supported by the exothermic character predicted for nine out of eleven calculated DEA reactions, thus operative upon attachment of electrons with about 0 eV.

SUPPLEMENTARY MATERIAL

See supplementary material for the electrospray ionization mass spectrum of OTfU, the ^1H and ^{13}C NMR spectra

of OTfU, as well as more computational data including conformational scan, dipole-bound states, calculated thresholds at different conditions, and other reaction pathways leading to the formation of the F⁻ anion.

ACKNOWLEDGMENTS

J.A., R.M., and F.F.d.S. acknowledge the Portuguese National Funding Agency FCT–MCTES through Grant Nos. PD/BD/114447/2016 and PD/BD/114452/2016 and researcher position No. IF-FCT IF/00380/2014, respectively, and the research Grant No. UID/FIS/00068/2013. This work was supported by the Radiation Biology and Biophysics Doctoral Training Programme (RaBBiT, PD/00193/2012) and UID/Multi/04378/2013 (UCIBIO). S.D. acknowledges support from FWF (P30332). This work was also supported by the Polish National Science Center (NCN) under the Grant No. UMO-2014/14/A/ST4/00405 (J.R.). The calculations have been carried out in the Wrocław Center for Networking and Supercomputing (wcss.wroc.pl), Grant No. 209 and at a local cluster.

- ¹S. Rockwell, I. Dobrucki, E. Kim, S. Marrison, and V. Vu, *Curr. Mol. Med.* **9**, 442 (2009).
- ²K. Tanzer, L. Feketeová, B. Puschnigg, P. Scheier, E. Illenberger, and S. Denifl, *Angew. Chem., Int. Ed.* **53**, 12240 (2014).
- ³K. Westphal, J. Wiczak, J. Miloch, G. Kciuk, K. Bobrowski, and J. Rak, *Org. Biomol. Chem.* **13**, 10362 (2015).
- ⁴H. Abdoul-Carime, M. A. Huels, F. Brüning, E. Illenberger, and L. Sanche, *J. Chem. Phys.* **113**, 2517 (2000).
- ⁵S. Makurat, L. Chomicz-Mańka, and J. Rak, *ChemPhysChem* **17**, 2572 (2016).
- ⁶L. Chomicz-Mańka, M. Zdrochowicz, F. Kasprzykowski, J. Rak, A. Buonauriguo, Y. Wang, and K. H. Bowen, *J. Phys. Chem. Lett.* **4**, 2853 (2013).
- ⁷Y. Park, K. Polska, J. Rak, J. R. Wagner, and L. Sanche, *J. Phys. Chem. B* **116**, 9676 (2012).
- ⁸S. M. Pimblott and J. A. LaVerne, *J. Phys. Chem. A* **101**, 5828 (1997).
- ⁹E. Alizadeh and L. Sanche, *Chem. Rev.* **112**, 5578 (2012).
- ¹⁰J. D. Gorfinkiel and S. Ptasinska, *J. Phys. B: At., Mol. Opt. Phys.* **50**, 182001 (2017).
- ¹¹H. Abdoul-Carime, M. A. Huels, E. Illenberger, and L. Sanche, *Int. J. Mass Spectrom.* **228**, 703 (2003).
- ¹²S. Denifl, S. Matejciak, B. Gstir, G. Hanel, M. Probst, P. Scheier, and T. D. Märk, *J. Chem. Phys.* **118**, 4107 (2003).
- ¹³S. Denifl, S. Matejciak, S. Ptasinska, B. Gstir, M. Probst, P. Scheier, E. Illenberger, and T. D. Märk, *J. Chem. Phys.* **120**, 704 (2004).
- ¹⁴A. M. Scheer, K. Afatooni, G. A. Gallup, and P. D. Burrow, *Phys. Rev. Lett.* **92**, 068102 (2004).
- ¹⁵R. Abouaf and H. Dunet, *Eur. Phys. J. D* **35**, 405 (2005).
- ¹⁶F. Kossoski, M. H. F. Bettega, and M. T. d. N. Varella, *J. Chem. Phys.* **140**, 024317 (2014).
- ¹⁷F. Kossoski and M. T. d. N. Varella, *Phys. Chem. Chem. Phys.* **17**, 17271 (2015).
- ¹⁸F. Ferreira da Silva, D. Almeida, R. Antunes, G. Martins, Y. Nunes, S. Eden, G. Garcia, and P. Limão-Vieira, *Phys. Chem. Chem. Phys.* **13**, 21621 (2011).
- ¹⁹B. Djordjevic, *J. Exp. Med.* **112**, 509 (1960).
- ²⁰R. L. Erikson and W. Szybalski, *Radiat. Res.* **20**, 252 (1963).
- ²¹M. Sosnowska, S. Makurat, M. Zdrochowicz, and J. Rak, *J. Phys. Chem. B* **121**, 6139 (2017).
- ²²S. Makurat, M. Zdrochowicz, L. Chomicz-Mańka, W. Kozak, I. E. Serdiuk, P. Wityk, A. Kawecka, M. Sosnowska, and J. Rak, *RSC Adv.* **8**, 21378 (2018).
- ²³S. Denifl, S. Ptasinska, B. Sonnweber, P. Scheier, D. Liu, F. Hagelberg, J. Mack, L. T. Scott, and T. D. Märk, *J. Chem. Phys.* **123**, 104308 (2005).
- ²⁴G. T. Crisp and B. L. Flynn, *Tetrahedron* **49**, 5873 (1993).
- ²⁵Y. Zhao and D. G. Truhlar, *Theor. Chem. Acc.* **120**, 215 (2008).
- ²⁶R. A. Kendall, T. H. Dunning, and R. J. Harrison, *J. Chem. Phys.* **96**, 6796 (1992).
- ²⁷D. E. Woon and T. H. Dunning, *J. Chem. Phys.* **98**, 1358 (1993).
- ²⁸L. A. Curtiss, P. C. Redfern, and K. Raghavachari, *J. Chem. Phys.* **126**, 084108 (2007).
- ²⁹A. Ribar, K. Fink, M. Probst, S. E. Huber, L. Feketeová, and S. Denifl, *Chem. - Eur. J.* **23**, 12892 (2017).
- ³⁰M. J. Frisch, G. W. Trucks, H. B. Schlegel, G. E. Scuseria, M. A. Robb, J. R. Cheeseman, G. Scalmani, V. Barone, G. A. Petersson, H. Nakatsuji, X. Li, M. Caricato, A. V. Marenich, J. Bloino, B. G. Janesko, R. Gomperts, B. Mennucci, H. P. Hratchian, J. V. Ortiz, A. F. Izmaylov, J. L. Sonnenberg, D. Williams-Young, F. Ding, F. Lipparini, F. Egidi, J. Goings, B. Peng, A. Petrone, T. Henderson, D. Ranasinghe, V. G. Zakrzewski, J. Gao, N. Rega, G. Zheng, W. Liang, M. Hada, M. Ehara, K. Toyota, R. Fukuda, J. Hasegawa, M. Ishida, T. Nakajima, Y. Honda, O. Kitao, H. Nakai, T. Vreven, K. Throssell, J. A. Montgomery, Jr., J. E. Peralta, F. Ogliaro, M. J. Bearpark, J. J. Heyd, E. N. Brothers, K. N. Kudin, V. N. Staroverov, T. A. Keith, R. Kobayashi, J. Normand, K. Raghavachari, A. P. Rendell, J. C. Burant, S. S. Iyengar, J. Tomasi, M. Cossi, J. M. Millam, M. Klene, C. Adamo, R. Cammi, J. W. Ochterski, R. L. Martin, K. Morokuma, O. Farkas, J. B. Foresman, and D. J. Fox, *GAUSSIAN 09, Revision D.01*, Gaussian, Inc., Wallingford, CT, 2013.
- ³¹W. Humphrey, A. Dalke, and K. Schulten, *J. Mol. Graphics* **14**, 33 (1996).
- ³²A. Ribar, S. E. Huber, M. A. Śmiałek, K. Tanzer, M. Neustetter, R. Schürmann, I. Bald, and S. Denifl, *Phys. Chem. Chem. Phys.* **20**, 5578 (2018).
- ³³J. W. Ochterski, *Thermochemistry in Gaussian* (Gaussian, Inc., 2000), p. 1.
- ³⁴J. Simons, *Acc. Chem. Res.* **39**, 772 (2006).
- ³⁵D. E. Woon and T. H. Dunning, *J. Chem. Phys.* **100**, 2975 (1994).
- ³⁶M. Gutowski and J. Simons, *J. Chem. Phys.* **93**, 3874 (1990).
- ³⁷J. Rak, P. Skurski, and M. Gutowski, *J. Chem. Phys.* **114**, 10673 (2001).
- ³⁸M. Gutowski, K. D. Jordan, and P. Skurski, *J. Phys. Chem. A* **102**, 2624 (1998).
- ³⁹S. Denifl, B. Sonnweber, G. Hanel, P. Scheier, and T. D. Märk, *Int. J. Mass Spectrom.* **238**, 47 (2004).
- ⁴⁰H. Abdoul-Carime, M. A. Huels, E. Illenberger, and L. Sanche, *J. Am. Chem. Soc.* **123**, 5354 (2001).
- ⁴¹R. Abouaf, J. Pommier, and H. Dunet, *Int. J. Mass Spectrom.* **226**, 397 (2003).
- ⁴²R. Schürmann, T. Tsering, K. Tanzer, S. Denifl, S. V. K. Kumar, and I. Bald, *Angew. Chem., Int. Ed.* **56**, 10952 (2017).
- ⁴³R. Schürmann, K. Tanzer, I. Dąbkowska, S. Denifl, and I. Bald, *J. Phys. Chem. B* **121**, 5730 (2017).
- ⁴⁴J. Rackwitz, J. Kopyra, I. Dąbkowska, K. Ebel, M. L. Ranković, A. R. Milosavljević, and I. Bald, *Angew. Chem., Int. Ed.* **55**, 10248 (2016).
- ⁴⁵S. Ptasinska, S. Denifl, B. Mróz, M. Probst, V. Grill, E. Illenberger, P. Scheier, and T. D. Märk, *J. Chem. Phys.* **123**, 124302 (2005).
- ⁴⁶S. Ptasinska, S. Denifl, S. Gohlke, P. Scheier, E. Illenberger, and T. D. Märk, *Angew. Chem., Int. Ed.* **45**, 1893 (2006).
- ⁴⁷G. Hanel, B. Gstir, S. Denifl, P. Scheier, M. Probst, B. Farizon, M. Farizon, E. Illenberger, and T. D. Märk, *Phys. Rev. Lett.* **90**, 188104 (2003).
- ⁴⁸S. Ptasinska, S. Denifl, P. Candori, S. Matejciak, P. Scheier, and T. D. Märk, *Chem. Phys. Lett.* **403**, 107 (2005).
- ⁴⁹S. Denifl, H. D. Flosadóttir, A. Edtbauer, O. Ingólfsson, T. D. Märk, and P. Scheier, *Eur. Phys. J. D* **60**, 37 (2010).
- ⁵⁰X. Li, L. Sanche, and M. D. Sevilla, *J. Phys. Chem. A* **106**, 11248 (2002).
- ⁵¹J. B. Hendrickson and P. L. Skipper, *Tetrahedron* **32**, 1627 (1976).
- ⁵²S. Ptasinska, D. Gschliesser, P. Bartl, I. Janik, P. Scheier, and S. Denifl, *J. Chem. Phys.* **135**, 214309 (2011).
- ⁵³J. C. Rienstra-Kiracofe, G. S. Tschumper, H. F. Schaefer, S. Nandi, and G. B. Ellison, *Chem. Rev.* **102**, 231 (2002).
- ⁵⁴C. Desfrancois, *Phys. Rev. A* **51**, 3667 (1995).
- ⁵⁵R. A. Bachorz, J. Rak, and M. Gutowski, *Phys. Chem. Chem. Phys.* **7**, 2116 (2005).
- ⁵⁶P. D. Burrow, G. A. Gallup, A. M. Scheer, S. Denifl, S. Ptasinska, T. Märk, and P. Scheier, *J. Chem. Phys.* **124**, 124310 (2006).
- ⁵⁷S. Denifl, S. Ptasinska, G. Hanel, B. Gstir, M. Probst, P. Scheier, and T. D. Märk, *J. Chem. Phys.* **120**, 6557 (2004).
- ⁵⁸F. Ferreira da Silva, C. Matias, D. Almeida, G. Garcia, O. Ingólfsson, H. D. Flosadóttir, B. Ómarsson, S. Ptasinska, B. Puschnigg, P. Scheier, P. Limão-Vieira, and S. Denifl, *J. Am. Soc. Mass Spectrom.* **24**, 1787 (2013).
- ⁵⁹R. Balog, J. Langer, S. Gohlke, M. Stano, H. Abdoul-Carime, and E. Illenberger, *Int. J. Mass Spectrom.* **233**, 267 (2004).

7.2 Formation of resonances and anionic fragments upon electron attachment to benzaldehyde

A detailed investigation on electron attachment to benzaldehyde is presented. Two experimental setups were used to study the electron energy dependence of DEA for various fragments, and absolute cross sections is presented. The experimental results are supported by a comprehensive set of theoretical calculations. Namely, quantum chemical calculations were performed by Prof. Dr. Ian Carmichael, Notre Dame University, USA; and by Dr. Lucas Cornetta and Prof. Dr. Márcio Varella, Universidade de São Paulo, Brazil who also performed electron scattering calculations. The results are summarized in the following publication:

Formation of resonances and anionic fragments upon electron attachment to benzaldehyde

J. Ameixa, E. Arthur-Baidoo, J. Pereira-da-Silva, M. Ryszka, I. Carmichael, L.M. Cornetta, M. T. do N. Varella, F. Ferreira da Silva, S. Ptasińska and S. Denifl, *Phys. Chem. Chem. Phys.* 22, 8171 (2020)

Author's contribution: I performed the measurements and analyzed the obtained data. Afterwards, I prepared the final figures and prepared the first version of the manuscript.



Formation of resonances and anionic fragments upon electron attachment to benzaldehyde†

Cite this: DOI: 10.1039/d0cp00029a

 J. Ameixa,^{ab} E. Arthur-Baidoo,^a J. Pereira-da-Silva,^b M. Ryszka,^c
 I. Carmichael,^c L. M. Cornetta,^d M. T. do N. Varella,^d F. Ferreira da Silva,^{ab}
 S. Ptasińska^{ce} and S. Denifl^{*,a}

Benzaldehyde is a simple aromatic aldehyde and has a wide range of applications in the food, pharmaceutical, and chemical industries. The positive electron affinity of this compound suggests that low-energy electrons can be easily trapped by neutral benzaldehyde. In the present study, we investigated the formation of negative ions following electron attachment to benzaldehyde in the gas-phase. Calculations on elastic electron scattering from benzaldehyde indicate a π^* valence bound state of the anion at -0.48 eV and three π^* shape resonances (0.78, 2.48 and 5.51 eV). The excited state spectrum of the neutral benzaldehyde is also reported to complement our findings. Using mass spectrometry, we observed the formation of the intact anionic benzaldehyde at ~ 0 eV. We ascribe the detection of the benzaldehyde anion to stabilization of the π^* valence bound state upon dissociative electron attachment to a benzaldehyde dimer. In addition, we report the cross sections for nine fragment anions formed through electron attachment to benzaldehyde. Investigations carried out with partially deuterated benzaldehyde show that the hydrogen loss is site-selective with respect to the incident electron energy. In addition, we propose several dissociation pathways, backed up by quantum chemical calculations on their thermodynamic thresholds. The threshold calculations also support that the resonances formed at higher energies lead to fragment anions observable by mass spectrometry, whereas the resonances at low electron energies decay only by electron autodetachment.

Received 3rd January 2020,
Accepted 14th March 2020

DOI: 10.1039/d0cp00029a

rsc.li/pccp

1. Introduction

Benzaldehyde (C_6H_5CHO , Chart 1) is an aromatic aldehyde with a wide range of applications, mainly in the food industry as a flavouring agent or preservative. It may also serve as an important intermediate to produce various organic compounds, *e.g.*, drugs, cosmetics, oils, inks, or plastics, thereby attracting the interest of the pharmaceutical and chemical industries.^{1,2} Moreover, it also

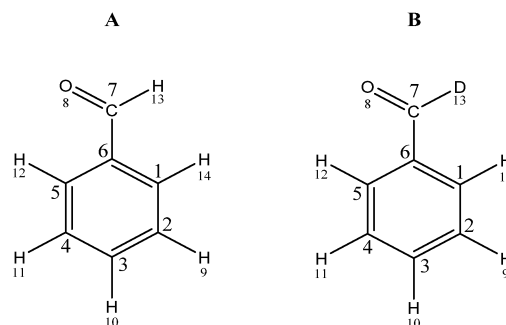


Chart 1 Chemical structures of (A) – benzaldehyde and (B) – benzaldehyde- α -d1 (d-benzaldehyde).

^a Institut für Ionenphysik und Angewandte Physik and Center for Molecular Biosciences (CMBI), Leopold-Franzens Universität Innsbruck, Technikerstraße 25/3, 6020 Innsbruck, Austria. E-mail: Stephan.denifl@uibk.ac.at

^b Atomic and Molecular Collisions Laboratory, CEFITEC, Department of Physics, Universidade NOVA de Lisboa, 2829-516 Caparica, Portugal. E-mail: f.ferreiradasilva@fct.unl.pt

^c Radiation Laboratory, University of Notre Dame, Notre Dame, Indiana 46556, USA

^d Instituto de Física, Universidade de São Paulo, Rua do Matão 1731, 05508-090 São Paulo, Brazil

^e Department of Physics, University of Notre Dame, Notre Dame, Indiana 46556, USA

† Electronic supplementary information (ESI) available: Thermodynamic thresholds calculated at the G4(MP2) ($T = 0$ K and $T = 298.15$ K) level for the observed anions, energy and width of the bound and resonant states obtained by SMCPP, and schematic diagram of the full active space used in the CASSCF/CASPT2 calculations. See DOI: 10.1039/d0cp00029a

occurs spontaneously in alcoholic beverages, dairy products, meat, poultry, and in a wide variety of fruits and vegetables.³

Benzaldehyde has chemotherapeutic relevance, as proposed in the late seventies by Takeuchi *et al.*⁴ Since then, benzaldehyde and its derivatives have been investigated and administered to patients with advanced inoperable carcinomas without measurable toxicity.^{4–7} The *in vitro* studies with human healthy and tumour cells have shown selective inhibition of the

growth of the tumour cells without measured effects on the healthy cells.⁶ Moreover, the combination of hyperthermia and benzaldehyde at doses that are nontoxic appears to enhance the cytotoxic effect.⁸ Additionally, an *in vivo* assay further uncovered the inhibition of pulmonary metastasis by benzaldehyde in tumour-inoculated mice.⁹ However, the underlying mode of operation of benzaldehyde at the molecular level is still unclear. Aldehydes, including benzaldehyde, bound to cellular macromolecules, in particular, to the amino group of proteins forming Schiff base adducts, may quench protein-mediated processes in the cell, for instance enzymes or the transport of molecules through the cell membrane.^{10–12} Consequently, a hypothesis suggested that the anti-cancer effect of benzaldehyde is based on the inhibition of the uptake of essential nutrients, which are required for the growth of cancer cells.¹³ In addition, another hypothesis suggested that the effect in cancer cells is associated with efficient inhibition of glutathione peroxidase (GPx) by benzaldehyde, since GPx belongs to a family of enzymes that defend the organism from oxidative damage, leading to an increased production of highly reactive oxygen species (ROS), and consequently oxidative stress.^{14,15} The latter species, in turn, *e.g.*, $O_2^{\bullet-}$, OH^{\bullet} , and O^{\bullet} , are harmful to DNA (free radical damage) and other biomolecules, thereby leading to mutations, cancer, and ultimately apoptosis.¹⁶

The ROS-induced DNA damage is also highly relevant in cancer radiotherapy. The ionisation of water following the interaction of high energy radiation with the cell tissue leads to the formation of ROS, which may react with DNA, as well as to the production of a large amount of secondary low-energy electrons (LEEs), with an energy distribution peaking around 10 eV.^{17–19} In this energy regime, LEEs may contribute to DNA damage, inducing mainly single- and double strand breaks, through dissociative electron attachment (DEA) reactions.^{20,21} This process occurs when a molecule resonantly captures an electron, forming a transient negative ion (TNI) that may decay into anionic fragment and neutral radicals.^{22–24}

The administration of radiosensitizers should enhance the sensitivity of tumours to high-energy radiation.²⁵ The related processes in the early physical–chemical stage of radiation damage are not fully understood yet. Recently, Meißner *et al.*²⁶ have shown that the first step in the radiosensitization of hypoxic tumour cells by nimorazole relies on the efficient formation of the radical anion species by associative attachment of LEEs. In another way of radiosensitization, LEEs may induce the dissociation of electrophilic compounds, through DEA reactions yielding reactive radicals that are precursors for DNA damage. For instance, nucleobases/nucleosides with an electrophilic group at the C₅-position have been used as radiosensitizers.^{27–29} These compounds exhibit high reactivity towards LEEs due to a positive electron affinity (EA). Benzaldehyde has an EA of ~ 0.35 eV,³⁰ thus it could serve as a radiosensitizer, although knowledge about the interactions of LEEs with benzaldehyde is limited. To the best of our knowledge, only two gas-phase studies on the interaction of LEEs with benzaldehyde have been carried out so far. Hacıoğlu *et al.*³¹ performed a DEA study with benzaldehyde, while Modelli *et al.*³² located shape resonances in benzaldehyde by electron transmission spectroscopy.

The studies described by Hacıoğlu *et al.*³¹ show that the most abundant anions formed through electron capture are O^- and the phenyl anion. Moreover, the parent anion was not observed in their study. The experimental attachment energies determined by Modelli and Burrow³² show two π^* shape resonances at 2.21 and 4.34 eV in addition to a bound state.

To reach a better understanding of the interaction of LEEs with benzaldehyde, we have investigated the formation of anions through electron attachment by means of two experimental set-ups. In addition, we performed a detailed theoretical study by calculating elastic electron scattering cross sections, the electronic excitation spectra for neutral benzaldehyde, and also the thermodynamic thresholds for the formation of the observed anions. The present experimental results show the formation of an intact molecular anion *via* a dimer and a phenyl anion that was observed as the most abundant fragment, in contrast to previous studies. Moreover, both computational chemistry and electron scattering calculations support our experimental results together with those from previous ETS experiments. Finally, we measured the DEA of benzaldehyde- α -d₁ (d-benzaldehyde) to clarify some dissociation pathways involving hydrogen loss.

2. Methods

2.1 Experimental set-up

Benzaldehyde (106 u) was purchased from Sigma-Aldrich (stated purity $\geq 99\%$). The sample is a liquid at room temperature with a vapour pressure of 195.7 Pa.³³ It was purified by performing several freeze–pump–thaw cycles before performing the studies. In both experimental set-ups, the vapour of the liquid was introduced into an interaction region *via* a gas inlet coupled with a precision valve. At the University of Innsbruck, a crossed electron-molecular beam setup combined with a quadrupole mass spectrometer (QMS) was used. The setup was described in detail elsewhere.³⁴ Briefly, the sample vapour enters the interaction chamber of a hemispherical electron monochromator (HEM), through a 1 mm-diameter, stainless-steel capillary, where it crosses with an electron beam. The HEM was tuned to generate the electron beam with an energy resolution of 120 meV at full width at half maximum (FWHM) with an incident electron current of 10–30 nA. The formed anions are extracted to the QMS by a weak electrostatic field. In the QMS, they are analysed by their mass-to-charge ratio. Finally, the mass-separated anions were detected by a channeltron-type secondary electron multiplier operated in single-pulse counting mode. The presented ion yields were obtained by recording the intensity of a given mass-separated anion as a function of the incident electron energy. The electron energy scale and electron energy resolution were determined by measuring the well-known resonances for the formation of SF_6^- from SF_6 and Cl^- from CCl_4 , at ~ 0 eV. Lastly, the electrons that pass the interaction region were collected using a Faraday plate and the obtained current is monitored using a picoammeter.

In this study, the dissociative electron attachment cross section, σ_{DEA} , was determined by comparing the ion yields of the fragment anions formed from benzaldehyde with the

well-known cross sections occurring at 0.8 eV for Cl^- from CCl_4 ($\sigma_{\text{DEA}} = 5.0 \times 10^{-20} \text{ m}^2$)³⁵ or at 5.2 eV for F^- from SF_6 ($\sigma_{\text{DEA}} = 5.0 \times 10^{-22} \text{ m}^2$).³⁶ For a given DEA reaction, the ion yields were corrected with respect to the partial pressures of the sample and the intensity of incident electron current under the given experimental conditions. The experimental uncertainty of the determined cross-section values is within one order of magnitude.

At the Radiation Laboratory at the University of Notre Dame, an experiment was performed consisting of a high-vacuum chamber equipped with a QMS from Hidden Analytical, Inc. and it has been described previously.³⁷ First, the effusive molecular beam is directed towards the entrance of the QMS, using a 1 mm diameter, stainless-steel capillary. Thereafter, the ions were formed by the interaction with electrons emitted by the internal filament (oxide-coated iridium wire) of the QMS. The anions were mass-analysed using the QMS and further detected using the channeltron-type secondary electron multiplier. The ion yield for a particular anion was recorded as a function of the electron energy. The electron energy scale was calibrated by measuring the well-known resonances of SF_6^- and F^- from SF_6 . The electron energy resolution was estimated to be approximately 500 meV (FWHM) for an incident electron current of 2 μA .

2.2 Computational methods

Apart from the scattering calculations and the electronic excitation spectra, all computations described below were performed with the Gaussian09 software package.³⁸

2.2.1 Geometry optimization. The ground state geometry of benzaldehyde was optimized using density functional theory (DFT), employing the hybrid functional B3LYP³⁹ and the aug-cc-pVTZ basis.⁴⁰ An essentially identical geometry was obtained using Møller–Plesset second-order perturbation theory (MP2) and the same basis. This geometry was employed in all calculations for the neutral and anion species, except for the vertical attachment energy (VAE) estimates obtained as empirically corrected virtual orbital energies (VOEs). In this case, the geometry and VOEs were calculated using the DFT/B3LYP/6-31G* method, following the prescription of Scheer *et al.*⁴¹

2.2.2 Electron scattering calculations. We have employed the Schwinger Multichannel method^{42,43} implemented with the Bachelet–Hamann–Schlüter⁴⁴ pseudopotentials (SMCPP). Details of the SMCPP variational approach to the collision problem and its implementation can be found elsewhere.⁴⁵ Here, we briefly mention that the expansion of the scattering wave function in the configuration state function (CSF) trial bases defines the static-exchange (SE) and SE plus polarization (SEP) approximations. The former employs CSFs given by $|\chi_{0\mu}\rangle = \mathcal{A}[\Phi_0 \otimes |\phi_\mu\rangle]$, where \mathcal{A} is the antisymmetrization operator, $|\Phi_0\rangle$ is the target ground state obtained in the Hartree–Fock (HF) approximation, and $|\phi_\mu\rangle$ is the scattering orbital. The SE scheme neglects correlation-polarization effects, which are accounted for by augmenting the SEP expansion with CSFs of the kind $|\chi_{n\mu}\rangle = \mathcal{A}[\Phi_n \otimes |\phi_\mu\rangle]$, where $|\Phi_n\rangle$ is a singly excited target state with either singlet or triplet spin coupling, although all CSFs are doublets. The construction of the CSF space

was based on the energy criterion proposed elsewhere,⁴⁰ which considers all configurations satisfying $\epsilon_{\text{particle}} + \epsilon_{\text{scattering}} - \epsilon_{\text{hole}} < \Delta$, where ϵ corresponds to the orbital energy and is an energy cutoff. We employed modified virtual orbitals generated from cationic cores with charge +2 and the cutoff $\Delta = -1.24 \text{ Ha}$. The CSF space was also symmetry decomposed, such that the A'' component comprised 4824 trial basis functions in the SEP approximation. The SMCPP calculations were restricted to the A'' irreducible representation of the cross section, where the signatures of the π^* shape resonances should be evident. While σ^* resonances could also be expected for benzaldehyde, they are usually broad and embedded into the large background arising from the dipolar interaction, thus having no clear signatures in the calculated cross sections (unless heavier atoms are found^{46,47}).

2.2.3 Dipole-bound states. The energy of the dipole bound state (DBS) was obtained according to Skurski *et al.*⁴⁸ In brief, to account for the diffuse character of the state, the aug-cc-pVTZ basis was augmented with sets of 6s6p diffuse functions centred on the hydrogen atoms H(10) and H(11), located close to the positive end of the dipole moment vector (atomic labels shown in Chart 1). The vertical DBS energy was computed using two methods, namely MP2 and coupled-clusters with single, double, and non-iterative triple excitations (CCSD(T)).

2.2.4 Thermodynamic thresholds. The dissociation thresholds for several channels were calculated at the B3LYP/aug-cc-pVTZ level of theory, firstly from enthalpy differences deduced from harmonic frequency calculations for a number of likely produced fragments, matching their masses with the observed mass-to-charge ratios. Based on these structures, enthalpies of formation for some selected fragments were further refined at the G4(MP2)⁴⁹ level of theory. In general, the zero-temperature thresholds are 0.2–0.5 eV lower than those obtained from enthalpy differences at room temperature (298.15 K).

2.2.5 Electronic excitation. The excited states of neutral benzaldehyde were calculated using the complete active space self-consistent field method and second-order perturbative corrections (CASSCF/CASPT2), as implemented in the OpenMOLCAS⁵⁰ software package. The calculations employed the ANO-L basis set with the contraction scheme [4s3p1d] for carbon and oxygen atoms, and [2s1p] for the hydrogen atoms. This basis set was calibrated for describing valence excited states at the CASPT2 level⁵¹ and it has been employed for some systems in previous studies of neutral and anionic species.^{52,53} The (12,10) active space comprised 12 electrons and 10 active orbitals in the reference HF ground state, namely four π -type and two n-type occupied orbitals, along with four π^* virtual orbitals. The same orbital space was employed for the anion, the only difference being the number of active electrons, (13,10). The occupied orbitals are labelled, from the (HOMO–5) to the HOMO level, as $\pi_4, \pi_2, \pi_3, \pi_1, \pi_2,$ and π_1 , while the unoccupied ones, from the LUMO to the LUMO+3 level, are labelled as π_1^* to π_4^* .

3. Results and discussion

3.1 Electron scattering calculations

The A'' symmetry component of the integral cross section (ICS), obtained in both the SE and SEP approximations for elastic

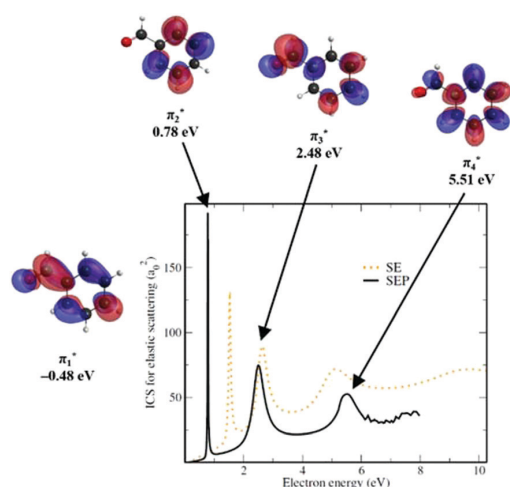


Fig. 1 A'' symmetry component of the elastic integral cross section (ICS). The dotted line corresponds to the SE approximation, while the solid line corresponds to the SEP results. The energies of the π^* resonances are indicated in the panel for the SEP calculations (π_1^* is a valence bound state, not represented in the graph). Virtual orbital plots calculated with compact basis sets are also shown to provide insight into the bound and resonance characters.

electron scattering, is presented in Fig. 1. The SE calculations show four shape resonances at 1.59, 2.65, 4.98 and 9.63 eV, which are labelled π_1^* to π_4^* sorted by increasing energy. Virtual orbital plots generated with compact basis sets (HF/6-31G*) are also shown to provide insight into the characters of the anion states. The inclusion of polarization effects (SEP approximation) shifts the resonances to lower energies, as expected, and the lowest lying π_1^* state becomes stable. The diagonalization of the scattering Hamiltonian represented in the CSF space indicates a valence bound state (VBS) at -0.48 eV (the energies of bound and resonance states are indicated as negative or as positive, respectively). From more sophisticated CCSD/aug-cc-pVDZ calculations, we obtained a vertical binding energy of -0.31 eV for the π_1^* anion state, which is in good agreement with the DFT estimation (~ -0.35 eV) reported by Buonaugurio *et al.*³⁰ In the SEP cross section, the higher lying π^* anion states have resonances located at 0.78, 2.48 and 5.51 eV. The positions and widths of the resonances are presented in Table 1, along with the empirically corrected VOs and the electron transmission spectroscopy (ETS) values reported by A. Modelli *et al.*³² There is good agreement between the SMCPP calculations and the

Table 1 Positions and widths (given in parenthesis) of the shape resonances of benzaldehyde (in eV). We show the results obtained with the SMCPP method and the scaled VOs calculated with the empirical scaling relation of Scheer *et al.*⁴¹ The ETS data of Modelli *et al.*³² are also indicated for comparison

	π_1^*	π_2^*	π_3^*	π_4^*
SMCPP	-0.48	0.78 (0.024)	2.48 (0.48)	5.51 (0.78)
Scaled VOs	-0.46	0.61	1.79	4.43
ETS data ³²	<0	0.71–0.85	2.21	4.34

experimental data, except for the π_4^* state. The discrepancy for the latter state is not surprising, since elastic scattering calculations, which neglect electronic excitations channels, often overestimate the energy of higher lying π^* anion states with mixed shape and core-excited character, by 0.5 to 1 eV (see Kossoski *et al.*⁴⁶ and references therein).

3.2 Excited states for neutral benzaldehyde (0 to ~ 9.5 eV)

We calculated the electronic excitation spectrum of neutral benzaldehyde with the CASSCF/CASPT2 method. While we did not include electronic excitation channels in the scattering calculations, the energy of the excited triplet and singlet states of the target molecule might be of help in assigning the type of core-excited resonances. The calculated values are listed in Table 2 for energies up to 8.2 eV (the ionisation potential is 9.5 eV⁵⁴). The dominant character of the excitations is also indicated whenever they could be clearly identified.

3.3 Electron attachment to benzaldehyde

Table 3 summarizes the observed anions and positions of the maxima for each ion yield together with the calculated thermodynamic thresholds. Ten different anions were identified, and all are formed at energies above 3.6 eV except for the benzaldehyde anion formed at ~ 0 eV. The lowest thermodynamic threshold for DEA to benzaldehyde lies at 2.53 eV corresponding to the formation of $C_6H_5^-$. Consequently, the shape resonances π_2^* and π_3^* identified here using the electron scattering calculations at 0.78 and 2.48 eV (see Section 3.1) are unlikely precursors for DEA to benzaldehyde, since the measured onsets for the formation of fragment anions occur at much higher energies. Therefore, the shape resonances π_2^* and π_3^* decay *via* autodetachment. The DEA cross sections are also listed in Table 3.

Hacaloglu *et al.*³¹ studied electron attachment to a collection of unsaturated carbonyls, including benzaldehyde, by means of a crossed-beam experiment comprising a trochoidal electron

Table 2 Vertical electronic states for neutral benzaldehyde obtained at the CASSCF/CASPT2 level of theory. S and T stand for singlet and triplet spin states, respectively

Electronic state (neutral)	Energy (eV)
S_0	0.00
$T_1(n_1 \rightarrow \pi_1^*)$	3.57
$S_1(n_1 \rightarrow \pi_1^*)$	3.83
$T_2(\pi_1 \rightarrow \pi_1^*)$	3.85
$T_3(\pi_2 \rightarrow \pi_1^*)$	4.18
$T_4(\pi_2 \rightarrow \pi_2^*)$	4.70
$T_5(\pi_1 \rightarrow \pi_2^*)$	4.80
$T_6(\pi_3 \rightarrow \pi_1^*)$	5.77
$S_2(\pi_1 \rightarrow \pi_1^*)$	5.93
$T_7(n_1 \rightarrow \pi_2^*)$	6.07
$S_3(n_1 \rightarrow \pi_2^*)$	6.30
T_8	6.42
T_9	6.54
S_4	6.69
S_5	6.73
$T_{10}(\pi_4 \rightarrow \pi_1^*)$	7.14
S_6	7.58
$T_{11}(\pi_2, n_1 \rightarrow \pi_1^*, \pi_2^*)$	8.05
S_7	8.19

Table 3 Mass-to-charge ratio (m/z) of the observed anionic fragments formed upon electron attachment to benzaldehyde, as well as measured DEA cross sections along with the respective resonance positions, sorted by increasing energy, and experimental thresholds. Thermodynamic thresholds were calculated at the G4(MP2) (indicated with ^a) or B3LYP/aug-cc-pVTZ (indicated with ^b) levels of theory

m/z	Anion	$\sigma_{\text{DEA}} (\times 10^{-24} \text{ m}^2)$	Resonance position (eV)			Threshold (eV)		
			1	2	3	Exp.	Theory	
106	$\text{C}_6\text{H}_5\text{CHO}^-$		~ 0			~ 0		
105	$[\text{C}_6\text{H}_5\text{CHO} - \text{H}]^-$	9.85	4.6	7.6	9.2	3.6	$\text{C}_1\text{-H}(14)$	2.98 ^a
							$\text{C}_2\text{-H}(9)$	2.92 ^a
							$\text{C}_3\text{-H}(10)$	2.83 ^a
							$\text{C}_4\text{-H}(11)$	2.86 ^a
							$\text{C}_5\text{-H}(12)$	2.68 ^a
							$\text{C}_7\text{-H}(13)$	2.80 ^a
90	$\text{C}_6\text{H}_5\text{CH}^* + \text{O}(^3\text{P})$	3.84	7.4			5.9	5.92 ^a	
	$\text{C}_6\text{H}_5\text{CH}^* + \text{O}(^1\text{D})$						7.97 ^a	
89	$\text{C}_6\text{H}_5\text{C}^-$	31.1	6.9	7.6		6.2	5.41 ^a	
88	$\text{C}_6\text{H}_4\text{C}^-$	15.8	6.8			5.9	2.92 ^a	
77	C_6H_5^-	95.8	4.7	6.5	7.0	3.8	2.53 ^a	
62	HC_5H^-	3.35	8.1			6.5	4.1 ^b	
49	C_4H^-	3.01	8.2			6.4	5.5 ^b	
17	OH^-	46.1	7.3	8.3	9.7	6.4	4.72 ^a	
16	O^-	23.5	7.8	8.9	10.5	6.5	6.02 ^a	

monochromator coupled with a QMS. Since the experimental details such as the incident electron current, electron energy resolution, calibration method for the electron energy scale and the working pressure were not mentioned in their work,³¹ we omit a comprehensive comparison with our results. To briefly summarize their study, the authors reported a total of seven anionic fragments. Six of them had the onset above 6.6 eV while the onset for the formation of C_6H_5^- was 1.5 eV. The latter value is substantially lower than the presently predicted thermodynamic threshold of 2.53 eV. Other major differences to the present results are related to the shape of the ion yields as well as the relative intensities of fragment anions. For example, O^- was observed as the most abundant fragment anion in their work.³¹

3.3.1 Formation of the benzaldehyde anion. Fig. 2 shows the ion yield for the intact benzaldehyde anion, m/z 106 $\text{C}_6\text{H}_5\text{CHO}^-$ (M), measured with the HEM instrument. The ion yield shows a narrow peak close to 0 eV electron energy and

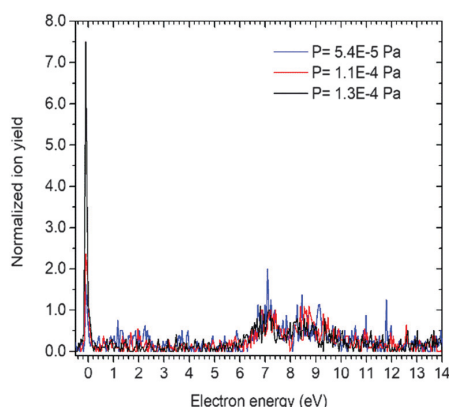


Fig. 2 Ion yield of $\text{C}_6\text{H}_5\text{CHO}^-$ measured at different working pressures in the HEM instrument. The ion yields were normalized with respect to the maximum of the signal at ~ 7.13 eV.

other structures between 6 and 10 eV. The higher energy features are assigned to the dehydrogenated benzaldehyde anion, $(\text{M} - \text{H})^-$, due to the isotopic contributions. We also studied the dependence of the ion yield at m/z 106 as a function of the working pressure of benzaldehyde in the chamber. The pressure range was between 5.4×10^{-5} and 1.3×10^{-4} Pa. At the lowest pressure, 5.4×10^{-5} Pa, the intensity of the ion yield measured at ~ 0 eV is comparable with the high-energy features of $(\text{M} - \text{H})^-$; while at higher pressures, the ion yield at ~ 0 eV starts to dominate. In general, any elevated pressure in the capillary may induce the formation of benzaldehyde dimers. It is well-known that benzaldehyde molecules can efficiently form linear and cyclic dimers, *via* intermolecular hydrogen bonds, $\text{C}=\text{O} \cdots \text{H}-\text{C}$, between the oxygen of a given benzaldehyde molecule and the H atom within the formyl moiety of a neighbouring molecule.⁵⁵ At higher pressure, the neutral density of dimers of benzaldehyde in the collision chamber is enhanced. Consequently, the intact benzaldehyde anion may form upon DEA to a dimer, as suggested by the pressure dependence on the ion yield obtained at ~ 0 eV (reaction (1)). Furthermore, due to its electron affinity, benzaldehyde admits a VBS (π_1^*) that lies ~ 0.48 eV below the ground state of the neutral. The respective singly occupied orbital of the VBS is shown in Fig. 3a. The experimental detection of the intact benzaldehyde anion is thus associated with an effective stabilization of the VBS by excision of the other benzaldehyde unit.

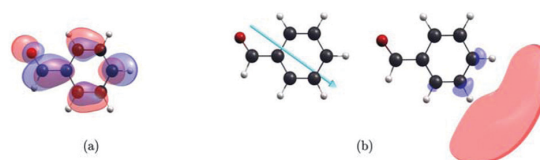
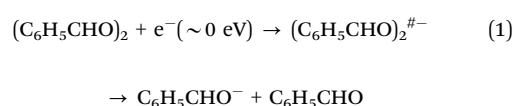


Fig. 3 (a) SOMO of the valence bound state (VBS) of the anion (A'' symmetry); (b) the permanent dipole moment vector of the neutral and the SOMO of the DBS (A' symmetry).

Under comparable pressures, the benzaldehyde anion was not observed in the study performed using the Notre Dame instrument. It is important to note that, when compared to the HEM instrument, the distinct characteristics of the ion source, *e.g.*, physical dimensions, a lower electron current close to 0 eV, the fact that the effusive beam is directed towards the hot filament, or the lower detection limit of the instrument, can influence the possibility of dimer formation and stability prior to electron interactions and thus the observation of the benzaldehyde anion. Nevertheless, besides the anionic monomer, we rule out that any further fragment anions are formed from DEA to dimers, since the neutral dimer density is very low. Furthermore, this is the only anion observed at ~ 0 eV, where the *s*-wave electron attachment cross section achieves its maximum.⁵⁶



3.3.2 Dehydrogenated benzaldehyde anion. The DEA reaction (2) represents the formation of the dehydrogenated benzaldehyde anion. In Fig. 4, the ion yield shows a weak contribution at 4.6 eV, which we assign to the π_4^* resonance with a mixed shape/core-excited character. The two higher-lying contributions centred at 7.6 and 9.2 eV are assigned as core-excited resonances. The estimated cross section for the formation of the dehydrogenated benzaldehyde anion is $9.85 \times 10^{-24} \text{ m}^2$. This small value indicates the low effectiveness of this fragmentation channel.

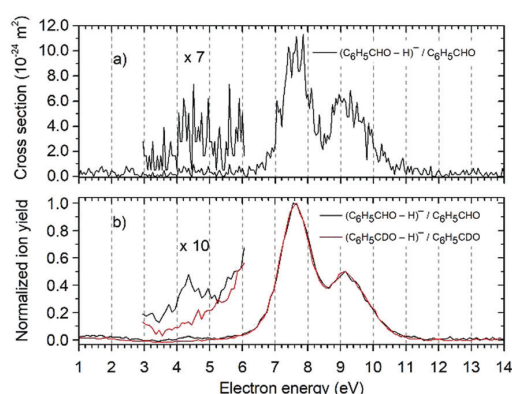
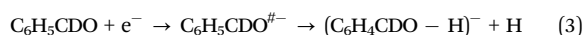
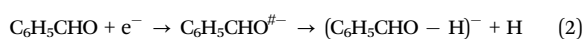


Fig. 4 Negative ion yields for dehydrogenated benzaldehyde. (a) Cross section for the formation of the dehydrogenated benzaldehyde anion from benzaldehyde measured with the HEM instrument. (b) Dehydrogenated parent anion formation from benzaldehyde (black) and d-benzaldehyde (red) measured with the Notre Dame instrument. The ion yield was normalized with respect to the maxima of the signal at 7.6 eV.

The dehydrogenation of biomolecules upon DEA has been described for several nucleobases.^{57–59} The experimental and theoretical studies carried out with thymine and uracil suggest that the dehydrogenation proceeds through a dipole-bound state (DBS)^{58,59} where an incoming electron is temporally captured. Therefore, we also investigated DBS as a possible doorway state for hydrogen loss by benzaldehyde. According to the DFT/B3LYP/aug-cc-pVDZ calculations, neutral benzaldehyde has a dipole moment around 3.6 D and is thus expected to hold a DBS.⁶⁰ Both the MP2 and CCSD(T) calculations performed with the diffuse basis sets seem to indicate very shallow DBSs, with binding energies of 1 meV and 2 meV, respectively. We note that the binding energies lie within the uncertainty of the calculations. In Fig. 3b, we show that the positive pole of the permanent dipole moment vector of the neutral is lying on the hydrogen atoms H(10) and H(11) as well as on the DBS single occupied molecular orbital (SOMO).

The calculated thermodynamic threshold values at the G4(MP)2 level of theory are listed in Table 3 for the loss of hydrogen from the distinct positions in benzaldehyde. The theoretical calculations show that hydrogen loss from benzaldehyde is always an endothermic reaction, even though the dehydrogenation from the phenyl moiety (C_5 position) appears to be energetically more favourable. Usually, the electron-induced dissociation mediated by a DBS gives rise to low-lying structures (< 3 eV) in the ion yield of the dehydrogenated parent anion measured from uracil, thymine,⁵⁸ adenine^{61,62} and their derivatives (OTf⁶³ and 2-chloroadenine⁶⁴), as well as 3-bromopyruvic acid.⁶⁵ In the case of benzaldehyde, however, such structures are not observable in the ion yield shown in Fig. 4. This suggests that the DBS does not play a role as a doorway state for the loss of hydrogen upon electron attachment, since the experimental onset for the observed dehydrogenated benzaldehyde anion occurs at ~ 3.6 eV, which is much higher than those for hydrogen loss in uracil, thymine, and their derivatives, due to the lack of strong polar N–H bonds. Furthermore, the experimental threshold is also too high in the energy scale of C–H vibrational excitation, which is typically ~ 0.4 eV for infra-red active modes. Thus, even if the vibrational Feshbach resonances (VFRs) are formed, we expect that it would be very unlikely that there would be a high enough tunnelling barrier to give rise to long-lived VFRs at such high energies.

The mentioned experimental onset lies above the calculated thermodynamic threshold for all hydrogen positions, which hinders the assignment of the dehydrogenation site to a particular position. Therefore, we investigated the dehydrogenation upon DEA to deuterated benzaldehyde- α -d₁ (d-benzaldehyde) to clarify the abstraction of hydrogen. Fig. 4b shows the formation of a dehydrogenated parent anion from DEA to d-benzaldehyde, as described by reaction (3). The intensity was normalized with respect to the maximum of the signals, at 7.6 eV. While the two structures at ~ 7.6 and ~ 9.2 eV are common for both compounds, the weak structure at 4.6 eV is suppressed completely in d-benzaldehyde. The suppression of this channel can be explained in terms of autodetachment as a result of the slower dissociation dynamics due to the presence of deuterium. The dehydrogenation from the

C₇ position is thus triggered by ~4.6 eV electrons. The selectivity of H loss from benzaldehyde upon electron capture is then reachable by proper tuning of the incident electron energy. The present observations support the rationale of DEA as a non-statistical dissociation process.⁶⁶

3.3.3 Stripping of the formyl group. The phenyl anion, C₆H₅⁻, together with the neutral counterpart formyl CHO[•] is formed through the cleavage of the C₆-C₇ bond upon DEA to benzaldehyde, as described by reaction (4). The anion yield exhibits a peak centred at about 4.7 eV, which arises from the π₄^{*} resonance. It is followed by a sharply rising feature at about 6.5 eV, having an asymmetric shape that suggests a shoulder at around 7.0 eV (Fig. 5a). These two contributions result from core-excited resonances within the energy range for electronic excitation. The phenyl anion stands as the most abundant anion with a maximum cross section of about 95.8 × 10⁻²⁴ m² at 6.5 eV.

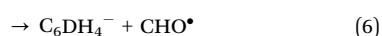
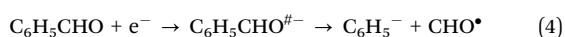


Fig. 5b shows the phenyl anion formation from DEA to d-benzaldehyde, as described by reaction (5), along with the ion yield detected at *m/z* 78. The formation of the phenyl anion either from benzaldehyde or d-benzaldehyde occurs at the same electron energies. The anion at *m/z* 78 may form *via* reaction (6) and is assigned to C₆H₄D⁻. It is formed not only through resonances centred at 4.7 and 6.5 eV, but also through higher-lying contributions at 7.5 and 8.5 eV. Its formation involves an internal rearrangement exchanging the deuterium atom from the formyl group with the hydrogen from the phenyl moiety, or due to a reaction involving ring opening. The four contributions may be attributed to these fragmentation mechanisms. The positions were determined by fitting the

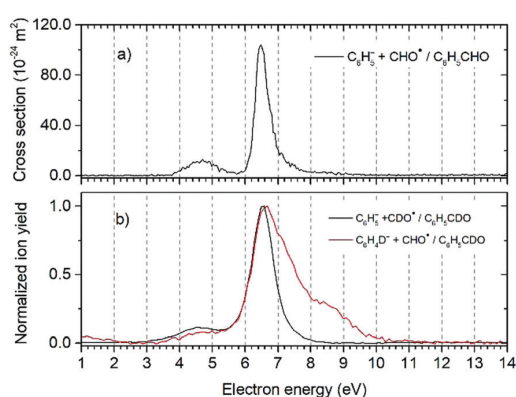
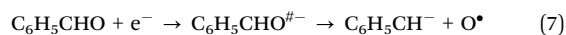


Fig. 5 (a) Cross section for the formation of the phenyl anion, *m/z* 77 C₆H₅⁻, from benzaldehyde measured with the HEM instrument. (b) (black) Formation of the phenyl anion from d-benzaldehyde, and formation of the deuterated phenyl anion, *m/z* 78 C₆H₄D⁻, from d-benzaldehyde (in red) measured with the Notre Dame instrument. The ion yield was normalized with respect to the maxima of both signals.

ion signal with Gaussian functions (please see Fig. S2 in the ESI†).

3.3.4 Cleavage of the C=O bond: loss of O[•]



The C₆H₅CH⁻ anion is formed by the cleavage of the C=O bond: loss of oxygen, as described by DEA reaction (7). This reaction yields the reactive oxygen radical O[•] as a neutral. C₆H₅CH⁻ is observed through a single core-excited resonance centred at 7.4 eV with a maximum cross section of about 3.84 × 10⁻²⁴ m² (Fig. 6). We report two thermodynamic thresholds that differ by the spin multiplicity of the oxygen atom, *i.e.* ~5.9 eV for triplet O(³P) and ~8.0 eV for doublet O(¹D). Hence, the experimental onset of 5.9 eV agrees with the neutral release of the triplet oxygen atom upon electron attachment to benzaldehyde. O⁻ is formed through a core-excited resonance with a cross section of about 23.5 × 10⁻²⁴ m² peaking at 8.9 eV (reaction (8)). The asymmetric shape of the feature seems to indicate two further contributions centred at about 7.8 and 10.5 eV (Fig. 6). The experimental onset of about 6.5 eV is in line with the predicted thermodynamic threshold of 6.02 eV for the formation of O⁻.

3.3.5 Concomitant cleavage of the C=O and C-H bonds: loss of OH[•]. The formation of C₆H₅C⁻ and the radical OH[•] occurs through a core-excited resonance with a cross section of about 31.1 × 10⁻²⁴ m² peaking at 6.9 eV, as represented by reaction (9). The shoulder may suggest a weaker contribution at 7.6 eV (Fig. 7). We predicted thermodynamic thresholds for loss of OH[•] by considering the position of the hydrogen atom involved in the reaction. The dehydrogenation from the formyl moiety (C₇ position) with further recombination with neutral oxygen arises as the thermodynamically most favourable reaction. The threshold for this reaction was estimated as 5.41 eV, which is below the experimental threshold of 6.2 eV. On the other hand, when the dehydrogenation occurs from the phenyl moiety, the respective

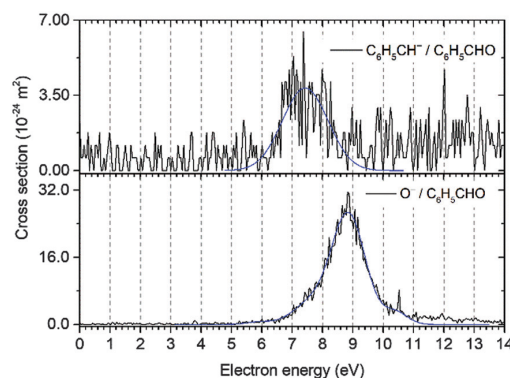
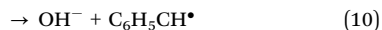


Fig. 6 Cross section for the formation of C₆H₅CH⁻ (top) and O⁻ (bottom) through DEA to benzaldehyde. The blue line corresponds to the convoluted Gaussian fit to guide the eye.

thermodynamic thresholds are higher and range from 5.41 eV up to 6.15 eV (Table S2 in the ESI†).



The hydroxide anion (OH^-) is formed *via* reaction (10) where $\text{C}_6\text{H}_5\text{C}^*$ is generated as a neutral radical. The ion yield shows a core-excited resonance with a maximum cross section of about $46.1 \times 10^{-24} \text{ m}^2$ occurring at 7.3 eV (Fig. 7). Furthermore, the slow decline of the signal may imply two further contributions at 8.3 and 9.7 eV. The thermodynamic threshold was also predicted by considering the various positions for dehydrogenation. The lowest threshold of 4.72 eV is obtained when the dehydrogenation occurs from the formyl group (C_7 position), similarly to the complementary anion, $\text{C}_6\text{H}_5\text{C}^*$. The experimental threshold of 6.4 eV lies above the predicted thermodynamic threshold in all cases. The further thresholds for this reaction range from 4.72 up to 5.98 eV and are presented in Table S2 in the ESI†. Moreover, the ion yields of the above-mentioned DEA reactions show structures occurring at about the same electron energy, which suggests that a common electronic state of the TNI undergoes a structural rearrangement to give OH^- or $\text{C}_6\text{H}_5\text{C}^-$ from benzaldehyde.

3.3.6 Loss of H_2O . $\text{H}_2\text{O}/(\text{OH} + \text{H})/(\text{O} + \text{H} + \text{H})$ is the neutral counterpart of the anion $\text{C}_6\text{H}_4\text{C}^-$. The ion yield for the formation of $\text{C}_6\text{H}_4\text{C}^-$ shows a single core-excited resonance with a maximum cross section of $15.8 \times 10^{-24} \text{ m}^2$ peaking at 6.8 eV, as described by reaction (11) and shown in Fig. 8a. This anion arises from rearrangement following DEA to benzaldehyde; therefore, we have investigated several possibilities for fragmentation and symmetry arguments were used to compact the threshold predictions. Table S2 in the ESI† summarizes the thermodynamic thresholds that lead to the formation of $\text{C}_6\text{H}_5\text{C}^-$ along with water elimination. The experimental onset of about 5.9 eV lies above the calculated thermodynamic thresholds in all cases, which does not allow a clear assignment. However, the lowest thermodynamic prediction of 2.92 eV for water elimination upon DEA to benzaldehyde suggests the recombination of hydrogen and oxygen from the

formyl moiety (C_7 position) together with an additional hydrogen from either C_5 or C_1 positions within the phenyl moiety.

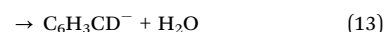
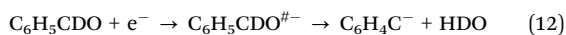
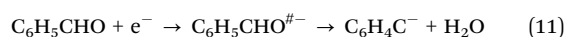


Fig. 8b shows the formation of m/z 88 $\text{C}_6\text{H}_4\text{C}^-$ with loss of semi-heavy water (HDO). The ion yield, represented in black, shows features occurring at 6.5 and 8.5 eV. The neutral HDO appears to be formed from dehydrogenation from a position within the phenyl moiety along with recombination with the deuterium and oxygen atoms from the formyl group (reaction (12)). The anion detected at m/z 89 is assigned as $\text{C}_6\text{H}_3\text{CD}^-$ formed with loss of neutral water upon DEA to d-benzaldehyde (reaction (13)). The ion yield of m/z 89 $\text{C}_6\text{H}_3\text{CD}^-$ also shows a contribution at ~ 6.5 eV. Its formation involves the reaction of a hydrogen atom removed from a position within the phenyl group, with deuterium from the formyl group. This anion may have a linear structure resulting from ring opening. However, from the current standpoint, in terms of experimental and theoretical approaches, we cannot describe the structure in detail.

3.3.7 Ring opening. Anionic pentadienylidene, HC_5H^- , is formed through a single core-excited resonance with a maximum cross section of about $3.35 \times 10^{-24} \text{ m}^2$ at 8.1 eV, as shown in Fig. 9. The possible thermodynamic threshold, E_{Thr} , for the DEA reactions that may lead to the formation of HC_5H^- can be predicted as follows:

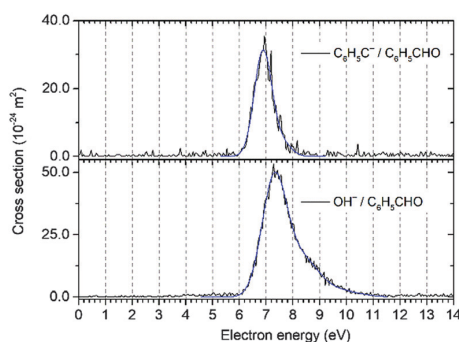
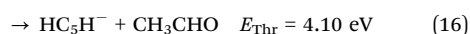
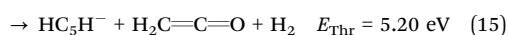
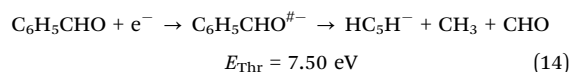


Fig. 7 Cross section for the formation of $\text{C}_6\text{H}_5\text{C}^-$ (top) and OH^- (bottom) through DEA to benzaldehyde. The blue line corresponds to the convoluted Gaussian fit to aid the eye.

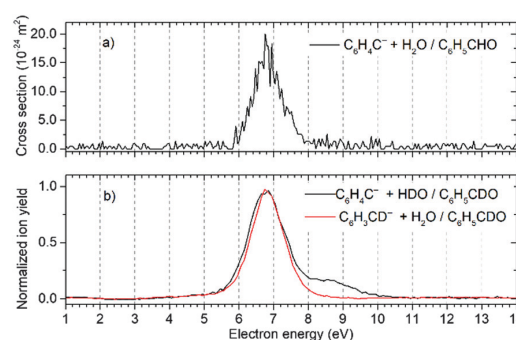


Fig. 8 (a) Cross section for the formation of $\text{C}_6\text{H}_4\text{C}^-$ with loss of neutral water, from benzaldehyde measured with the HEM instrument. (b) Formation of $\text{C}_6\text{H}_4\text{C}^-$ with loss of semi-heavy water (HDO) from d-benzaldehyde (in black) and formation of $\text{C}_6\text{H}_3\text{CD}^-$ with loss of neutral water from d-benzaldehyde (in red) measured with the Notre Dame instrument. The ion yield was normalized with respect to the maximum of the signal, respectively.

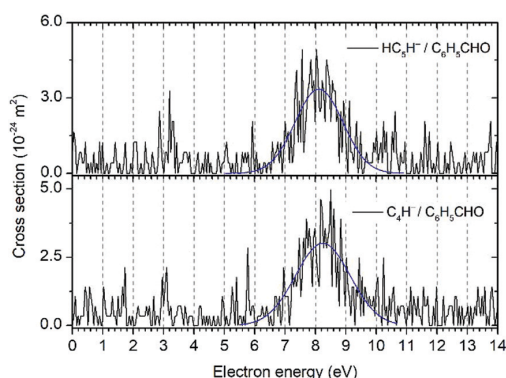
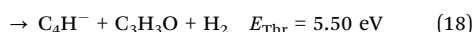
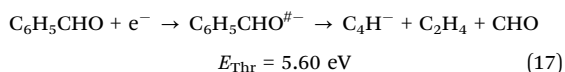


Fig. 9 Cross section for the formation of HC_5H^- (top) and C_4H^- (bottom) through DEA to benzaldehyde. The blue line corresponds to the convoluted Gaussian fit to aid the eye.

The DEA reaction (14) describes the formation of HC_5H^- alongside both methyl and formyl groups as neutrals. However, both neutral products may recombine during the DEA process generating neutral acetaldehyde. For this pattern, the thermodynamic threshold of 7.5 eV is thus reduced to 4.1 eV, as described by reaction (16). On the other hand, reaction (15) that considers a distinct set of neutral byproducts, such as ketene ($\text{H}_2\text{C}=\text{C}=\text{O}$) and molecular hydrogen, has a thermodynamic threshold of 5.2 eV. Consequently, at the onset of the measured ion yield (6.5 eV), only the dissociation pathways described by reactions (15) and (16) are energetically accessible. Further studies, namely stepwise electron spectroscopy,²⁴ would be required in order to experimentally characterize the neutrals formed alongside HC_5H^- upon DEA to benzaldehyde.

The anion C_4H^- is also formed through a single core-excited resonance with a maximum cross section of $3.01 \times 10^{-24} \text{ m}^2$ at 8.2 eV, as shown in Fig. 9. The formation of this anion may involve complex fragmentation within the molecule, similarly to that suggested for HC_5H^- ; and follows *via*:



The DEA reactions (17) and (18) that represent the formation of C_4H^- possess closely lying thermodynamic thresholds, although the considered neutral by-products are different. The reaction (17) considers the formation of ethene and formyl as neutrals, while reaction (18) considers $\text{C}_3\text{H}_3\text{O}$ and molecular hydrogen. The experimental onset for the formation of C_4H^- is about 6.4 eV, which is higher than both thermodynamic thresholds. Finally, it should be noted that the anions C_4H^- and HC_5H^- display a contribution centred at the same electron energy, which is evidence that both anionic species may share an electronic state of the TNI.

4. Conclusions

In the present study, we have comprehensively investigated electron attachment to benzaldehyde with three different

approaches, namely mass spectrometry, electron scattering and quantum chemistry calculations. This combination provides an in-depth analysis of benzaldehyde's fragmentation, since mass spectrometry allowed the identification of long-lived charged species, while the scattering calculations provide the short-lived states. Furthermore, the quantum chemistry study gives insight into the dissociation reactions and neutral products.

The formation of the intact benzaldehyde anion at energies close to 0 eV occurs *via* DEA to the dimer. This process is associated with an effective stabilization of the valence bound state π_1^* of the anion. The rich fragmentation pattern comprises nine fragment anions formed with modest DEA cross sections peaking at relatively higher energies. Further, the lower lying resonances found by theoretical calculations do not result in DEA due to thermodynamic barriers for the predicted fragmentation patterns. Therefore, these resonances can only decay by electron autodetachment.

Because the phenyl moiety in benzaldehyde resembles benzene, similar to the present study, three π^* shape resonances were identified for benzene using the SMCPP method.⁶⁷ The first two resonances have been pointed out as degenerate and occurring at ~ 1.4 eV, while the third resonance occurs at ~ 4.9 eV. The presence of the formyl moiety in benzaldehyde breaks the degeneracy of the two first π^* states, estimated here at 0.78 and 2.48 eV. The same characteristic was noted previously for other benzene-related compounds, such as phenol, by using the same method.⁶⁸

The study with d-benzaldehyde clarified that H loss from benzaldehyde is remarkably selective with respect to the incident electron energy, where the π_4^* shape resonance at 4.6 eV is suppressed upon deuteration of the formyl moiety, while the higher-lying core-excited resonances are preserved for both compounds.

In conclusion, the results obtained here deliver a comprehensive description of the low-energy electron-induced dissociation of benzaldehyde and may thus contribute to better knowledge of this compound for medical applications such as anti-cancer therapies. The electron-induced loss of O^* , OH^* and a collection of further radicals and anions seem to suggest that the anti-cancer effect of benzaldehyde may be enhanced in concomitant radiotherapy and chemotherapy, though further studies, *e.g.*, in aqueous solution or in water clusters, are required in order to model cellular conditions.

Conflicts of interest

There are no conflicts to declare.

Acknowledgements

JA and JPS acknowledge the Portuguese National Funding Agency FCT-MCTES through grants PD/BD/114447/2016 and PD/BD/142768/2018, respectively. FFS acknowledges the research grant PTDC/FIS-AQM/31215/2017. This work was also

supported by Radiation Biology and Biophysics Doctoral Training Programme (RaBBiT, PD/00193/2012); UIDB/04378/2020 (UCIBIO); and UIDB/00068/2020 (CEFITEC). SD acknowledges support from the FWF, Vienna (P30332). IC and SP received support from the US Department of Energy Office of Science and the Office of Basic Energy Sciences under Award Number DE-FC02-04ER15533. This is contribution number NDRL 5266 from the Notre Dame Radiation Laboratory. MTNV and LMC acknowledge support from the São Paulo Research Foundation (FAPESP, Grant No. 2015/17273-5 and 2017/24145-9). MTNV also acknowledges the Brazilian National Council for Scientific and Technological Development (CNPq), Grant No. 304571/2018-0. The calculations were partly performed with HPC resources from STI at the University of São Paulo.

Notes and references

- 1 E. Demir, S. Kocaoglu and B. Kaya, *Food Chem. Toxicol.*, 2010, **48**, 1239–1242.
- 2 W. M. Kluwe, C. A. Montgomery, H. D. Giles and J. D. Prejean, *Food Chem. Toxicol.*, 1983, **21**, 245–250.
- 3 V. J. Feron, H. P. Til, F. de Vrijer, R. A. Woutersen, F. R. Cassee and P. J. van Bladeren, *Mutat. Res. Toxicol.*, 1991, **259**, 363–385.
- 4 S. Takeuchi, M. Kochi, K. Sakaguchi, K. Nakagawa and T. Mizutani, *Agric. Biol. Chem.*, 1978, **42**, 1449–1451.
- 5 M. Kochi, S. Takeuchi, T. Mizutani, K. Mochizuki, Y. Matsumoto and Y. Saito, *Cancer Treat. Rep.*, 1980, **64**, 21–23.
- 6 K. Ariyoshi-Kishino, K. Hashimoto, O. Amano, J. Saitoh, M. Kochi and H. Sakagami, *Anticancer Res.*, 2010, **30**, 5069–5076.
- 7 H. Sakagami, K. Asano, K. Fukuchi, K. Gomi, H. Ota, K. Kazama, S. Tanuma and M. Kochi, *Anticancer Res.*, 1991, **11**, 1533–1538.
- 8 A. Ishida, N. Miwa and S. Mizuno, *Cancer Res.*, 1983, **43**, 4216–4220.
- 9 H. Ochiai, S. Niwayama and K. Masuyama, *J. Cancer Res. Clin. Oncol.*, 1986, **112**, 216–220.
- 10 T. Miyakawa, J.-L. Zundel and K. Sakaguchi, *Biochem. Biophys. Res. Commun.*, 1979, **87**, 1024–1030.
- 11 K. Sakaguchi, T. Miyakawa, S. Takeuchi, K. Nakagawa and E. Hayase, *Agric. Biol. Chem.*, 1979, **43**, 1775–1777.
- 12 J. M. Dornish, E. O. Pettersen, R. Oftebro and J.-E. Melvik, *Eur. J. Cancer Clin. Oncol.*, 1984, **20**, 1287–1293.
- 13 M. Watanuki and K. Sakaguchi, *Cancer Res.*, 1980, **40**, 2574–2579.
- 14 T. Tabatabaie and R. A. Floyd, *Toxicol. Appl. Pharmacol.*, 1996, **141**, 389–393.
- 15 Z. Ulker, L. Alpsy and A. Mihmanli, *Hum. Exp. Toxicol.*, 2013, **32**, 858–864.
- 16 C. von Sonntag, *Free-Radical-Induced DNA Damage and Its Repair – A Chemical Perspective*, Springer, 2006.
- 17 S. M. Pimblott and J. A. LaVerne, *J. Phys. Chem. A*, 1997, **101**, 5828–5838.
- 18 X. Ren, E. Wang, A. D. Skitnevskaya, A. B. Trofimov, K. Gokhberg and A. Dorn, *Nat. Phys.*, 2018, **14**, 1062–1066.
- 19 X. Ren, E. J. Al Maalouf, A. Dorn and S. Denifl, *Nat. Commun.*, 2016, **7**, 11093.
- 20 B. Boudaïffa, P. Cloutier, D. Hunting, M. A. Huels and L. Sanche, *Science*, 2000, **287**, 1658–1660.
- 21 E. Alizadeh and L. Sanche, *Chem. Rev.*, 2012, **112**, 5578–5602.
- 22 I. Baccarelli, I. Bald, F. A. Gianturco, E. Illenberger and J. Kopyra, *Phys. Rep.*, 2011, **508**, 1–44.
- 23 J. D. Gorfinkiel and S. Ptasinska, *J. Phys. B: At., Mol. Opt. Phys.*, 2017, **50**, 182001.
- 24 Z. Li, A. R. Milosavljević, I. Carmichael and S. Ptasinska, *Phys. Rev. Lett.*, 2017, **119**, 053402.
- 25 E. M. Zeman, *Clinical Radiation Oncology*, Elsevier, 4th edn, 2015.
- 26 R. Meißner, J. Kočišek, L. Feketeová, J. Fedor, M. Fárník, P. Limão-Vieira, E. Illenberger and S. Denifl, *Nat. Commun.*, 2019, **10**, 2388.
- 27 J. Rak, L. Chomicz, J. Wiczak, K. Westphal, M. Zdrochowicz, P. Wityk, M. Żyndul, S. Makurat and Ł. Golon, *J. Phys. Chem. B*, 2015, **119**, 8227–8238.
- 28 J. Rackwitz, J. Kopyra, I. Dąbkowska, K. Ebel, M. L. Ranković, A. R. Milosavljević and I. Bald, *Angew. Chem., Int. Ed.*, 2016, **55**, 10248–10252.
- 29 R. Schürmann, T. Tsering, K. Tanzer, S. Denifl, S. V. K. Kumar and I. Bald, *Angew. Chem., Int. Ed.*, 2017, **56**, 10952–10955.
- 30 A. Buonaugurio, X. Zhang, S. T. Stokes, Y. Wang, G. B. Ellison and K. H. Bowen, *Int. J. Mass Spectrom.*, 2015, **377**, 278–280.
- 31 J. Hacaloglu, A. Gokmen, S. Suzer, E. Illenberger and H. Baumgartel, *J. Phys. Chem.*, 1989, **93**, 7095–7098.
- 32 A. Modelli and P. D. Burrow, *J. Phys. Chem.*, 1984, **88**, 3550–3554.
- 33 G. R. De Maré, T. Lehman and M. Termonia, *J. Chem. Thermodyn.*, 1973, **5**, 829–832.
- 34 S. Denifl, S. Ptasinska, B. Sonnweber, P. Scheier, D. Liu, F. Hagelberg, J. Mack, L. T. Scott and T. D. Märk, *J. Chem. Phys.*, 2005, **123**, 104308.
- 35 D. Klar, M. W. Ruf and H. Hotop, *Int. J. Mass Spectrom.*, 2001, **205**, 93–110.
- 36 L. G. Christophorou and J. K. Olthoff, *Int. J. Mass Spectrom.*, 2001, **205**, 27–41.
- 37 M. M. Dawley and S. Ptasinska, *Int. J. Mass Spectrom.*, 2014, **365–366**, 143–151.
- 38 M. J. Frisch, G. W. Trucks, H. B. Schlegel, G. E. Scuseria, M. A. Robb, J. R. Cheeseman, G. Scalmani, V. Barone, G. A. Petersson, H. Nakatsuji, X. Li, M. Caricato, A. V. Marenich, J. Bloino, B. G. Janesko, R. Gomperts, B. Mennucci, H. P. Hratchian, J. V. Ortiz, A. F. Izmaylov, J. L. Sonnenberg, D. Williams-Young, F. Ding, F. Lipparini, F. Egidi, J. Goings, B. Peng, A. Petrone, T. Henderson, D. Ranasinghe, V. G. Zakrzewski, J. Gao, N. Rega, G. Zheng, W. Liang, M. Hada, M. Ehara, K. Toyota, R. Fukuda, J. Hasegawa, M. Ishida, T. Nakajima,

- Y. Honda, O. Kitao, H. Nakai, T. Vreven, K. Throssell, J. A. Montgomery Jr., J. E. Peralta, F. Ogliaro, M. J. Bearpark, J. J. Heyd, E. N. Brothers, K. N. Kudin, V. N. Staroverov, T. A. Keith, R. Kobayashi, J. Normand, K. Raghavachari, A. P. Rendell, J. C. Burant, S. S. Iyengar, J. Tomasi, M. Cossi, J. M. Millam, M. Klene, C. Adamo, R. Cammi, J. W. Ochterski, R. L. Martin, K. Morokuma, O. Farkas, J. B. Foresman and D. J. Fox, Gaussian Inc., Wallingford CT, 2009.
- 39 A. D. Becke, *J. Chem. Phys.*, 1993, **98**, 5648–5652.
- 40 T. H. Dunning, *J. Chem. Phys.*, 1989, **90**, 1007–1023.
- 41 A. M. Scheer and P. D. Burrow, *J. Phys. Chem. B*, 2006, **110**, 17751–17756.
- 42 K. Takatsuka and V. McKoy, *Phys. Rev. A: At., Mol., Opt. Phys.*, 1981, **24**, 2473–2480.
- 43 K. Takatsuka and V. McKoy, *Phys. Rev. A: At., Mol., Opt. Phys.*, 1984, **30**, 1734–1740.
- 44 G. B. Bachelet, D. R. Hamann and M. Schlüter, *Phys. Rev. B: Condens. Matter Mater. Phys.*, 1982, **26**, 4199–4228.
- 45 L. M. Cornetta, K. Coutinho, S. Canuto and M. T. do N. Varella, *Eur. Phys. J. D*, 2016, **70**, 176.
- 46 F. Kossoski, M. H. F. Bettega and M. T. do N. Varella, *J. Chem. Phys.*, 2014, **140**, 024317.
- 47 F. Kossoski and M. T. do N. Varella, *Phys. Chem. Chem. Phys.*, 2015, **17**, 17271–17278.
- 48 P. Skurski, M. Gutowski and J. Simons, *Int. J. Quantum Chem.*, 2000, **80**, 1024–1038.
- 49 L. A. Curtiss, P. C. Redfern and K. Raghavachari, *J. Chem. Phys.*, 2007, **127**, 124105.
- 50 I. Fdez. Galván, M. Vacher, A. Alavi, C. Angeli, F. Aquilante, J. Autschbach, J. J. Bao, S. I. Bokarev, N. A. Bogdanov, R. K. Carlson, L. F. Chibotaru, J. Creutzberg, N. Dattani, M. G. Delcey, S. S. Dong, A. Dreuw, L. Freitag, L. M. Frutos, L. Gagliardi, F. Gendron, A. Giussani, L. González, G. Grell, M. Guo, C. E. Hoyer, M. Johansson, S. Keller, S. Knecht, G. Kovačević, E. Källman, G. Li Manni, M. Lundberg, Y. Ma, S. Mai, J. P. Malhado, P. Å. Malmqvist, P. Marquetand, S. A. Mewes, J. Norell, M. Olivucci, M. Oppel, Q. M. Phung, K. Pierloot, F. Plasser, M. Reiher, A. M. Sand, I. Schapiro, P. Sharma, C. J. Stein, L. K. Sørensen, D. G. Truhlar, M. Ugandi, L. Ungur, A. Valentini, S. Vancoillie, V. Veryazov, O. Weser, T. A. Wesolowski, P.-O. Widmark, S. Wouters, A. Zech, J. P. Zobel and R. Lindh, *J. Chem. Theory Comput.*, 2019, **15**, 5925.
- 51 P.-O. Widmark, P.-Å. Malmqvist and B. O. Roos, *Theor. Chim. Acta*, 1990, **77**, 291–306.
- 52 R. Pou-Amérigo, M. Merchán and E. Ortí, *J. Chem. Phys.*, 1999, **110**, 9536–9546.
- 53 R. Pou-Amérigo, L. Serrano-Andrés, M. Merchán, E. Ortí and N. Forsberg, *J. Am. Chem. Soc.*, 2000, **122**, 6067–6077.
- 54 L. Klasinc, B. Kovac and H. Gusten, *Pure Appl. Chem.*, 1983, **55**, 289–298.
- 55 G. B. Tolstorozhev, I. V. Skornyakov, M. V. Bel'kov, O. I. Shadyro, S. D. Brinkevich and S. N. Samovich, *Opt. Spectrosc.*, 2012, **113**, 179–183.
- 56 I. Bald, J. Langer, P. Tegeder and O. Ingólfsson, *Int. J. Mass Spectrom.*, 2008, **277**, 4–25.
- 57 S. Ptasińska, S. Denifl, B. Mróz, M. Probst, V. Grill, E. Illenberger, P. Scheier and T. D. Märk, *J. Chem. Phys.*, 2005, **123**, 124302.
- 58 P. D. Burrow, G. A. Gallup, A. M. Scheer, S. Denifl, S. Ptasińska, T. Märk and P. Scheier, *J. Chem. Phys.*, 2006, **124**, 124310.
- 59 S. Denifl, S. Ptasińska, G. Hanel, B. Gstir, M. Probst, P. Scheier and T. D. Märk, *J. Chem. Phys.*, 2004, **120**, 6557–6565.
- 60 T. Sommerfeld, *J. Phys. Chem. A*, 2004, **108**, 9150–9154.
- 61 D. Huber, M. Beikircher, S. Denifl, F. Zappa, S. Matejcik, A. Bacher, V. Grill, T. D. Märk and P. Scheier, *J. Chem. Phys.*, 2006, **125**, 084304.
- 62 S. Gohlke, H. Abdoul-Carime and E. Illenberger, *Chem. Phys. Lett.*, 2003, **380**, 595–599.
- 63 J. Ameixa, E. Arthur-Baidoo, R. Meißner, S. Makurat, W. Kozak, K. Butowska, F. Ferreira da Silva, J. Rak and S. Denifl, *J. Chem. Phys.*, 2018, **149**, 164307.
- 64 F. Kossoski, J. Kopyra and M. T. do N. Varella, *Phys. Chem. Chem. Phys.*, 2015, **17**, 28958–28965.
- 65 F. Ferreira da Silva, M. T. do N. Varella, N. C. Jones, S. Vrønning Hoffmann, S. Denifl, I. Bald and J. Kopyra, *Chem. – Eur. J.*, 2019, **25**, 5498–5506.
- 66 S. Ptasińska, S. Denifl, V. Grill, T. D. Märk, E. Illenberger and P. Scheier, *Phys. Rev. Lett.*, 2005, **95**, 093201.
- 67 A. S. Barbosa and M. H. F. Bettega, *J. Chem. Phys.*, 2017, **146**, 154302.
- 68 E. M. De Oliveira, S. D. A. Sanchez, M. H. F. Bettega, A. P. P. Natalense, M. A. P. Lima and M. T. do N. Varella, *Phys. Rev. A: At., Mol., Opt. Phys.*, 2012, **86**, 20701, DOI: 10.1103/PhysRevA.86.020701.

Summary & Outlook

The goal of this PhD thesis was to extend the current knowledge on the radiosensitization mechanism within the physico-chemical stage of radiation damage by studying the formation of ions and neutral radicals in collision processes with radiosensitizer compounds. In order to fulfill such goal, three mass spectrometry setups were used to study electrospray ionization of ronidazole and electron interactions with biomolecules, especially dissociative electron attachment to 5-trifluoromethanesulfonyl-uracil (OTfU), and to benzaldehyde.

8.1 Collision-induced dissociation of biomolecules

Part I - collision-induced dissociation of biomolecules - described the study of fragmentation of protonated ronidazole in a high-energy CID experiment. Low-energy CID experiments, as well as density functional theory (DFT) quantum chemical calculations were also performed at the Université de Lyon. The main fragmentation channel observed in both low- and high-energy CID studies leads to m/z 140 ion formation involving the release of neutral counterpart $-\text{NH}_2\text{CO}_2\text{H}$ after intramolecular proton transfer. DFT calculations revealed that proton transfer can proceed from (i) the N_3 position of the imidazole ring, and (ii) the $-\text{CH}_3$ group. Electrospray ionization of a ronidazole solution prepared with deuterated solvents showed that, in high-energy CID, the proton transfer reaction proceeds via both channels with contributions of 81% and 19%, respectively, while in low-energy CID only

pathway (i) is observed. Moreover, the KER of the proton transfer reaction leading to m/z 140 ion formation was determined in the high-energy CID experiment, and it amounts to 10-23 meV, while the release of NO^\bullet radical has a KER value of 339 meV. This investigation contributes to the understanding of the nitroimidazole chemistry, in terms of fragment formation and determination of KER values for the most important dissociation channels. The obtained outcomes are very relevant for the development and design of nitroimidazolic compounds with potential radiosensitizer properties, as well as for the detection and screening methods of such drugs in water and food.

8.2 Electron interactions with biomolecules

Part II - electron interactions with biomolecules - discussed the potential radiosensitizers 5-trifluoromethanesulfonyl-uracil (OTfU), and benzaldehyde, in terms of negative ion formation and resonance energies.

OTfU is a modified pyrimidine, with a triflate group (-OTf, CF_3SO_3) at uracil (U) C_5 position. The OTf group has a large electron affinity of 6.22 eV, constituting thereby an efficient electron scavenger. Makurat *et al.*[176] studied DEA to 5-trifluoromethanesulfonyl-2'-deoxyuridine (OTfdU) in aqueous solution, a similar compound based on 2'-deoxyuridine (dU). The study showed that OTfdU is efficiently decomposed upon dissociative electron attachment (DEA) in an aqueous solution, in which dU formation, along with the formation of triflyl (Tf^-) anion by cleavage of the $\text{C}_5\text{-O}$ bond was observed as the dominating ion. In a bottom-up approach, OTfU a smaller compound without the sugar unit was investigated in the gas-phase, and quantum chemical studies provided the thermochemical thresholds for the observed DEA reactions. OTf^- formation alongside the reactive uracil-5-yl was identified as the most abundant ion formed, in line with the formation of Br^- observed in theoretical and experimental DEA studies with 5-bromouracil (5-BrU).[70, 76, 77] Providing this, the radiosensitization mechanism by OTfU (and OTfdU), a potential radiosensitizer of the class of the modified pyrimidines, regarding negative ion and radicals formation was explored in the gas-phase, as well as in aqueous solution. Furthermore, as far as the administration of a radiosensitizer is concerned, its toxicity shall be as low as

reasonably possible. In fact, OTfdU showed low cytotoxicity against human breast cancer cells in a concentration range of 0 up to 2×10^{-4} M.[176] In summary, both studies endorse the use of OTfU (and OTfdU) as radiosensitizer drugs in concomitant chemo- and radio-therapy treatments.

Benzaldehyde is a simple aromatic compound, which was investigated as a chemotherapeutic drug to fight cancer.[177, 178] The formation of temporary negative ions, as well as the dissociation into anionic fragment was studied with three approaches. Calculations on electron scattering from benzaldehyde indicate a π^* valence bound state of the anion of -0.48 eV, and three π^* shape resonances located at 0.78, 2.48 and 5.51 eV. In addition to mass spectrometry employed to identify the long-lived charged species produced upon electron attachment, quantum chemical calculations predicted the thermochemical threshold for the observed anions. The formation of the molecular anion of benzaldehyde occurred via DEA to a dimer at electron energies close to ~ 0 eV. This process is associated with stabilization of the π^* valence bound state of the anion. Further, nine fragment anions were detected with modest DEA cross sections at relatively higher electron energies. C_6H_5^- is the most abundant anion with a DEA cross section of 95.8×10^{-24} m² at 6.5 eV. The lower-lying shape resonances identified by electron scattering calculations only lead to spontaneous electron emission, since the DEA features were observed at higher electron energies.

Furthermore, it was demonstrated that DEA to d-benzaldehyde shows a selective H loss with respect to the electron energy, since the π_4^* shape resonance at 4.6 eV is suppressed in the deuterated form. In the studies with d-benzaldehyde, the formation of novel fragment anions containing deuterium was identified, namely C_6DH_4^- and $\text{C}_6\text{H}_3\text{CD}^-$, through higher-lying features not exhibited in standard benzaldehyde. The molecular structure of such anions is yet to be investigated. Finally, these findings present an in-depth analysis of the electron attachment process to benzaldehyde, although the potential use as a radiosensitizer requires further investigations, for instance in solution or in hydrated conditions in order to tentatively mimic the conditions within biological media.

8.3 Outlook

The investigations performed throughout this thesis represent an important progress in the search of a complete description of the radiosensitization mechanism. Several additional studies can be, however, carried out in order to increase the impact of the presented findings, not only in the field of radiosensitizers or radiation-induced damage to DNA. In this respect, the home-built ESI source may be modified to yield solvated ions bridging the gap between the gas- and the solution phases. The currently installed ion funnel is efficient in transferring ions from the atmospheric pressure to the high vacuum stages of the ESI source. However, the electrosprayed ions undergo several collisions with the background gas often leading to fragmentation of weakly-bounded water clusters, though biomolecular clusters, such as histidine clusters can be produced. Therefore, its replacement by a skimmer cone may avoid the fragmentation of water clusters. Nevertheless, the skimmer-based alternative may reduce the total ion current produced by the ESI-source, since supersonic expansion at the interface between the atmospheric and high vacuum stages of the ESI source may lead to a highly divergent ion beam, that cannot be efficiently focused on the entrance slit of the mass spectrometer. Hence, in principle, the formation of water clusters in the current ESI source may be explored in the future. Another possibility for future work is the study of electron-transfer dissociation, instead of collision-induced dissociation. The study of electron-induced fragmentation of ions can be realized by replacing the currently installed collision cell with a electron gun.

Regarding the electron attachment experiments, it may be relevant to explore more complex radiosensitizer compounds and compare their reactivity towards LEEs with the reactivity of already studied compounds, accordingly to the bottom-up approach. Studies involving water clusters or aqueous solutions are also highly relevant to understand the radiosensitization mechanism. Regarding the design and development of novel radiosensitizer compounds, further *in vitro* studies with healthy and tumour cells may be carried out, since DEA experiments are not able to assess the side-effects of the mentioned compounds to the cells, and, in turn to the patient. Moreover, the determination of absolute

DEA cross sections can be very useful in order to exactly quantify the efficiency of the formation of negative ions upon electron attachment. Though Wippi experimental setup can be employed to determine absolute DEA cross sections, several improvements can be implemented to reduce the uncertainty of the measured cross section values, as previously discussed in section 6.1.8.

References

- ¹World Health Organization, *Cancer*, (2020) <https://www.who.int/news-room/fact-sheets/detail/cancer>.
- ²D. H. Roukos, “Genome-wide association studies: how predictable is a person’s cancer risk?”, *Expert Review of Anticancer Therapy* **9**, 389–392 (2009).
- ³L. Pecorino, *Molecular biology of cancer: mechanisms, targets, and therapeutics*, Third edition (Oxford University Press, 2012).
- ⁴M. Joiner and A. van der Kogel, eds., *Basic clinical radiobiology*, Fifth edit (CRC Press / Taylor & Francis Group, Boca Raton, FL, 2018).
- ⁵G. P. Delaney and M. B. Barton, “Evidence-based Estimates of the Demand for Radiotherapy”, *Clinical Oncology* **27**, 70–76 (2015).
- ⁶Y. Zheng, D. J. Hunting, P. Ayotte, and L. Sanche, “Role of secondary low-energy electrons in the concomitant chemoradiation therapy of cancer”, *Physical Review Letters* **100**, 198101 (2008).
- ⁷P. J. Eifel, “Concurrent chemotherapy and radiation therapy as the standard of care for cervical cancer”, *Nature Clinical Practice Oncology* **3**, 248–255 (2006).
- ⁸E. M. Zeman, *Clinical Radiation Oncology*, edited by L. L. Gunderson and J. E. Tepper, Fourth Edition (Elsevier, Philadelphia, USA, 2015).
- ⁹E. Hall and A. Giaccia, *Radiobiology for the Radiologist*, Eighth edition (Lippincott Williams & Wilkins, Philadelphia, USA, 2019).

- ¹⁰J. E. Turner, *Atoms, Radiation and Radiation Protection*, Third edit (Wiley-VCH Verlag GmbH & Co. KGaA, Weinheim, Germany, 2007).
- ¹¹S. Lehnert, *Biomolecular action of ionizing radiation* (CRC Press/Taylor & Francis Group, Boca Raton, FL, 2007).
- ¹²E. Alizadeh and L. Sanche, “Precursors of solvated electrons in radiobiological physics and chemistry”, *Chemical Reviews* **112**, 5578–5602 (2012).
- ¹³S. Le Caër, “Water Radiolysis: Influence of Oxide Surfaces on H_2 Production under Ionizing Radiation”, *Water* **3**, 235–253 (2011).
- ¹⁴C. von Sonntag, *Free-Radical-Induced DNA Damage and Its Repair - A Chemical Perspective* (Springer, 2006).
- ¹⁵E. Alizadeh, T. M. Orlando, and L. Sanche, “Biomolecular Damage Induced by Ionizing Radiation: The Direct and Indirect Effects of Low-Energy Electrons on DNA”, *Annual Review of Physical Chemistry* **66**, 379–398 (2015).
- ¹⁶B. D. Michael and P. O’Neill, “A Sting in the Tail of Electron Tracks”, *Science* **287**, 1603 LP –1604 (2000).
- ¹⁷I. Bald, E. Illenberger, and J. Kopyra, “Damage of DNA by Low Energy Electrons (< 3 eV)”, *Journal of Physics: Conference Series* **373**, 12008 (2012).
- ¹⁸J. Nguyena, Y. Maa, T. Luoa, R. G. Bristowb, D. A. Jaffrayc, and Q. B. Lua, “Direct observation of ultrafast-electron-transfer reactions unravels high effectiveness of reductive DNA damage”, *Proceedings of the National Academy of Sciences of the United States of America* **108**, 11778–11783 (2011).
- ¹⁹International Commission on Radiation Units and Measurements, *Average Energy Required to Produce an Ion Pair (Report 31)*, tech. rep. (ICRU, Washington DC, 1979).
- ²⁰S. M. Pimblott and J. A. LaVerne, “Production of low-energy electrons by ionizing radiation”, *Radiation Physics and Chemistry* **76**, 1244–1247 (2007).
- ²¹A. Kumar, D. Becker, A. Adhikary, and M. D. Sevilla, “Reaction of electrons with DNA: Radiation damage to radiosensitization”, *International Journal of Molecular Sciences* **20**, 3998 (2019).

-
- ²²M. D. Sevilla, D. Becker, A. Kumar, and A. Adhikary, “Gamma and ion-beam irradiation of DNA: Free radical mechanisms, electron effects, and radiation chemical track structure”, *Radiation Physics and Chemistry* **128**, 60–74 (2016).
- ²³J. Ma, F. Wang, S. A. Denisov, A. Adhikary, and M. Mostafavi, “Reactivity of pre-hydrated electrons toward nucleobases and nucleotides in aqueous solution”, *Science Advances* **3**, e1701669 (2017).
- ²⁴A. Kumar, J. A. Walker, D. M. Bartels, and M. D. Sevilla, “A Simple ab Initio Model for the Hydrated Electron That Matches Experiment”, *The journal of physical chemistry. A* **119**, 9148–9159 (2015).
- ²⁵B. Boudaïffa, P. Cloutier, D. Hunting, M. A. Huels, and L. Sanche, “Resonant formation of DNA strand breaks by low-energy (3 to 20 eV) electrons.”, *Science* **287**, 1658–1660 (2000).
- ²⁶F. Martin, P. D. Burrow, Z. Cai, P. Cloutier, D. Hunting, and L. Sanche, “DNA strand breaks induced by 0-4 eV electrons: The role of shape resonances”, *Physical Review Letters* **93**, 068101 (2004).
- ²⁷M. A. Huels, B. Boudaïffa, P. Cloutier, D. Hunting, and L. Sanche, “Single, double, and multiple double strand breaks induced in DNA by 3-100 eV electrons”, *Journal of the American Chemical Society* **125**, 4467–4477 (2003).
- ²⁸A. O. Colson, B. Besler, and M. D. Sevilla, “Ab initio molecular orbital calculations on DNA base pair radical ions: Effect of base pairing on proton-transfer energies, electron affinities, and ionization potentials”, *Journal of Physical Chemistry* **96**, 9787–9794 (1992).
- ²⁹S. Denifl, P. Sulzer, D. Huber, F. Zappa, M. Probst, T. D. Märk, P. Scheier, N. Injan, J. Limtrakul, R. Abouaf, and H. DUNET, “Influence of functional groups on the site-selective dissociation of adenine upon low-energy electron attachment”, *Angewandte Chemie - International Edition* **46**, 5238–5241 (2007).
- ³⁰D. Huber, M. Beikircher, S. Denifl, F. Zappa, S. Matejcik, A. Bacher, V. Grill, T. D. Märk, and P. Scheier, “High resolution dissociative electron attachment to gas phase adenine”, *Journal of Chemical Physics* **125**, 084304 (2006).

- ³¹G. Hanel, B. Gstir, S. Denifl, P. Scheier, M. Probst, B. Farizon, M. Farizon, E. Illenberger, and T. D. Märk, “Electron Attachment to Uracil: Effective Destruction at Subexcitation Energies”, *Physical Review Letters* **90**, 4 (2003).
- ³²S. Denifl, S. Ptasińska, G. Hanel, B. Gstir, M. Probst, P. Scheier, and T. D. Märk, “Electron attachment to gas-phase uracil”, *Journal of Chemical Physics* **120**, 6557–6565 (2004).
- ³³S. Ptasińska, S. Denifl, B. Mróz, M. Probst, V. Grill, E. Illenberger, P. Scheier, and T. D. Märk, “Bond selective dissociative electron attachment to thymine.”, *The Journal of chemical physics* **123**, 124302 (2005).
- ³⁴S. Ptasińska, S. Denifl, V. Grill, T. D. Märk, P. Scheier, S. Gohlke, M. A. Huels, and E. Illenberger, “Bond-selective H- ion abstraction from thymine.”, *Angewandte Chemie (International ed. in English)* **44**, 1647–50 (2005).
- ³⁵S. Ptasińska, S. Denifl, B. Mróz, M. Probst, V. Grill, E. Illenberger, P. Scheier, and T. D. Märk, “Bond selective dissociative electron attachment to thymine”, *Journal of Chemical Physics* **123**, 124302 (2005).
- ³⁶S. Denifl, S. Ptasińska, M. Probst, J. Hrušák, P. Scheier, and T. D. Märk, “Electron attachment to the gas-phase DNA bases cytosine and thymine”, *Journal of Physical Chemistry A* **108**, 6562–6569 (2004).
- ³⁷S. Denifl, S. Ptasińska, M. Cingel, S. Matejcik, P. Scheier, and T. D. Märk, “Electron attachment to the DNA bases thymine and cytosine”, *Chemical Physics Letters* **377**, 74–80 (2003).
- ³⁸S. Ptasińska, S. Denifl, S. Gohlke, P. Scheier, E. Illenberger, and T. D. Märk, “Decomposition of thymidine by low-energy electrons: Implications for the molecular mechanisms of single-strand breaks in DNA”, *Angewandte Chemie - International Edition* **45**, 1893–1896 (2006).
- ³⁹S. Ptasińska, S. Denifl, P. Scheier, and T. D. Märk, “Inelastic electron interaction (attachment/ionization) with deoxyribose”, *Journal of Chemical Physics* **120**, 8505–8511 (2004).

-
- ⁴⁰I. Bald, J. Kopyra, and E. Illenberger, “Selective excision of C5 from D-ribose in the gas phase by low-energy electrons (0-1 eV): Implications for the mechanism of DNA damage”, *Angewandte Chemie - International Edition* **45**, 4851–4855 (2006).
- ⁴¹I. Baccarelli, F. A. Gianturco, A. Grandi, N. Sanna, R. R. Lucchese, I. Bald, J. Kopyra, and E. Illenberger, “Selective bond breaking in β -D-ribose by gas-phase electron attachment around 8 eV”, *Journal of the American Chemical Society* **129**, 6269–6277 (2007).
- ⁴²O. Ingólfsson, ed., *Low-Energy Electrons: Fundamentals and Applications*, First (Pan Stanford Publishing, Singapore, 2019).
- ⁴³J. Kopyra, C. Koenig-Lehmann, and E. Illenberger, “On the absolute value for the cross-section of dissociative electron attachment (DEA) to the DNA base thymine”, *International Journal of Mass Spectrometry* **281**, 89–91 (2009).
- ⁴⁴P. Wardman, “Chemical Radiosensitizers for Use in Radiotherapy”, *Clinical Oncology* **19**, 397–417 (2007).
- ⁴⁵L. Chomicz, M. Zdrowowicz, F. Kasprzykowski, J. Rak, A. Buonaugurio, Y. Wang, and K. H. Bowen, “How to find out whether a 5-substituted uracil could be a potential DNA radiosensitizer”, *Journal of Physical Chemistry Letters* **4**, 2853–2857 (2013).
- ⁴⁶M. D. Prados, C. Scott, H. Sandler, J. C. Buckner, T. Phillips, C. Schultz, R. Urtasun, R. Davis, P. Gutin, T. L. Cascino, H. S. Greenberg, and W. J. Curran, “A phase 3 randomized study of radiotherapy plus procarbazine, CCNU, and vincristine (PCV) with or without BUdR for the treatment of anaplastic astrocytoma: A preliminary report of RTOG 9404”, *International Journal of Radiation Oncology Biology Physics* **45**, 1109–1115 (1999).
- ⁴⁷H. Abdoul-Carime, M. A. Huels, E. Illenberger, and L. Sanche, “Sensitizing DNA to secondary electron damage: Resonant formation of oxidative radicals from 5-halouracils”, *Journal of the American Chemical Society* **123**, 5354–5355 (2001).
- ⁴⁸H. Abdoul-Carime, P.-C. Dugal, and L. Sanche, “Damage Induced by 1-30 eV Electrons on Thymine- and Bromouracil-Substituted Oligonucleotides”, *Radiation Research* **153**, 23–28 (2000).

- ⁴⁹H. Abdoul-Carime, M. A. Huels, E. Illenberger, and L. Sanche, “Formation of negative ions from gas phase halo-uracils by low-energy (0-18 eV) electron impact”, *International Journal of Mass Spectrometry* **228**, 703–716 (2003).
- ⁵⁰K. Ariyoshi-Kishino, K. Hashimoto, O. Amano, J. Saitoh, M. Kochi, and H. Sakagami, “Tumor-specific cytotoxicity and type of cell death induced by benzaldehyde.”, *Anti-cancer research* **30**, 5069–76 (2010).
- ⁵¹J. M. Henk, K. Bishop, and S. F. Shepherd, “Treatment of head and neck cancer with CHART and nimorazole: Phase II study”, *Radiotherapy and Oncology* **66**, 65–70 (2003).
- ⁵²J. M. Brown and W. R. Wilson, “Exploiting tumour hypoxia in cancer treatment”, *Nature Reviews Cancer* **4**, 437–447 (2004).
- ⁵³X. Han, M. Jin, K. Breuker, and F. W. McLafferty, “Extending top-down mass spectrometry to proteins with masses great than 200 kilodaltons”, *Science* **314**, 109–112 (2006).
- ⁵⁴B. T. Chait, “Mass spectrometry: Bottom-up or top-down?”, *Science* **314**, 65–66 (2006).
- ⁵⁵J. H. Gross, *Mass spectrometry: A textbook*, Second edition (Springer-Verlag Berlin Heidelberg, 2011), pp. 1–753.
- ⁵⁶J. B. Fenn, M. Mann, C. K. Meng, S. F. Wong, and C. M. Whitehouse, “Electrospray ionization for mass spectrometry of large biomolecules”, *Science* **246**, 64–71 (1989).
- ⁵⁷J. B. Fenn, M. Mann, C. K. Meng, S. F. Wong, and C. M. Whitehouse, “Electrospray ionization principles and practice”, *Mass Spectrometry Reviews* **9**, 37–70 (1990).
- ⁵⁸L. Feketeová, A. L. Albright, B. S. Sørensen, M. R. Horsman, J. White, R. A. O’Hair, and N. Bassler, “Formation of radical anions of radiosensitizers and related model compounds via electrospray ionization”, *International Journal of Mass Spectrometry* **365-366**, 56–63 (2014).
- ⁵⁹S. Pandeti, L. Feketeová, T. J. Reddy, H. Abdoul-Carime, B. Farizon, M. Farizon, and T. D. Märk, “Nitroimidazolic radiosensitizers investigated by electrospray ionization time-of-flight mass spectrometry and density functional theory”, *RSC Advances* **7**, 45211–45221 (2017).

- ⁶⁰J. M. Khreis, S. Pandeti, L. Feketeová, and S. Denifl, “High-energy collision-induced dissociation of radiosensitizer anions: Nimorazole and metronidazole”, *International Journal of Mass Spectrometry* **431**, 1–7 (2018).
- ⁶¹J. M. Khreis, J. Reitshammer, V. Vizcaino, K. Klawitter, L. Feketeová, and S. Denifl, “High-energy collision-induced dissociation of ions, $[His + H]^+$ and $[His - H]^-$, and histidine dimer $[His_2 + H]^+$ ”, *Rapid Communications in Mass Spectrometry* (2017).
- ⁶²S. Pandeti, J. Ameixa, J. M. Khreis, L. Feketeová, F. Chirot, T. J. Reddy, H. Abdoul-Carime, F. Ferreira da Silva, S. Denifl, R. A. O’hair, B. Farizon, M. Farizon, and T. D. Märk, “Decomposition of protonated ronidazole studied by low-energy and high-energy collision-induced dissociation and density functional theory”, *Journal of Chemical Physics* **151**, 164306 (2019).
- ⁶³A. Ribar, K. Fink, M. Probst, S. E. Huber, L. Feketeová, and S. Denifl, “Isomer Selectivity in Low-Energy Electron Attachment to Nitroimidazoles”, *Chemistry - A European Journal* **23**, 12892–12899 (2017).
- ⁶⁴K. Tanzer, L. Feketeová, B. Puschnigg, P. Scheier, E. Illenberger, and S. Denifl, “Reactions in Nitroimidazole and Methylnitroimidazole Triggered by Low-Energy (0-8 eV) Electrons”, *Journal of Physical Chemistry A* **119**, 6668–6675 (2015).
- ⁶⁵K. Tanzer, L. Feketeová, B. Puschnigg, P. Scheier, E. Illenberger, and S. Denifl, “Reactions in Nitroimidazole Triggered by Low-Energy (0 - 2 eV) Electrons: Methylation at N1-H Completely Blocks Reactivity”, *Angewandte Chemie - International Edition* **53**, 12240–12243 (2014).
- ⁶⁶F. Kossoski and M. T. d. N. Varella, “How does methylation suppress the electron-induced decomposition of 1-methyl-nitroimidazoles?”, *Journal of Chemical Physics* **147**, 164310 (2017).
- ⁶⁷R. Meißner, J. Kočišek, L. Feketeová, J. Fedor, M. Fárník, P. Limão-Vieira, E. Illenberger, and S. Denifl, “Low-energy electrons transform the nimorazole molecule into a radiosensitiser”, *Nature Communications* **10**, 2388 (2019).
- ⁶⁸“Electron scattering from molecules and molecular aggregates of biological relevance”, *Journal of Physics B: Atomic, Molecular and Optical Physics* **50**, 182001 (2017).

- ⁶⁹A. M. Scheer, K. Aflatooni, G. A. Gallup, and P. D. Burrow, “Bond Breaking and Temporary Anion States in Uracil and Halouracils: Implications for the DNA Bases”, *Physical Review Letters* **92**, 068102 (2004).
- ⁷⁰R. Abouaf and H. Dunet, “Structures in dissociative electron attachment cross-sections in thymine, uracil and halouracils”, *European Physical Journal D* **35**, 405–410 (2005).
- ⁷¹F. Kossoski, M. H. F. Bettega, and M. T. do N. Varella, “Shape resonance spectra of uracil, 5-fluorouracil, and 5-chlorouracil”, *Journal of Chemical Physics* **140**, 024317 (2014).
- ⁷²S. Denifl, S. Matejcik, B. Gstir, G. Hanel, M. Probst, P. Scheier, and T. D. Märk, “Electron attachment to 5-chloro uracil”, *Journal of Chemical Physics* **118**, 4107–4114 (2003).
- ⁷³S. Denifl, S. Matejcik, S. Ptasińska, B. Gstir, M. Probst, P. Scheier, E. Illenberger, and T. D. Mark, “Electron attachment to chlorouracil: A comparison between 6-ClU and 5-ClU”, *Journal of Chemical Physics* **120**, 704–709 (2004).
- ⁷⁴H. Abdoul-Carime, P. Limão-Vieira, S. Gohlke, I. Petrushko, N. J. Mason, and E. Illenberger, “Sensitization of 5-bromouridine by slow electrons”, *Chemical Physics Letters* **393**, 442–447 (2004).
- ⁷⁵H. Abdoul-Carime, M. A. Huels, F. Brüning, E. Illenberger, and L. Sanche, “Dissociative electron attachment to gas-phase 5-bromouracil”, *Journal of Chemical Physics* **113**, 2517–2521 (2000).
- ⁷⁶H. Abdoul-Carime, M. A. Huels, F. Brüning, E. Illenberger, and L. Sanche, “Dissociative electron attachment to gas-phase 5-bromouracil”, *Journal of Chemical Physics* **113**, 2517–2521 (2000).
- ⁷⁷F. Kossoski and M. T. do N. Varella, “Negative ion states of 5-bromouracil and 5-iodouracil”, *Physical Chemistry Chemical Physics* **17**, 17271–17278 (2015).
- ⁷⁸J. Rackwitz, J. Kopyra, I. Dąbkowska, K. Ebel, M. L. Ranković, A. R. Milosavljević, and I. Bald, “Sensitizing DNA Towards Low-Energy Electrons with 2-Fluoroadenine”, *Angewandte Chemie International Edition* **55**, 10248–10252 (2016).

- ⁷⁹R. Schürmann, T. Tsering, K. Tanzer, S. Deniff, S. V. Kumar, and I. Bald, “Resonant Formation of Strand Breaks in Sensitized Oligonucleotides Induced by Low-Energy Electrons (0.5-9 eV)”, *Angewandte Chemie - International Edition* **56**, 10952–10955 (2017).
- ⁸⁰F. Kossoski, J. Kopyra, and T. N. Do Varella, “Anion states and fragmentation of 2-chloroadenine upon low-energy electron collisions”, *Physical Chemistry Chemical Physics* **17**, 28958–28965 (2015).
- ⁸¹M. Dole, L. L. Mack, R. L. Hines, D. O. Chemistry, R. C. Mobley, L. D. Ferguson, and M. B. Alice, “Molecular beams of macroions”, *The Journal of Chemical Physics* **49**, 2240–2249 (1968).
- ⁸²M. Yamashita and J. B. Fenn, “Electrospray ion source. Another variation on the free-jet theme”, *Journal of Physical Chemistry* **88**, 4451–4459 (1984).
- ⁸³J. B. Fenn, “Electrospray wings for molecular elephants (Nobel lecture)”, *Angewandte Chemie - International Edition* **42**, 3871–3894 (2003).
- ⁸⁴P. Kebarle and U. H. Verkerk, “Electrospray: From ions in solution to ions in the gas phase, what we know now”, *Mass Spectrometry Reviews* **28**, 898–917 (2009).
- ⁸⁵N. B. Cech and C. G. Enke, “Practical implications of some recent studies in electrospray ionization fundamentals”, *Mass Spectrometry Reviews* **20**, 362–387 (2001).
- ⁸⁶G. J. Van Berkel and V. Kertesz, “Using the electrochemistry of the electrospray ion source”, *Analytical Chemistry* **79**, 5510–5520 (2007).
- ⁸⁷X. Wu, R. D. Oleschuk, and N. M. Cann, “Characterization of microstructured fibre emitters: In pursuit of improved nano electrospray ionization performance”, *Analyst* **137**, 4150–4161 (2012).
- ⁸⁸L. Rayleigh, “XX. On the equilibrium of liquid conducting masses charged with electricity”, *The London, Edinburgh, and Dublin Philosophical Magazine and Journal of Science* **14**, 184–186 (1882).
- ⁸⁹S. Nguyen and J. B. Fenn, “Gas-phase ions of solute species from charged droplets of solutions”, *Proceedings of the National Academy of Sciences of the United States of America* **104**, 1111–1117 (2007).

- ⁹⁰L. Konermann, E. Ahadi, A. D. Rodriguez, and S. Vahidi, “Unraveling the mechanism of electrospray ionization”, *Analytical Chemistry* **85**, 2–9 (2013).
- ⁹¹J. V. Iribarne and B. A. Thomson, “On the evaporation of small ions from charged droplets”, *The Journal of Chemical Physics* **64**, 2287–2294 (1976).
- ⁹²T. C. Rohner, N. Lion, and H. H. Girault, “Electrochemical and theoretical aspects of electrospray ionisation”, *Physical Chemistry Chemical Physics* **6**, 3056–3068 (2004).
- ⁹³E. Ahadi and L. Konermann, “Ejection of solvated ions from electrosprayed methanol/water nanodroplets studied by molecular dynamics simulations”, *Journal of the American Chemical Society* **133**, 9354–9363 (2011).
- ⁹⁴C. D. Daub and N. M. Cann, “How are completely desolvated ions produced in electrospray ionization: Insights from molecular dynamics simulations”, *Analytical Chemistry* **83**, 8372–8376 (2011).
- ⁹⁵M. Wilm, “Principles of electrospray ionization”, *Molecular & Cellular Proteomics* **10** (2011).
- ⁹⁶J. Fernandez De La Mora, “Electrospray ionization of large multiply charged species proceeds via Dole’s charged residue mechanism”, *Analytica Chimica Acta* **406**, 93–104 (2000).
- ⁹⁷A. T. Iavarone and E. R. Williams, “Mechanism of charging and supercharging molecules in electrospray ionization”, *Journal of the American Chemical Society* **125**, 2319–2327 (2003).
- ⁹⁸E. Ahadi and L. Konermann, “Modeling the behavior of coarse-grained polymer chains in charged water droplets: Implications for the mechanism of electrospray ionization”, *Journal of Physical Chemistry B* **116**, 104–112 (2012).
- ⁹⁹M. Z. Steinberg, K. Breuker, R. Elber, and R. B. Gerber, “The dynamics of water evaporation from partially solvated cytochrome c in the gas phase”, *Physical Chemistry Chemical Physics* **9**, 4690–4697 (2007).
- ¹⁰⁰A. Patriksson, E. Marklund, and D. Van Der Spoel, “Protein structures under electrospray conditions”, *Biochemistry* **46**, 933–945 (2007).

-
- ¹⁰¹H. Metwally, Q. Duez, and L. Konermann, “Chain ejection model for electrospray ionization of unfolded proteins: evidence from atomistic simulations and ion mobility spectrometry”, *Analytical Chemistry* **90**, 10069–10077 (2018).
- ¹⁰²L. Tiefenthaler, J. Ameixa, P. Martini, S. Albertini, L. Ballauf, M. Zankl, M. Goulart, F. Laimer, K. von Haeften, F. Zappa, and P. Scheier, “An intense source for cold cluster ions of a specific composition”, *Review of Scientific Instruments* **91**, 033315 (2020).
- ¹⁰³K. Levsen and H. Schwarz, “Collisional activation mass spectrometry - A new probe for determining the structure of ions in the gas phase”, *Angewandte Chemie International Edition in English* **15**, 509–519 (1976).
- ¹⁰⁴J. Bordas-Nagy and K. R. Jennings, “Collision-induced decomposition of ions”, *International Journal of Mass Spectrometry and Ion Processes* **100**, 105–131 (1990).
- ¹⁰⁵R. R. Julian, S. R. Mabbett, and M. F. Jarrold, “Ion funnels for the masses: experiments and simulations with a simplified ion funnel”, *Journal of the American Society for Mass Spectrometry* **16**, 1708–1712 (2005).
- ¹⁰⁶J. Liigand, A. Laaniste, and A. Kruve, “pH effects on electrospray ionization efficiency”, *Journal of the American Society for Mass Spectrometry* **28**, 461–469 (2017).
- ¹⁰⁷J. M. Khreis, “Development of an electrospray spray ionization source and collision studies with molecules of technical and medical relevance”, PhD Thesis (Universität Innsbruck, Austria, 2018).
- ¹⁰⁸T. Kelly, A. V. Tolmachev, J. S. Page, K. Tang, and R. D. Smith, “The ion funnel: Theory, implementations, and applications”, *Mass Spectrometry Reviews* **29**, 294–312 (2010).
- ¹⁰⁹S. A. Shaffer, K. Tang, G. A. Anderson, D. Prior, H. R. Udseth, and R. D. Smith, “A novel ion funnel for focusing ions at elevated pressure using electrospray ionization mass spectrometry”, *Rapid Communications in Mass Spectrometry* **11**, 1813–1817 (1997).
- ¹¹⁰S. A. Shaffer, D. C. Prior, G. A. Anderson, H. R. Udseth, and R. D. Smith, “An ion funnel interface for improved ion focusing and sensitivity using electrospray ionization mass spectrometry”, *Analytical Chemistry* **70**, 4111–4119 (1998).

- ¹¹¹S. A. Shaffer, A. Tolmachev, D. C. Prior, G. A. Anderson, H. R. Udseth, and R. D. Smith, “Characterization of an improved electrodynamic ion funnel interface for electrospray ionization mass spectrometry”, *Analytical Chemistry* **71**, 2957–2964 (1999).
- ¹¹²D. Gerlich, *Inhomogeneous RF Fields: A Versatile Tool for the Study of Processes with Slow Ions*, edited by C.-Y. Ng, M. Baer, I. Prigogine, and S. A. Rice (John Wiley & Sons, Inc., 1992).
- ¹¹³A. V. Tolmachev, T. Kim, H. R. Udseth, R. D. Smith, T. H. Bailey, and J. H. Futrell, “Simulation-based optimization of the electrodynamic ion funnel for high sensitivity electrospray ionization mass spectrometry”, *International Journal of Mass Spectrometry* **203**, 31–47 (2000).
- ¹¹⁴R. Wester, “Radiofrequency multipole traps: Tools for spectroscopy and dynamics of cold molecular ions”, *Journal of Physics B: Atomic, Molecular and Optical Physics* **42** (2009).
- ¹¹⁵D. J. Douglas, A. J. Frank, and D. Mao, “Linear ion traps in mass spectrometry”, *Mass Spectrometry Reviews* **24**, 1–29 (2005).
- ¹¹⁶J. Reitshammer, “Electrospray Ionisation Studies with Histidine”, MSc. Thesis (Universität Innsbruck, Austria, 2017).
- ¹¹⁷H. G. Dehmelt, “Radiofrequency Spectroscopy of Stored Ions I: Storage”, *Advances in Atomic, Molecular and Optical Physics* **3**, 53–72 (1968).
- ¹¹⁸E. Teloy and D. Gerlich, “Integral cross sections for ion-molecule reactions. I. The guided beam technique”, *Chemical Physics* **4**, 417–427 (1974).
- ¹¹⁹D. J. Douglas and J. B. French, “Collisional focusing effects in radio frequency quadrupoles”, *Journal of the American Society for Mass Spectrometry* **3**, 398–408 (1992).
- ¹²⁰E Harting and F. Read, *Electrostatic lenses* (Elsevier Scientific Pub. Co, Amsterdam, 1976).
- ¹²¹O. Klemperer and M. E. Barnett, *Electron Optics*, Third edition (Cambridge University Press, Cambridge, 1971).
- ¹²²D. W. Heddle, *Electrostatic lens systems, 2nd edition*, Second edition (CRC Press, 2000).

- ¹²³O. Sise, M. Ulu, and M. Dogan, “Multi-element cylindrical electrostatic lens systems for focusing and controlling charged particles”, *Nuclear Instruments and Methods in Physics Research, Section A: Accelerators, Spectrometers, Detectors and Associated Equipment* **554**, 114–131 (2005).
- ¹²⁴E. Alizadeh, F. Ferreira da Silva, F. Zappa, A. Mauracher, M. Probst, S. Deniff, A. Bacher, T. D. Märk, P. Limão-Vieira, and P. Scheier, “Dissociative electron attachment to nitromethane”, *International Journal of Mass Spectrometry* **271**, 15–21 (2008).
- ¹²⁵L. G. Christophorou, *Electron-Molecule interactions and their application*, Vol. 1 (Elsevier, 1984).
- ¹²⁶E. Illenberger and J. Momigny, *Gaseous Molecular Ions: An Introduction to Elementary Processes Induced by Ionization* (Springer US, New York, 1992).
- ¹²⁷A. D. McNaught and A. Wilkinson, eds., *IUPAC: Compendium of Chemical Terminology*, 2nd ed. (Blackwell Science, 1997).
- ¹²⁸I. W. Griffiths, E. S. Mukhtar, R. E. March, F. M. Harris, and J. H. Beynon, “Comparison of photo-excitation of ions and collisional excitation using gases”, *International Journal of Mass Spectrometry and Ion Physics* **39**, 125–132 (1981).
- ¹²⁹VG-Analytical, *VG ZAB Manual*, edited by VG Analytical LTD, 1988.
- ¹³⁰Dr. Sjuts Optotechnik GmbH, *Channel electron multipliers and complete measurement systems*, (2020) http://www.sjuts.com/index_english.html.
- ¹³¹M. Neustetter, “Low energy electron interactions with small molecular clusters”, PhD Thesis (Universität Innsbruck, Austria, 2016).
- ¹³²J. N. Bull, J. W. Lee, and C. Vallance, “Absolute electron total ionization cross-sections: Molecular analogues of DNA and RNA nucleobase and sugar constituents”, *Physical Chemistry Chemical Physics* **16**, 10743–10752 (2014).
- ¹³³P.J. Linstrom and W.G. Mallard, eds., *NIST Chemistry WebBook, NIST Standard Reference Database Number 69* (National Institute of Standards and Technology, Gaithersburg MD, 2020), p. 20899.

- ¹³⁴I. Bald, J. Langer, P. Tegeder, and O. Ingólfsson, “From isolated molecules through clusters and condensates to the building blocks of life”, *International Journal of Mass Spectrometry* **277**, 4–25 (2008).
- ¹³⁵L. G. Christophorou, “The lifetimes of metastable negative ions”, *Advances in Electronics and Electron Physics* **46**, 55–129 (1978).
- ¹³⁶R. A. Popple, C. D. Finch, K. A. Smith, and F. B. Dunning, “Dissociative electron attachment to CCL_4 : lifetime of the CCL_4^-* intermediate”, *Journal of Chemical Physics* **104**, 8485–8489 (1996).
- ¹³⁷R. N. Compton, L. G. Christophorou, G. S. Hurst, and P. W. Reinhardt, “Nondissociative electron capture in complex molecules and negative-ion lifetimes”, *The Journal of Chemical Physics* **45**, 4634–4639 (1966).
- ¹³⁸E. Illenberger, “Electron-attachment reactions in molecular clusters”, *Chemical Reviews* **92**, 1589–1609 (1992).
- ¹³⁹O. Ingólfsson, F. Weik, and E. Illenberger, “Formation and decay of negative ion resonances in gaseous and condensed molecules”, *International Reviews in Physical Chemistry* **15**, 133–151 (1996).
- ¹⁴⁰R. M. Thorman, T. P. Ragesh Kumar, D. Howard Fairbrother, and O. Ingólfsson, “The role of low-energy electrons in focused electron beam induced deposition: Four case studies of representative precursors”, *Beilstein Journal of Nanotechnology* **6**, 1904–1926 (2015).
- ¹⁴¹F. Ferreira da Silva, “Electron driven reactions in complexes embedded in superfluid helium droplets”, PhD Thesis (Universität Innsbruck, Austria, 2009).
- ¹⁴²Z. Li, M. Ryszka, M. M. Dawley, I. Carmichael, K. B. Bravaya, and S. Ptasińska, “Dipole-supported electronic resonances mediate electron-induced amide bond cleavage”, *Physical Review Letters* **122**, 073002 (2019).
- ¹⁴³T. Sommerfeld, “Dipole-bound states as doorways in (dissociative) electron attachment”, *Journal of Physics: Conference Series* **4**, 245–250 (2005).

-
- ¹⁴⁴S. Ptasińska, S. Denifl, P. Scheier, E. Illenberger, and T. D. Märk, “Bond- and site-selective loss of H atoms from nucleobases by very-low-energy electrons (< 3 eV)”, *Angewandte Chemie - International Edition* **44**, 6941–6943 (2005).
- ¹⁴⁵P. D. Burrow, G. A. Gallup, A. M. Scheer, S. Denifl, S. Ptasińska, T. Märk, and P. Scheier, “Vibrational Feshbach resonances in uracil and thymine”, *Journal of Chemical Physics* **124**, 124310 (2006).
- ¹⁴⁶T. Sommerfeld, “Intramolecular electron transfer from dipole-bound to valence orbitals: Uracil and 5-chlorouracil”, *Journal of Physical Chemistry A* **108**, 9150–9154 (2004).
- ¹⁴⁷J. Ameixa, E. Arthur-Baidoo, R. Meißner, S. Makurat, W. Kozak, K. Butowska, F. Ferreira da Silva, J. Rak, and S. Denifl, “Low-energy electron-induced decomposition of 5-trifluoromethanesulfonyl-uracil: A potential radiosensitizer”, *The Journal of Chemical Physics* **149**, 164307 (2018).
- ¹⁴⁸M. S. Child, “The condon reflection principle in collision dynamics”, *Molecular Physics* **35**, 759–770 (1978).
- ¹⁴⁹E. P. Wigner, “On the behavior of cross sections near thresholds”, *Physical Review* **73**, 1002–1009 (1948).
- ¹⁵⁰S. Barsotti, M. W. Ruf, and H. Hotop, “Clear experimental evidence for p-wave attachment-threshold Behavior in electron attachment to chlorine molecules”, *Physical Review Letters* **89**, 083201 (2002).
- ¹⁵¹M. Braun, M.-W. Ruf, I. I. Fabrikant, and H. Hotop, “Observation of p-wave threshold behavior in electron attachment to F_2 Molecules”, *Phys. Rev. Lett.* **99**, 253202 (2007).
- ¹⁵²E. Vogt and G. H. Wannier, “Scattering of ions by polarization forces”, *Physical Review* **95**, 1190–1198 (1954).
- ¹⁵³I. I. Fabrikant, “Long-range effects in electron scattering by polar molecules”, *Journal of Physics B: Atomic, Molecular and Optical Physics* **49**, 222005 (2016).
- ¹⁵⁴I. I. Fabrikant and H. Hotop, “Low-energy behavior of exothermic dissociative electron attachment”, *Physical Review A - Atomic, Molecular, and Optical Physics* **63**, 1–10 (2001).

- ¹⁵⁵H. Hotop, M. W. Ruf, M. Allan, and I. I. Fabrikant, “Resonance and threshold phenomena in low-energy electron collisions with molecules and clusters”, *Advances in Atomic, Molecular and Optical Physics* **49**, 85–216 (2003).
- ¹⁵⁶G. Denifl, “Electron attachment and ionization of molecules and clusters of atmospheric relevance”, PhD Thesis (Universität Innsbruck, Austria, 1998).
- ¹⁵⁷D. Muigg, “Inelastic interaction of monochromatized electrons with molecules and clusters of atmospheric relevance”, PhD Thesis (Universität Innsbruck, Austria, 1998).
- ¹⁵⁸P. Sulzer, “Dissociative electron attachment to explosives and biomolecules”, PhD Thesis (Universität Innsbruck, Austria, 2008).
- ¹⁵⁹N. W. McLachlan, *Theory and Application of Mathieu Functions* (Oxford University Press, New York, 1951).
- ¹⁶⁰G. Hanel, T. Fiegele, A. Stamatovic, and T. D. Märk, “Dissociative electron attachment to N_2O clusters: Attachment spectra for $(N_2O)_nO^-$ anions (n=0-7) from about 0 up to 25 eV”, *International Journal of Mass Spectrometry* **205**, 65–75 (2001).
- ¹⁶¹G. Denifl, D. Muigg, A. Stamatovic, and T. D. Märk, “Dissociative electron attachment to CO and NO: The O^- production threshold revisited”, *Chemical Physics Letters* **288**, 105–110 (1998).
- ¹⁶²D. Klar, M. W. Ruf, and H. Hotop, “Dissociative electron attachment to CCl_4 molecules at low electron energies with meV resolution”, *International Journal of Mass Spectrometry* **205**, 93–110 (2001).
- ¹⁶³L. G. Christophorou and J. K. Olthoff, “Electron attachment cross sections and negative ion states of SF_6 ”, *International Journal of Mass Spectrometry* **205**, 27–41 (2001).
- ¹⁶⁴J. H. Moore, C. C. Davis, M. A. Coplan, and S. C. Greer, *Building scientific apparatus - A Practical Guide to Design and Construction*, Fourth edition (Cambridge University Press, 2009).
- ¹⁶⁵S. Engmann, M. Stano, P. Papp, M. J. Brunger, S. Matejčík, and O. Ingólfsson, “Absolute cross sections for dissociative electron attachment and dissociative ionization of cobalt tricarbonyl nitrosyl in the energy range from 0 eV to 140 eV”, *Journal of Chemical Physics* **138**, 044305 (2013).

-
- ¹⁶⁶M. M. Dawley and S. Ptasińska, “Dissociative electron attachment to gas-phase N-methylformamide”, *International Journal of Mass Spectrometry* **365-366**, 143–151 (2014).
- ¹⁶⁷Z. L. Kastner, “Dissociative electron attachment to gas phase biomolecules”, PhD Thesis (Notre Dame University, USA, 2017).
- ¹⁶⁸L. G. Christophorou and J. K. Olthoff, “Electron interactions with SF_6 ”, *Journal of Physical and Chemical Reference Data* **29**, 267–330 (2000).
- ¹⁶⁹I. I. Fabrikant, H. Hotop, and M. Allan, “Elastic scattering, vibrational excitation, and attachment in low-energy electron- SF_6 scattering: Experiment and effective range theory”, *Physical Review A - Atomic, Molecular, and Optical Physics* **71** (2005).
- ¹⁷⁰M. Fenzlaff, R. Gerhard, and E. Illenberger, “Associative and dissociative electron attachment by SF_6 and SF_5Cl ”, *The Journal of Chemical Physics* **88**, 149–155 (1988).
- ¹⁷¹T. P. Ragesh Kumar, B. Brynjarsson, B. Ómarsson, M. Hoshino, H. Tanaka, P. Limão-Vieira, D. B. Jones, M. J. Brunger, and O. Ingólfsson, “Negative ion formation through dissociative electron attachment to the group IV tetrachlorides: Carbon tetrachloride, silicon tetrachloride and germanium tetrachloride”, *International Journal of Mass Spectrometry* **426**, 12–28 (2018).
- ¹⁷²E. M. Davidson, *Process of extinguishing fires*, 1910.
- ¹⁷³S. C. Chu and P. D. Burrow, “Dissociative attachment of electrons in the chloromethanes”, *Chemical Physics Letters* **172**, 17–22 (1990).
- ¹⁷⁴K. Aflatooni and P. D. Burrow, “Total cross sections for dissociative electron attachment in dichloroalkanes and selected polychloroalkanes: the correlation with vertical attachment energies”, *Journal of Chemical Physics* **113**, 1455–1464 (2000).
- ¹⁷⁵G. Upton and I. Cook, *A dictionary of statistics*, Oxford Paperback Reference (OUP Oxford, 2008).
- ¹⁷⁶S. Makurat, M. Zdrowowicz, L. Chomicz-Mańka, W. Kozak, I. E. Serdiuk, P. Wityk, A. Kawecka, M. Sosnowska, and J. Rak, “5-Selenocyanato and 5-trifluoromethanesulfonyl derivatives of 2'-deoxyuridine: Synthesis, radiation and computational chemistry as well as cytotoxicity”, *RSC Advances* **8**, 21378–21388 (2018).

References

- ¹⁷⁷S. Takeuchi, M. Kochi, K. Sakaguchi, K. Nakagawa, and T. Mizutani, “Benzaldehyde as a carcinostatic principle in figs”, *Agricultural and Biological Chemistry* **42**, 1449–1451 (1978).
- ¹⁷⁸M Kochi, S Takeuchi, T Mizutani, K Mochizuki, Y Matsumoto, and Y Saito, “Antitumor activity of benzaldehyde”, *Cancer Treatment Reports* **64**, 21–23 (1980).

List of publications and conference abstracts

A.A List of publications

1. E. Arthur-Baidoo, J. Ameixa, P. Ziegler, F. Ferreira da Silva, M. Ončák, and S. Denifl, *Reactions in tirapazamine induced by the attachment of low-energy electrons: Dissociation versus roaming of OH*, *Angew. Chemie Int. Ed.*, DOI: 10.1002/anie.202006675 (2020).
2. J. Ameixa, R. Meißner, E. Arthur-Baidoo, C. Lochmann, M. Ončák, M. K. Beyer, F. Ferreira da Silva, and S. Denifl, *Electron-induced decomposition of the coenzyme Q₀*, *J. Phys. Conf. Ser.* 1412, 152060 (2020).
3. J. Ameixa, E. Arthur-Baidoo, J. Pereira-Da-Silva, M. Ryszka, I. Carmichael, L. M. Cornetta, M. T. Do N. Varella, F. Ferreira Da Silva, S. Ptasińska, and S. Denifl, *Formation of resonances and anionic fragments upon electron attachment to benzaldehyde*, *Phys. Chem. Chem. Phys.* 22, 8171 (2020).
4. L. Tiefenthaler, J. Ameixa, P. Martini, S. Albertini, L. Ballauf, M. Zankl, M. Goulart, F. Laimer, K. von Haeften, F. Zappa, and P. Scheier, *An intense source for cold cluster ions of a specific composition*, *Rev. Sci. Instrum.* 91, 033315 (2020).
5. S. Pandeti, J. Ameixa, J. M. Khreis, L. Feketeová, F. Chirot, T. J. Reddy, H. Abdoul-Carime, F. Ferreira da Silva, S. Denif, R. A. J. O’Hair, B. Farizon, M. Farizon and T. D. Märk, *Decomposition of protonated ronidazole studied by low-energy and high-*

- energy collision-induced dissociation and density functional theory*, J. Chem. Phys., 2019, 151, 164306.
6. J. Ameixa, E. Arthur-Baidoo, R. Meißner, S. Makurat, W. Kozak, K. Butowska, F. Ferreira da Silva, J. Rak and S. Denifl, *Low-energy electron-induced decomposition of 5-trifluoromethanesulfonyl-uracil: A potential radiosensitizer*, J. Chem. Phys., 2018, 149, 164307.
 7. J. M. Khreis, J. Ameixa, F. Ferreira da Silva and S. Denifl, *Interactions of low-energy electrons with the FEBID precursor chromium hexacarbonyl ($Cr(CO)_6$)*, Beilstein J. Nanotechnol., 2017, 8, 2583–2590.
 8. F. Ferreira da Silva, J. Ameixa, J. Khreis and S. Denifl, *Electron attachment studies with 2,3-dimethoxy-5-methyl-1,4-benzoquinone* in Journal of Physics: Conference Series, IOP Publishing, 2017, vol. 875, p. 062034.
 9. J. Khreis, J. Ameixa, M. Neustetter, J. Reitshammer, F. Ferreira da Silva and S. Denifl, *Low-energy electron interactions with chromium hexacarbonyl $Cr(CO)_6$* in Journal of Physics: Conference Series, IOP Publishing, 2017, vol. 875, p. 062003.
 10. E. Lange, K. Krupa, J. Ameixa, A. S. Barbosa, D. F. Pastega, P. Limão-Vieira, M. H. F. Bettega, F. Blanco, G. García and F. Ferreira da Silva, *Elastic Differential Cross Sections for Electron Scattering with Dichloromethane* in Journal of Physics: Conference Series, IOP Publishing, 2017, vol. 875, p. 062036.
 11. A. S. Barbosa, M. T. do N. Varella, S. D. A. Sanchez, J. Ameixa, F. Blanco, G. García, P. Limão-Vieira, F. Ferreira da Silva and M. H. F. Bettega, *Theoretical and experimental study on electron interactions with chlorobenzene: Shape resonances and differential cross sections*, J. Chem. Phys., 2016, 145, 084311.
 12. D. F. Pastega, E. Lange, J. Ameixa, A. S. Barbosa, F. Blanco, G. García, M. H. F. Bettega, P. Limão-Vieira and F. Ferreira da Silva, *Combined experimental and theoretical study on the differential elastic scattering cross sections for acetone by electron impact energy of 7.0-50 eV*, Phys. Rev. A, 2016, 93, 032708.

A.B Conference abstracts

A.B.1 Posters

1. *Stability of damaged coronene*

J. Ameixa, M. Gatchell, M. Ji, S. Denifl, H. Cederquist, H.T. Schmidt and H. Zettergren

MD-GAS– First annual meeting of the COST Action CA18212, February 18th to 21st, 2019, Caen, France

2. *Low-energy electron interactions with benzaldehyde*

J. Ameixa, E. Arthur-Baidoo, J. Pereira-da-Silva, M. Ryszka, F. Ferreira da Silva, I. Carmichael, S. Ptasinska and S. Denifl

I NOVA Biophysica, September 4th to 6th, 2019, Lisbon, Portugal

3. *Electron-induced decomposition of the coenzyme Q0*

J. Ameixa, R. Meißner, E. Arthur-Baidoo, C. Lochmann, M. Ončák, M .K. Beyer, F. Ferreira da Silva, S. Denifl

XXXIst ICPEAC, July 23rd to 30th, 2019, Deauville, France

4. *Dissociative electron attachment to 5-trifluoromethanesulfonyl-uracil*

E. Arthur-Baidoo, J. Ameixa, R. Meißner, S. Makurat, W. Kozak, K. Butowska, F. Ferreira da Silva, J. Rak, and S. Denifl

XXXIst ICPEAC, July 23rd to 30th, 2019, Deauville, France

5. *Electron attachment to OTfU: A novel potential radiosensitizer*

E. Arthur-Baidoo, J. Ameixa, R. Meißner, S. Makurat, W. Kozak, K. Butowska, F. Ferreira da Silva, J. Rak, and S. Denifl

7th Center for Molecular Biosciences Innsbruck (CMBI) Meeting, September 19th to 20th, 2018, Innsbruck, Austria

6. *Positive and negative ion formation upon collision induced dissociation of 2-Formylphenylboronic acid*

J. Ameixa, J. Khreis, F. Ferreira da Silva, S. Denifl

XXIst Symposium on Atomic, Cluster and Surface Physics – SASP 2018, February 11th to 16th, 2018, Obergurgl, Austria

7. ***Low-energy electron scattering from radiosensitizers: associative vs. dissociative attachment***

S. Denifl, R. Meißner, J. Ameixa, E. Arthur-Baidoo, C. Lochmann, L. Feketeova, E. Illenberger, J. Kocisek, J. Fedor, F. Ferreira da Silva, P. Limão-Vieira, S. Makurat, W. Kozak, J. Rak

V International conference on Dynamics of Systems on the Nanoscale – DySoN 2018, October 8th to 12th, Potsdam, Germany

8. ***Dissociative electron ionization studies with chromium hexacarbonyl $Cr(CO)_6$***

J. Khreis, J. Ameixa, M. Neustetter, F. Ferreira da Silva, S. Denifl

CELINA 2017 - The fourth meeting of COST Action CM1301, May 13th to 16th 2017, Porto, Portugal

9. ***Low-energy electron interactions with chromium hexacarbonyl $Cr(CO)_6$***

F. Ferreira da Silva, J. Ameixa, J. Khreis, S. Denifl

XXX ICPEAC, July 26th to 1st of August 2017, Cairns, Australia

10. ***Elastic differential cross sections for electron scattering with dichloro methane***

E. Lange, K. Krupa, J. Ameixa, A. S. Barbosa, D. F. Pastega, P. Limão-Vieira, M. H. F. Bettega, F. Blanco, G. Garcia, F. Ferreira da Silva

XXX ICPEAC, July 26th to 1st of August 2017, Cairns, Australia

11. ***Comparison between electron energy loss spectrum and VUV photoabsorption spectrum of halothane***

E. Lange, J. Ameixa, P. Limão-Vieira, F. Ferreira da Silva

5^o ENURS Encontro Nacional de Utilizadores de Radiação Sincrotrão, June 17th 2016, Oeiras, Portugal

12. ***Experimental evidence of the low-lying triplet states of halothane as studied by electron energy loss spectroscopy method***

E. Lange, J. Ameixa, P. Limão-Vieira, F. Ferreira da Silva

ECAMP 12, September 5th to 9th, 2016 Frankfurt am Main, Germany

13. *Low-energy electron interactions with chromium hexacarbonyl*

J. Khreis, J. Ameixa, M. Neustetter, J. Reitshammer, F. Ferreira da Silva, S. Denifl

3rd CELINA annual meeting (CELINA 2016), 18th to 20th May 2016, Kraków, Poland

14. *Elastic differential cross sections for acetone by 7-50 eV energy electron impact*

E. Lange, G. Meneses, J. Ameixa, D. F. Pastega, M. H. F. Bettega, G. García, P. Limão-Vieira, F. Ferreira da Silva

XIX ICPEAC, 22nd to 28th July 2015, Toledo, Spain

A.B.2 Talks

1. *Electron attachment to OTfU: a novel potential radiosensitizer*

68th Annual Meeting of the Austrian Physical Society, September 11th to 14th 2019, Graz, Austria

Curriculum Vitae

1. Personal data

- **Name:** João Francisco Favinha Ameixa
- **Birth Date:** 21st of August 1992
- **Mobile phone:** 00351 926 837 650

2. Education and qualifications

- **PhD student in Radiation Biology & Biophysics – RaBBiT, University NOVA of Lisbon, Portugal & PhD student in Physics, Innsbruck Universität, Austria** Under the supervision of Professor Dr. Stephan Denifl and Professor Dr. Filipe Ferreira da Silva;
- **MSc. in Biomedical Engineering**, 2015, University NOVA of Lisbon, Portugal.

3. Attended meetings

- **MD-GAS– First annual meeting of the COST Action CA18212**, February 18th to 21st, 2020, Caen, France
- **I NOVA Biophysica International Conference**, September 4th to 6th, 2019, Lisboa, Portugal
- **XXXIst International Conference on Photonic, Electronic and Atomic Collisions (ICPEAC)**, July 23rd to 30th, 2019, Deauville, France

-
- **7th Center for Molecular Biosciences Innsbruck (CMBI) Meeting**, September 19th to 20th, 2018, Innsbruck, Austria
 - **68th Annual Meeting of the Austrian Physical Society**, September 11th to 14th, 2018, Graz, Austria
 - **XXIst Symposium on Atomic, Cluster and Surface Physics – SASP 2018**, February 11th to 16th, 2018, Obergurgl, Austria
 - **CELINA 2017 - The fourth meeting of COST Action CM1301**, May 13th to 16th, 2017, Porto, Portugal
 - **XIX International symposium on Electron-Molecule Collisions and Swarms - POSMOL**, July 17th to 20th, 2015, Lisboa, Portugal

4. Short-term scientific missions

- December, 16th to 20th 2019, DESIREE, AlbaNova University Centre - Stockholm University, Sweden;
- March, 25th to 29th 2019, DESIREE, AlbaNova University Centre - Stockholm University, Sweden;
- 1st of May to 1st of July 2017, Radiation Laboratory, Notre Dame University, United States of America
- February, 14th to 27th 2016, Institut für Ionenphysik und Angewandte Physik, Innsbruck Universität, Austria, "Dissociative electron attachment to Cr(CO)₆"

5. Thesis

- **Electronic States Characterization of the Anesthetic Halothane by High Resolution Electron Energy Loss Spectroscopy**, under the supervision of Professor Dr. Filipe Ferreira da Silva and Professor Dr. Paulo Limão-Vieira. MSc. Thesis (Grade: 19 out of 20), University NOVA of Lisbon, October 2016.

6. Training courses

- Top Down and Structural Mass Spectrometry: a practical course, December 19th to December 21st, 2016, Lisbon, Portugal.
- CELINA Training School on FEBIP (Focused Electron Beam Induced Pro-

cesses), July 3rd to July 5th, 2016, Vienna, Austria.

7. Teaching

- Winter semester 2019/2020
 - Physics II (Thermodynamics): Laboratory course and problem-solving lectures. (3h/week)

8. Other activities

- Music
 - Member of the UniversitätChor Innsbruck, since 2017 to 2019.
 - Member of Portuguese typical musical group of students - anTUNiA - Tuna de Ciências e Tecnologia da Universidade Nova de Lisboa, since 2014;
 - Musical Director of a Portuguese typical musical group of students - anTUNiA - Tuna de Ciências e Tecnologia da Universidade Nova de Lisboa, 2016;
 - Musician at Banda Filarmónica da Sociedade Recreativa 1^o de Janeiro, Castro Verde, Portugal, since 1998 to 2018;
 - 8^o grau at Conservatório Regional do Baixo Alentejo (CRBA), Beja (8^o grau in Musical Formation and Saxophone, 7^o grau de Classe de Conjunto, 2^o grau in Analysis of Composition Techniques and Music History);
- Others
 - Vice-President of the General Meeting Board of Sociedade Recreativa 1^o de Janeiro, Castro Verde, since 2011 to 2015.
 - Member of the organizing committee of the XXIV Tágides - Festival Internacional de Tunas Universitárias - Almada.

